THE UNIVERSITY OF CALGARY

ASSESSMENT OF A LASER SCANNING SYSTEM FOR DEFORMATION MONITORING APPLICATIONS

by

Nedal Naim Al-Hanbali

A THESIS

SUBMITTED TO THE FACULTY OF GRADUATE STUDIES
IN PARTIAL FULFILMENT OF THE REQUIREMENTS FOR
THE DEGREE OF DOCTOR OF PHILOSOPHY

DEPARTMENT OF GEOMATICS ENGINEERING

CALGARY, ALBERTA

APRIL, 1998

National Library of Canada
Acquisitions and Bibliographic Services
395 Wellington Street
Ottawa ON K1A 0N4
Canada

Bibliothèque nationale du Canada
Acquisitions et services bibliographiques
395, rue Wellington
Ottawa ON K1A 0N4
Canada

Your file Votre référence

Our file Notre référence

0-612-34654-4

Canada

Abstract

The Laser Scanning System (LSS) is a laser-based three-dimensional vision system. The LSS uses an auto-synchronization scanning scheme and is based on the triangulation principle and the Sheimpflug condition. The LSS provides fast and accurate three-dimensional deformation measurements and is designed for close-range measurements, with a maximum field of view of 34°X40°.The importance of using the LSS is its capability of measuring short-term point movements and surface movements utilizing a single station setup. An additional benefit is that it is a non-contact measurement system.

Using the LSS to measure three-dimensional movements in operating machinery is an application of leading-edge technology. The thesis explores the possibilities of using the LSS to monitor deformations in industrial applications. The development of software applications are also discussed and explained. Two approaches are discussed in this thesis to measure deformations. The first approach is to use the LSS calibrated parameters to measure point movements. The second approach is a local scaling method involving the direct interpretation of raw data. This approach is useful in showing surface deformations. In addition, the in-lab and on-site test results of using the LSS for non-contact measurements using the local scaling approach are presented and discussed.

The thesis reviews and discusses optical arrangements and characteristics of the LSS within the context of active triangulation range sensors. The thesis also reviews the ray

tracing and the mathematical model of the scanner, and includes an investigation of the capabilities and limitations of the LSS.

Within the context of system calibration, the following are explained: the LSS geometry and interpretation of its digital data, collinearity equations, and the calibration of LSS parameters. The thesis also discusses insights into the LSS assumptions and distortion effects and the associated distortion model. The model simulation, the instrument repeatability, the LSS predicted precision and some design aspects, as well as short and long distance calibrations are also discussed. Additionally, the thesis provides a detailed explanation of how to use a model-based approach and the least squares adjustment method to calibrate the LSS and also discusses the output results of the method.

Acknowledgments

This thesis is part of a research project named ***The Dynamic Alignment Project***. The motivation behind using the Laser Scanning System (LSS) is to develop a fast, non-contact measurement method for dynamic deformation monitoring. This development may complement and/or replace the state-of-the-art surveying engineering methods using electronic theodolite or electronic total station systems.

Professor W. F. Teskey was my supervisor for this thesis. He contributed his experience and knowledge in the area of Precise Engineering and Deformation surveys. He is a dear and kind friend who is and was always available with support, advice and direction. He was very encouraging and supportive throughout my graduate studies program.

I want to extend my appreciation and gratitude to *Dr. M. A. Chapman* for his valuable discussions, advice, assistance, and encouragement. He contributed his experience and knowledge in the areas of digital imaging and close-range photogrammetry. Also, thanks and appreciation to *Dr. S. E. El-Hakim* who enriched me with his knowledge of digital imaging and the Laser Scanning System. Dr. M. J. Collins and Dr. K.P. Schwarz assisted by answering a number of theoretical questions related to the mathematical models and their help is appreciated.

I would like to thank the Visual Information Technology Group at the National Research Council Canada, for their support while I worked as a guest researcher. Special thanks

and appreciation to Mr. Jacques Domey and to Mr. Marc Rioux, and also, to Luc Cournoyer, J.-Angelo Beraldin, and François Blais who supported me and answered my questions related to the Laser Scanning System technology. Furthermore, Luc Cournoyer helped us by providing his technical support and assistance to perform the lab tests (at The NRC labs) and the on-site test (at the Sheerness Generating Station) using the NRC laser scanner and his help is appreciated.

The effort of Robert Radovanovic is highly appreciated. He assisted in ray tracing and re-derivation of the mathematical model of the Laser Scanning System using AutoCAD software. He also assisted in performing precise surveys using an electronic theodolite system. Also, special thanks to Dr. Naser El-Sheimy, Derek Lichti and Ahmed H. Mohamed for providing helpful advice and computer programming support on many occasions.

I would like to thank Mr. Khaled Rafih and his brother Kasim Rafih for their continuous computer support (software and hardware) throughout my graduate studies, and special thanks and gratitude to Ms. Norsiah Jumaen, Mr. Ryan Tarves and Mr. Khaled Rafih for proofreading my thesis.

The technical and the secretarial staff in the Department of Geomatics Engineering, The University of Calgary assisted with this research work. Many other graduate students, especially Mohamed Mostafa and Ray Obidowski, and professors in the department have also contributed to my knowledge and motivation throughout the last four years.

The Dynamic Alignment Project (DAP), which provided the financial support for my research work, is a collaborative research and Development project involving the department of Geomatics Engineering at The University of Calgary, the Natural Science and Engineering Research Council of Canada (NSERC), the National Research Council of Canada, and a number of large industrial firms in Western Canada. The principle collaborating industrial partner is Kadon Electro Mechanical Services Ltd. of Calgary. The funding provided through the DAP by NSERC, Kadon, and the other industrial partners is gratefully acknowledged.

Dedication

To Maha, my wife

Who stood fast with me, and encouraged me with her continuous patience and support. Words are inadequate to thank her for her precious help.

Table of Contents

List of Tables

List of Figures

List of Abbreviations

- 3-D Three dimensional.
- CCD Charged Couple Device.
- DAP Dynamic Alignment Project.
- EDM Electronic Distance Measurement.
- Hz Hertz.
- IAP Industrial Alignment Project.
- LASER Light Amplitude by Stimulated Emission of Radiation
- LSS Laser Scanning System.
- NRC National Research Council of Canada.
- NSERC Natural Science and Engineering Research Council of Canada.
- PC Personal Computer.
- PEDS Precise Engineering and Deformation Surveys.
- RMS Root Mean Square.
- TF Target Field.
- VIT Visual Information Technology.

CHAPTER ONE

INTRODUCTION

1.1 Research Objectives

The purpose of this thesis is to explore and closely examine the Laser Scanning System's potential for machinery alignment monitoring in close-range (±1.5 m) industrial applications. Additionally, the thesis will explain and discuss the details of developing a calibration program and procedure for the NRC Laser Scanning System (LSS).

The Laser Scanning System (LSS) is a laser-based three-dimensional vision system that has been patented by the National Research Council of Canada (NRC). The system technique is based on an auto-synchronized triangulation scanning scheme. The system provides fast and reliable three-dimensional deformation measurements and can measure objects between 0.5 m to 100 m (∞ in definition) with a field of view of up to 34° X 40°. This flexible system can provide control over the scanned area and depth. The system provides two output images: an intensity image and a depth-coded image (see Beraldin et. al., 1993).

This laser scanning technology can reconstruct surfaces and measure continuous point movements (see Rioux, 1984). There are two advantages of this scanner: first, it utilizes a single station setup, and second, it is a non-contact measurement instrument.

To achieve the Dynamic Alignment Project (DAP, Section 1.2) goal of using the Laser Scanning System (LSS) for dynamic deformation monitoring, certain tasks must be completed:

1. Develop software for PC-based machines using a Windows operating system (e.g. Windows 3.1, Windows 95 or Windows NT 4) for image acquisition, displaying and processing that is suitable for the laser scanner images.

2. Develop interface software for PC-based machines using a Windows operating system to control the operation of the LSS.

3. Investigate and develop a procedure to directly interpret the scanner raw data images (e.g. the depth-coded images and the intensity images output) for deformation measurements.

4. Understand and review the mathematical model derivation of the LSS, and perform ray tracing to explore the capabilities and limitations of the system.

5. Develop and modify a calibration program for the LSS.

6. Develop a procedure and build a suitable target field to calibrate the LSS at the University of Calgary's Laser Scanning Lab.

The completion of these tasks was an essential step for further research, development and modification of the LSS for our research group (the Precise Engineering and Deformation Survey group (PEDS)) in the Department of Geomatics Engineering at the University of

Calgary. Building such experience enabled the group to have a better understanding of the capabilities of the system, so that it would to be used for different applications.

1.2 History, Background and Goals of The DAP

In 1993, the Dynamic Alignment Project (DAP) was approved as a Collaborative Research and Development project involving the Department of Geomatics Engineering at The University of Calgary, the Natural Science and Engineering Research Council of Canada, the National Research Council of Canada, and a number of large industrial firms in Western Canada. The principle collaborating industrial partner is Kadon Electro Mechanical Services Ltd. of Calgary.

The DAP is the major project in the area of Precise Engineering and Deformation Survey (PEDS) (see Al-Hanbali, 1993 and Al-Hanbali and Teskey, 1993), succeeding the first successful project, the Industrial Alignment Project (IAP). The objective of the DAP is the development of improved systems and procedures for monitoring alignment changes in heavy machinery, that make use of recent advances in Videometrics and laser scanning hardware.

The author joined the PEDS group for his Doctoral degree to develop a methodology and software for the DAP using a state-of-the-art LSS that is patented to and developed by the Visual Information Technology, National Research Council of Canada (NRC), Ottawa.

The task was interesting and challenging since the research work requires a strong background in the area of PEDS and photogrammetry and digital imaging, and extensive knowledge of computer programming and software.

Several factors have affected the research direction and the decision-making process. First, the chosen laser scanner was one of its kind and, therefore, the instrumentation was new to our group and so assistance was needed from its developers (i.e. Visual Information Technology, NRC). Second, the system developed by the NRC has a unique and complicated mathematical model, and is still undergoing development and modifications. Certain effects caused by manufacturing imperfections of the system had to be taken into consideration. The third factor was that no professor in our department had done research work related to the laser scanner instrumentation or its mathematical model. Fourth, the NRC system software was originally developed for the Unix operating system and Silicon-Graphics-based machines (the interface software needed to operate the LSS and the software needed for digital image processing). However, the decision made for the DAP was to use PC-based machines and the Windows Operating System (i.e. Windows 3.1, Windows 95 or Windows NT).

These factors combined together made the task more difficult and time consuming. However, the task was an important research step for our PEDS group to initiate this line of research and to set up a laser scanner lab. Furthermore, the author spent a year at the NRC to familiarize himself with this new technology in terms of instrumentation, software development, and the mathematical model background. He was trained on how

to operate the scanner and was made aware of some factors that can affect the performance and accuracy of the scanner. During that time, he also developed phase I of an Interface software that runs under the Windows operating system using a 486/DX2 or Pentium PC to operate the LSS.

Methods and techniques developed for the DAP should have a degree of precision that meets the needs of industrial applications. The degree of precision these applications require can be as high as 0.1 mm for short-range applications (see Teskey and Lovse, 1994 and Teskey et al., 1995a). Typical ranges for deformations in such applications are between 0.1 mm and 5.0 mm. Preference is always given to non-contact methods that are quick in terms of instrument-setup procedure.

Several research strategies have been taken in the DAP. One strategy is to develop new techniques and methods utilizing currently available off-the-shelf instruments. For example, a new targeting technique was developed utilizing a total station instrument (i.e. a precise electronic theodolite system with an EDM) so that movements of targets can be monitored continuously and precisely up to 0.1 mm (see Teskey et al., 1995b).

Another targeting technique was developed to allow sensor integration that makes use of a CCD camera (Kodak DCS420). The technique is versatile and fast in terms of instrument-setup requirements and datum definition, and allows for continuous monitoring with a good precision (0.2 mm) (see Obidowski et al., 1995). "**Continuous monitoring**" can be defined as data collection at time intervals short enough to monitor

the trend of change in movements. For example, in a typical industrial application, the time interval required to monitor the thermal growth of operating machinery during startup or shutdown is about 1 to 0.2 Hz (see Teskey et. al., 1994). The LSS has the potential to be used to monitor the thermal growth of operating machinery during startup or shutdown within such time interval.

1.3 Precise Engineering and Deformation Survey Development and Needs

The current state-of-the-art survey engineering methods in short-range deformation monitoring are limited to periodic deformation monitoring. In "**periodic deformation monitoring**" a complete set of measurements (usually survey network measurements), from which movements of points are subsequently computed, might be taken every few hours (e.g. on operating machinery), see Teskey et. al. (1994), Fuss and Teskey (1993) and Bayly (1993).

Because of the time required to take the measurements and to carry out the computations, it is very difficult to reduce the period to less than a few hours. Thus, important short-term deformations are completely missed in periodic deformation monitoring. Recently developed laser scanning instruments allow for the possibility of dynamic deformation monitoring (continuous collection of information about measurements), thus addressing this problem, see Teskey and Lovse (1994). For medium-range (200 m) to long-range (one km) deformation monitoring, the time-of-flight laser instruments provide moderately

accurate depth information. Teskey and Lovse (1994) did some preliminary testing for a time-of-flight laser instrument (Wild DIOR3012S Laser ranger).

For short-range (±1.5 m) applications, laser scanners based on auto-synchronized triangulation scanning schemes might be suitable for precise and reliable continuous collection of measurements. These instruments can be used to monitor both surface movements and point movements.

DYNAMIC DEFORMATION MONITORING: can be defined as continuous collection and analysis of deformation data. It should utilize only a single station from which observations to the deforming object are made. Stability of the single observing station is therefore of critical importance. The laser scanner provides depth coded and intensity images of a particular scene from one setup from which one can reconstruct three-dimensional objects. It is also a true non-contact instrument because no reflectors need to be mounted on the surface.

One component of the DAP is the use of the LSS for the development and testing of non-contact systems for monitoring changes in alignment of operating machinery. Three Workshop demonstrations were organized for industry to show the LSS capabilities, see Al-Hanbali (1993a, 1994) and Al-Hanbali and Laurent (1995). The changes in alignment (along with changes in size and shape of the operating machines) are due to temperature changes and changes in operating forces. These changes usually occur over periods of several minutes to several hours. Shown in Figure 1.1 is a turbine-gearbox-pump

combination, a typical machinery combination where alignment is critical. The figure also shows the survey network that was used to estimate the changes in alignment from shutdown (cold) to operating (hot) conditions (Bayly, 1993) by means of periodic deformation monitoring.

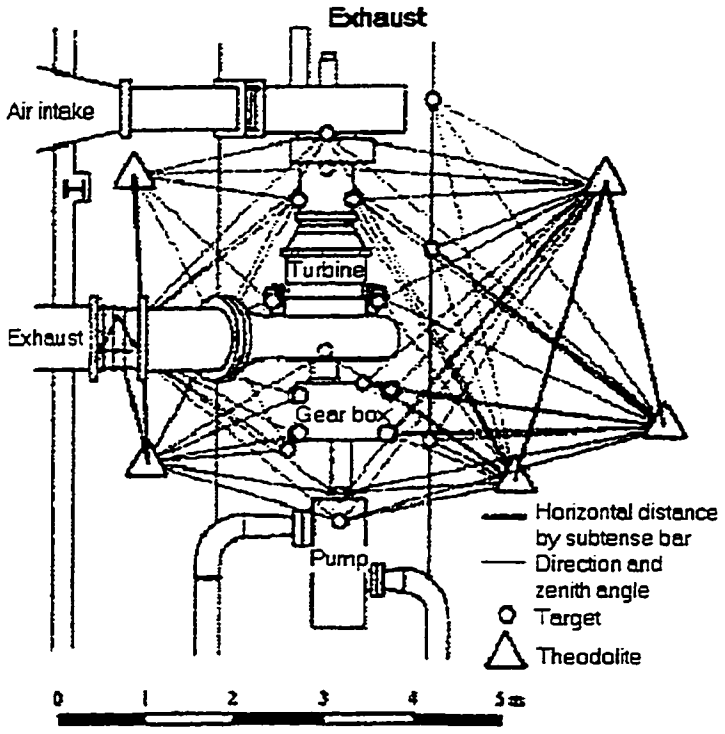

Figure 1.1: Alignment in a Turbine-Gear Box-Pump Combination (from Bayly, 1993).

1.4 Visual Information Technology (VIT) Line of Research

Visual Information Technology (VIT) is a group within the National Research Council of Canada. The Visual Information Technology (VIT) group has developed a three-dimensional laser scanning system. The laser scanner is based on a patented longitudinal (where the instantaneous field of view is parallel to the scan, see Blais et. al. (1988)) auto-synchronized scheme using triangulation principles, see Rioux (1984). Rioux et. al. (1987) showed that large fields of view with small triangulation angle can be obtained using an auto-synchronization technique and the Sheimpflug condition (see Section 2.2.2) without sacrificing precision. The auto-synchronization scanning scheme allowed a considerable reduction in the optical head size as well as reduction in the shadow effects because of the small triangulation angle.

Throughout the DAP time-span and as one of the VIT strategic goals , the VIT has provided the support required to use the Synchronized Laser Scanning System for deformation monitoring. The VIT has provided its technology and expertise and also has built an instrument for The University of Calgary for only the basic hardware cost.

1.5 Important Assumptions for the Laser Scanning System

The following are some important assumptions for the laser scanning system:

1. A pinhole model is assumed for the collecting lens to simplify mathematical model derivations.

2. The Sheimpflug condition is satisfied and optimal focusing is achieved. The condition requires that the detection axis, the projection axis and the lens axis intersect at the same point. Assuming a perfect Sheimpflug condition will mean that any point on each projected laser line is in focus on the tilted detector plane. Therefore, a good view of the scene objects is maintained. However, if the auto-synchronization approach (see Section 2.2.4) is introduced, the intersection of the three planes forms a small circle instead of a point. Hence the condition is not completely achieved and therefore yields less than optimal focusing.

3. The scanning mirrors are assumed to be finite in thickness and perfectly flat. They have a perfect front and back silver-coat, and assumed to have no wobble or jitter effects in the axis of rotation.

4. The rotating and the fixed mirrors of the instrument are assumed to be mounted perfectly. This should make the axis rotation of the X-axis rotating mirror and the axes of the fixed mirrors parallel, and that these axes are perpendicular to the axis of rotation of the Y-axis rotating mirror.

5. The galvanometer driven mirrors are calibrated and adjusted to compensate for temperature and drift effects.

6. Refraction effects are not considered as one of the error sources. If refraction is expected, a fan can be used to mix the air and to provide homogenous medium.

1.6 Overview of the Thesis

The following are the major components of this thesis:

1. Research objectives, history, background and assumptions are summarized in Chapter One.

2. The Laser Scanning System optical arrangements in the context of the active optical range imaging sensors, the system capabilities and the advantages and disadvantages of the system versus a CCD camera are explained in Chapter Two.

3. The mathematical model analysis and the ray tracing of the scanner's optical arrangements are explored and explained in Chapter Three.

4. System calibration, calibration procedure development, and the LSS internal, interior orientation, and exterior orientation parameters are explained. System repeatability and LSS expected precision, model simulation, distortion effects, theoretical aspects,

the calibration using the least squares method and the testing results for measuring deformations using calibrated parameters are explained in Chapter Four.

5. The local scaling approach, the developed software, the testing and the LSS potential for industrial deformation monitoring are discussed in Chapter Five. The approach of deriving the deformation directly from the raw-data of the LSS images by local scaling without LSS calibration is explored. (i.e. the depth distances for the Z-axis deformations are derived from the depth-coded image data, and the X and Y axes deformations are derived from the intensity image data). Suggested deformation measurement methodology using calibrated parameters is also explained in Chapter Five.

6. Conclusion and recommendations are summarized in Chapter Six.

CHAPTER TWO

THE LASER SCANNING SYSTEM

2.1 Active, Optical Range Imaging Sensor

2.1.1 Introduction

Active, optical range imaging sensors collect three-dimensional coordinate data from object surfaces. These range sensors are unique imaging devices because the image data points explicitly represent scene surface geometry in a sampled form; hence, the data points can be directly interpreted as a three-dimensional structure, which eliminates many of the problems encountered in other types of imagery. However, most low-level problems such as filtering, segmentation, and edge detection remain the same as in other types of imagery. Another advantage of range sensors is that many of them can acquire both range images and registered intensity images, which can be useful for image digitization and edge detection.

The range sensors are useful in a wide variety of applications especially in automaton applications such as shape acquisition, bin picking, assembly, inspection, gauging, robot navigation, medical diagnosis, and cartography. A survey of range-imaging methods done by Besl P.J. et. al. (1988) provided a simple methodology for quantitative performance comparisons. The paper addressed and compared six different optical principles that have been used to actively obtain range images, two of which are addressed through the Dynamic Alignment Project research work: i.e. the radar and the triangulation principles.

The study shows that the radar and triangulation methods are more versatile and suitable for a large field of view without compromising precision and accuracy. In general, one radar principle is based on detecting and measuring the time-of-flight of a reflected pulse wave (e.g. laser radar). Distance is calculated based on the speed of the emitted wave and the time elapsed, similar to what bats use (ultrasonic radar) as their vision system. Triangulation is based on the law of sines for measuring the range to remote points. Section 2.2 describes the details of this principle.

For accurate and precise depth measurements, Blais et. al. (1988) suggested the use of time of flight instruments (radar principle) for medium to long distance measurements and triangulation instruments for short distances. Sequeira et. al. (1995) developed a new 3-D scene analysis system to automatically reconstruct a 3-D geometric model of a real-world scene from multiple range images acquired by a Laser Range Finder (a time-of-flight laser radar) mounted on board a mobile robot. Teskey and Lovse (1994) did preliminary testing for the Dynamic Alignment Applications and indicated that range instruments (such as the Wild DIOR3012S time-of-flight instrument) are suitable for medium-range (200 m) to long-range (1 km) applications. The paper also suggested the use of laser scanners based on auto-synchronized triangulation scanning schemes for short-range (1.5 m) applications for precise and continuous collection of measurements.

Al-Hanbali and Teskey (1994) performed preliminary testing to address the use of the NRC Laser Scanning System for three-dimensional dynamic deformation monitoring.

This paper was part of the Dynamic Alignment Project research work and was also considered an important step that led to this thesis.

Besl (1984) discussed briefly the four basic types of range sensors, based on the viewing constraints, scanning mechanism and object movement possibilities. These are:

1. **Point Sensor:** The sensor measures the distance to a single visible surface point from a single viewpoint along a single ray. A range image can be created if (i) the object of interest is physically moved in two directions in front of the point-ranging sensor, (ii) the point-ranging sensor itself is moved while scanning in two directions over the scene, or (iii) the scene object is stepped in one direction while the point sensor is moved in the other direction while scanning.

2. **Line or Circle Sensor:** The sensor measures the distance to visible surface points that lie in a single 3-D plane or cone that contains the single viewpoint or viewing direction. A range image can be created if (i) the scene object is moved orthogonal to the sensing plane or cone or (ii) the sensor, itself, is moved while scanning over the scene in the orthogonal direction.

3. **Field of View Sensor:** The sensor measures the distance to many visible surface points that lie within a given field of view relative to a single viewpoint or viewing direction. No scene motion is required as the sensor creates a range image directly.

4. **Multiple View Sensor System:** The system locates surface points relative to more than one viewpoint or viewing direction. Because all surface points of interest are not visible or cannot be adequately measured from a single viewpoint or viewing direction as the scene object or the sensor are not permitted to move.

The Laser Scanning System can perform all of the above sensor tasks. A point sensor can be utilized to scan and create a line or circle along one axis (i.e. a line or circle sensor), then scan orthogonal to the line or circle axis to create a field of view scene (i.e. a field of view sensor). Any combination of point, line/circle and field of view sensors can be used to create a multiple view sensor. The combinations are: (i) rotating and/or translating the scene in front of the sensor; (ii) maneuvering the sensor(s) around the scene with a robot; (iii) using multiple sensors in different locations to capture the appropriate views; or any combination of the above.

2.1.2 Definitions of Sensor Performance Parameters

Active refers to the use of a beam of radiation, generally laser, for depth measurement techniques, where **passive techniques** do not require a controlled source of light. In the context of **Dynamic Alignment Project,** the word **dynamic** refers to the continuous collection and analysis of deformation data.

The following are useful definitions of some concepts related to image acquisition strategies and to the geometry of the **NRC Laser Scanning System** (see Boulanger et. al. 1992, by Besl P.J. et. al. (1988) and Beraldin et. al. 1994) :

Resolution: The smallest spatial interval that can be registered.

Accuracy: The difference between true and measured mean value.

Precision: The closeness of approach to the arithmetic mean of each reading.

Repeatability: For repeated measurements, repeatability is an indicator of the closeness of the precision to the resolution of the instrument.

Dynamic Range: In the context of digital 3-D imaging, **dynamic range** is the difference between the maximum and the minimum values the position detector can register.

Depth coded image: A two-dimensional digital image that provides the main source of three-dimensional information. The image is digitized into a grid of pixels, each pixel is labeled with a pair of x and y coordinates that correspond to the column and the row numbers. The registered value of each pixel corresponds to the depth information. The dynamic range of the registered value, for example, of the LSS is a 16 bits integer (i.e. the numerical value is between 0 and 32768).

Intensity Image: This image is similar to the depth-coded image except that the registered value corresponds to the intensity of the laser spot. The dynamic range of the registered value, for example, of the LSS is a 12 bit integer (i.e. the numerical value is between 0 and 4096). This image is very similar to the CCD camera and is useful for edge detection and target location.

Image Resolution, Size or Dimension: The total number of pixels along the x and y axes for a specific field of view.

Range Resolution: The smallest change in range that a sensor can report, see Figure 2.1

Baseline: The distance between the sensor principal point or the lens center and the laser source deflection point. It determines the physical size of the sensor head.

Field of View: The volume that can be scanned, see Figure 2.1.

Angular Field of View: The total angle that the sensor can scan of the field of view, see Figure 2.1.

Standoff Distance: The distance between the sensor and the closest measurable position, see Figure 2.1.

Depth Distance: The distance between the sensor and the measurable position, see Figure 2.1.

Depth of Field: The length of the distance interval over which the sensor can perform measurements, see Figure 2.1.

In Figure 2.1, **r** is the detected depth and **Z**-axis and **X**-axis are the depth axis and the horizontal image axes of the range sensor, respectively.

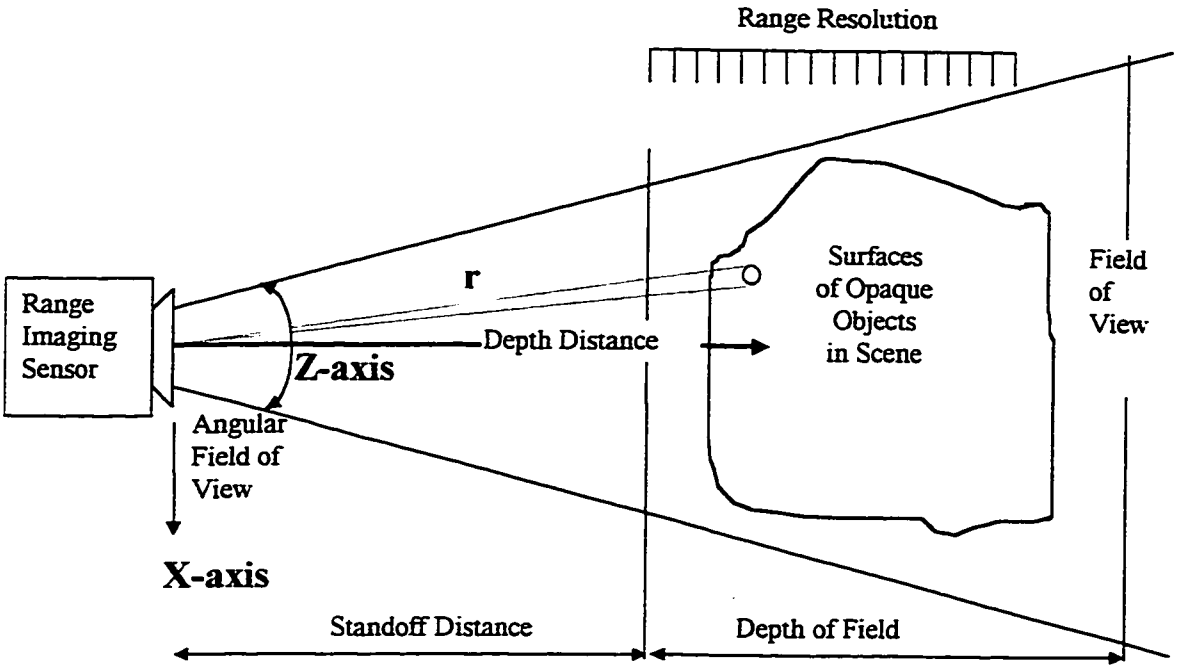

Figure 2.1: Range imaging sensor with angular scan.

2.2 Optical Arrangement

2.2.1 Basic Optical Triangulation

The standard geometrical optics of an active triangulation system are shown in Figure 2.2 (Blais et. al., 1988). The system is composed of a laser beam generator, a scanning mirror to deflect the laser beam, a lens and a position detector (a one array Charged Couple Device (CCD) sensor for the LSS). The laser beam is deflected toward the object of interest. The 2-D coordinate position of a point is calculated based on the spot position on the CCD sensor of the reflected beam **p**, the projection angle θ, the total length of the CCD sensor **P**, the base line **d** (the distance between the lens and the deflector of the laser beam) and the effective focal length $\mathbf{f_o}$ (the distance between the lens and the CCD sensor). The equations of the 2-D coordinate position of a point are:

$$z = \frac{d\, f_o}{p + f_o \tan(\theta)} \qquad \text{Equation 2.1a}$$

and $\quad x = z \tan(\theta) \qquad \text{Equation 2.1b}$

According to the lens law, if the object is in focus, then the relationship between the effective focal length $\mathbf{f_0}$, the object depth l, and the focal length **f** is:

$$\frac{1}{f_o} + \frac{1}{l} = \frac{1}{f} \quad \Longrightarrow \quad f_o = l\, f/(l - f) \qquad \text{Equation 2.2}$$

Note that if ℓ is assumed to be at infinity, the focal length f is approximately equal to the effective focal length (if $\ell \approx \infty$ then $\mathbf{f} \cong \mathbf{f_o}$).

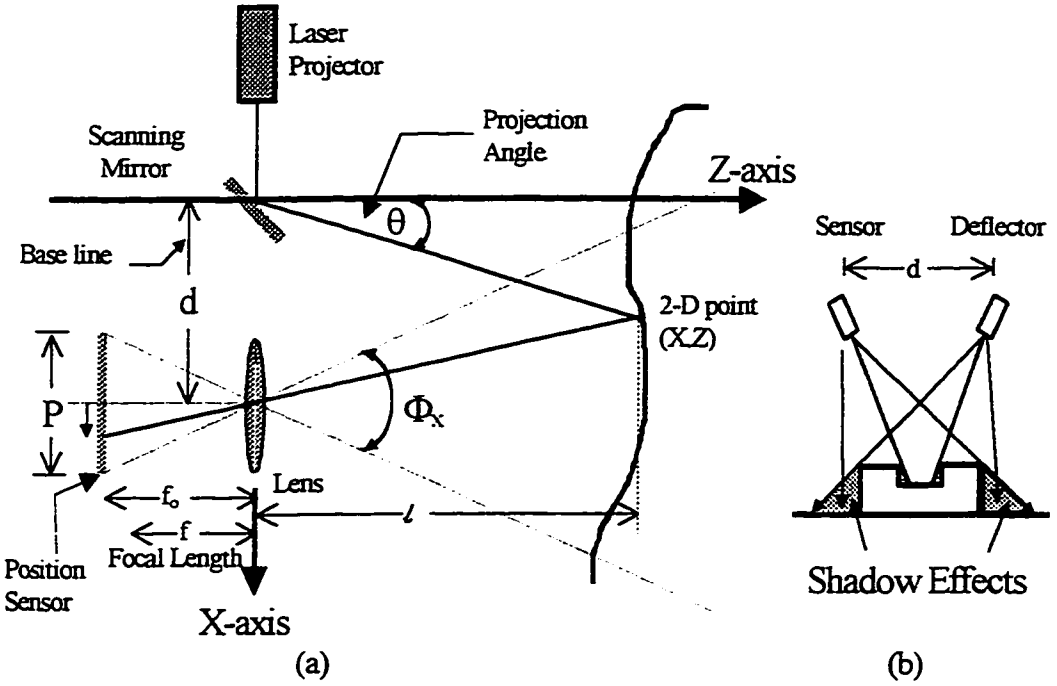

Figure 2.2:(a)Optical arrangement of the active triangulation principle. (b)Shadow effects.

Equations 2.1a and 2.1b show that, for a chosen active triangulation system, if the base line distance **d** and the effective focal length $\mathbf{f_o}$ are precisely determined and can be fixed, then the range resolution of a triangulation system is limited only by the ability to accurately measure the angle θ and the horizontal position **p**. Using the law of propagation of errors and assuming **d** and $\mathbf{f_o}$ are constant, then the standard deviation of the error along the z axis (σ_z) as a function of the standard deviation of the error of the angle θ and of the horizontal position **p** (σ_θ and σ_p) is given in Equation 2.3. The

standard deviation of the error along x axis (σ_x) as a function of the standard deviation of the error in the angle θ and in the distance **z** (σ_θ and σ_z), is given in Equation 2.4.

$$\sigma_z^2 = \left(\frac{z^2}{f_o\, d}\right)^2 \sigma_p^2 + \left(\frac{z^2}{d\cos^2(\theta)}\right)^2 \sigma_\theta^2 \qquad \text{Equation 2.3}$$

$$\sigma_x^2 = (\tan(\theta))^2\, \sigma_z^2 + \left(\frac{z^2}{\cos^2(\theta)}\right)^2 \sigma_\theta^2 \qquad \text{Equation 2.4}$$

Equation 2.3 leads to important criteria for an active triangulation system. The standard deviation of the error along the z-axis, σ_z, is inversely proportional to both the effective focal length $\mathbf{f_o}$ and the baseline distance **d**, and is directly proportional to the square of the range **z**. This implies that these systems provide better precision for close-range measurement than for medium-range to long-range measurements. However, the size of the baseline distance **d** and the effective focal length $\mathbf{f_o}$ are limited to the desired optical head and by the shadow effects (i.e. larger baseline distance results in larger optical head and more undesired shadow effects). As shown in Figure 2.2, shadows effects are produced when either the sensor or the deflector cannot reach the same area or region.

Another important factor in designing this type of system is the overall field of view Φ_x, see Figure 2.2a. In the conventional triangulation geometry, the field of view Φ_x of a sensor, where the light beam can be scanned over the whole field of view, is given by:

$$\Phi_x = 2\tan^{-1}\left(\frac{P}{2f_o}\right) \qquad \text{Equation 2.5}$$

where **P** is the total length of the position detector. From Equation 2.5, a compromise between field of view, precision of the 3-D measurements, and shadow effect is to be considered (Beraldin et. al., 1993).

2.2.2 Synchronized Scanner

Synchronizing an active triangulation scanner provides a larger field of view with small triangulation angles and a reduction of shadow effects. Synchronization is achieved by rotating, at the same time, the position detector the same rotational angle θ as the deflection of the laser beam. This can be achieved by implementing and synchronizing two rotating deflecting mirrors at points **O1** and **O2** in Figure 2.3a. The mechanism of rotating the position detector forms a unique feature called an instantaneous field of view. Figure 2.3b illustrates the instantaneous field of view of the position sensor as it follows the laser spot scanning the object of interest. Note that the focal length of the lens is only related to the desired depth of field or measurements range.

2.2.2.1 Ambient Light Immunity

A unique feature of the synchronized scanner geometry is its immunity to ambient light. The collection system (i.e. the lens and the position detector) acts as a tracking system so that the instantaneous field of view (the collection system) is following the projected laser beam (see Figure 2.3b). The signal-to-noise ratio for each profile point is very high, since the CCD image on the scene is aligned with the direction of the scan. Therefore,

specular reflection from ambient light would interfere only when the instantaneous field of view is covering the area of concern, (Rioux et. al., 1987).

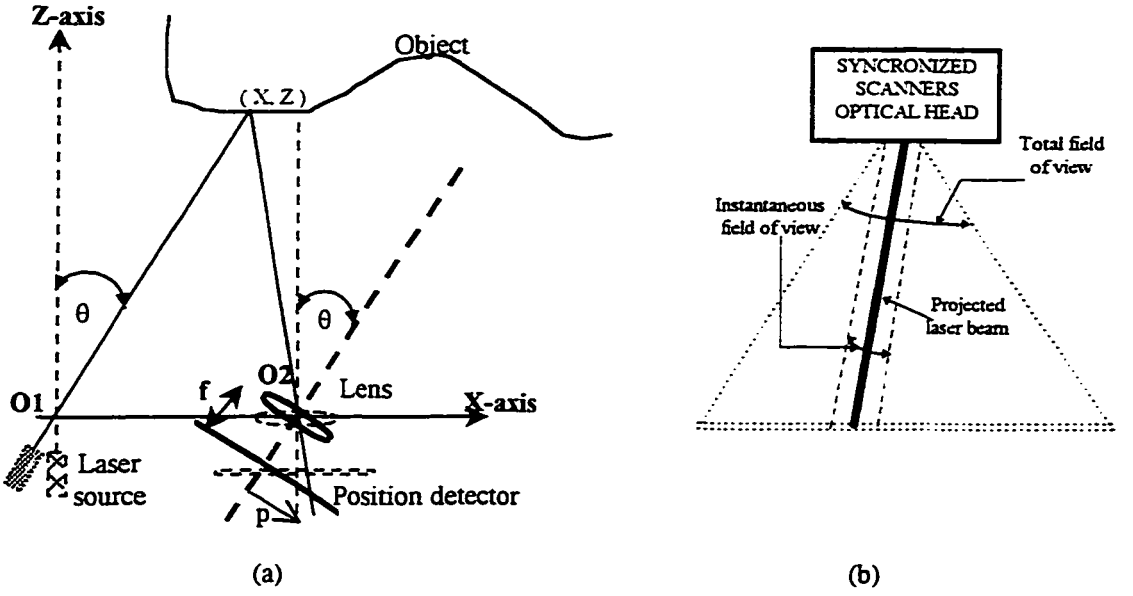

Figure 2.3: Synchronized scanners. (a) Optical arrangement of the synchronization principle. (b) Ambient light immunity is improved due to the alignment of the CCD with the scanned line.

2.2.3 Sheimpflug Condition

In photogrammetry, the Sheimpflug condition is used for rectification purposes to produce sharp imagery. Focusing is achieved by satisfying the lens law of optics, Equation 2.2 (see Manual of Photogrammetry, 1980):

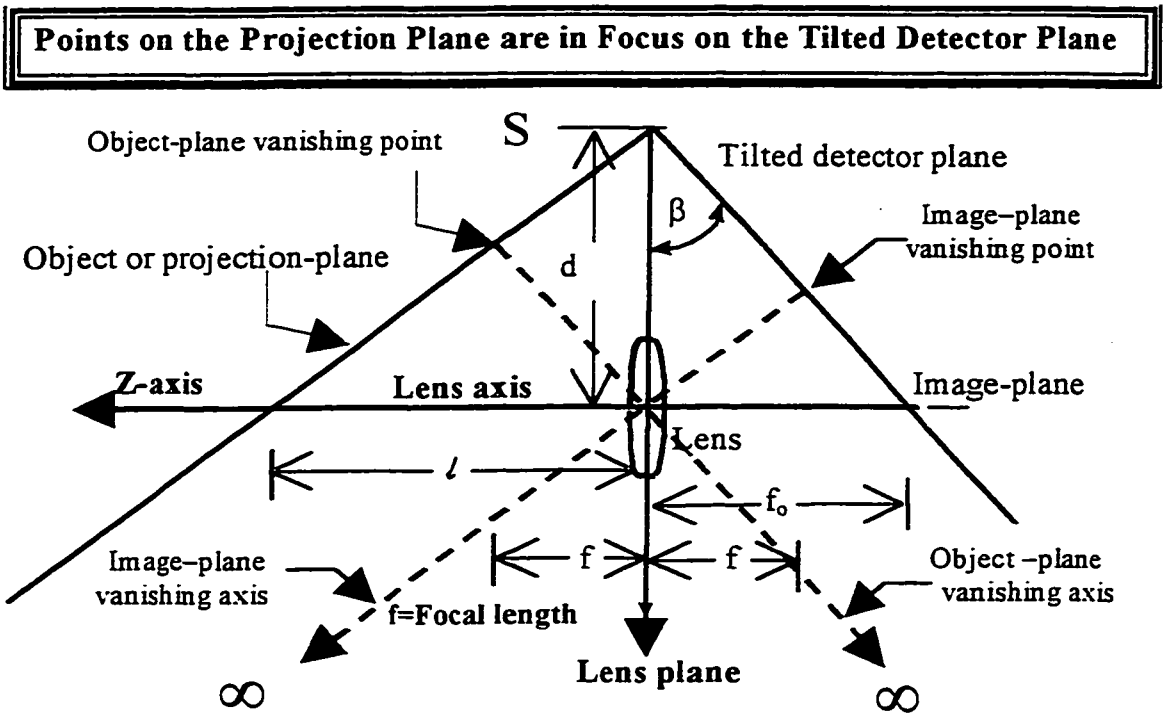

Figure 2.4a: Sheimpflug Condition: optical arrangement of object-plane and image-plane with respect to the lens plane.

The optical arrangement of object-plane and image-plane with respect to the lens plane is illustrated in Figure 2.4a. The Sheimpflug condition is achieved when the three planes (i.e. image, object and lens planes) intersect along a line (in Figure 2.4a, the point **S** is on this intersection line). The object-plane vanishing point is at a distance equal to the focal length **f** from the lens plane to the image at infinity. Similarly, the image-plane vanishing point is along a plane projected through the lens from an object at infinity. Also, the planes passing through these two vanishing points and the lens center are parallel to the image-plane and to the object-plane, respectively.

The importance of using the Sheimpflug condition is that **any point on the projection plane will satisfy the lens law of optics and, hence, is in focus on the image plane**. The Sheimpflug condition is considered an advantage to the system to achieve **optimal focusing** because of the use of coherent light projection (laser ray), see Figure 2.4b. Furthermore, this arrangement allows one to get a very large depth of view and to keep lens aperture at maximum, thus reducing speckle noise and improving signal strength, see Rioux et. al. (1987) and Blais et. al. (1988). From Figure 2.4a, the tilt angle β is defined as:

$$\beta = \tan^{-1}\left(\frac{f_o}{d}\right) \qquad \text{where} \qquad f_o = {(f\,l)}/{(l-f)} \qquad \text{Equation 2.6}$$

2.2.3.1 Lateral Magnification

The lateral magnification ratio is useful in finding the ratio of the spot size of the laser beam on the object compared with its desired size on the position sensor. Lateral magnification is defined as the image size over the object size (i.e. (image size)/(object size) = **p1/x1** from Figure 2.4b).

$$M_l = \frac{p1}{x1} = \frac{px1/\cos(\beta)}{x1} \cong \frac{f_o}{l\cos(\beta)} = \frac{f}{(l-f)\cos(\beta)} \qquad \text{Equation 2.7}$$

Points on the Projected Laser Ray are in Focus on the Position Detector

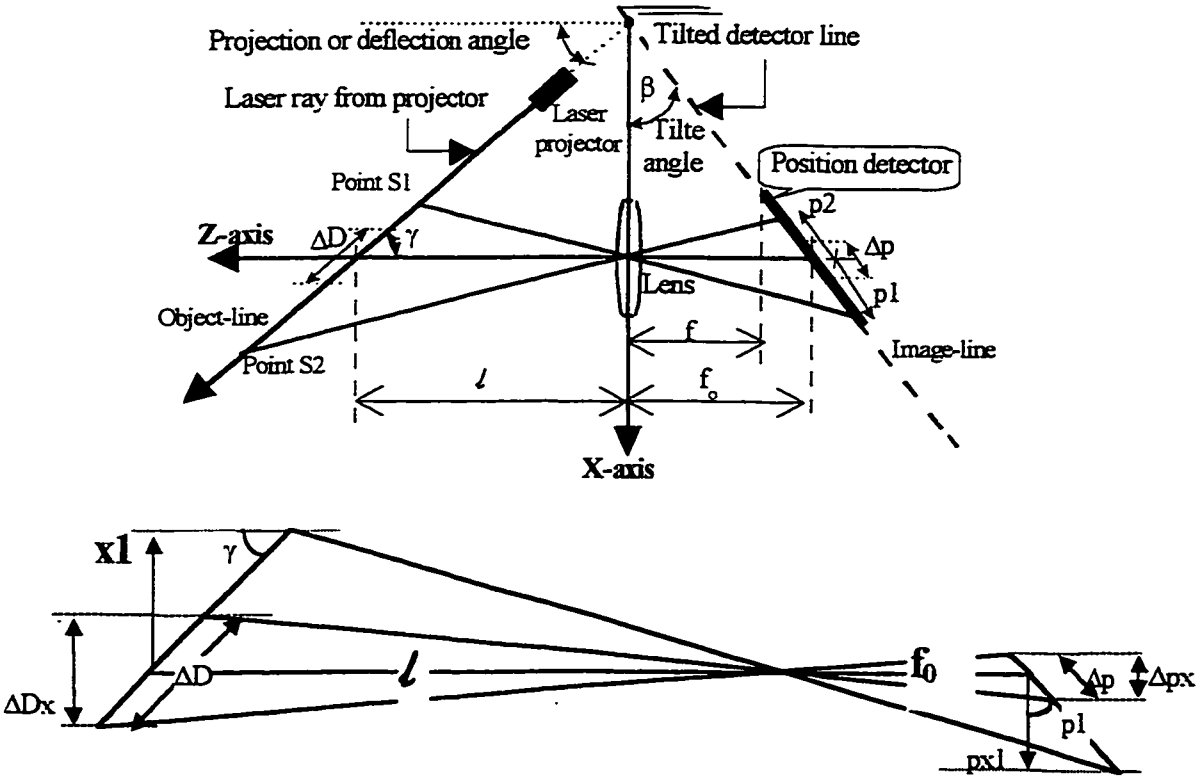

Figure 2.4b: Sheimpflug condition: projected laser ray optical arrangements.

It is important to note that in order to use the LSS sub-pixel peak detector efficiently (for more details see Blais and Rioux 1986, Baribeau and Rioux 1991a and 1991b) an image of the beam should be wider than a pixel. Typically, the lateral magnification factor is between 0.1 and 1.0. (The LSS lateral magnification factor is 0.126.)

2.2.3.2 Range (Longitudinal) Magnification

Longitudinal magnification is defined as the ratio of the displacement of the laser spot image on the position sensor to the change in range of the scene (i.e. **Δp/ΔD**, see Figure 2.4b):

$$M_R = \frac{\Delta p}{\Delta D} = \frac{\Delta px/\cos(\beta)}{\Delta Dx/\sin(\gamma)} \cong \frac{f_o \sin(\gamma)}{l\cos(\beta)} = M_l \sin(\gamma) \qquad \text{Equation 2.8}$$

This relationship $\mathbf{M_R}$ shows the non-linear variation of the size of the object on the CCD sensor due to the lateral magnification $\mathbf{M_L}$ and the projection or deflection angle γ. (The Longitudinal magnification factor is 1:108=0.0093.)

2.2.4 Auto-synchronized Scanner

The auto-synchronized scanner, an innovative approach introduced by Rioux (1984), is based on the synchronized scanning approach (synchronizing the projection of the laser spot with its detection) and the Sheimpflug condition. Figure 2.5 illustrates the mechanism of the auto-synchronization scheme. Auto-synchronization means that the projection of the laser spot and the deflection of the detection axis are synchronized

automatically by using one rotating mirror and two fixed mirrors. The rotating mirror is silver-coated on both sides while the fixed mirrors are silver-coated on the front. To compare the synchronization approach to the auto-synchronization approach, points of deflection **O1** and **O2** in Figure 2.3a are the same as points **O′** and **O″** in Figure 2.5a.

Implementing auto-synchronization allows considerably smaller optical head size than the synchronized systems. Also, implementing the Sheimpflug condition achieves optimal focusing. Therefore, better signal to noise ratio and sharper images are obtained. This also improves edge detection and, hence, provides more precise measurements.

As illustrated in Figure 2.5a, the laser ray is first deflected by the rotating mirror by half the angle θ, and then is deflected by the fixed mirror. When the beam is deflected back by an object, the point of deflection on the object is the detected object-space point. To detect this point, the beam must first be deflected by the other fixed mirror and then by the other side of the rotating mirror that goes through the lens to form a laser-spot image on the CCD sensor.

In Figure 2.5a, the dashed-line circle is composed of object-space points that constitute the geometrical trajectory of the principal point and the deflection points O', O''.

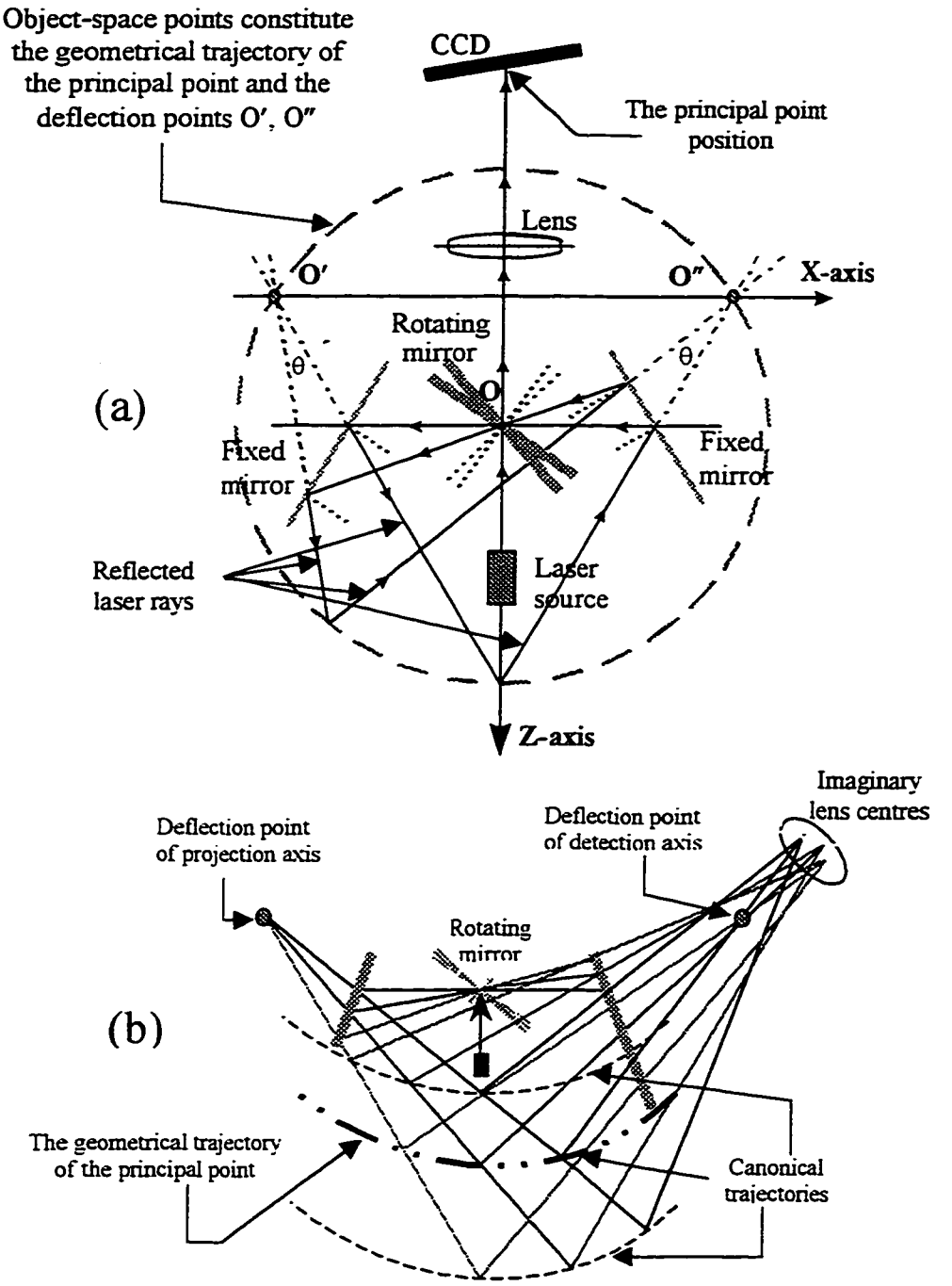

Figure 2.5: (a) Optical arrangement of the Auto-Synchronize scanner. (b) Canonical trajectories at different depth values.

The auto-synchronization approach has an interesting geometrical property that shows the canonical (spherical in this case) form of acquisition. For every point on the position sensor, there exists a canonical geometrical trajectory of detected object-space points, each object point is distinguished by its projection angle θ. An angle θ at the points of deflection, points **O′** and **O″** in Figure 2.5a, results from the rotating mirror deflecting the laser beam an angle equal to half the size of θ.

The object points along the dashed-line circle in the figure are detected by step-wise deflections of the laser beam. The principal point is the image position on the CCD sensor of the scanner. As illustrated in the figure, intersecting the projected laser ray axis and the reflected axis by a deflection angle θ produces each point on the trajectory. When the ray is reflected back, it coincides with the same spot position on the CCD sensor. Figure 2.5b shows several geometrical trajectories for various spot positions on the sensor. These trajectories are only related to the desired depth of field or measurements range.

2.3 The University of Calgary Laser Scanning System (LSS)

2.3.1 General Specifications

The laser scanner for The University of Calgary is a dual-axis laser scanner that can operate in either raster or Lissajous mode. The camera dimensions are 270 mm X 180 mm X 100 mm. The field of view of the laser scanner can be as large as 34° X 40°, the standoff distance is 0.5 m and it can measure objects up to 100 m (∞ in definition). The laser scanner can detect returning light from almost any type of surface, even with the surface as much as 60° off perpendicular from the incident laser beam. This latter characteristic is very important for many applications, and distinguishes this type of laser scanner from theodolite-mounted laser scanners. A compact and versatile high-speed dual-galvanometer controller was designed specifically to steer the laser beam to any spatial location within the field of view of the camera, see Blais et. al. (1988). The angular resolution of each galvanometer is 1/300 000 radians. The system has a rotation stage for larger horizontal field of view with an angular resolution of 1/50 000 radians.

The scanner provides the user with two types of images (dimensions are in pixels): a depth coded image and an intensity image. The size of the image can be changed according to the size of the scanned object, the field of view and the resolution required. The size of an image does not have to be identical in both directions of a scan and each image can vary in size from 32 to 4096 pixels per line (based on a multiple of 2). The image can also be a single point image (field of view is 0° X 0°). The acquisition speed

can be as high as 18 kHz. For example, a scene of 512X512 pixels can be captured, using the raster mode, in about 14 seconds. If only a small part of the scene is needed to be captured (e.g. vibration monitoring), using the Lissajous mode and 128 elements, the scan rate of the scene can be as high as 137 Hz., see Blais et. al. (1991) and Blais et. al. (1993).

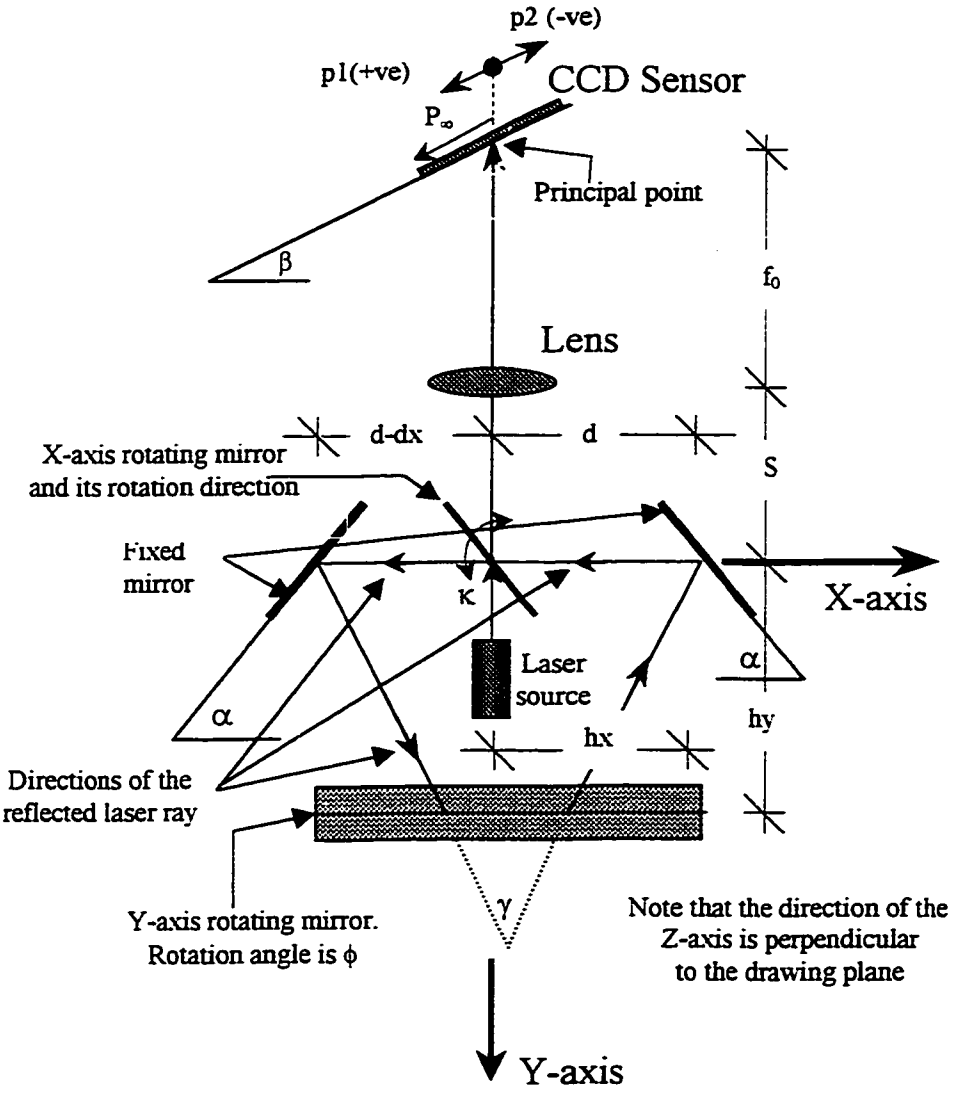

Figure 2.6: Optical arrangement geometry unfolded along the X-axis scanner.

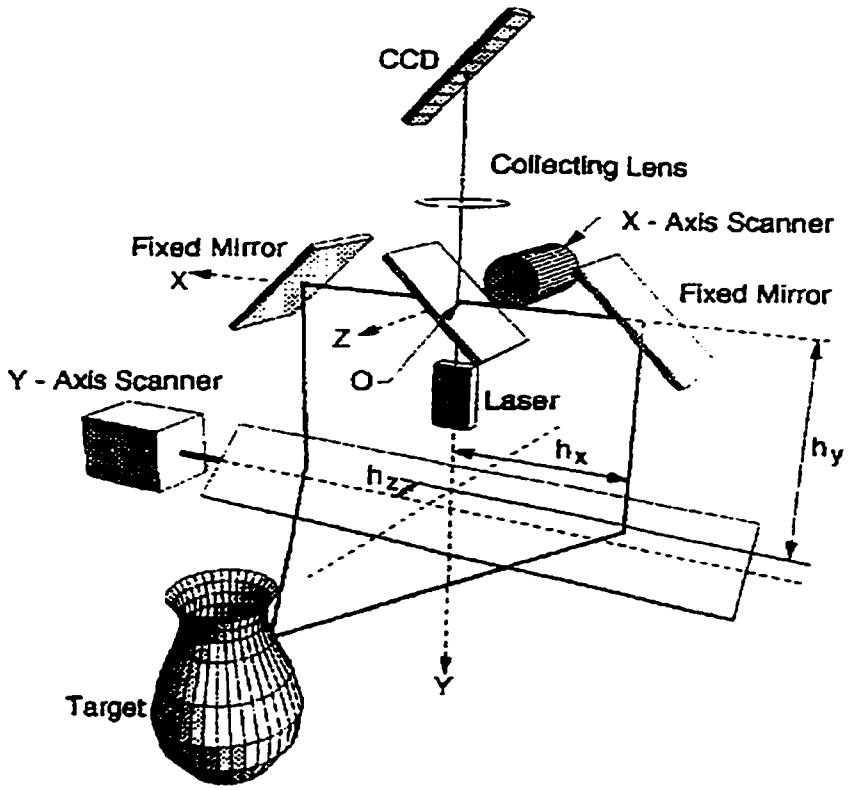

Figure 2.7 Dual-axis synchronized scanner in schematic representation (from Beraldin et. al., 1993).

The dual-axis laser scanner is shown schematically in Figure 2.6. Figure 2.7 shows un-folded geometry along the X-axis scanner and the optical arrangement of the dual-axis laser scanner in schematic representation. Assuming that the scanner is set up (on a tripod for example) with the axis of the pulsed laser aligned vertically. The X-axis scanner (i.e., the galvanometer) measures the angular position of a given point of interest in the horizontal plane, while the Y-axis scanner (i.e., galvanometer) measures the angular position of the same point in the vertical plane, or vise versa. As shown in the Figures 2.5, 2.6, and 2.7, the distance to any point of interest is computed by triangulation. Two mirrors on either side of the Z-axis scanner act as a "**baseline**" and, as the scanning

mirror (on the vertical axis between the two fixed mirrors) rotates, the position of the returning laser light on the CCD position detector shifts according to the distance from the point of interest.

2.3.2 Position Sensor

The position sensor is a CCD (Charged Couple Device) linear array solid-state photo-detectors composed of 512 pixels with a length of 0.05 mm each. Using the sub-pixel resolution peak detector (see Blais and Rioux, 1986 and Blais et. al., 1988), the resolution obtained for each pixel is approximately in the order of 1/64. Hence, a laser spot position on the sensor has a dynamic range of 0 to 32768 digital value (i.e. 512X64=32768). It is important to note that an image of a laser spot should be wider than a pixel. In practice, the measured position is limited to between 1/5 to 1/8 of a pixel, principally because of the distortion of the imaged spot created by the speckle of the laser light. For more details on this see Blais and Rioux (1986), and Baribeau and Rioux (1991a and 1991b).

Furthermore, peak intensity is measured with a RMS accuracy of 1/10 of a pixel. Using a 512-pixel CCD running at a pixel clock rate of 10 MHz, a typical resolution of 1/5000 in depth at a rate of 20 000 3-D data points per second is obtained. Hence, the maximum acquisition speed of the LSS is 20 000 elements per second (i.e. acquisition rate of 20 kHz.) However, the practical acquisition speed is 18 000 elements per second.

2.3.3 Scanning and Acquisition Strategies

Several strategies can be used to acquire three-dimensional imagery. These strategies are dependent on the use of: only the X-axis galvanometer, the X-axis galvanometer and a rotational or translation stage, or both the X-axis and Y-axis galvanometers. Also, these strategies are dependent on the mechanism these axes are driven through.

Blais et. al. (1991) listed the five strategies that the LSS can perform to scan the scene and read the information available. These are:

1. **Point mode:** is a random access approach where individual pixels are addressed and range is measured. To drive the scanner, a single geometrical feature extraction algorithm can be used where both galvanometer-axes are set to one specific position.

2. **Vector mode:** is a random orientated line scan where a profile is read at a desired orientation. Length of the line and spacing are fully programmable where one or both galvanometer-axes can be driven along the required path.

3. **Raster mode:** is used in digital cameras, where each line in an image is read sequentially. In this case, both galvanometer-axes are driven along either a triangular or a ramp schematic pattern. Using the ramp pattern will drive the scanner to scans along one direction while it is going upward and then cause it to step downward and start scanning along the subsequent line. However, using a triangular pattern will

yield the scanner to scan along both directions. Figure 2.8 illustrates these patterns and the acquisition direction.

4. **Lissajous pattern:** is created by driving the two X-axis and Y-axis galvanometers with sine waves of different frequencies and by adjusting their relative phases and amplitudes. It is used for tracking operations, see Blais et. al. (1991) and Blais et. al. (1993). Figure 2.8 illustrates some of these patterns.

5. **Rosettes pattern:** is created, similar to Lissajous mode, by driving the two X-axis and Y-axis galvanometers with sine waves of different frequencies and by adjusting their relative phases and amplitudes.

This thesis will concentrate on the use of the first three modes for imagery acquisition, especially the third mode (i.e. raster mode) for image acquisition using the triangular pattern.

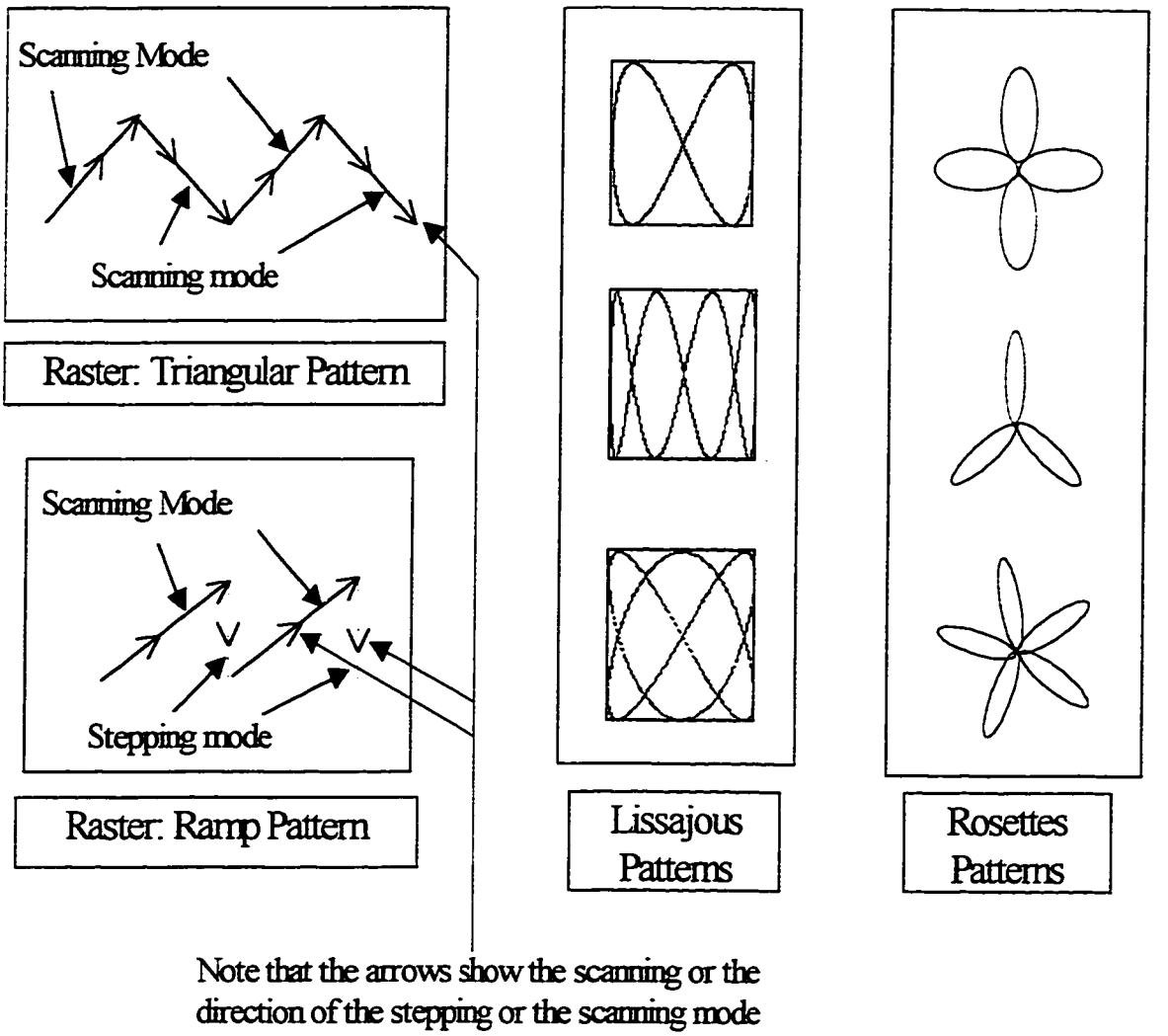

Figure 2.8: Raster, Lissajous and Rosettes acquisition patterns.

2.4 The Laser Scanner System (LSS) versus a Stereo CCD Camera System

This comparison illustrates the importance and the usefulness of active-range sensors compared to the well-established and developed methods of non-topographic photogrammetry using modern high-resolution CCD cameras. The currently, stereo CCD camera system has proved to be a fast, reliable, well-developed and precise method. Although, the system has some limitations in resolution, field of view and surface reconstruction and modeling. The following sections discuss the difference in capabilities between the two systems.

2.4.1 Control Field and Speed

The versatility of the LSS permits the use of various field of views with a specific image-resolution for a particular scene and vice versa (i.e. the use of various image resolutions with a specified field of view for a particular scene). This is a useful feature, since acquiring a high-resolution image for a small field of view generally improves edge-detection and surface modeling and therefore results in higher precision. Note that the image resolution is limited to the laser spot size on the scanned object, and therefore higher resolution in this case results in the sensor duplicating the same object-space point position. This is not desirable in many cases and should be avoided.

The LSS versatility, however, has its drawbacks. For example, each time the image-resolution is changed or the field of view is changed, the LSS internal parameters must be re-calibrated. Another example of a LSS drawback is that the higher the image-resolution the longer the time required for the image acquisition, which in some applications can be an important factor. Generally speaking, a CCD video camera system is much faster than the LSS. For example, an image of 512X512 pixel takes the scanner 14 seconds to capture, compared to 30 images (or frames) per second for the CCD camera. However, one should not forget that the LSS provides in addition to the intensity image a depth coded image which is a very important feature.

2.4.2 Edge Detection

Because of the synchronization during the sampling process, a typical CCD camera has better edge detection precision along one axis than its other axis. Hence, in a typical camera calibration, at least two images orthogonal to each other are taken from the same position to ensure the same precision in both axes (normally the X and Y axes). This problem is not encountered when using the LSS because it is basically a point-range sensor (i.e. sampling is done independently for each pixel). Note that the intensity image of the scanner is used for edge detection.

The LSS has less sensitivity detecting edges than a CCD camera with proper light illumination. This is because at edges the incident laser beam often encounters sudden changes in surface height, surfaces with large reflectance variations and/or rough

surfaces, which would result in an erroneous detection of edges. This effect is compounded because the laser spot is not infinitesimally small. Another consideration is that the reflection of the incident laser spot on an edge is sometimes not predictable and therefore might not be sensed (e.g. if the incident angle is more than 60°). Since the LSS intensity image is not directly related to depth information, the intensity image is used to extract edges instead of the depth coded image.

Figure 2.9 illustrates the effect of different surface reflectance as an example of edge detection error, see El-Hakim and Beraldin (1994, 1995). In the figure, as the laser spot crosses the transition the imaged spot will lose most of its symmetry, and hence the centroid of the light distribution will shift to indicate a longer distance between the camera and the object being inspected. The result is small height pump in the range map near the transition but has less effect on the intensity value.

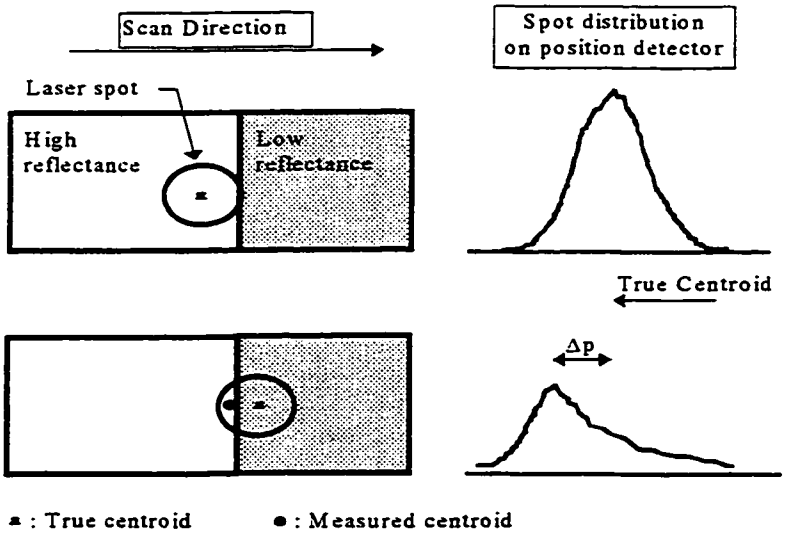

Figure 2.9: Edge error due to scanning spot m (see El-Hakim and Beraldin, 1995).

Figure 2.10 illustrates that the intensity image of the CCD camera has better transition in the light intensity before and after the edge whereas the scanner image has better sharpness at the edges of the target. In fact, in most cases, the pixel digital value of the intensity (the dynamic range is from 0 to 5 000) immediately after the edge or at the edge falls to zero (the laser spot is not sensed) although before and after the edge the digital value is not zero.

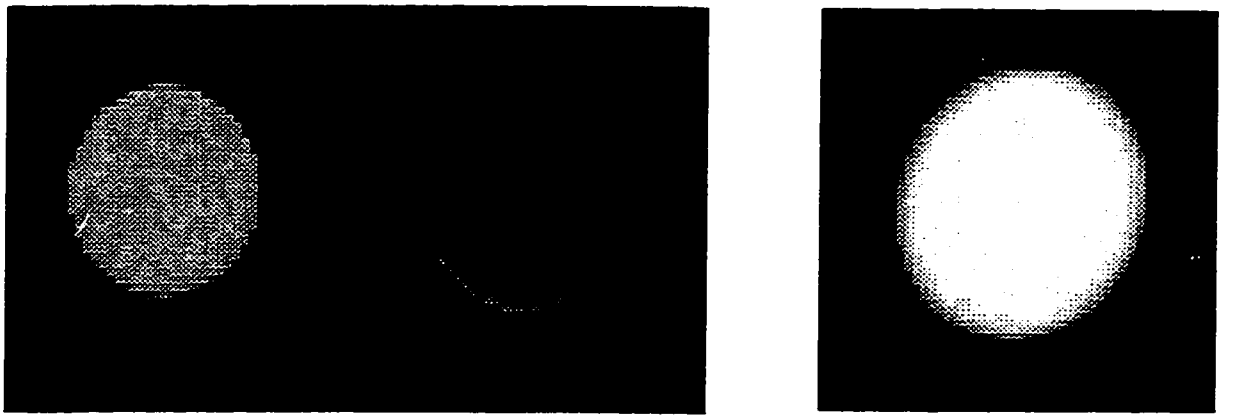

(i)LSS Intensity Image (ii)LSS depth coded Image (iii)CCD Intensity Image

Figure 2.10: Images of a retro-reflective target. (i) The LSS intensity image. (ii) The LSS depth coded image. (iii) A CCD intensity image.

2.4.3 Surface Measurements, Reconstruction and Modeling

The LSS can provide a complete set of 3-D data for scanned surfaces, as long as there are no discontinuities such as edges. As discussed in the section above, the LSS may produce erroneous results for edges and therefore special procedures must be performed to detect and to match edges or fit surfaces together. A CCD camera system is capable of

accurately extracting edges and surface features such as targets. Therefore, the LSS and a CCD camera system are complementary to each other. El-Hakim and Beraldin (1994, 1995) have shown that, for close-range measurements (up to 3 m), accurate and complete data can be achieved by integrating the two systems.

2.4.4 Standoff Distance, Depth of Field and Precision

The Laser Scanning System is most precise when the depth distance is equal to its standoff distance. For CCD cameras, it is totally dependent on the configuration and required application. However, the concept is similar to the LSS, the closer the object the better is the precision.

2.4.5 Hardware

The camera of the LSS is compact in size, however, the controlling system and the laser power source are large. This makes it hard to maneuver the system (see Figure 2.11 and Figure 2.12), and it is preferable, if possible, to have one system per monitoring site, rather than moving it from one site to another. In contrast, with new digital camera technology, CCD digital cameras (e.g. the Kodak DC 420, see Figure 2.12) are very light, versatile and practical for industrial applications, and are less expensive than the LSS. However, the LSS is still a prototype model not a production system like CCD cameras.

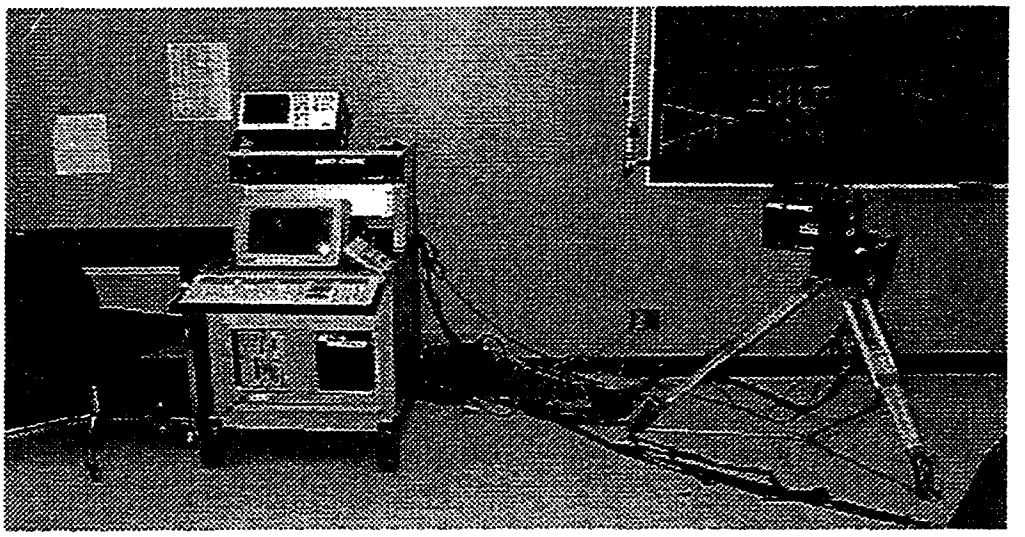

Figure 2.11: The Laser Scanning System (LSS).

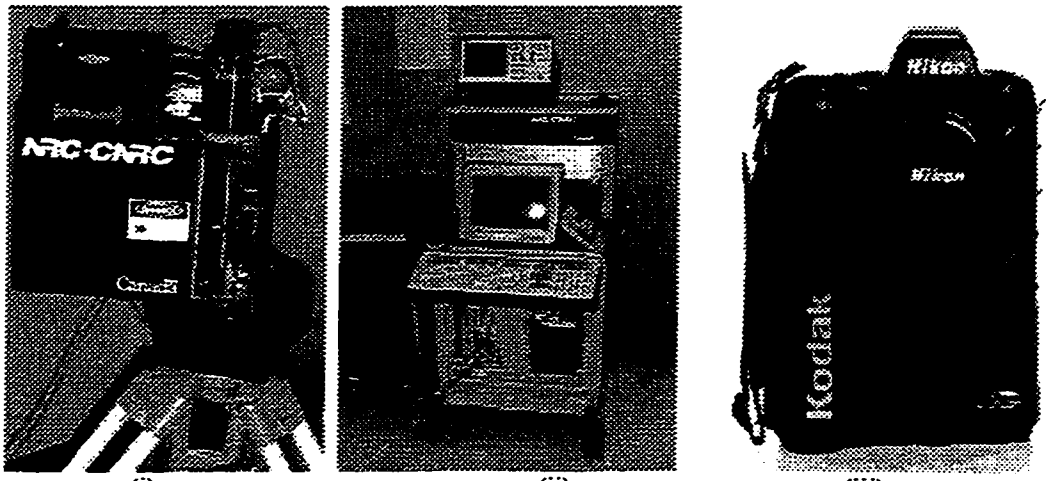

(i) (ii) (iii)

Figure 2.12(i): LSS camera. (ii) LSS controller. (iii)The Kodak DC420.

2.5 Applications

So far, the LSS system has been successfully utilized at The University of Calgary and has demonstrated a good potential for other type of applications. This thesis explores the potential of using this system for precise deformation measurements in either in-lab or on-site conditions.

The following are some applications that the system has been used for by the NRC: Robotics vision for different applications (Rioux 1994) such as nuclear site cleanup, see NRC report (1993/1994); Real-time tracking laser range scanner for space applications, see Blais et. al. (1993) and Blais et. al. (1991); Reverse Engineering, see Boulanger et. al. (1992) and Boulanger (1993); Three-Dimensional Pavement Inspection, see Blais et. al. (1992); Differential Inspection for Manufactured Goods, see Rioux et. al. (1993).

CHAPTER THREE

RAY TRACING AND THE MATHEMATICAL MODEL

3.1 Introduction

Calibration is the process of finding the LSS parameters for converting the scanned image data to Cartesian coordinates based on the LSS mathematical model. Therefore, better understanding of the mathematical model results in better interpretation of the scanned images, which improves the precision and the accuracy of the LSS measurements for point movements and surface deformations. The collinearity equations of the LSS are completely different from conventional stereo-CCD cameras, since the system's optical arrangements and acquisition strategies are based on different concepts (see Section 2.2). The LSS acquires its data similar to a laser theodolite system. In the LSS, each pixel value **p** at position $\mathbf{P_X}$ and $\mathbf{P_Y}$, in the depth coded image, corresponds to **R**, which is the measured slope distance between the laser theodolite and the measured point. The coordinates P_X and P_Y in the image correspond to the horizontal and vertical angles of the theodolite's telescope, respectively.

To explain the geometry of the LSS, the projective transformation equations are given for both the static case and the dynamic, or the auto-synchronized case (see Beraldin et. al. 1993, 1994). The static case is actually one particular condition of the dynamic case, described to clarify the method used to extract the camera model. For the dynamic case derivations, equations are given first for a single-scan axis, the symmetrical and the asymmetrical cases, and then for the asymmetrical dual-scan axes.

3.2 Static Geometry

The word static indicates the stationary condition of the projection angle, collection axis and lens axis (see Beraldin et. al. 1993, 1994). The geometry corresponds to the simplest case of a triangulation-based range sensor taking advantage of the Sheimpflug optical arrangements (see Section 2.2.3). In the following sub-sections the assumptions as well as the geometry are discussed and explained.

3.2.1 Assumptions

First, the projection axis, collection axis and lens plane are assumed to be perfectly aligned to intersect at one point, point **O** in Figures 3.1 and 3.2, and, hence the Sheimpflug condition is assumed to be satisfied. The second assumption is that the lens is removed and replaced by a pinhole model, see Figure 3.2.

3.2.2 Geometry and Projective Transformation

Satisfying the Sheimpflug condition yields optimal focusing, which means any point on the projection axis is in focus on the detection axis. Also, the lens aperture can be kept at maximum, thus reducing speckle noise and improving signal to noise ratio, see Baribeau and Rioux (1991a and 1991b). The detection sensor is composed of a one array of 512 elements CCD-sensor.

From Figure 3.1, the focal length of the lens **f**, in this case, is the distance between the lens plane and the vanishing point **C** on the image plane at the edge of the **CCD** sensor. The principal point **A** of the **CCD**-sensor (i.e. **p** is equal to zero) is the intersection point of the collection axis, when it is perpendicular to the lens plane, and the detection axis. The effective focal length $\mathbf{f_0}$ is the distance from the lens plane to the principal point **A.**

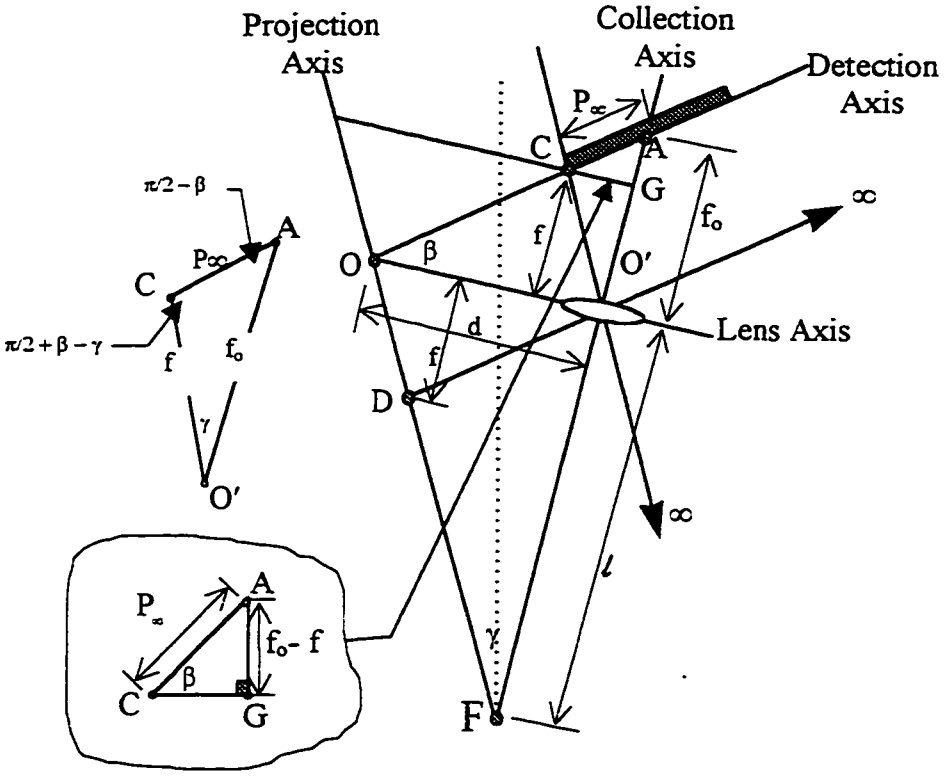

Figure 3.1: Sheimpflug geometry.

The distance $\mathbf{P}_\infty$ corresponds to the position of the vanishing point **C** on the image plane of the position detector. In Figure 3.1, applying the sine law to triangle **O'AC** yields the following:

$$\frac{P_\infty}{\sin(\gamma)} = \frac{f_0}{\sin(\pi/2+\beta-\gamma)} = \frac{f_0}{\cos(\beta-\gamma)} \qquad \text{Equation 3.1}$$

The triangle **ACG** has a right angle at point **G**, hence $\mathbf{P}_\infty$ is computed as:

$$P_\infty = \frac{f_0-f}{\sin(\beta)} \qquad \text{Equation 3.2}$$

From Equations 3.1 and 3.2, the relationship between $\mathbf{P}_\infty$, the focal length **f**, the effective focal length $\mathbf{f}_o$, the triangulation angle γ for the principal point (i.e. p=0), and the tilt angle β of the Sheimpflug condition is given by:

$$P_\infty = f_0\frac{\sin(\gamma)}{\cos(\beta-\gamma)} = \frac{f_0-f}{\sin(\beta)} \qquad \text{Equation 3.3}$$

The collinearity equation of the static geometry can be determined by deriving an equation that relates the spot position **p** in the image plane to the location of a point in the object plane $\mathbf{r}_p$. From Figure 3.2, the similarity of triangles **O'AC** and **O'ED** and of triangles **O'BC** and **O'FD** lead to:

$$\frac{P_\infty}{v_0} = \frac{v_i}{r_0 - r_{-\infty}} \qquad \text{Equation 3.4}$$

$$\frac{P_\infty - p}{v_0} = \frac{v_i}{r_p - r_{-\infty}} \qquad \text{Equation 3.5}$$

Note that $\mathbf{r_\infty}$ is the location of the vanishing point **D** on the object plane and $\mathbf{r_0}$ is the projection of the principal point, point **A**, on the object plane, point **E**. Substituting Equation 3.4 into Equation 3.5 yields an equation that describes the static geometry:

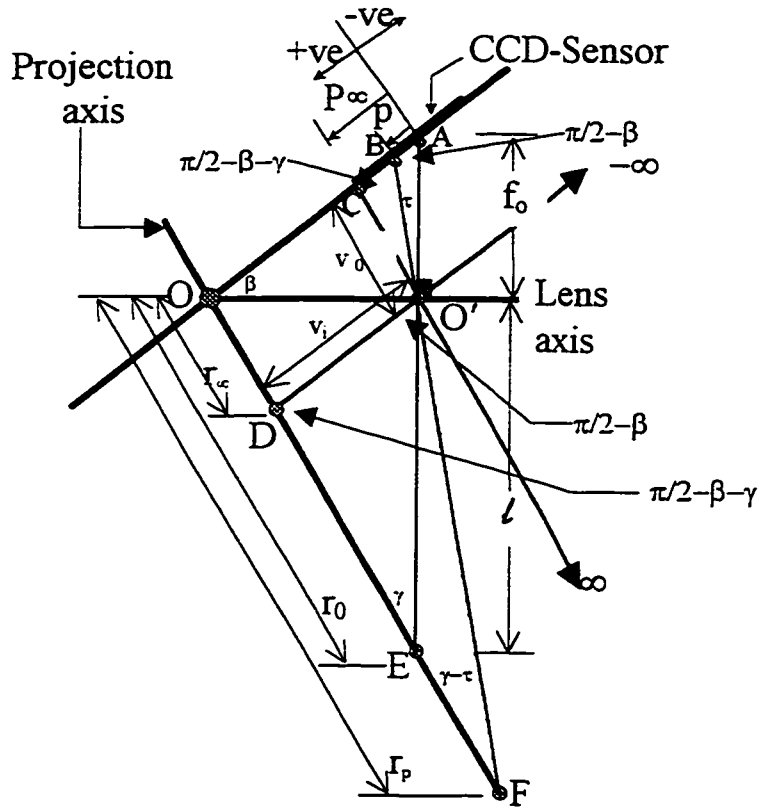

Figure 3.2: Static model geometry.

$$\frac{r_p - r_{-\infty}}{r_0 - r_{-\infty}} = \frac{P_\infty}{P_\infty - p} \qquad \text{Equation 3.6}$$

Rearranging Equation 3.6 provides an equation that relates the distance **r** along the projection axis to the spot position **p** on the CCD-sensor.

$$r(p) = r_p = r_{-\infty} + P_\infty \frac{r_0 - r_{-\infty}}{P_\infty - p} \qquad \text{Equation 3.7}$$

Equation 3.7 acts as the projective transformation equation for active triangulation. The collinear transformation equation is found by inverting Equation 3.7:

$$p = P_\infty \cdot \left(1 - \frac{r_0 - r_{-\infty}}{r_p - r_{-\infty}}\right) \qquad \text{Equation 3.8}$$

Equation 3.7 is a canonical form for ideal imagery described by Rioux (1984).

3.3 Dynamic (Synchronized Scanning) Geometry

Dynamic geometry is produced by continuously synchronizing the change in the angle of the projection axis and the collection axis with respect to the detection axis and the lens plane, respectively. It depicts the equivalent geometry explained in Section 2.2.4 of the auto-synchronization approach for a triangulation-based range sensor taking advantage of the Sheimpflug satisfying optical arrangements (see Beraldin et. al. 1993, 1994).. In the following sub-sections the assumptions as well as the geometry are discussed and

explained. For the purpose of simplicity, the single scan axis case is discussed first, followed by the dual scan axis case.

3.3.1 Assumptions

In addition to the static model assumptions, the scanning mirrors are considered to be infinitesimally thin, perfectly flat, and perfectly mounted with respect to the scanner's axes. The wobble and jitter effects of the galvanometers along the axes of rotation are assumed to be negligible. The imperfections in mounting of the side mirrors in their proper locations and orientations with respect to each other and with respect to the rotating mirrors are also neglected. The galvanometer driven mirrors are assumed to be calibrated and adjusted to take care of the temperature effects. Refraction effects are also not considered as a source of error. The laser source is assumed to be mounted such that the laser ray always hits the center of the X-axis rotating mirror, as shown in Figure 3.3.

3.3.2 Symmetrical Single-Scan Axis Scanner

The single scan axis case composed of a line or a circle sensor (see Section 2.1) that has a scanning mirror along the axis or the path of interest. Figure 3.3 illustrates a cross-section of an auto-synchronized single-scan axis scanner that is described in Section 2.2.4. As shown in the figure, the X-axis of the scanner is along the line connecting the center of the rotation mirror and the centers of the fixed mirrors. At the initial configuration (i.e. static case, the initial position of the rotating mirror is at angle $\kappa_0=\pi/4$), the scanner's X-

axis coincides with the laser ray reflected from the rotating mirror, and also coincides with the same ray when reflected back by the fixed mirror to the rotating mirror.

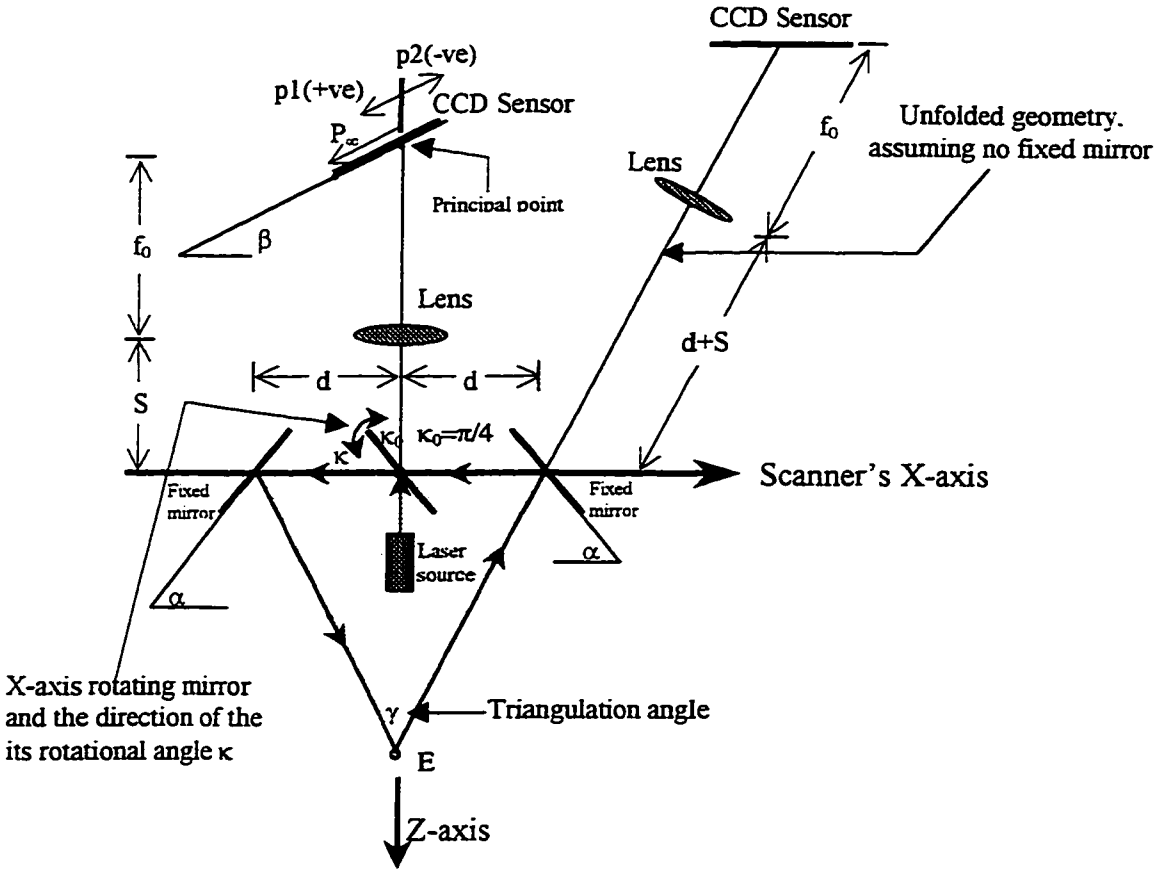

Figure 3.3: Cross-section of a single-scan axis scanner including the unfolded geometry (assuming no fixed mirror).

The triangulation angle formed is γ and the laser spot image formed on the CCD sensor is the principal point. The extracted information from object surface is in the X-Z plane of the scanner. Figure 3.3 shows the sign convention of the measured value **p** on the CCD-sensor that is used in the derivation of the mathematical model in this thesis. The **p** value is positive if it is to the left of the principal point (**p=0**) and vise versa. The figure also

shows the unfolded geometry assuming there is no fixed mirror. An exploration of the equivalence of both the folded and the unfolded geometry is in following section.

3.3.2.1 Ray Tracing

Figure 3.4a illustrates the auto-synchronized scanner geometry. Points **O′** and **O″** in the figure are the points of deflection (pivot points) of a synchronized scanner. The figure shows the scanner's X-axis and also the X-axis of the deflection points, points **O′** and **O″**. The X-axis of the deflection points is used first for the derivations of the mathematical model, then resultant equations are shifted to the scanner's X-axis.

The dashed-line circle in Figure 3.4a corresponds to the geometrical trajectory, composed of object points, of the principal point on the CCD-sensor. Figure 3.4b shows that the important feature of the auto-synchronized scanner is that the reflected rays from the fixed mirror, if extended from their other end, intersect at one point, point **O′**, similarly at point **O″**. Note that the length of any reflected laser ray between the rotating mirror at point **O** and the fixed mirror is exactly the same as the distance of its extension between the fixed mirror and the deflection point **O′**.

To simplify the geometry and the derivation of the mathematical model, Figure 3.4c illustrates the unfolded geometry of a deflected ray, traced from the object point to the spot position on the CCD-sensor. The spot position of this deflected ray is in this case the principal point **A**. The deflected ray is indicated as a straight line that goes through the

fixed mirror then through the lens to form a laser spot image on the CCD-sensor. This is achieved by ignoring the presence of the fixed and the rotating mirrors. Note that the position of the rotating mirror, point **O** in Figure 3.4a, is equivalent to the deflection point **O″** as illustrated in Figure 3.4c.

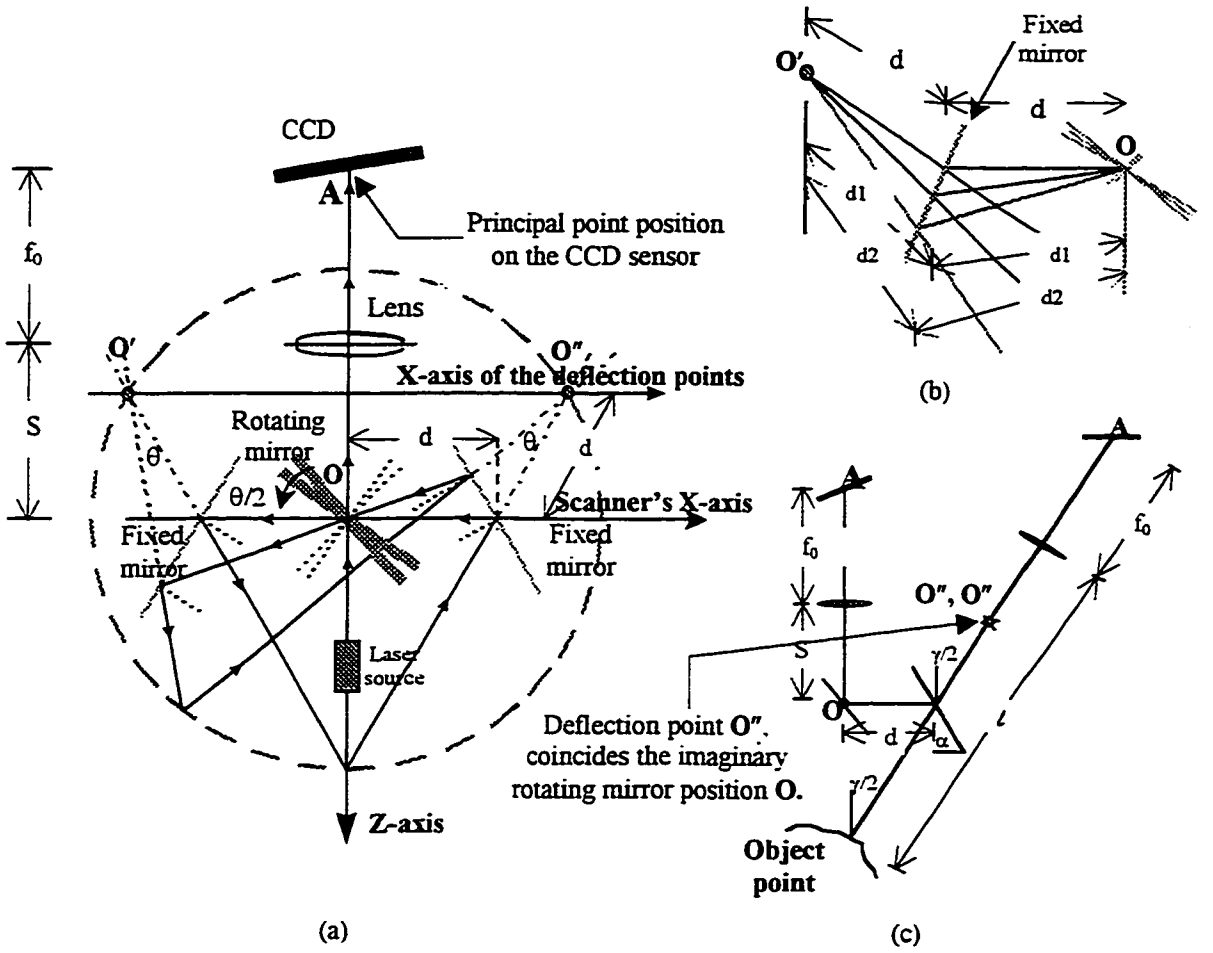

Figure 3.4: (a) Geometry of a single-scan axis auto-synchronized scanner. (b) The geometrical representation of the relationship between the rotation mirror at point **O**, the fixed mirror and the deflection point **O′**. (c) Unfolded geometry assuming no fixed mirror.

In Figure 3.5a, the geometry shows that when the rotating mirror is rotated from its initial position by an angle κ, the deflection angle at the pivot points **O′** and **O″** and the deflection angle of the laser beam form the angle θ.

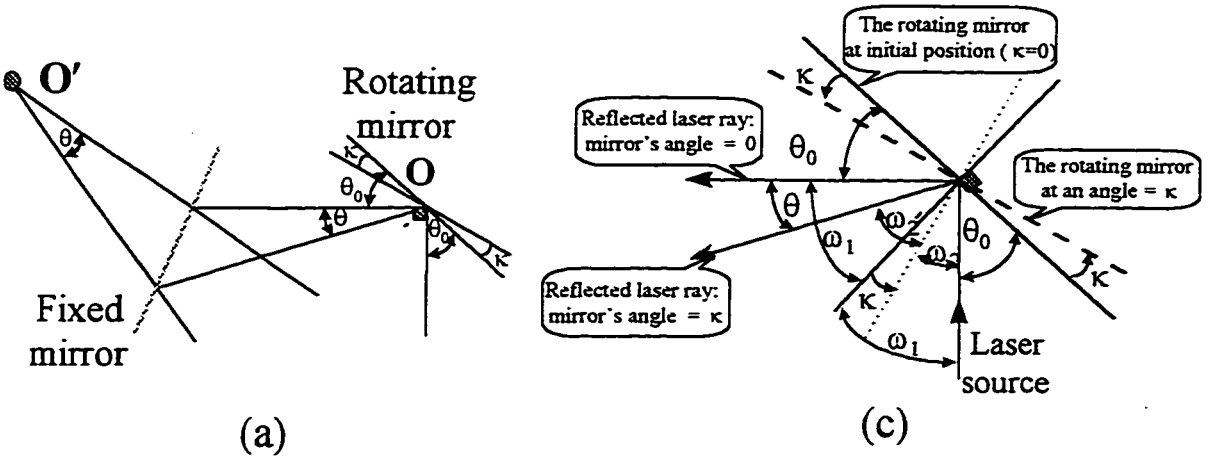

Figure 3.5: (a) Geometrical representation of the relationship between the rotation angle κ and the resultant deflection angle θ. (b) Detailed geometry to derive the relationship between the angles κ and θ.

To derive the relationship between the two angles κ and θ, Figure 3.5a illustrates the detailed geometry. Comparing two positions of the rotating mirror derives the relationship. The first position is when the mirror is at its initial position (κ=0). The second position is when the mirror is rotated an angle κ. Summation of the angles at point **O** for each position results in:

First position: $\pi - 2\,\theta_0 + 2\,\omega_1 = 0$ Equation 3.10

Second position: $\pi - (\theta_0 - \kappa) + (\theta_0 + \kappa) + \theta + 2\,\omega_2 = 0$ Equation 3.11

Simplifying Equation 3.11 and substituting for $\omega_2 = \omega_1 - \kappa$, yields:

$$\pi + 2\theta_0 + 2\omega_1 + \theta - 2\kappa = 0 \qquad \text{Equation 3.12}$$

Subtracting Equation 3.10 from Equation 3.12 produces the following relationship:

$$\theta = 2\kappa \qquad \text{Equation 3.13}$$

This relationship shows that rotating the mirror by an angle κ produces a deflection angle θ that is double the value of the rotational angle κ. The relationship is also the same at the other deflection point **O''**. The derivation of the mathematical model is initially based on the deflection angle, taking into consideration the relationship between the deflection angle and the rotational angle of the mirror.

Before using the unfolded geometry of mathematical derivations, it is important to prove that the unfolded geometry is equivalent to the actual geometry. Figure 3.6 shows the geometry of both cases, folded and unfolded. Equivalence can be proven if each axis of the folded geometry is traced, using both the rotating and the fixed mirrors, to coincide with its corresponding axis of the unfolded geometry. The following are axes of interest: the vanishing axes of object plane ($+\infty$) and image plane ($+\infty$), the detection axis and the lens axis. Note that the unfolded geometry shown in Figure 3.6 is equivalent to the static case shown in Figure 3.2 where the rotating mirror is inclined at an angle $\pi/4$ from the vertical axis, and triangle OAE is the same in both figures.

To prove the congruency of triangle **A″C″O″**, the edges of triangle **ACO′** are traced. Note that the line connecting points **C** and **O′** is the vanishing axis of the image plane (+∞). The line connecting points **A** and **O′** is the line perpendicular to the lens axis, and the line connecting points **C** and **A** is the detection axis. The vanishing axis of the object plane (-∞) is also traced. Point **A** is the principal point, point **C** is the vanishing point on the image plane, and point **O′** is the center of the lens. Note that the Sheimpflug condition is achieved when the detection, the projection and the lens axes intersect at point **O** shown in Figure 3.6.

One can trace these points and rays as follows: first, the ray of interest goes from the point or the axis of interest of the folded case to be reflected by the rotating mirror. Then the ray is reflected by the fixed mirror (to the right of the rotating mirror), and is extended from its other direction to reach its proposed target point or axis of the unfolded case, see Figure 3.6. AutoCAD was used to do the ray tracing accurately, and as shown in the figure, the geometry of the two cases proved to be identical. Therefore, using the geometry of the unfolded case for mathematical derivations would be equivalent to using the geometry of the folded case.

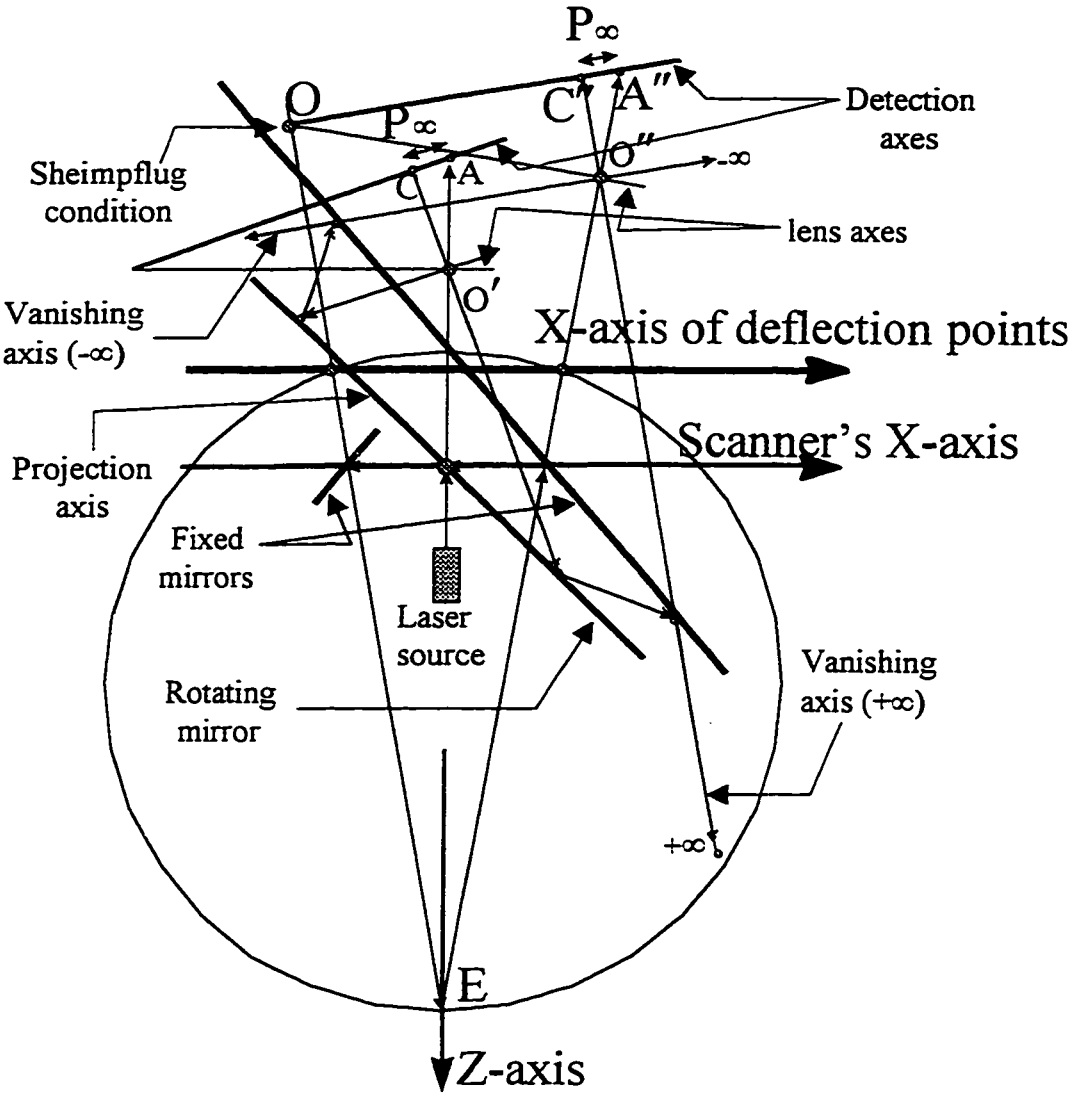

Figure 3.6: Ray Tracing of points **A**, **C** and **O'** and the vanishing axis (-∞).

3.3.2.2 Derivations of the Collinearity Equations for a Symmetrical Single-Scan Axis Scanner

Figure 3.7a represents the equivalent geometry of a synchronized rotation of the projection and the collection axes by an angle θ. Superimposed on the figure is the static geometry in dashed lines equivalent to the triangle **OEA** in Figures 3.2 and 3.6. To achieve the static geometry the X-axis rotating mirror is at its initial position, inclined at

an angle of $\pi/4$ from the vertical axis. The rectangular coordinate system used is the axis joining the equivalent position of the pivot points (deflection points **O′** and **O″** in Figure 3.5a) of the projection and collection axes. These two positions are points **a** and **b** on the X-axis in Figure 3.7a. The Z-axis extends from a point midway between points **a** and **b** towards infinity and bisects the projection and collection paths (for **p=0** and θ**=0**) at their intersection. This representation neglects the effect of the finite thickness of the scanning mirror, and the location and the orientation of the rotating mirror and the fixed mirrors.

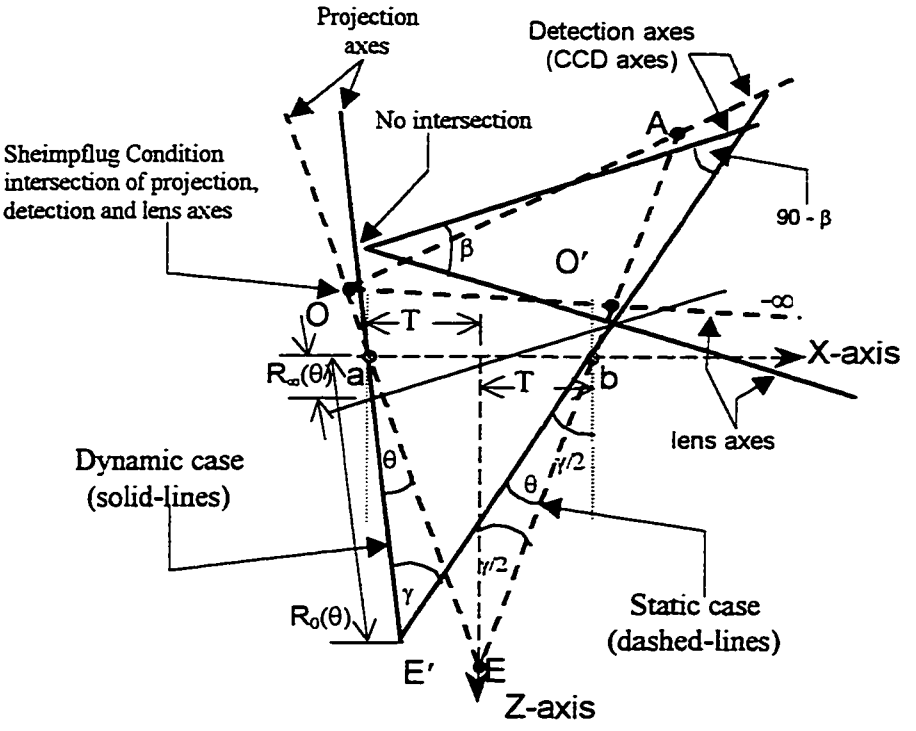

Figure 3.7a: A dynamic geometrical model (solid-lines) superimposed on the static model (dashed-lines).

The synchronized geometry implies that for the principal point at a spot position **p=0** (point **A** in Figure 3.7a) the acute angle between the projection and collection paths will always be equal to γ. From this consideration all other angles can be inferred (e.g. the angle α which is the tilt angle of the fixed mirrors is a function of γ where $\gamma = 4\alpha - \pi$).

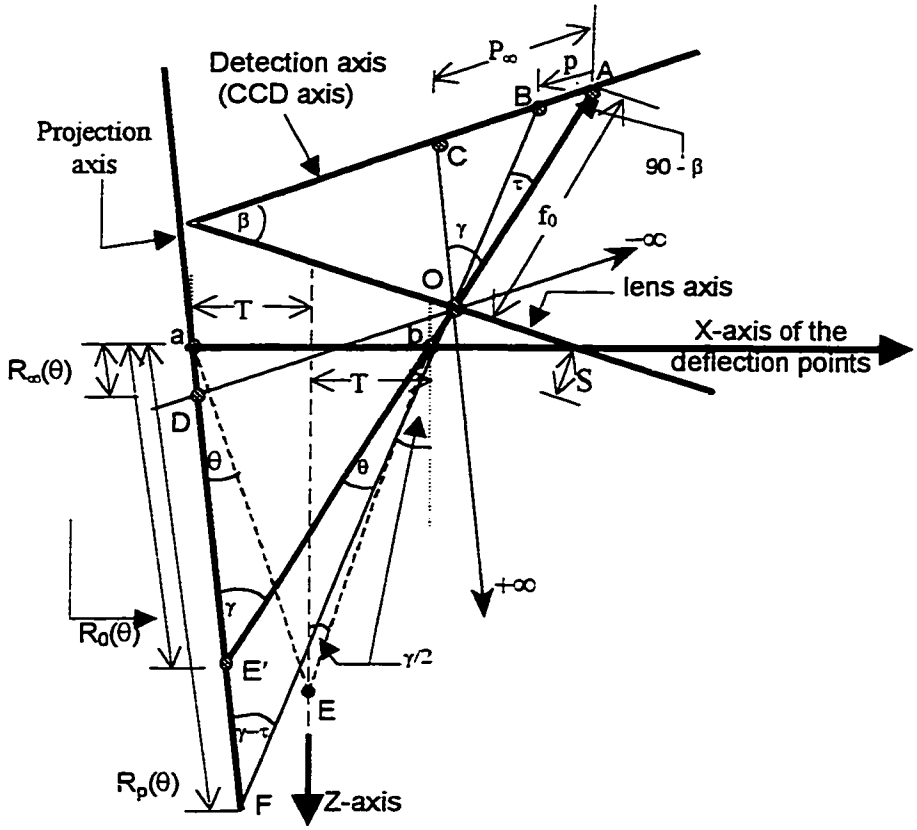

Figure 3.7b: The geometrical details of the dynamic model (solid-lines) with some details of the static model (dashed-lines).

Note that in the static case the Sheimpflug condition is achieved. However, once the dynamic case is introduced by rotating the projection and collection axes by angle θ, the

region of intersection no longer represents a point. It is actually a circle that increases in diameter as the deflection angle increases. The other factors that affect the size of this error circle are the size of the angle β, the standoff distance, and the baseline between the two pivot (deflection) points **2T**. This analysis was made using the AutoCAD software.

Figure 3.7b illustrates the synchronized geometry of the dynamic case and all details needed for the mathematical derivation. The collinearity equation of the laser scanner is extracted from the similarity of triangles **OAC** and **OE'D** and of triangles **OBC** and **OFD** (see Figure 3.7 for geometrical details). The Equation is given as :

$$\frac{R_p(\theta) - R_{-\infty}(\theta)}{R_0(\theta) - R_{-\infty}(\theta)} = \frac{P_\infty}{P_\infty - p} \qquad \text{Equation 3.14}$$

where: $\mathbf{R_p(\theta)}$ is the distance $\mathbf{R(\theta)}$ along the projection axis corresponding to **p** (depth value at **i** and **j** image coordinates), $\mathbf{R_\infty(\theta)}$ is the location of the vanishing point on the projection axis, $\mathbf{R_0(\theta)}$ is the location corresponding to the principal point A (**p = 0**), and $\mathbf{P_\infty}$ is the location of the vanishing point on the detection axis.

Using photogrammetry terminology, Equation 3.14 is referred to as the projective transformation equation for this triangulation method. The collinear transformation equation is found by inverting equation 3.14:

$$p = P_\infty \left(1 - \frac{R_0(\theta) - R_{-\infty}(\theta)}{R_p(\theta) - R_{-\infty}(\theta)}\right) \qquad \text{Equation 3.15}$$

Decomposing Equation 3.14 in its orthogonal directions results in:

$$\frac{X_p(\theta) - X_{-\infty}(\theta)}{X_0(\theta) - X_{-\infty}(\theta)} = \frac{Z_p(\theta) - Z_{-\infty}(\theta)}{Z_0(\theta) - Z_{-\infty}(\theta)} = \frac{P_\infty}{P_\infty - p} \qquad \text{Equation 3.16}$$

Therefore, the **X** and **Z** coordinates for a given angle θ and a depth value **p**, are:

$$X_g(p,\theta) = X_{-\infty}(\theta) + P_\infty \frac{X_0(\theta) - X_{-\infty}(\theta)}{P_\infty - p} \qquad \text{Equation 3.17}$$

$$Z_g(p,\theta) = Z_{-\infty}(\theta) + P_\infty \frac{Z_0(\theta) - Z_{-\infty}(\theta)}{P_\infty - p} \qquad \text{Equation 3.18}$$

3.3.2.2.1 Derivation of R_0, X_0 and Z_0:

Figure 3.8a illustrates the geometry needed for deriving $\mathbf{R_0(\theta)}$. The figure shows the deflection points, and the static and dynamic geometry related to the object scene. The dashed circle corresponds to the geometrical trajectory of the principal point for different rotational angles θ. The distance between point **a** and **E′** is $\mathbf{R_0(\theta)}$. Note that γ is constant since the intersection of the collection and projection axes circumscribe a circle with the intersection point **E′** and the deflection (pivot) points, **a** and **b**, being on the circle. Applying the sine law to triangle **abE′** and substituting $\phi = \pi/2 - \theta - \gamma/2$, results in:

$$\frac{R_0}{\sin(\phi)} = \frac{2T}{\sin(\gamma)} \Rightarrow R_0 = 2\frac{T}{\sin(\gamma)}\cos(\theta + \gamma/2) \qquad \text{Equation 3.19}$$

Decomposing the components of $\mathbf{R_0}$ with respect to the **X-Z** coordinates as shown in Figure 3.8b produces the following:

$$X_0 = R_0 \sin(\alpha) - T$$ Equation 3.20

$$Z_0 = R_0 \cos(\alpha)$$ Equation 3.21

where $\alpha = \gamma/2 - \theta$

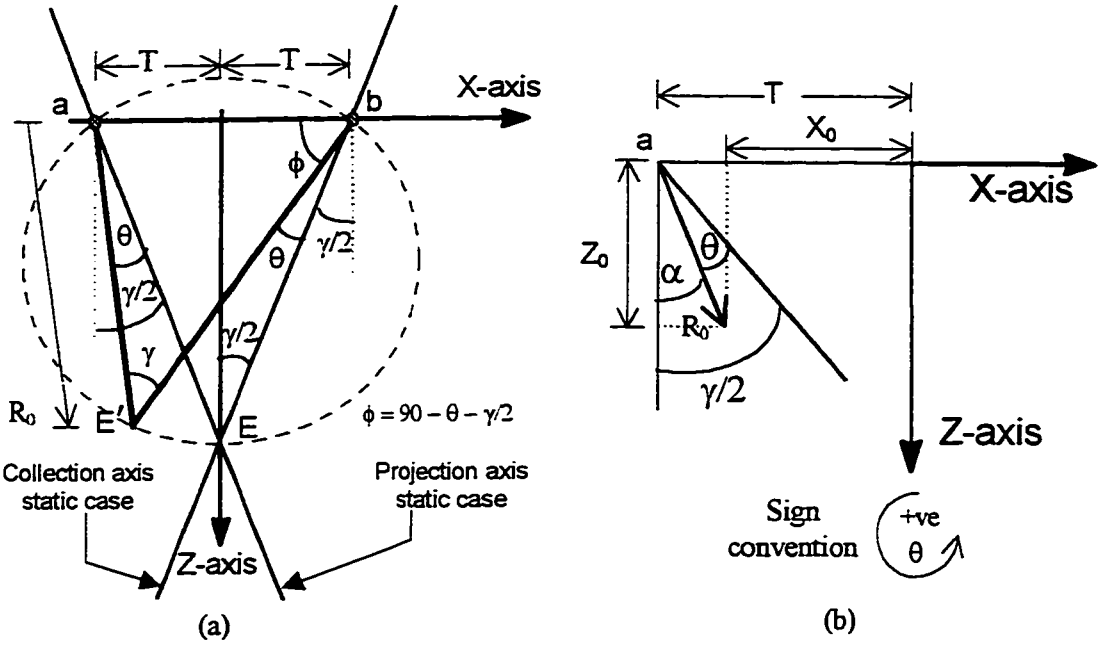

Figure 3.8: Geometrical details to derive R_0, X_0 and Z_0.

Substituting $\mathbf{R_0}$ from Equation 3.19 into Equations 3.20 and 3.21, applying the sign convention shown in Figure 3.8b (i.e. θ is positive in the counter-clock wise direction), and then simplifying gives:

$$X_0 = T\frac{\sin(2\cdot\theta)}{\sin(\gamma)}$$ Equation 3.22

$$Z_0 = T\frac{\left(\cos(2\cdot\theta)+\cos(\gamma)\right)}{\sin(\gamma)}$$ Equation 3.23

3.3.2.2.2 Derivation of R_∞, X_∞ and Z_∞:

Figure 3.9a illustrates an expanded view of the geometrical details required for derivations. In the figure, the following are important relationships:

$\phi 1 = \beta - \gamma/2 - \theta$ Equation 3.24a

$\alpha 1 = \pi/2 + \gamma/2 + \theta$ Equation 3.24b

$\omega = \pi/2 + \gamma - \beta$ Equation 3.24c

In Figure 3.8b, applying the sine law to triangle **aa'a"**and substituting for $\phi 1$ and ω from Equations 3.24a and 23.24c, results in:

$$\frac{R_\infty}{\sin(\phi 1)} = \frac{X1}{\sin(\omega)} \Rightarrow R_\infty = \frac{X1}{\sin(\pi/2-\beta+\gamma)}\sin(\beta-\theta-\gamma/2)$$ Equation 3.25

where $X1 = 2T - Y1$ Equation 3.26a

Applying the sine law to triangle **a"Ob, Y1** gives

$$\frac{Y1}{\sin(\pi/2-\beta)} = \frac{S}{\sin(\phi 1)} \Rightarrow Y1 = \frac{S}{\sin(\beta-\theta-\gamma/2)}\cos(\beta)$$ Equation 3.26b

Substituting Y1 into Equation 3.26a, then X1 into Equation 3.25 and simplifying produces:

$$R_{\infty} = \frac{2T\sin(\beta-\theta-\gamma/2)-S\cos(\beta)}{\cos(\beta-\gamma)}$$ Equation 3.27

Decomposing the components of $\mathbf{R_0}$ with respect to the **X-Z** produces the following:

$$X_{\infty} = R_{\infty}\sin(\gamma/2-\theta)-T$$ Equation 3.28

$$Z_{\infty} = R_{\infty}\cos(\gamma/2-\theta)$$ Equation 3.29

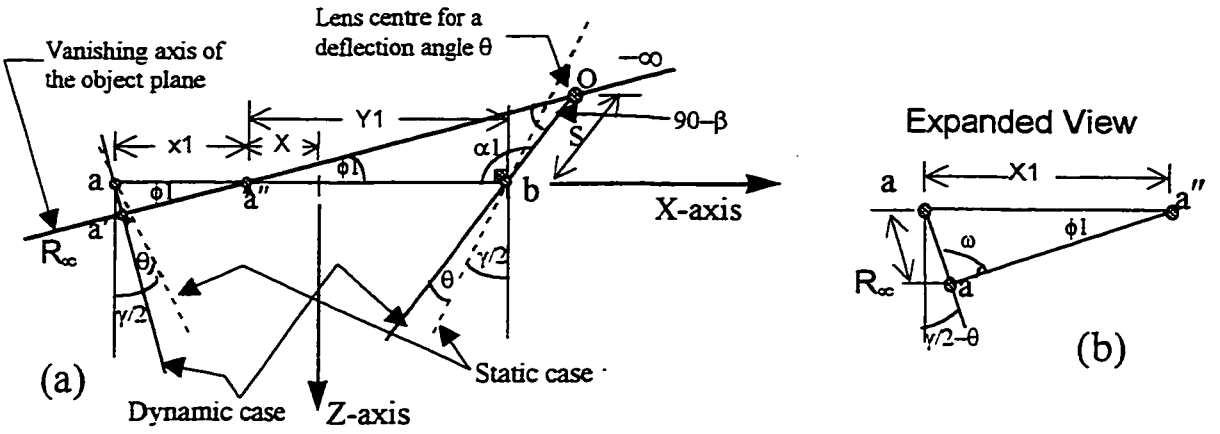

Figure 3.9: Geometrical details to derive R_{∞} and Z_{∞}.

Substituting $\mathbf{R_{\infty}}$ from Equation 3.27 into Equations 3.28 and 3.29, applying the sign convention shown in Figure 3.8b (i.e. θ is positive in the counter-clock wise direction), and then simplifying gives:

$$X_{\infty} = -\frac{T\cos(\beta+2\theta)+\sin(\gamma/2+\theta)S\cos(\beta)}{\cos(\beta-\gamma)}$$ Equation 3.30

$$Z_{\infty} = \frac{T[\sin(\beta-\gamma)+\sin(\beta+2\theta)]-\cos(\gamma/2+\theta)S\cos(\beta)}{\cos(\beta-\gamma)}$$ Equation 3.31

3.3.2.2.3 The Collinearity Equations with respect to the Scanner's X-axis

Figure 3.10 illustrates the X-axis of the scanner and the X-axis of the deflection points. Note that the Z-axis remains the same in both cases. The shift to the scanner's X-axis affects only the Z component as follows:

$$Z_{new} = Z_{old} - d\cos(\gamma/2) \qquad \text{Equation 3.32}$$

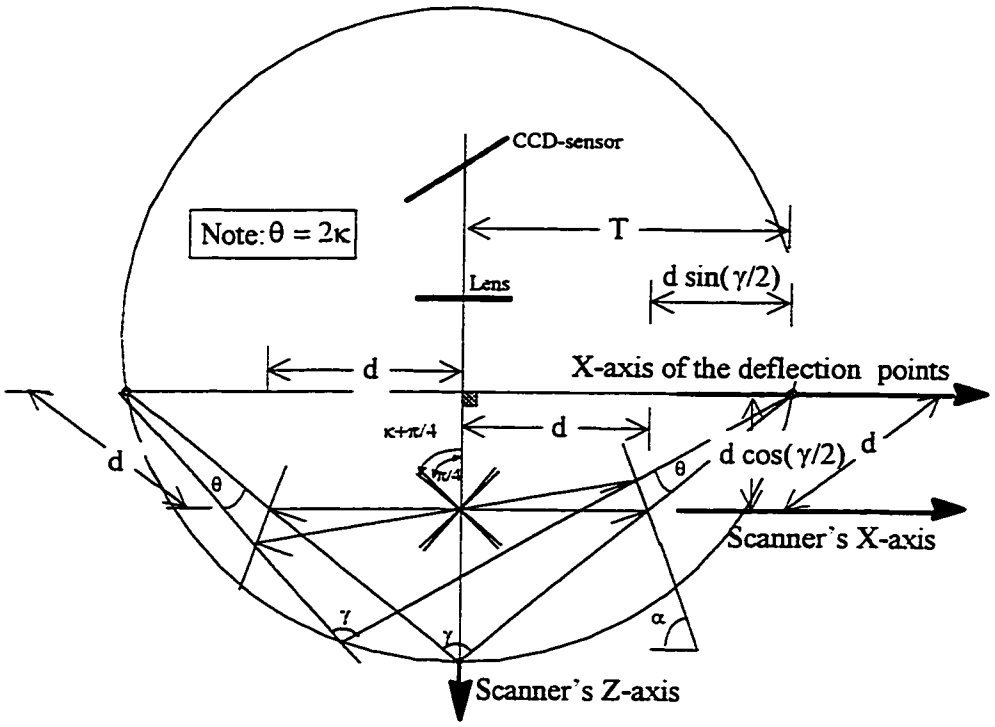

Figure 3.10: The geometrical difference between the scanner's X-axis and the X-axis of the deflection (pivot) points.

To use the physical parameters of the scanner, the distance **d** and the angle α replace the distance **T** and the triangulation angle γ using the following relationships:

$$T = d\sin(\gamma/2)+d$$ Equation 3.33

$$\gamma = 4\alpha-\pi$$ Equation 3.34

Applying Equations 3.32 to Equations 3.22, 3.23, 3.30 and 3.31, substituting Equations 3.33 and 3.34, and then simplifying produces the following:

$$X_0(\theta) = d(\cos(2\alpha)-1)\frac{\sin(2\theta)}{\sin(4\alpha)}$$ Equation 3.35

$$Z_0(\theta) = d(\cos(2\alpha)-1)\frac{[\cos(2\theta)+1+2\cos(2\alpha)]}{\sin(4\alpha)}$$ Equation 3.36

$$X_\infty(\theta) = \frac{-d(\cos(2\alpha)-1)\cos(\beta+2\theta)-\cos(2\alpha+\theta)S\cos(\beta)}{\cos(\beta-4\alpha)}$$ Equation 3.37

$$Z_\infty(\theta) = \frac{-d[-\sin(\beta+2\theta)[\cos(2\alpha)-1]-\sin(\beta-4\alpha)+\sin(\beta-2\alpha)]+\sin(2\alpha+\theta)S\cos(\beta)}{\cos(\beta-4\alpha)}$$

Equation 3.38

3.3. 3 Asymmetrical Single-Scan Axis Scanner

The center of the rotating mirror and the scanner's Z-axis are shifted to the left a distance **dx** from the center point between the two fixed mirrors, see Figure 3.11. All other components of the asymmetrical single-axis scanner are the same as in the symmetrical scanner.

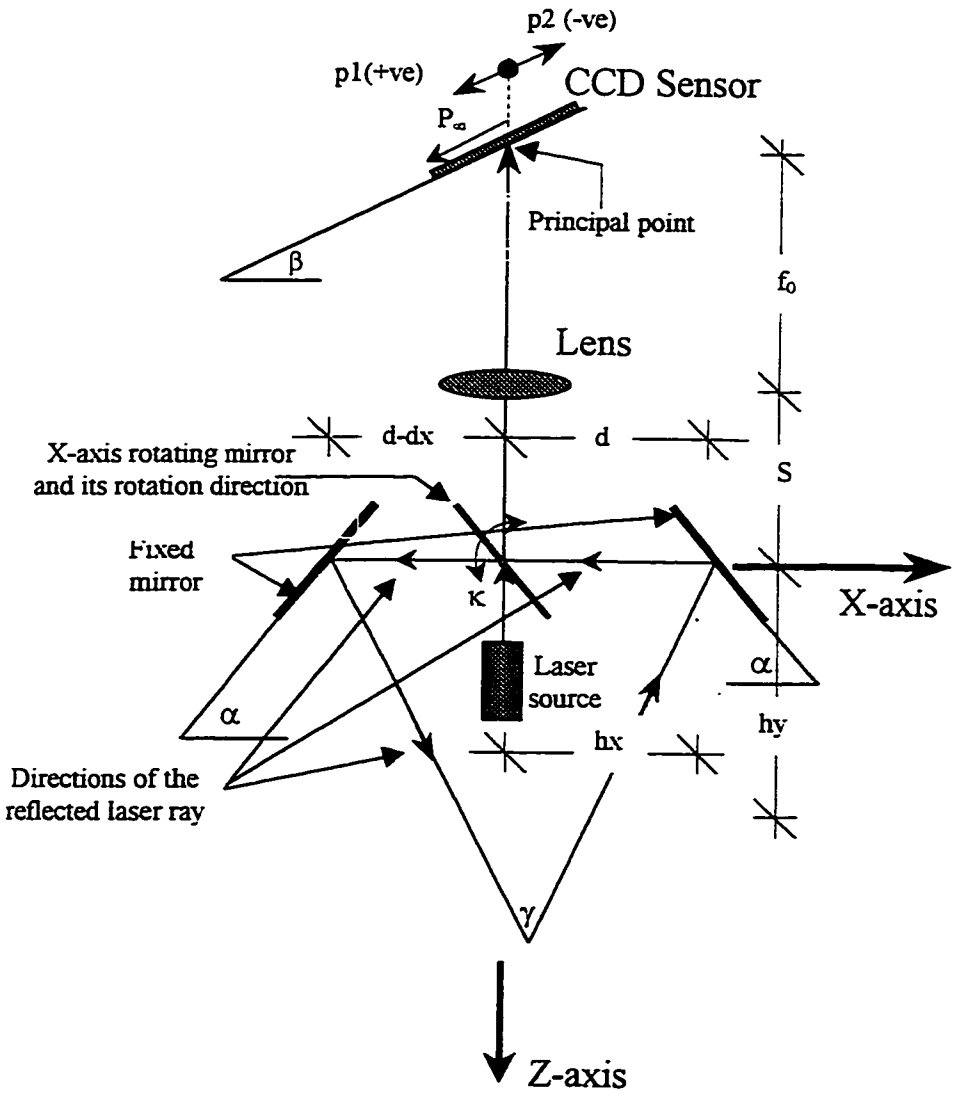

Figure 3.11: Cross-section of the asymmetrical single-axis scanner.

3.3.3.1 Ray Tracing

To illustrate the difference between the asymmetrical and the symmetrical single-scan axis scanners, Figure 3.12 illustrates the ray tracing for the asymmetrical geometry superimposed onto the ray tracing for the symmetrical geometry. The components of the symmetrical scanner are the rotating mirror, the lens, the CCD-sensor, and the two fixed mirrors **M1** and **M3**. The larger circle and the deflection points **P1** and **P3** also represent the geometrical trajectory of the principal point for the symmetrical scanner. The components of the asymmetrical scanner are the same as the symmetrical one except that the fixed mirror **M1** is replaced by the fixed mirror **M2**.

Note that the smaller circle and the deflection points **P2** and **P3** represent the geometrical trajectory of the principal point for the asymmetrical scanner. It is also important to remember that the asymmetrical scanner has all the characteristics of the symmetrical scanner. The following summarizes these important characteristics: each spot position on the sensor has a canonical geometrical trajectory; the unfolded geometry is equivalent to the folded one; the length of a reflected laser ray between the rotating mirror and the fixed mirror is equal to its extension between the same fixed mirror and the deflection point. Another important feature is that the deflection angle θ is double the scanning angle κ. Also, it can be proven that the angle γ, as shown in Figure 3.12, is the same for both the asymmetrical and symmetrical geometry.

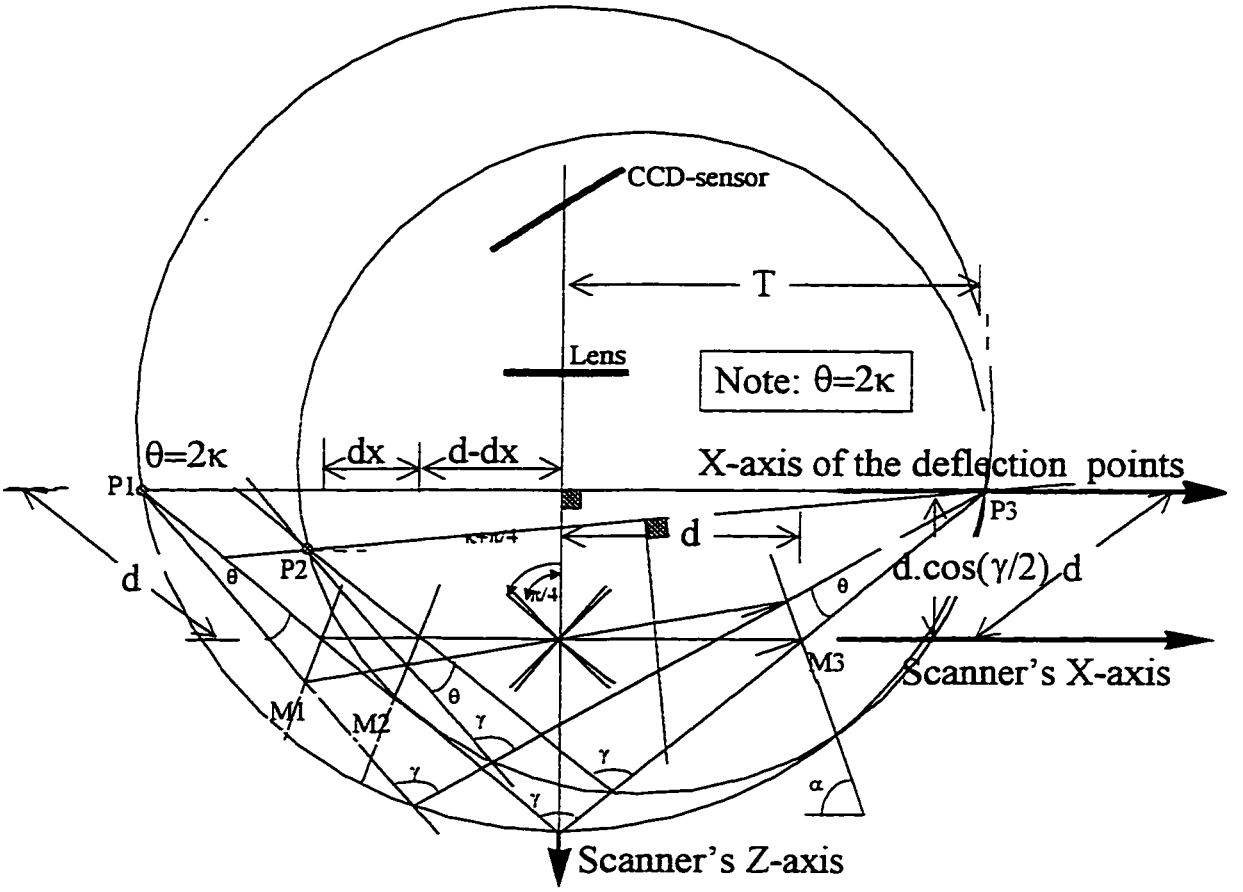

Figure 3.12: The asymmetrical geometry superimposed on the symmetrical one.

Note that the introduced shift in the position of the rotating mirror **dx** shifted the position of the deflection point from point P1 to point P2, see Figure 3.12. This shift can be accommodated by modifying the collinearity equations of the symmetrical scanner by modifying the equations of the variables $\mathbf{R_0(\theta)}$ and $\mathbf{R_\infty(\theta)}$, see Figure 3.13a. The figure shows the two correction vectors $\delta\mathbf{R_0(\theta)}$ and $\delta\mathbf{R_\infty(\theta)}$. Figure 3.13b illustrate the unfolded geometry for the static case (the deflection angle θ is zero) and the dynamic case (a deflection angle of θ). The two triangles shown in Figure 3.13 provide useful relations and information for the derivations of the shift values $\delta\mathbf{R_0(\theta)}$ and $\delta\mathbf{R_\infty(\theta)}$.

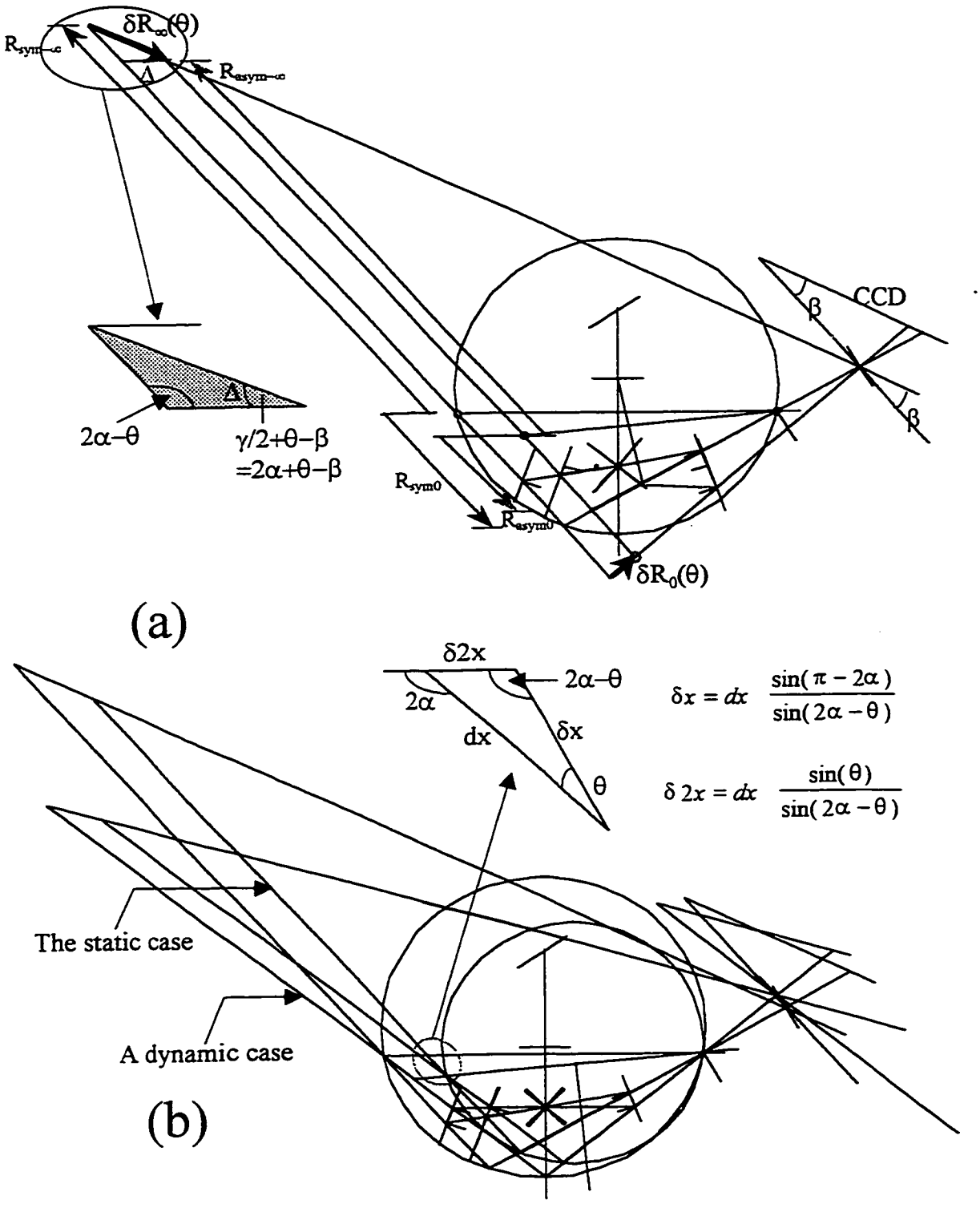

Figure 3.13: (a) The unfolded geometry of the symmetrical model and the asymmetrical one. (b) The unfolded geometry for the static case and a dynamic case.

3.3.3.2 Derivations of the Collinearity Equation for Asymmetrical Single-Scan Axis Scanner

The two correction vectors $\delta\mathbf{R}_0$ and $\delta\mathbf{R}_\infty$, shown in Figure 3.13a, are the result of moving the left mirror a distance **dx**. The **X** and **Z** components of these two correction vectors $\delta\mathbf{X}_0$, $\delta\mathbf{Z}_0$, $\delta\mathbf{X}_\infty$ and $\delta\mathbf{Z}_\infty$ are used as follows:

$$Xasym_0(\theta) = Xsym_0(\theta) - dx\, X\delta_0(\theta) \qquad \text{Equation 3.39}$$

$$Xasym_\infty(\theta) = Xsym_\infty(\theta) - dx\, X\delta_\infty(\theta) \qquad \text{Equation 3.40}$$

$$Zasym_0(\theta) = Zsym_0(\theta) - dx\, Z\delta_0(\theta) \qquad \text{Equation 3.41}$$

$$Zasmy_\infty(\theta) = Zsym_\infty(\theta) - dx\, Z\delta_\infty(\theta) \qquad \text{Equation 3.42}$$

Therefore, the collinearity equations are given as:

$$Xasym_g(p,\theta) = Xasym_{-\infty}(\theta) + P_\infty \frac{[Xasym_0(\theta) - Xasym_{-\infty}(\theta)]}{P_\infty - p} \qquad \text{Equation 3.42}$$

$$Zasym_g(p,\theta) = Zasym_{-\infty}(\theta) + P_\infty \frac{[Zasym_0(\theta) - Zasym_{-\infty}(\theta)]}{P_\infty - p} \qquad \text{Equation 3.42}$$

3.3.4 Dual Scan Axis Collinearity Equation

As shown in Figure 3.14, the second scan axis is achieved by adding the Y-axis rotation mirror to the single scan axis case. It is assumed that the scanning mirror is thin and flat and no wobble is present in the axis of rotation. From the geometry shown in Figure 3.14, the X, Y, Z coordinates of the collinearity equation are derived as:

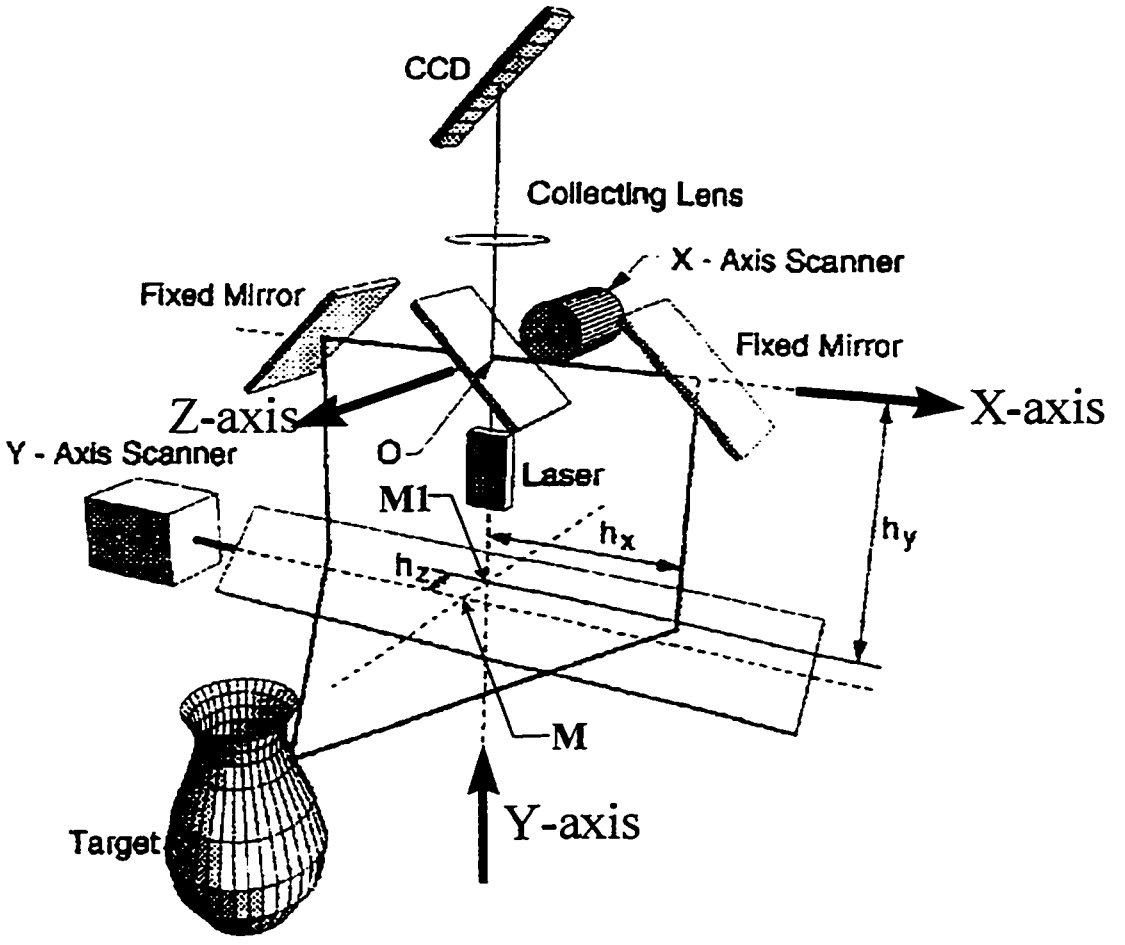

Figure 3.14: The dual-axis scanner in schematic view (from Beraldin et. al., 1993).

$$X_s(\bar{p},\theta) = X_g(p,\theta) + X_0 \qquad \text{Equation 3.43}$$

$$Y_s(\bar{p},\theta,\phi) = (Z_g(p,\theta) - h_y + h_z \tan(\pi/4-\varphi))\sin(\phi) - h_y + h_z \tan(\pi/4-\varphi) + Y_0 \qquad \text{Equation 3.44}$$

$$Z_s(\bar{p},\theta,\phi) = (Z_g(p,\theta) - h_y + h_z \tan(\pi/4-\varphi))\cos(\phi) + Z_0 \qquad \text{Equation 3.45}$$

Simplifying Equations 3.44 and 3.45 results in:

$$Y_s(\bar{p},\theta,\phi) = (Z_g(p,\theta) - h_y)\sin(\phi) - h_y + h_z \cos(\phi) + Y_0 \qquad \text{Equation 3.46}$$

$$Z_s(\bar{p},\theta,\phi) = (Z_g(p,\theta) - h_y)\cos(\phi) - h_z \sin(\phi) + h_z + Z_0 \qquad \text{Equation 3.47}$$

In the equations above, $\mathbf{X_0}$, $\mathbf{Y_0}$ and $\mathbf{Z_0}$ are the coordinates of the center of the scanner's axis, point **O** in Figure 3.14. The coordinate pairs $X_g(p,\theta)$ and $Z_g(p,\theta)$ is the position of a point that would be measured with a single-scan axis laser scanner with respect to the scanner's axes. The angles θ and ϕ are the deflection angles of the **X** and **Y** scanner axes driven by galvanometers. The distances $\mathbf{h_z}$ and $\mathbf{h_y}$ are the shift between the scanner's coordinate axes at point **O** and the rotating mirror axes at point **M**, see Figure 3.14.

Equation 3.43 shows that the introduced Y-axis rotation mirror does not affect the X-coordinate of the measured point, assuming perfect mirror mounting. However, the Y and Z coordinates in Equations 3.44 and 3.45, are measured as the Y-axis rotating mirror deflects the laser ray along the Y-Z plane. Figure 3.15 illustrates and shows that the size

of the deflection angle ϕ is double the size of the mechanical angle φ of the rotating mirror. The sign convention of the angle ϕ (i.e. positive counter clock-wise) is also shown in Figure 3.15.Equations 3.43, 3.46 and 3.47 form the basis for the derivation of the design matrices for camera calibration.

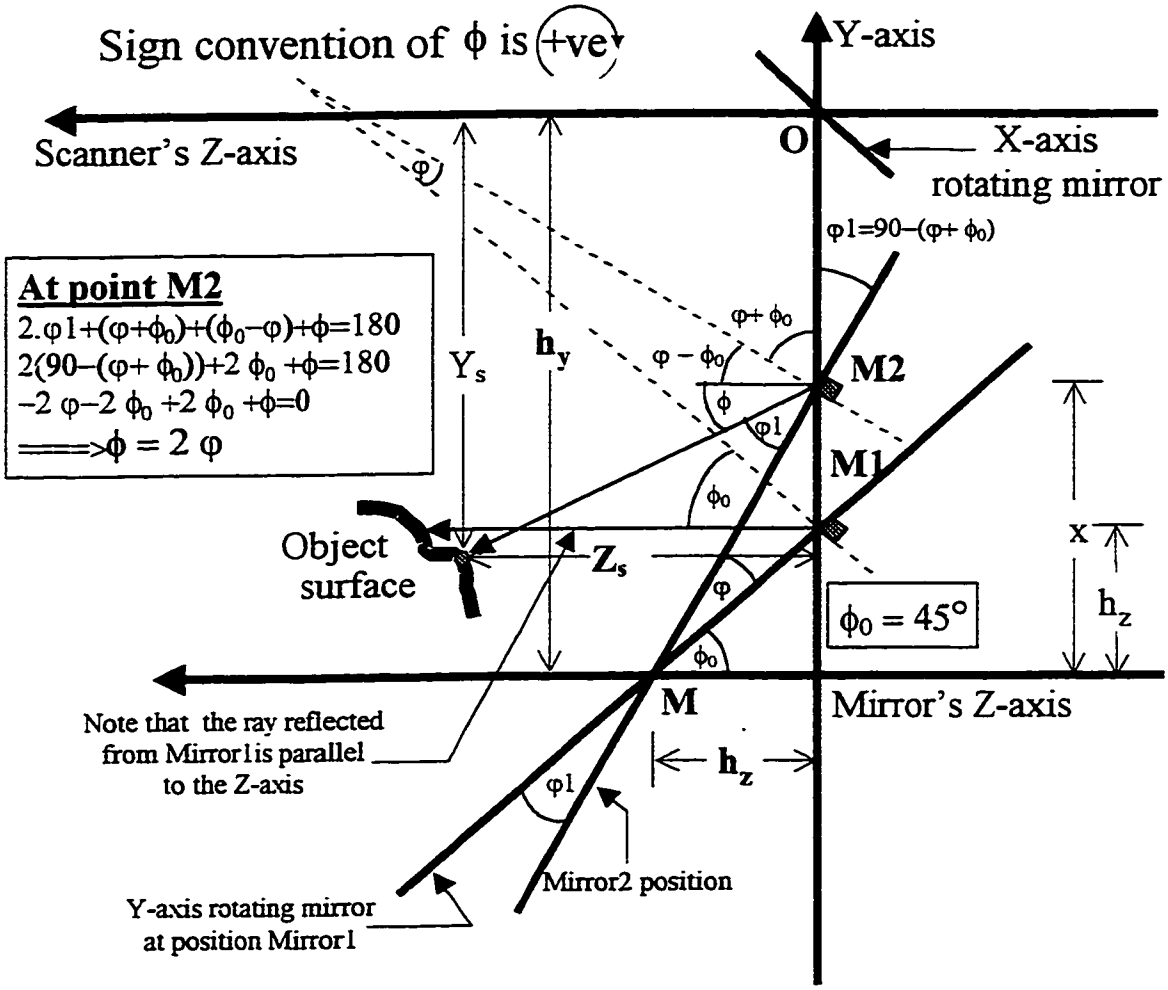

Figure 3.15: Cross-section along the Z-Y plane of the dual-axis scanner.

CHAPTER FOUR

SYSTEM CALIBRATION

4.1 The LSS Geometry and Interpretation of Digital Data

As explained in Section 2.3, the LSS produces both depth-coded images and intensity images. The digital data encoded in both images is the pixel-registered value and the pixel coordinates **i** and **j**. The registered value of each pixel ($\mathbf{p_0}$) in a depth coded image corresponds to the distance from the upper edge of the CCD sensor to the point where the laser beam hits the sensor, see Figure 4.1a. Mapping each element of the 512 element one-dimensional array CCD sensor to 1/64 of a pixel forms the dynamic range of the depth value ($\mathbf{p_0}$) for each pixel in the image. The range values would therefore be between 0 and 32768. The actual **p** used in the mathematical model is the distance from the principal point of the CCD sensor to the spot position (positive sign to the left of the principal point as shown in Figure 4.1a). This produces a principal point spot position **p** equal to zero. Equation 4.1 shows the relationship of the spot position **p** as a function of the measured digital value $\mathbf{p_0}$ and the sensor parameters: **PixelSize**, **Pscale**, **SensorLength**, and $\mathbf{P_\infty}$.

$$p = p_0 \cdot \frac{PixelSize}{Pscale} - SensorLength + P_\infty \qquad \text{Equation 4.1}$$

where: $\mathbf{p_0}$ is the registered value of each pixel in the depth coded image, and

$$P_\infty = f_0 \sin(4 \cdot \alpha) \,/\, \cos(\beta - 4 \cdot \alpha), \qquad \text{Equation 4.2}$$

$\mathbf{P_\infty}$, α, and β are shown in Figure 4.1a, and

PixelSize is the length of each pixel, equal to 0.05 mm. **Pscale** is the mapped ratio of each pixel, equal to 1/64. **SensorSize** is the size of the one-dimensional CCD sensor, which is 512 pixels. **SensorLength** is the total length of the CCD sensor in mm,

SensorLength = **PixelSize** X **SensorSize** = 0.05 X 512 = 25.6 mm. The pixel value in either the depth coded image or the intensity image is a positive value (i.e. 0 to 4096 or 0 to 32768). If there is no return laser signal at a specific pixel, the digital value of the pixel is registered in both images as **-1**. An example of such a situation is when the laser beam hits the edges of an object during acquisition, which produces pixel-registered values of **-1s** around the edges of objects in laser images.

The registered value of each pixel **I** in the intensity image is the intensity of the laser beam at that spot on the CCD sensor. The dynamic range of the intensity image is between 0 and 4096. The intensity image is useful for detecting edges and locating target centres. The pixel coordinates **i** and **j** for each pixel are the same in both the depth-coded image and the intensity image. The image-coordinates **i** and **j** correspond to the X and Y coordinates of an object point, see Figure 4.1, and are directly related to the rotational angles θ and ϕ, which are related to the X-axis and Y-axis galvanometers (i.e. $\theta=2\kappa$ and $\phi=2\varphi$), and are given as:

$$\theta = \theta_0 + i \cdot \delta\theta \quad \text{And} \quad \phi = \phi_0 + j \cdot \delta\phi \qquad \text{Equation 4.3}$$

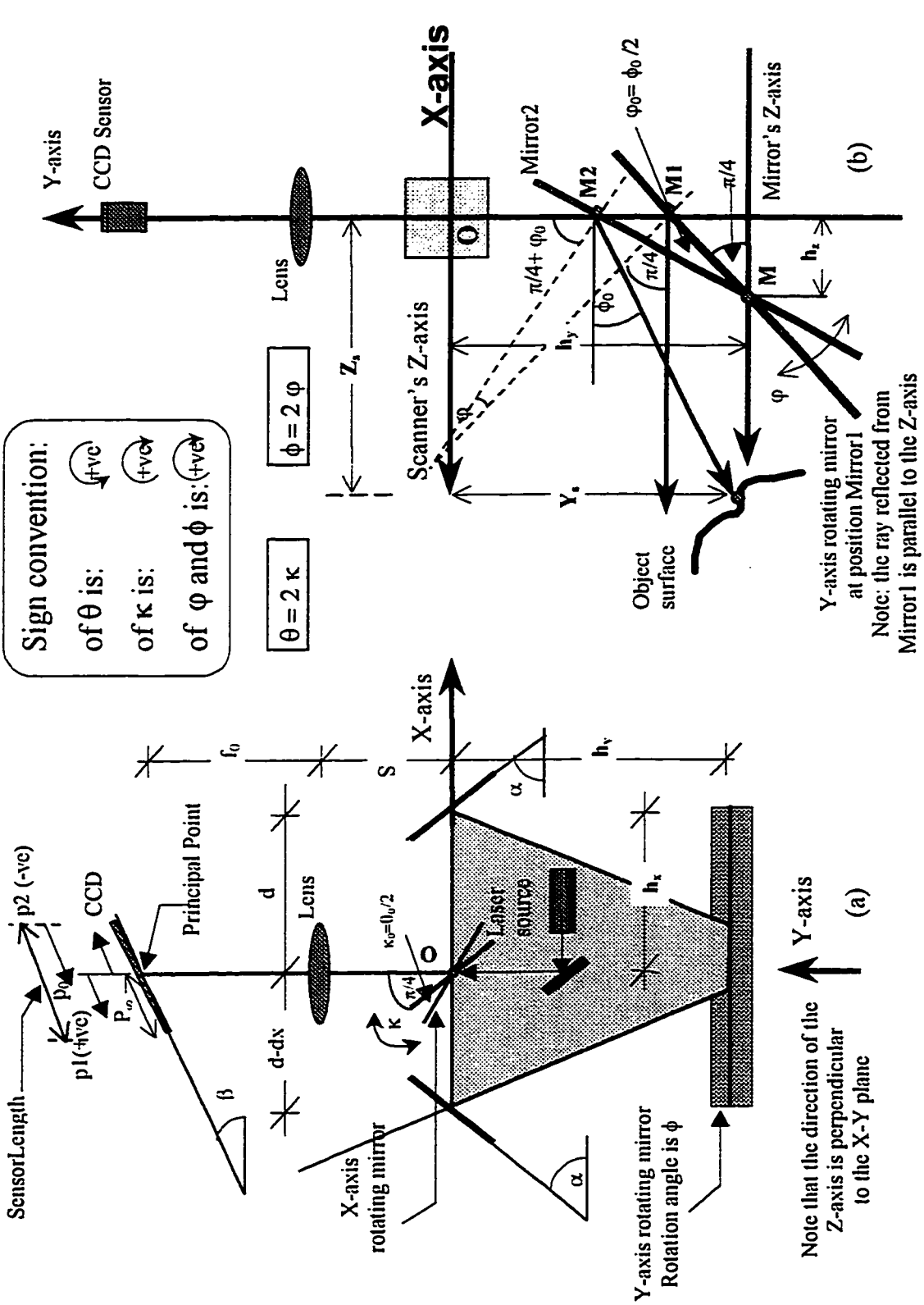

Figure 4.1: (a) Cross-section along the X- and Y axes of the LSS. (b) Cross-section along the Y- and Z- axes of the LSS.

The angles θ_0 and ϕ_0 are the initial angular field of view and $\delta\theta$ and $\delta\phi$ are the step angles, and are double the size of κ_0, φ_0 and $\delta\kappa$, $\delta\varphi$ of the **X**-axis and **Y**-axis of the rotational mirrors (galvanometers) constants, see Figures 4.1a and 4.1b. These variables are assumed to be constant for each LSS configuration (e.g. angular field of view, lens mode, acquisition strategy, image resolution, and/or other configurations).

Figure 4.1 illustrates the position of the rotation mirrors where each mirror is set at an angle $\pi/4$ from the vertical axis. The geometry corresponding to this condition is equivalent to the static geometry of the scanner. When the scanner starts scanning, the X-axis and Y-axis mirrors are set at angles κ_0 and φ_0 from static geometry position.

4.2 The LSS Mathematical Model

In a standard unit system (e.g. metric units), the X, Y, and Z coordinates of a point are functions of **p**, θ and ϕ, and are, therefore, functions of $\mathbf{p}_0$, **i**, and **j**. In the following sections, the internal parameters and the interior orientation parameters, the exterior parameters, the collinearity equations and the distortion model are explained and discussed. The LSS parameters, the mathematical model and the distortion model play an important role in the transformation (calibration) from the laser image coordinates to metric coordinates in order to produce three-dimensional scenes, and to further improve the precision of measurements.

4.2.1 Internal and Interior Orientation Parameters of the LSS

As illustrated in Figure 4.1, the internal parameters of the LSS are:

1. $\mathbf{f_0}$: the effective focal length or the distance from the lens plane to the position detector.

2. $\mathbf{P_\infty}$: the location of the vanishing point on the detection axis, equation 4.2.

3. β: the tilt angle of the position detector found according to design specifications, see Section 4.4.4.

4. α: the tilt angle of the fixed mirrors.

5. γ: the triangulation angle.

   where $\gamma = 4\alpha - \pi$ Equation 4.4

6. **S** : the distance between the lens and the effective position of the collection axis (i.e. the centre of the X-axis rotating mirror).

7. **d**: the distance between the centres of the fixed and the rotating mirrors (where $\mathbf{d = h_X}$).

8. **T**: half the distance between the projection and collection pivots (i.e. deflection points),

where $T = d\sin(\gamma/2)+d$ Equation 4.5

9. **dx**: the shift of the centre of the X-axis rotating mirror.

10. $\mathbf{h_Y}$: the distance between the centres of the rotating Y-axis mirror and the fixed mirrors along the Y-axis.

11. $\mathbf{h_Z}$: the distance between the Y-axis of the scanner and the Y-axis mirrors along the Z-axis.

The physical values of these internal parameters of The University of Calgary Laser Scanning System are (given by the NRC, see NRC sheets 1995):

◆ d = 48 mm	S = 26.27 mm	h_y = 43 mm
◆ β = 50.187°	α = 46.05°	h_z = 5 mm
◆ f_o = 108.810 mm	P_∞ = 11.469 mm	dx = 11 mm

The interior orientation parameters of the LSS are:

1. $\theta_0 = 2\ \kappa_0$: the angular position of the X-axis rotating mirror from its initial position when the LSS starts scanning.

2. $\delta\theta = 2\ \delta\kappa$: the incremental angle per scanning line along the X-axis of the scanner,

where $\delta\theta = \dfrac{\text{angular field of view along the X-axis}}{\text{number of pixels per line}}$ Equation 4.6

3. $\phi_0 = 2\,\varphi_0$: the angular position of the Y-axis rotating mirror from its initial position when the LSS starts scanning.

4. $\delta\phi = 2\,\delta\varphi$: the incremental angle per pixel along the Y-axis of the scanner,

where: $\delta\phi = \dfrac{\text{angular field of view along the Y-axis}}{\text{number of scanning lines}}$ Equation 4.7

The angles θ_0 and ϕ_0 and the incremental angles $\delta\theta$ and $\delta\phi$ define the interior orientation parameters. These angles depend on the chosen angular field of view and the size of the acquired image (i.e. number of lines and number of pixels per line). The operator specifies the angular field of view, the number of lines and the number of pixels per line according to the required resolution, precision and coverage of the scene.

4.2.2 Exterior Orientation Parameters

The exterior orientation parameters of the LSS define the image position and orientation in the object space. The object space coordinates of the centre of the LSS coordinate system (i.e. three translations Xo, Yo, and Zo) define the position of the photograph. The orientation refers to the spatial relationship between the object coordinate system (X, Y, and Z) and the LSS coordinate system. The orientation angles are ω, Φ, and K which correspond to the rotational angles about the X-axis, Y-axis and Z-axis, respectively.

Figure 4.2a illustrates the three translations and the three orientations. For calibration purposes, the object space axes are imagined to be rotated sequentially; firstly, about the object space X-axis through angle ω; secondly, about the once-rotated Y-axis through angle Φ; and thirdly, about the twice rotated Z-axis through angle K. Thus, the final positions of object space points are transformed to the LSS coordinate system using the exterior orientation parameters, as in the example in Figure 4.2b. The rotation matrix R is written as:

$$R=R_K \cdot R_\Phi \cdot R_\omega \qquad \text{Equation 4.8}$$

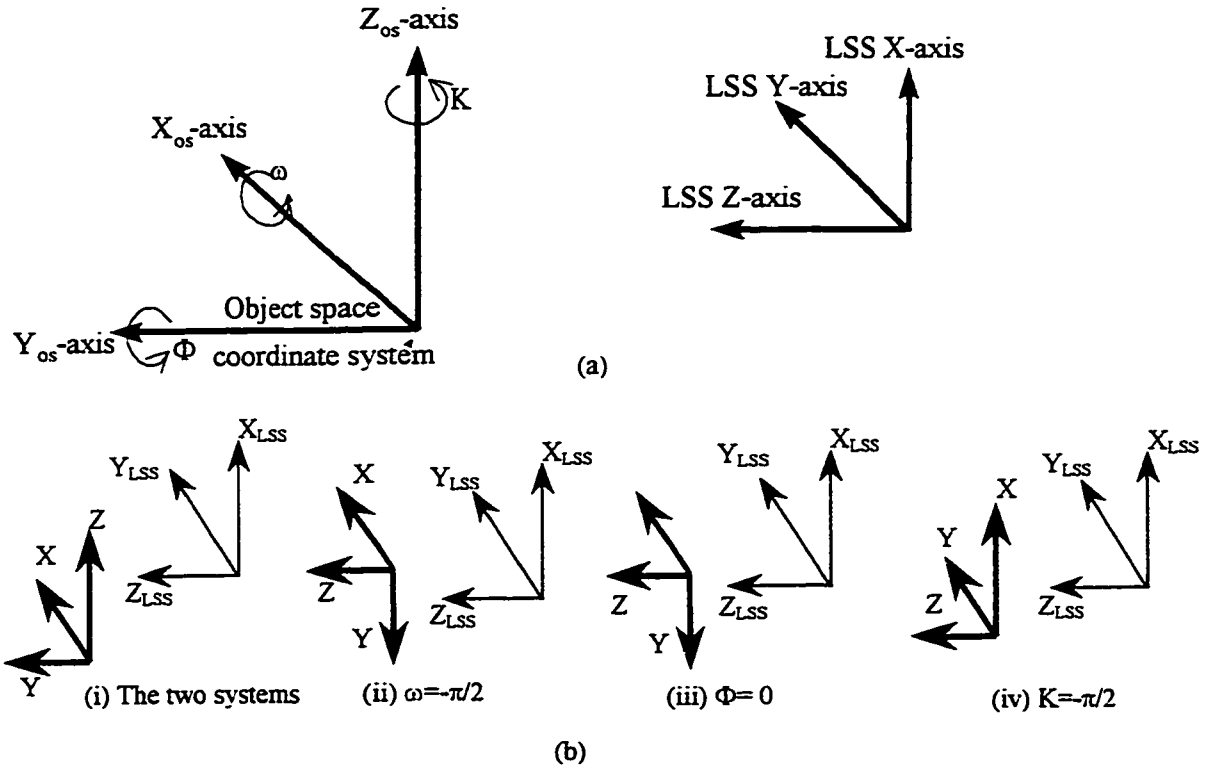

Figure 4.2: (a) The object space and the LSS coordinate systems. (b) Transformation of object space to LSS coordinate system.

$$R(\mathrm{K},\Phi,\omega)=\begin{bmatrix}\cos\Phi\cos\mathrm{K} & \cos s\omega\sin\mathrm{K}+\sin\omega\sin\Phi\cos\mathrm{K} & \sin\omega\sin\mathrm{K}-\cos\omega\sin\Phi\cos\mathrm{K}\\ -\cos\Phi\sin\mathrm{K} & \cos\omega\cos\mathrm{K}-\sin\omega\sin\Phi\sin\mathrm{K} & \sin\omega\cos\mathrm{K}+\cos\omega\sin\Phi\sin\mathrm{K}\\ \sin\Phi & -\sin\omega\cos\Phi & \cos\omega\cos\Phi\end{bmatrix}$$

Equation 4.9

$$\begin{Bmatrix}X\\Y\\Z\end{Bmatrix}_{LSS}=R(\mathrm{K},\Phi,\omega)\begin{bmatrix}X-X_0\\Y-Y_0\\Z-Z_0\end{bmatrix}_{Object\ Space(OS)}$$

Equation 4.10

4.2.3 The Collinearity Equations

As discussed in Chapter 3, the following are the collinearity equations:

$$X_s(\bar{p},\theta)=X_g(p,\theta)+X_0$$

Equation 4.11

$$Y_s(\bar{p},\theta,\phi)=(Z_g(p,\theta)-h_y)\sin(\phi)-h_y+h_z\cos(\phi)+Y_0$$

Equation 4.12

$$Z_s(\bar{p},\theta,\phi)=(Z_g(p,\theta)-h_y)\cos(\phi)-h_z\sin(\phi)+h_z+Z_0$$

Equation 4.13

where:

$$X_g(p,\theta)=X_{-\infty}(\theta)-dx\delta X_\infty(\theta)+P_\infty\frac{[X_0(\theta)-dx\delta X_0(\theta)-X_{-\infty}(\theta)+dx\delta X_\infty(\theta)]}{P_\infty-p}$$

Equation 4.14

$$Z_g(p,\theta)=Z_{-\infty}(\theta)-dx\delta Z_\infty(\theta)+P_\infty\frac{[Z_0(\theta)-dx\delta Z_0(\theta)-Z_{-\infty}(\theta)+dx\delta Z_\infty(\theta)]}{P_\infty-p}$$

Equation 4.15

and where:

$$X_0(\theta) = d(\cos(2\alpha)-1)\frac{\sin(2\theta)}{\sin(4\alpha)}$$ Equation 4.16

$$Z_0(\theta) = d(\cos(2\alpha)-1)\frac{[\cos(2\theta)+1+2\cos(2\alpha)]}{\sin(4\alpha)}$$ Equation 4.17

$$X_\infty(\theta) = \frac{-d(\cos(2\alpha)-1)\cos(\beta+2\theta)-\cos(2\alpha+\theta)S\cos(\beta)}{\cos(\beta-4\alpha)}$$ Equation 4.18

$$Z_\infty(\theta) = \frac{-d[-\sin(\beta+2\theta)[\cos(2\alpha)-1]-\sin(\beta-4\alpha)+\sin(\beta-2\alpha)]+\sin(2\alpha+\theta)S\cos(\beta)}{\cos(\beta-4\alpha)}$$ Equation 4.19

$$\delta X_0(\theta) = \frac{\cos(2\alpha-\theta)(-\sin(\theta+2\alpha)+\sin(\theta))}{\sin(4\alpha)}$$ Equation 4.20

$$\delta X_\infty(\theta) = \frac{\sin(2\alpha-\theta-\beta)(\sin(\theta+2\alpha)-\sin(\theta))}{\cos(4\alpha-\beta)}$$ Equation 4.21

$$\delta Z_0(\theta) = \frac{\sin(2\alpha-\theta)(-\sin(\theta+2\alpha)+\sin(\theta))}{\sin(4\alpha)}$$ Equation 4.22

$$\delta Z_\infty(\theta) = \frac{\cos(2\alpha-\theta-\beta)(-\sin(\theta+2\alpha)+\sin(\theta))}{\cos(4\alpha-\beta)}$$ Equation 4.23

The coordinate pairs $Xg(p,\theta)$ and $Zg(p,\theta)$, defined by Equations 4.14 and 4.15, are the position of a point that would be measured with a single-scan axis laser scanner. The angles θ and ϕ are the step angles to form the required angular field of view and are double the size of the mechanical angles κ and φ of the X and Y scanner axes driven by

galvanometers. Substituting Equations 4.16 to 4.23 into Equations 4.14 and 4.15 and simplifying results in:

$$X_g(p,\theta) = \frac{p\,a1(\theta) - f_0\,a2(\theta)}{f_0 \sin(2\alpha 1) - p\cos(2\alpha 1 - \beta)} \qquad \text{Equation 4.24}$$

where:

$$\begin{aligned} a1(\theta) = {} & -d\cos(\beta+2\theta) + d\cos(\beta+2\theta)\cos(\alpha 1) + \cos(\theta+\alpha 1)S\cos(\beta) \\ & + \sin(\beta+\theta-\alpha 1)dx\sin(\theta) - \sin(\beta+\theta-\alpha 1)dx\sin(\theta+\alpha 1) \end{aligned} \qquad \text{Equation 4.24a}$$

$$a2(\theta) = d\sin(2\theta) - d\sin(2\theta)\cos(\alpha 1) + \cos(\theta-\alpha 1)dx\sin(\theta) - \cos(\theta-\alpha 1)dx\sin(\theta+\alpha 1) \qquad \text{Equation 4.24b}$$

and:

$$Z_g(p,\theta) = \frac{p\,b1(\theta) - f_0\,b2(\theta)}{f_0 \sin(2\alpha 1) - p\cos(2\alpha 1 - \beta)} \qquad \text{Equation 4.25}$$

where:

$$\begin{aligned} b1(\theta) = {} & d\sin(\beta+2\theta) - d\sin(\beta+2\theta)\cos(\alpha 1) + d\sin(2\alpha 1-\beta) - d\sin(\alpha 1-\beta) \\ & - \sin(\theta+\alpha 1)S\cos(\beta) + \cos(\beta+\theta-\alpha 1)dx\sin(\theta) - \cos(\beta+\theta-\alpha 1)dx\sin(\theta+\alpha 1) \end{aligned} \qquad \text{Equation 4.25b}$$

$$\begin{aligned} b2(\theta) = {} & d\cos(2\theta) + d\cos(\alpha 1) - d\cos(2\theta)\cos(\alpha 1) - d\cos(2\alpha 1) \\ & - \sin(\theta-\alpha 1)dx\sin(\theta) - \sin(\theta-\alpha 1)dx\sin(\theta+\alpha 1) \end{aligned} \qquad \text{Equation 4.25c}$$

with $\alpha 1 = 2*\alpha$. The collinearity equations, Equations 4.11, 4.12, and 4.13, can be rewritten in functional form, taking into consideration the exterior orientation parameter, as follows:

$$f_x = 0 = X_g(p, \theta) - X_{LSS}$$ Equation 4.26

$$f_y = 0 = (Z_g(p, \theta) - h_y)\sin(\phi) - h_y + h_z \cos(\phi) - Y_{LSS}$$ Equation 4.27

$$f_z = 0 = (Z_g(p, \theta) - h_y)\cos(\phi) - h_z \sin(\phi) + h_z - Z_{LSS}$$ Equation 4.28

where X_{LSS}, Y_{LSS} and Z_{LSS} are the 3-D coordinates of an object space point given in the LSS coordinate system. Each can be written as a function of the scale factor, the rotation matrix between the object space coordinate system and the LSS coordinate system and the position of an object space point coordinates with respect to the LSS centre, given as:

$$X_{LSS} = \lambda R_x(\mathrm{K}, \Phi, \omega)[X - X_0]_{OS}$$ Equation 4.29

$$Y_{LSS} = \lambda R_y(\mathrm{K}, \Phi, \omega)[Y - Y_0)]_{OS}$$ Equation 4.30

$$Z_{LSS} = \lambda R_z(\mathrm{K}, \Phi, \omega)[Z - Z_0)]_{OS}$$ Equation 4.31

where λ is the scale between the LSS coordinate system and the control field (target field) coordinate system. The value of the scale factor is assumed equal to one.

Substituting Equations 4.10, 4.24 and 4.25 into Equations 4.26, 4.27 and 4.28 and simplifying results in the basic collinearity equations that form the basic equations for the derivation of the design matrices for camera calibration. The resultant equations are:

$$p\,a1(\theta) - f_0\,a2(\theta) + X_{LSS}[f_0 \sin(2\alpha 1) - p\cos(2\alpha 1 - \beta)] = 0$$ Equation 4.32

$$[p\,b1(\theta)-f_0\,b2(\theta)]\sin(\phi)+[Y_{LSS}-h_y(\sin(\phi)+1)+h_z\cos(\phi)][f_0\sin(2\alpha 1)-p\cos(2\alpha 1-\beta)]=0$$

Equation 4.33

$$[p\,b1(\theta)-f_0\,b2(\theta)]\cos(\phi)+[Z_{LSS}-h_y\cos(\phi)+h_z(1-\sin(\phi))][f_0\sin(2\alpha 1)-p\cos(2\alpha 1-\beta)]=0$$

Equation 4.34

the parameters **p**, $\mathbf{P}_\infty$, θ, and ϕ are given in Equations 4.1, 4.2 and 4.3

There are a total of twenty-two parameters to be solved for. These parameters consist of: two sensor parameters (PixelSize and Pscale), nine internal parameters (**d**, **S**, $\mathbf{h_y}$, β, α, $\mathbf{h_z}$, $\mathbf{f_o}$, $\mathbf{P}_\infty$ and **dx**), four interior orientation parameters (θ_0, ϕ_0, $\delta\theta$, and $\delta\phi$), one scale factor and six exterior orientation parameters ($\mathbf{X_0}$, $\mathbf{Y_0}$, $\mathbf{Z_0}$, ω, Φ, and K).

4.2.4 Model Simulation

Before starting the calibration process of the LSS, it is important to understand the geometry of the derived mathematical model by studying the data generated from the model using simulated observations. Then the simulate data is used for the LSS calibration before using real measured data. This section deals with the different aspects of the mathematical model simulation assuming that the above-explained mathematical model is the perfect model for the LSS system and that there are no distortion effects.

In the two dimensional case, the collinearity equations, Equations 4.24 and 4.25, can be inverted to derive the depth value p in terms of the coordinates of the points in object space (i.e. **x** and **z** coordinates) and the image space coordinates (i.e. **i**). The resulting

collinearity equations can be used to check the compatibility and the final solution for object space coordinates. Note that each inverted equation should mathematically provide exactly the same depth value p. The same process is applied to the three-dimensional case, where three equations are inverted, and all inverted equations should provide the same depth value p for a particular object point.

Figure 4.3 illustrates the three-dimensional output produced by simulated input imagery data for three geometrical positions of the scanner. In the first case (equivalent to the static case in Section 3.2), the two rotational mirrors are positioned at i=j=256 pixels, and the p values ranging from 1000 to 31000 with an interval of 1000. As illustrated in Figure 4.3a, the simulated object space points fit one line, which is the projected laser ray line. The figure also illustrates that the plotted object space points are denser close to the LSS, although the p value is increased by the same interval of 1000. This shows that the closer the object points are to the LSS, the better the resolution

In the second and the third cases, the depth value p is kept at the principal point position on the CCD sensor. In the second case, the Y-axis rotating mirror is positioned at j = 256 pixels, and the X-axis rotating mirror is rotated over a range of angles, θ, corresponding to i values ranging from 0 to 512 pixels, with an interval of 16 pixels. In the third case, the X-axis rotating mirror is positioned at i = 256 pixels, and the Y-axis rotating mirror is rotated over a range of angles, ϕ, corresponding to j values ranging from 0 to 512 pixels, with an interval of 16 pixels. As shown in Figures 4.3b and 4.3c, both cases show the canonical form for ideal imagery. n and the resolution of the LSS.

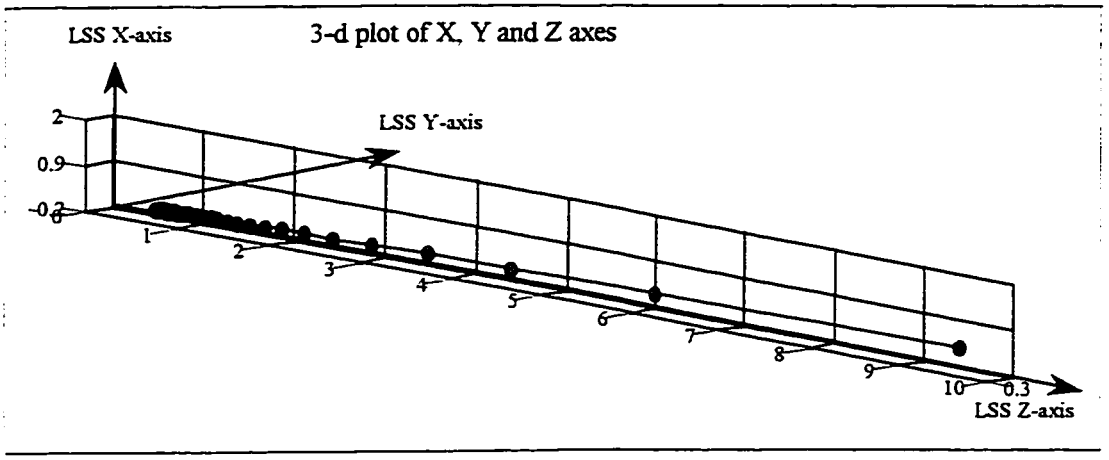

(a) Case I: i=j=256 and p=>1000,2000,3000,4000,.....30000,31000.

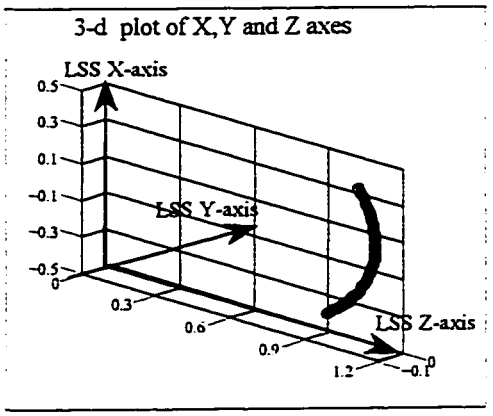

(b) Case II. p at principal point
& j=256 and i=>0-16-32-...512.

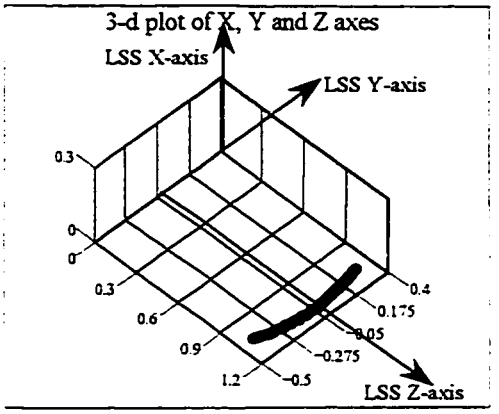

(c) Case III. p at principal point
& i=256 and j=>0-16-32-...512.

Figure 4.3: Three-dimensional output of object space points for simulated data.

Figure 4.4a shows the canonical surfaces of simulated data with each surface corresponding to a particular p value (i.e. five surfaces for p values of 1000, 10000, 15000, 20000 and 25000). For each p value, the range of pixel positions of i and j are from 0 to 512 pixels, with an interval of 64 pixels. For simulation purposes to perform the LSS calibration, plane surface data was extracted from the canonical surface data by interpolation at depth distance of 0.5, 1.0 and 1.5 metres, see Figure 4.4.b.

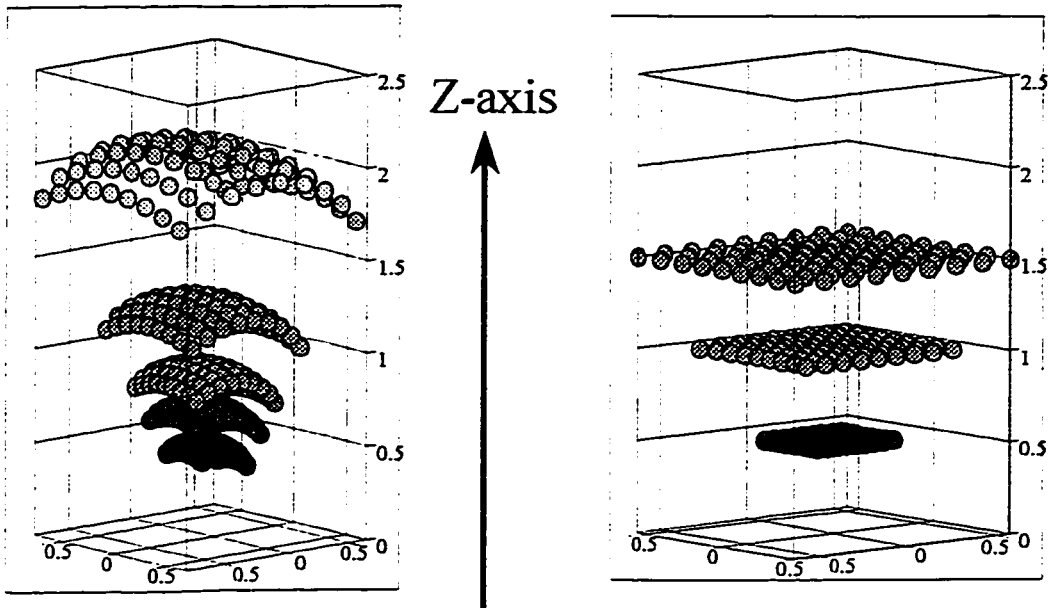

(a) Case IV: Canonical surfaces of p values: 1000, 10000, 15000, 20000 and 25000 and for a range of i and j values of 0,64,128,192,256,320,384,448,512.

(b) Case IV: Plane surfaces at 0.5, 1.0 and 1.5 metres from the LSS for a range of i and j values of 0,64,128,192,256,320,384,448,512.

Figure 4.4: Three-dimensional surfaces of simulated data.

A two dimensional plot of object space points at equal i and j intervals (i.e. 64 pixels each) for a depth distance of 1.5 metres is shown in Figure 4.5. Note that the LSS is a point sensor which measures point coordinates in a polar form (i.e. measures a depth distance at its i and j angular projections of the laser ray from the centre of the LSS). Hence, the plotted points for equal i and j intervals should be further apart as these points are further away from the centre of the LSS coordinate system. The plotted points in the figure shows that the distance between two consecutive points is larger along the Y-axis than along the X-axis over the same i and j intervals (i.e. 64 pixel each). This shows that the LSS has better resolution along its X-axis than its Y-axis. Furthermore, Figure 4.5

illustrates the nonlinear relationship between the X-axis and the Y-axis coordinates. This is logical since the Y- and Z-axes coordinates are derived form the $\mathbf{Z_g}$ (the depth distance of a two dimensional case, Equation 4.25) and the Y-axis deflection angle ϕ, see Equations 4.26 and 4.27. Note, also, that the X-axes coordinates are derived form the $\mathbf{X_g}$ (the horizontal distance of a two dimensional case, Equation 4.24), see Equations 4.26.

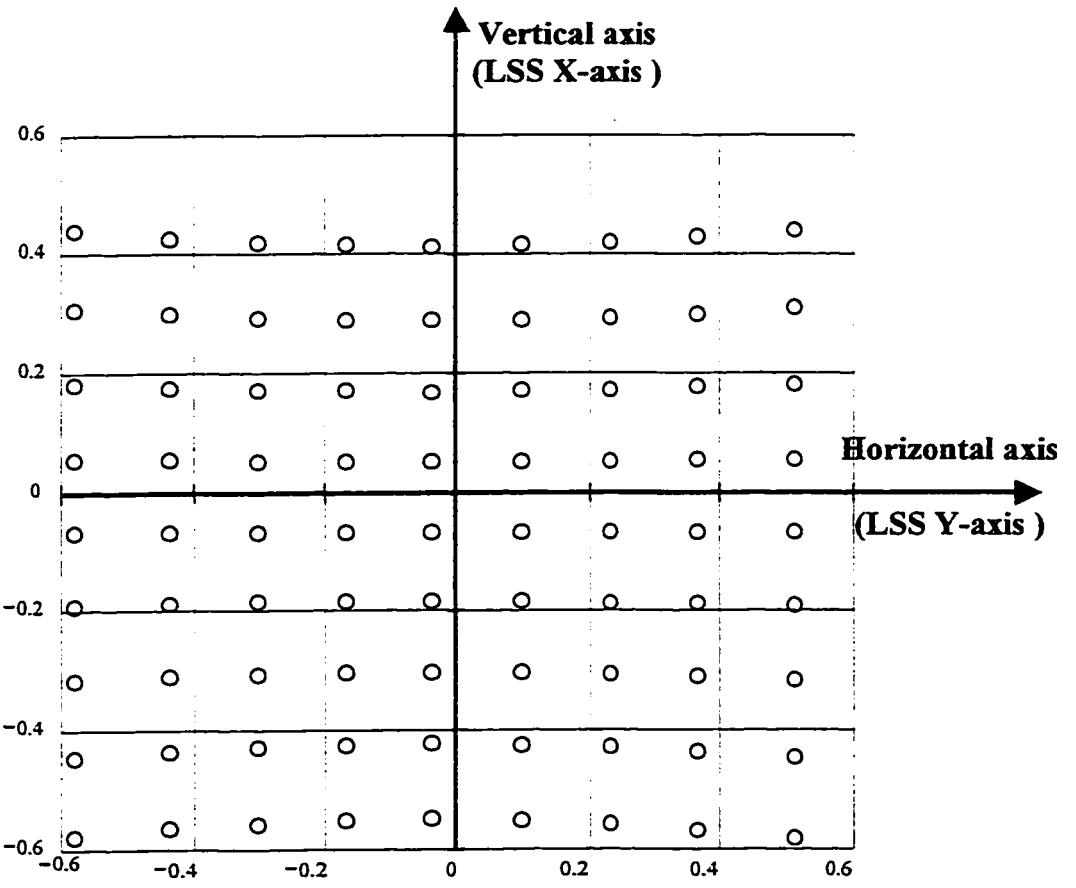

Figure 4.5: Two-dimensional coordinates of object space point at a depth of field of 1.5 metre from the LSS.

4.2.5 Distortion Parameters

To model the behavior of the LSS, one has to model the distortions that influence the captured data. Modeling distortions introduces new parameters, in addition to the twenty-four parameters of the mathematical model to be solved for. The mathematical model one uses to model introduced distortions, determines the number of the distortion coefficients. The following discusses important distortion effects.

4.2.5.1 Insight into LSS Assumptions

Assumptions are important to assist one in deriving a suitable mathematical model. They are also helpful in reaching a specific solution. However, the researcher should have a good understanding of the consequences of these assumptions in terms of introduced errors and distortions. This will give the researcher insight into anticipated problems, and may lead to modification of the mathematical model.

The following summarizes the assumptions of the LSS mathematical model:

1. The Sheimpflug condition is satisfied for all deflection angles to maintain the optimal focusing criteria.

2. The auto-synchronization mechanism is achieved by neglecting the effects of the rotating mirror's thickness, the laser source tilt angle, and imperfections of mirror's mountings.

3. The lens model is replaced by a pin-hole model to simplify the derivation of the mathematical model.

4. The various effects of the galvanometers are ignored.

The ray tracing is done using AutoCAD simulation. Figure 4.6a illustrates the perfect LSS geometry based on the above assumptions. Every object-space point on the geometrical trajectory of the principal point (the dashed circle) has projected and detected axes which pass through the deflection points of the LSS. Any other object-space point that is not on the geometrical trajectory, but it is on any projected axis, passes through its corresponding principal point assembly. The distortion effects, if any, of these assumptions are discussed in the following sections.

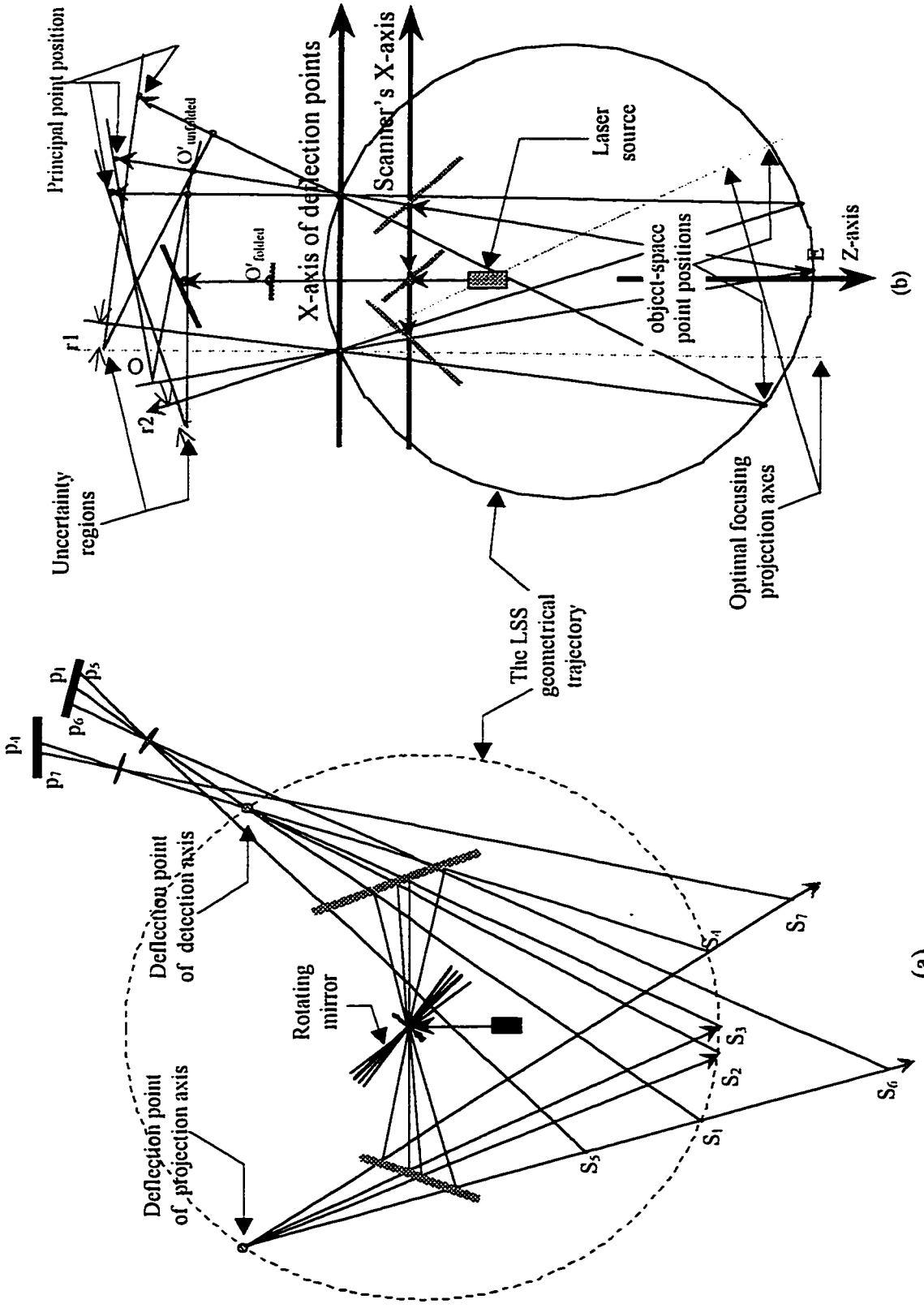

Figure 4.6: (a) Auto-synchronization (b) The Sheimpflug condition distortions.

4.2.5.2 Sheimpflug Condition

As discussed in Section 3.3.2.2 for the symmetrical single-scan axis scanner, the Sheimpflug condition is achieved in the static case (i.e. the deflection angle is zero), as the projection axis, the collection axis, and the lens intersect at one point. However, in the dynamic case, an uncertainty region is formed instead of an intersection point. For the asymmetrical single-scan axis scanner, analysis done using AutoCAD shows that the Sheimpflug condition is achieved at a deflection angle of approximately 2.86 degrees as shown in Figure 4.6c. The figure illustrates the relationship between the rotation/deflection angle θ and the diameter of the uncertainty circle $\mathbf{r_i}$ (see Figure 4.6b) along the detection axis. Figure 4.6b illustrates the uncertainty regions for the asymmetrical scanner. The diameters of these regions increase as the deflection angle θ increases.

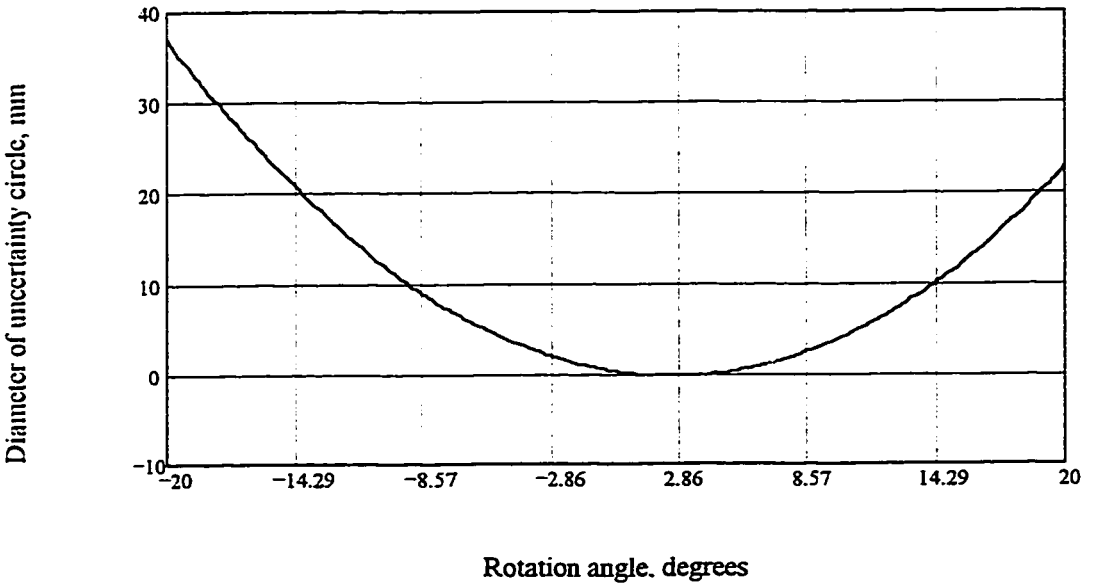

Figure 4.6c: The distortion curve of the Sheimpflug condition.

Figure 4.6b also shows the imaginary projection axes (the dashed-lines) that would satisfy the Sheimpflug condition to achieve optimal focusing. These lines should pass through the deflection point and the intersection point of the detection and the lens axes.

The effect of this is that as the rotational angle increases or decreases, the sharpness of the image decreases as the diameter of the laser spot speckle increases. The distortion becomes more noticeable near edges of objects: for example sudden change in surface heights, surfaces with large reflectance variations, and rough surfaces, see Section 2.4.2. However, these distortions are partially compensated for and decreased since coherent light (i.e. the laser beam) and a sub-pixel peak detector are used.

Third order polynomial functions can be used to model this distortion. The polynomials are function of the pixel position **i** to correct the depth value **p** and the rotation angle θ, and function of the pixel position **j** to correct the rotation angle ϕ. The polynomial functions are given as follows:

$$P(p,i) = p + i.d_1 + i^3.d_2 \qquad \text{Equation 4.35}$$

$$\theta(p,i) = \theta_o + i.d\theta \quad + i^3.d_3 \qquad \text{Equation 4.36}$$

$$\phi(j) = \phi_o + j.d\phi + j^3.d_4 \qquad \text{Equation 4.37}$$

4.2.5.3 Auto-synchronization and the Laser-Source Tilt Angle Effect

The imperfection in mounting the laser source causes the laser beam to hit the X-axis rotating mirror with an introduced tilt angle $\Delta\tau$. This moves the position of the deflection point to a location near the original position, see Figure 4.7. In fact, the deflection point is a small uncertainty region with a diameter of 0.04 mm for a tilt angle of 1 arc-min, which can be assumed to be negligible, see Figure 4.7. Therefore, this movement has a small affect on the auto-synchronization condition. However, the new position of the deflected point **O'''** changes the circular geometrical trajectory and the value of the triangulation angle γ as illustrated in Figure 4.8, which results in changing the values of $R_0(\theta)$ and $R_\infty(\theta)$.

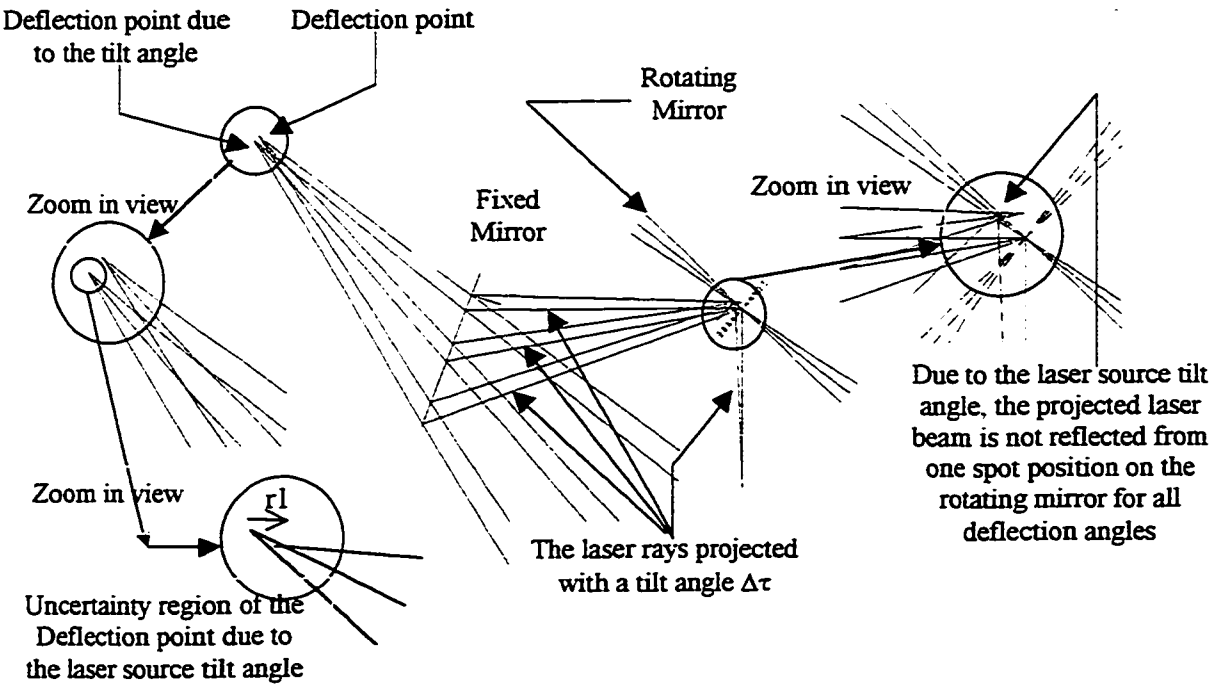

Figure 4.7: The laser-source tilt angle effect.

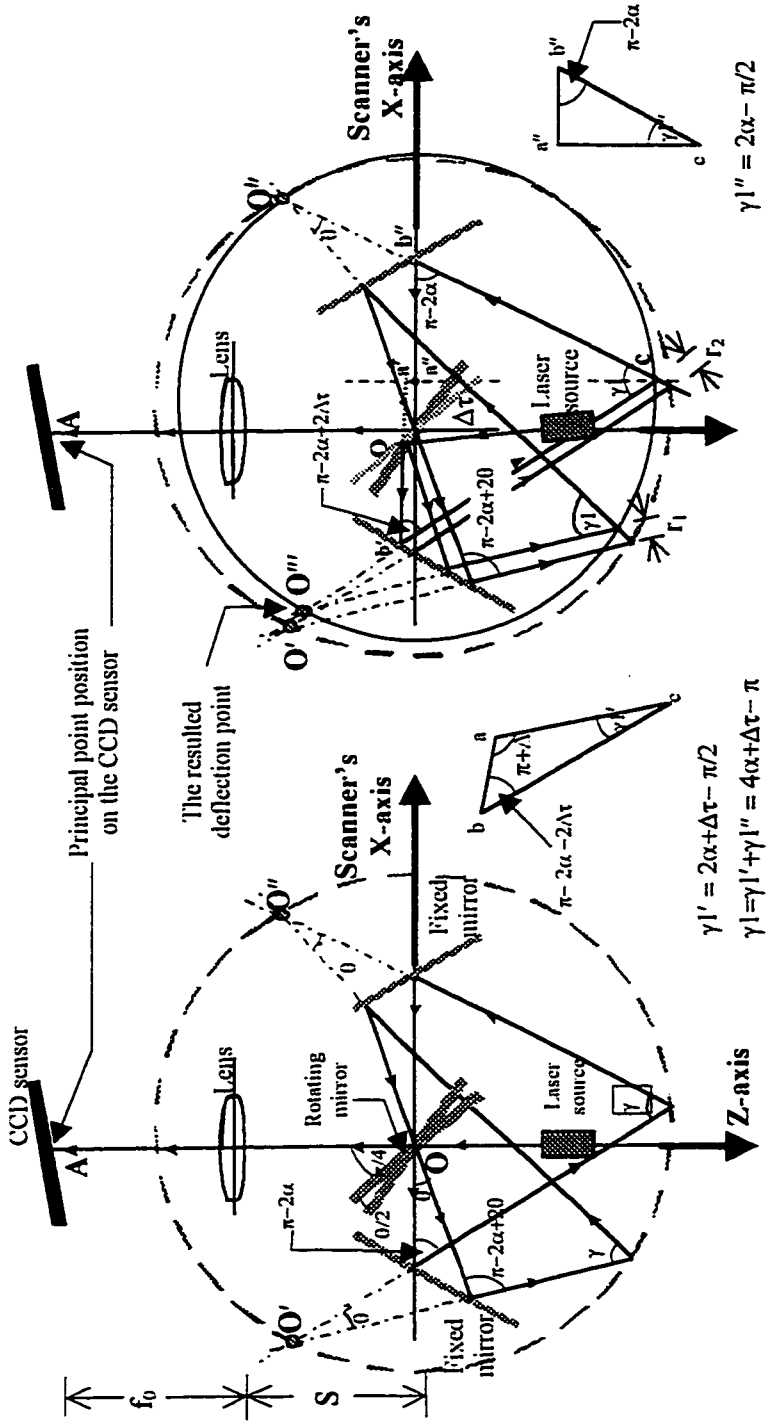

Figure 4.8: The relationship between the original triangulation angle γ and the resultant triangulation angle γ1. **(a)** the original geometry (b) the geometry produced by superimposing the laser-source tilt angle over the original geometry.

This change in the values of $R_0(\theta)$ and $R_\infty(\theta)$ is similar in concept to the difference between the case of asymmetrical single-scan scanner and symmetrical single-scan axis, as explained in Section 3.3.3.

As shown in Figure 4.8, the new value of the triangulation angle is given as:

$$\gamma 1 = \gamma + \Delta\tau = 4\alpha + \Delta\tau - \pi \qquad \text{Equation 4.38}$$

where $\gamma 1$ is the resultant triangulation angle due to the effect of the laser source tilt angle $\Delta\tau$. In the collinearity equations (Equations 4.32, 4.33 and 4.34), the angle $\alpha 1$ (where $\alpha 1 = 2\alpha$, $\alpha = \gamma/4 + \pi/4$ and $\alpha 1 = \gamma/2 + \pi/2$) is substituted in place of the angle γ. Hence, this distortion increases the value of $\alpha 1$ to be:

$$\alpha 1 = \gamma 1/2 + \pi/2 = (\gamma + \Delta\tau + \pi)/2 \qquad \text{Equation 4.39}$$

The tilt angle $\Delta\tau$ also affects the value of $\mathbf{P}_\infty$ (Equation 4.2) to become:

$$\begin{aligned} P_\infty &= f_0 \sin(4\alpha + \Delta\tau) / \cos(\beta - 4\alpha - \Delta\tau) \\ &= f_0 \sin(2\alpha 1) / \cos(\beta - 2\alpha 1) \end{aligned} \qquad \text{Equation 4.40}$$

Therefore, the value of the parameter $\alpha 1$ determined from the calibration is the value of both the angle α and the tilt angle $\Delta\tau$. If the angle α is known precisely, then the tilt angle $\Delta\tau$ can be determined. Since the angle $\alpha 1$ is used to determine the 3-D coordinates of a point, hence this will minimize the errors of this effect. However, the effect of

having an uncertainty region instead of a single point introduces some distortions. This distortion is dependent on the deflection angle values.

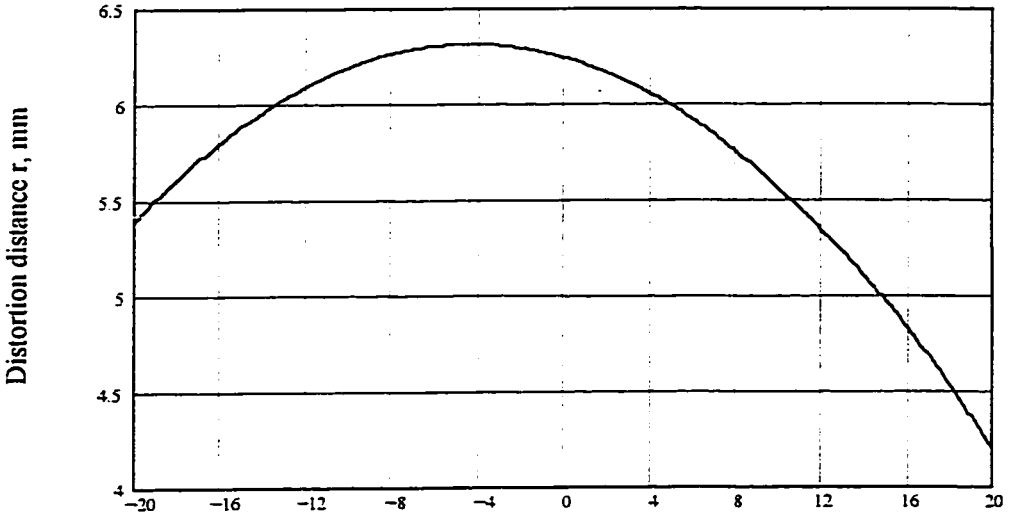

Figure 4.9: The laser-source tilt angle effect on the values of $\mathbf{R_0}$ for an introduced tilt angle of one arc-min.

The shift values $\mathbf{r_i}$ shown in Figure 4.8 are the difference vectors of $\mathbf{R_0}$ values for an introduced tilt angle of 1 arc-min. The shift distance increases and decreases depending on the rotation/deflection angle θ as illustrated in Figure 4.9. This illustrates that the distortion is dependent on the angular values θ and ϕ (or i and j image coordinates). Hence, this effect can be modeled using the same distortion model suggested for the Sheimpflug condition case (i.e. Equations 4.35, 4.36 and 4.37).

4.2.5.4 Auto-synchronization and the Rotating Mirror Thickness Effect

When the rotating mirror thickness is neglected, a common point of reflection at the centre of the mirror is formed. Since, the rotating mirror has a finite thickness, the effect of the thickness causes the reflected laser rays to intersect in a region of uncertainty, rather than at a single point (i.e. the deflection point). This is because the deflection point is actually an image of the point of reflection at the centre of the rotating mirror, point **O**. As shown in the figure, there is no common point of deflection from the rotating mirror, since for each introduced rotational angle θ, the laser ray is reflected at a different point from the rotating mirror, forming a similar region of uncertainty to the deflection region. As a result, the auto-synchronization condition is not fully satisfied and, therefore, an error in the deflection angle is introduced. Also, the centre of the deflection uncertainty region is actually shifted from the original deflection point position.

Furthermore, as illustrated in Figure 4.10, the position of the projected laser from the laser source affects the centre position of the uncertainty region of deflection. According to the instrument drawing (NRC AutoCAD drawings), the mirror thickness is 2 mm and the laser source is mounted such that the projected laser ray, **L1**, passes through the centre of the mirror. The resultant deflection region, **R1**, is the one farthest from the original deflection point **O′**.

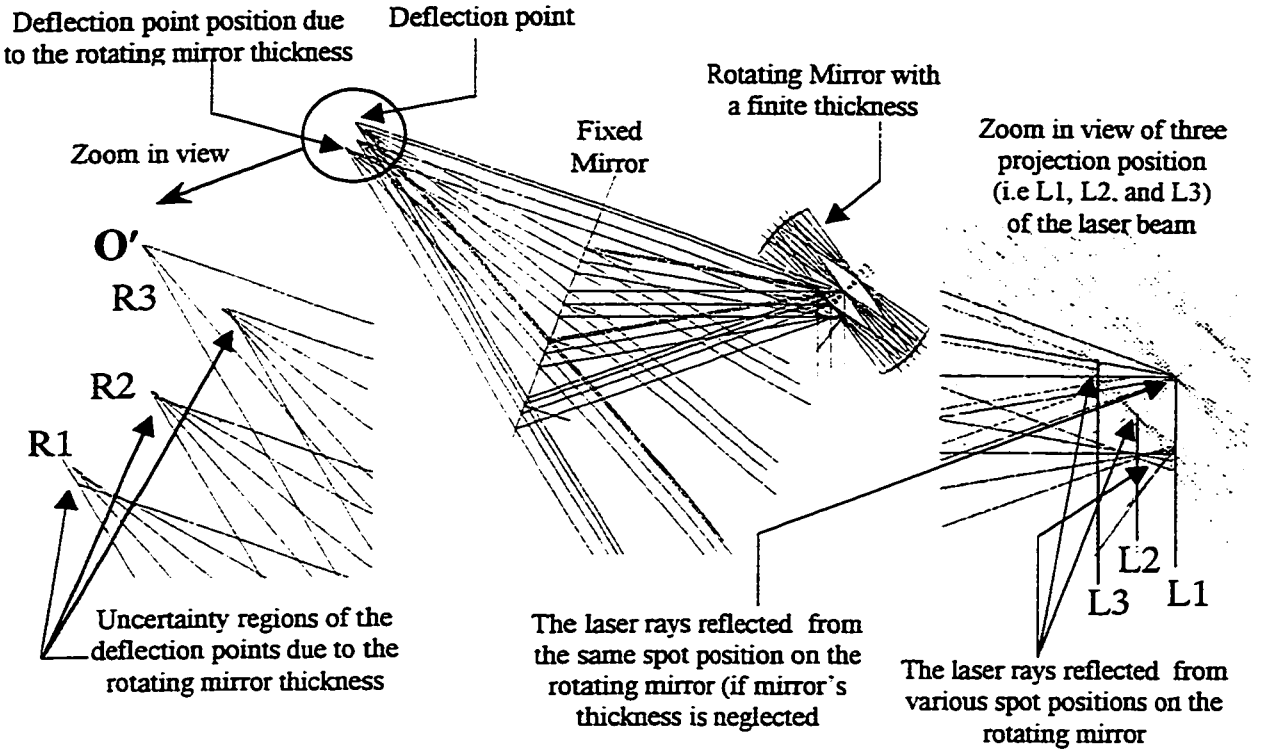

Figure 4.10: The rotating mirror thickness effect on the deflection point.

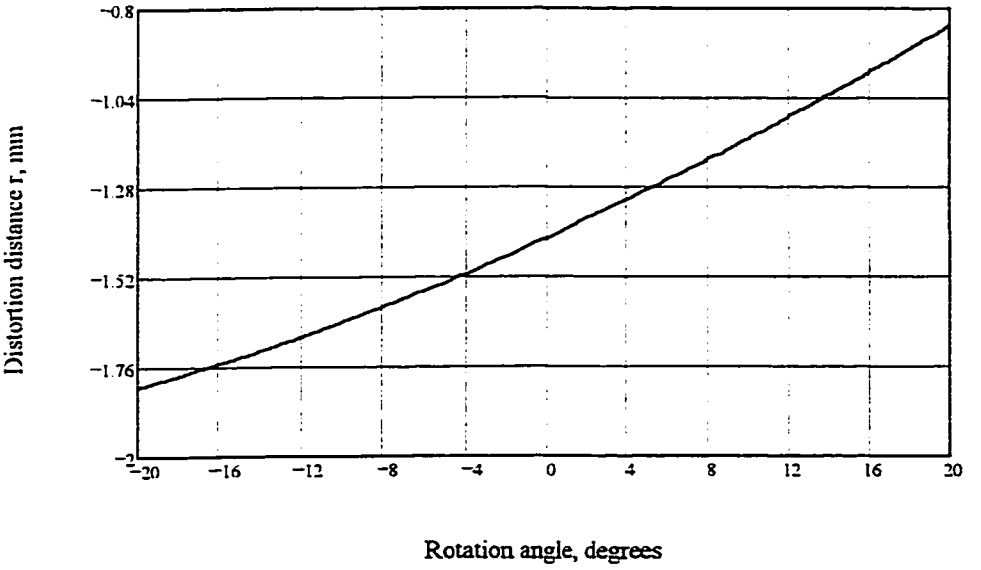

Figure 4.11: The rotating mirror thickness effect on the values of $\mathbf{R_0}$.

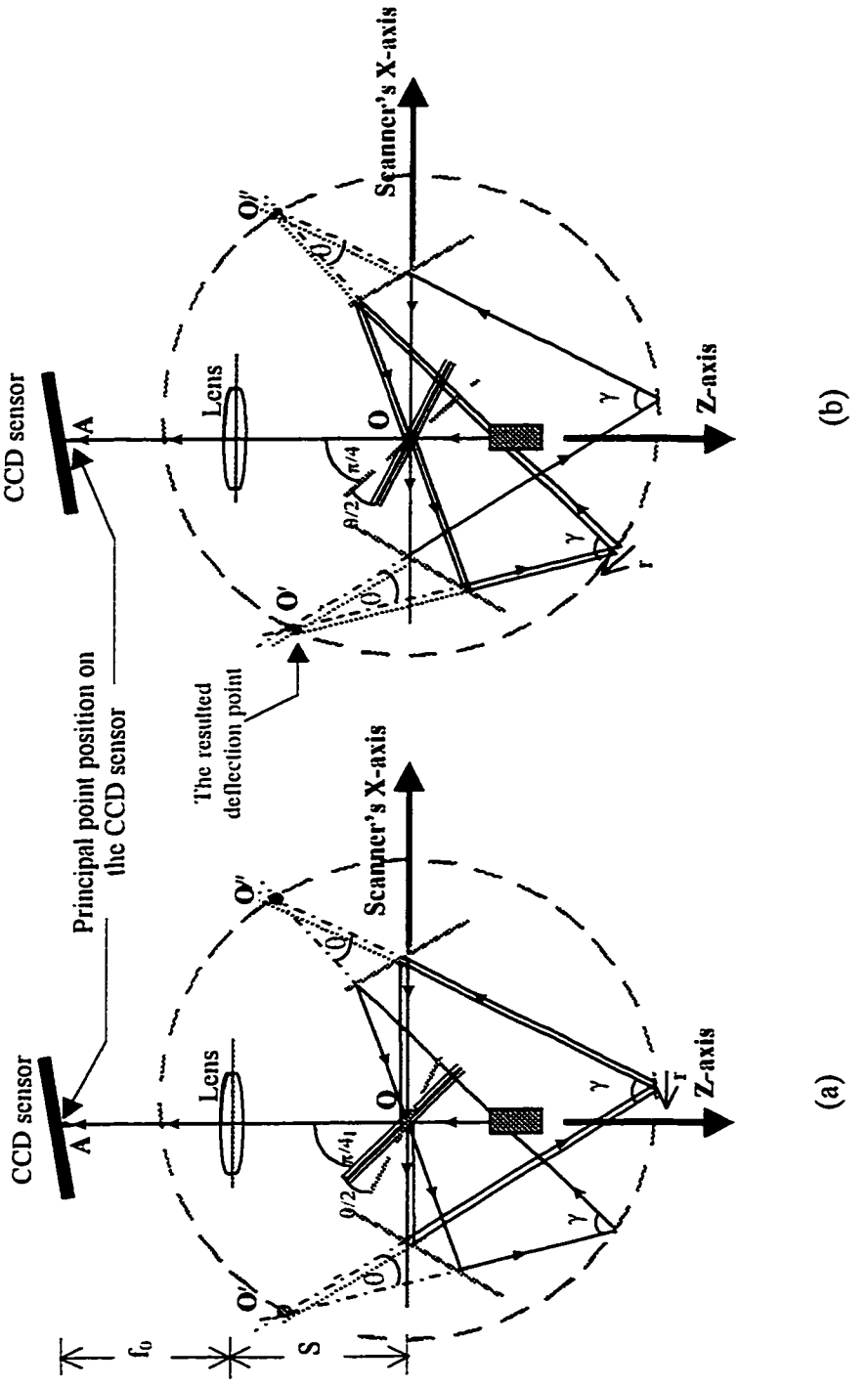

Figure 4.12: The rotating mirror thickness shifts the position of the deflection points. (a) The thick mirror is mounted at $\pi/4$ from the Z-axis superimposed on the original model. (b) The thick mirror is rotated an angle $\theta/2$ from the its original position superimposed on the original model.

Figure 4.12 illustrates the effect of the mirror thickness on the position of the deflection points, assuming the resultant deflection region to be a point. The mirror thickness effect on the reflected laser rays and the resultant deflection points are superimposed on the original geometry.

As shown in the figure, the deflection points **O′** and **O″** are shifted an equal distance to the left of their original position. The distortion effect is shown in Figure 4.12 as shift values $\mathbf{r_i}$ in the values of $\mathbf{R_0}$ (note that similar shift errors are introduced in the values of $\mathbf{R_\infty}$). The shift distance increases as the rotation/deflection angle θ increases as illustrated in Figure 4.11, and therefore, the distortion is dependent on the angular values of θ and ϕ (or i and j image coordinates). These distortion effects are similar to the laser source tilt angle distortion effects and therefore the same distortion model (i.e. Equations 4.35, 4.36 and 4.37) would be suitable.

4.2.5.5 Combination of the Laser-source Tilt Angle and the Rotating Mirror Thickness Effects

Figure 4.13 shows the two effects combined together. Figure 4.14 shows that the two effects are opposite in sign. Also, the figure shows that the effect of a laser-source tilt angle of 1 arc-min is much larger than that of a rotating mirror thickness of 2 mm, which makes the tilt angle effect more dominant.

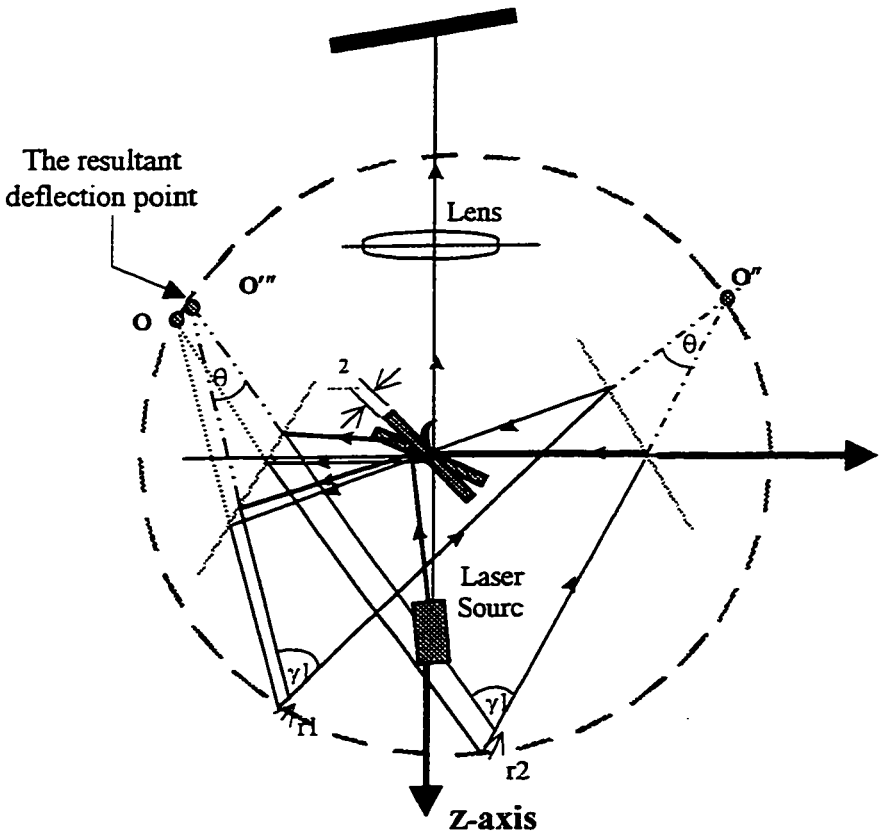

Figure 4.13: The effect of combining the laser-source tilt angle and the mirror thickness.

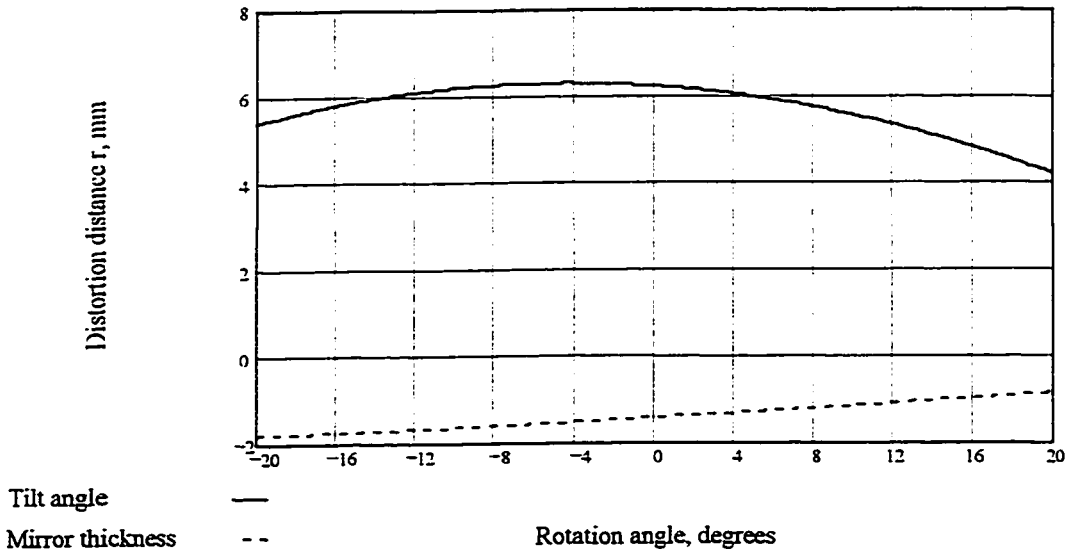

Figure 4.14: The laser-source tilt angle and the rotating mirror thickness effects on the values of $\mathbf{R_0}$.

4.2.5.6 The Effect of Imperfections in Mirror Mounting

This effect would require a re-derivation of the mathematical model of the LSS, since it would affect the projection of the laser ray, the tilt angles of the fixed mirrors and the orthogonality between the LSS axes. For example, the axis of rotation of the X-axis rotating mirror and the axis of the fixed mirror are assumed to be parallel. A tilt of one arc-minute of the fixed mirror axis from this parallel direction, shifts the reflected laser ray spot position on the fixed mirror from the its theoretical position a small distance of 0.3 micrometers, sideways (i.e. perpendicular to the laser ray direction and along the fixed mirror axis direction). Note that, theoretically, both the incident ray and the reflected ray should be in the same plane. This effect, also, increases the length of the base distance d a value of 0.002 micrometers, which is a negligible value. However, this effect is not the focus of this thesis. It is currently under investigation at the NRC.

4.2.5.7 The Lens Model and Radial Lens Distortion:

Radial lens distortion occurs due to imperfections in lens polishing. This effect is a common problem and can be modeled as follows(see Moffitt and Mikhail, 1980):

$$\delta r = \frac{\Delta f}{f} \cdot r + r^3 . c_1 + r^5 . c_2 + r^7 . c_3 + \ldots higher \quad order \quad terms \qquad \text{Equation 4.41}$$

where **r** is the radial distance from the principal position to the position of interest on the image, **δr** is the distortion effect, **f** is the focal length, **Δf** is the change in the focal length (see Figure 4.15a and 4.15b), and $\mathbf{c_1}$, $\mathbf{c_2}$, and $\mathbf{c_3}$ are the polynomial coefficients. Since the

LSS is a point sensor, each pixel in the scanned image is independent from other pixels and, therefore, the lens distortion only affects the depth value.

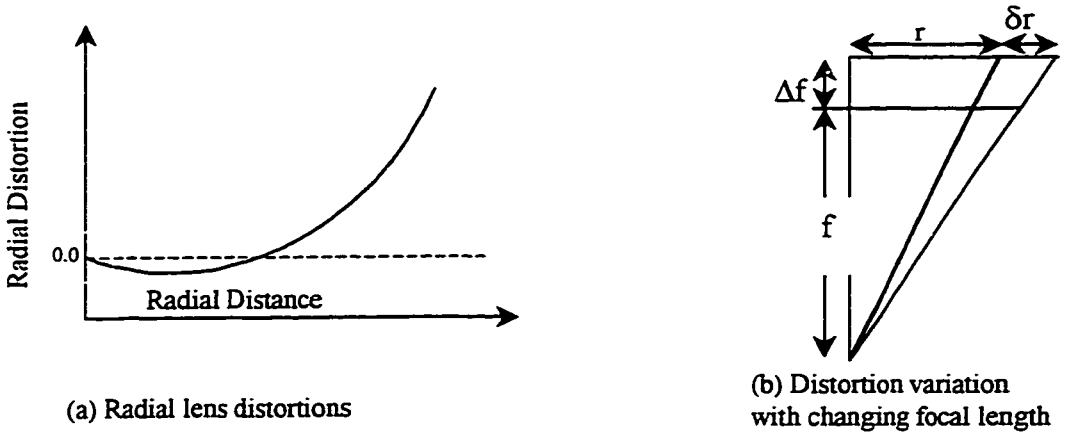

(a) Radial lens distortions

(b) Distortion variation with changing focal length

Figure 4.15: Lens distortion effects.

Assuming there is no change in the focal length and using the second term of the polynomial of Equation 4.41, the equation can be simplified (i.e. $\Delta p=p^3.d_5$) and, therefore, Equation 4.35 becomes as follows:

$$P(p,i) = p + i \cdot d_1 + i^3.d_2 + p^3.d_5 \qquad \text{Equation 4.42}$$

4.2.5.8 Compensation of the Step Angle along the Y-axis Rotation Mirror

As shown on Figure 4.16a, the position of each pixel along the Y-axis is affected by the pixel position along the X-axis due to the continuous movement of both the X-axis and the Y-axis galvanometers. To correct this effect, a third term is added to get the rotational angle ϕ, and Equation 4.37 becomes:

$$\phi(j) = \phi_s + \left(j + \frac{i + 0.5}{1024} \right) d\phi + j^3 d_4 \qquad \text{Equation 4.43}$$

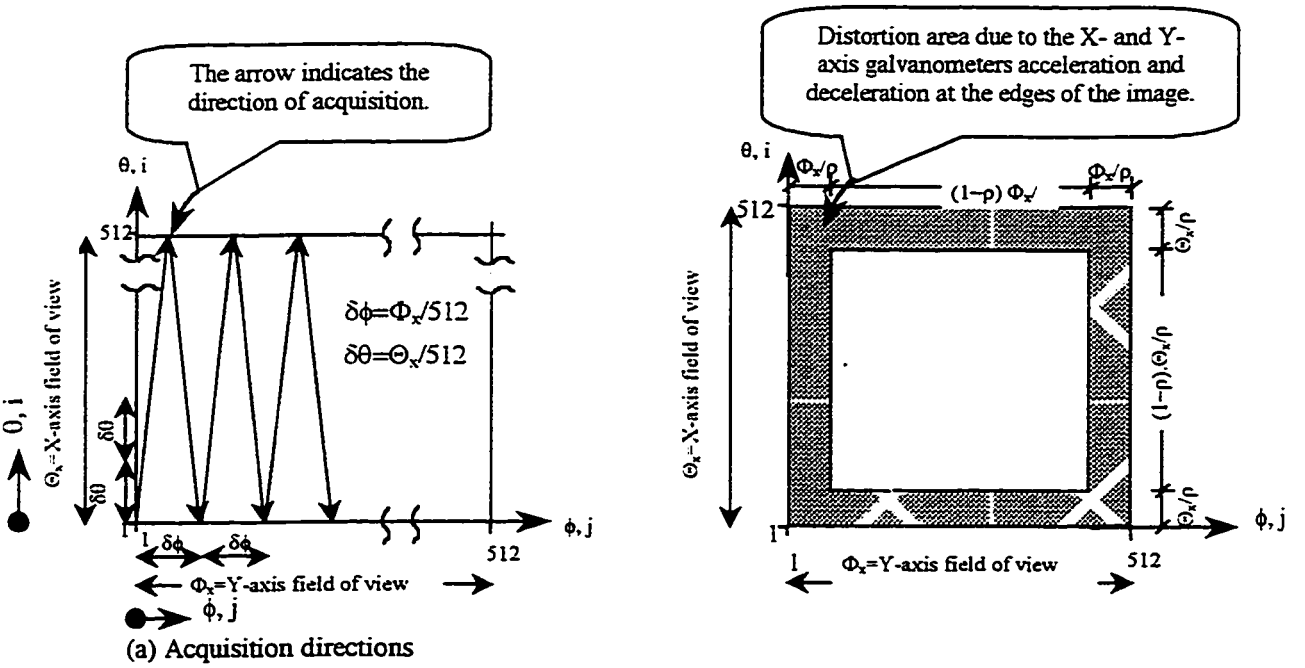

Figure 4.16: Galvanometer distortion effects.

4.2.5.9 The Acceleration and Deceleration of the Rotating Mirrors and Wobble and Jitters Effects of the Galvanometers

The effect of acceleration and deceleration of the rotating mirror (driven by a galvanometer) takes place as each mirror approaches the boundary of the field of view, where distortions become recognizable. Figure 4.16a illustrates an acquisition configuration where the image resolution is 512X512 pixels, and the acquisition directions are from bottom to top for the X-axis galvanometer, and from left to right for the Y-axis galvanometer.

To avoid distortion in the image, acquisition should not take place until the galvanometers stabilize at a constant speed after their acceleration or deceleration. In a typical situation, the galvanometer accelerates or decelerates near the edges of the field of view (say $1/\rho$ of the image size) when the mirror starts, ends or changes its rotation direction. Therefore, to eliminate this effect, the effective field of view should be within the following boundaries (see the white area in Figure 4.16b):

$$\frac{I}{\rho} \le i \ge \frac{7}{\rho} I \quad and \quad \frac{J}{\rho} \le j \ge \frac{7}{\rho} J \qquad \text{Equation 4.44}$$

where I and J are the X-axis and the Y-axis image-resolution, and i and j are the pixel coordinates in the image. The LSS is designed such that its angular field of view is less than the angular field of view of the rotating mirrors, so that, the

acceleration/deceleration effects are eliminated. The wobble and jitter effects of the galvanometers are assumed to be negligible.

4.2.5.10 The Distortion Model

The distortion model used in this thesis is a modified version of the NRC's model The distortion model used by the NRC that was given to the author is based on a third order polynomial function and is shown in the following equations:

$$P(p,i) = p + i\,d_1 + i^3\,d_2 \qquad \text{Equation 4.45}$$

$$\theta(p,i) = \theta_0 + i\,d\theta + i^3\,d_3 + p^3\,d_5 \qquad \text{Equation 4.46}$$

$$\phi(j) = \phi_0 + j\,d\phi + j^3\,d_4 \qquad \text{Equation 4.47}$$

The modified distortion model used in this thesis is based on Equations 4.42, 4.36 and 4.43, which are explained in the previous sections (Section 4.2.5.2 to Section 4.2.5.9). Therefore, the three polynomial functions that absorb the distortion effects in the depth values p, the X-axis rotational angle θ and the Y-axis rotational angle ϕ (Equations 4.42, 4.36 and 4.43) are:

$$P(p,i) = p + i\,d_1 + i^3\,d_2 + p^3\,d_5 \qquad \text{Equation 4.42}$$

$$\theta(p,i) = \theta_0 + i\,d\theta + i^3\,d_3 \qquad \text{Equation 4.36}$$

$$\phi(j) = \phi_0 + \left(j + \frac{i + 0.5}{1024} \right) d\phi + j^3 d_4 \qquad \text{Equation 4.43}$$

Note that i and j are the image coordinates in pixels corresponding to the X and Y axes, θ_0 and ϕ_0 are the initial orientation angles of the laser scanner, and **p** is the inputted depth value at the i and j coordinates. The first polynomial, Equation 4.45, has three coefficients $\mathbf{d_1}$, $\mathbf{d_2}$, and $\mathbf{d_5}$. The first two coefficients correct distortions occurring in the pixel value **p** (depth value) due to inconsistencies in the X-axis galvanometer step rotations and other imperfections that are affected by the pixel position **i** in the image coordinates (e.g. drift effects). The third coefficient $\mathbf{d_5}$ corrects errors in the measured depth value **p**, and is mainly due to lens distortions. The second polynomial, Equation 4.46, has one coefficient $\mathbf{d_3}$, which corrects distortions occurring in the value of the X-axis rotational angles, θ. The coefficient compensates distortions related to the pixel position **i** that are due to several effects (e.g. distortions due to the laser source tilt angle and the rotating mirror thickness). The third polynomial, Equation 4.47, has one coefficient, $\mathbf{d_4}$ related to the pixel position j. The coefficient compensates for distortions occurring in the Y-axis rotational angles ϕ due to inconsistencies of the Y-axis galvanometer step rotations and other imperfections that are affected by the pixel position **j** in the image coordinates (e.g. drift effects).

4.3 Short and Long Distance Calibration

Adequate sharpness is maintained at a depth distance of up to 1.5 to 2.0 metres from the LSS. As discussed previously, as the depth of field to the object space point increases the resolution and the precision of the instrument decreases. Also, the sharpness of these points in image space is reduced due to the assumption that the Sheimpflug condition is satisfied for any dynamic case, see Section 3.3.2.2. As a result, the LSS has to be calibrated twice. The first calibration is called close-range calibration and is for object space points that are within a depth distance of 2.0 metres from the LSS (i.e. the standoff distance is 0.5 metres and the depth of field is up to 1.5 metres) and the lens is set to focusing mode. Long-range calibration is for points at a depth of field of more than 2.0 metres with the lens set to infinity mode. The main difference between the two calibrations is that the focal length setting is different each time and as a result the other parameters change slightly.

Since industrial applications required high precision for deformation measurements, this thesis deals only with short distance calibration. To achieve suitable precision in a typical application, the LSS is setup at depth distances ranging from 0.75 to 1.5 metres.

4.4 Instrument Repeatability and Predicted Precision

4.4.1 Observations, Object Surface, and the Laser Power

For reliable results, the laser power of the LSS must be adjusted according the reflectance characteristics of object surfaces. For example, the target field used for the LSS repeatability testing is composed of a styrofoam black surface with stick-on circular white retro-reflective targets that are mounted in a grid form, see Figure 4.17.

For accurate results, lower laser power must be used to pick up the targets. The intensity image, shown in Figure 4.17b, illustrates that with higher laser power the targets are not clear and, therefore, wrong results would be obtained.

The target field is at depth distance of 1.6 metres from the LSS. The registered values of depth-coded images are color-coded and shown in the palette, see Figure 4.17c. The palette shows that the required range to display the depth-coded image is from 24000 to 29500. The target field surface and the retro-reflective targets have a registered value ranging from 24 500 to 25 500.

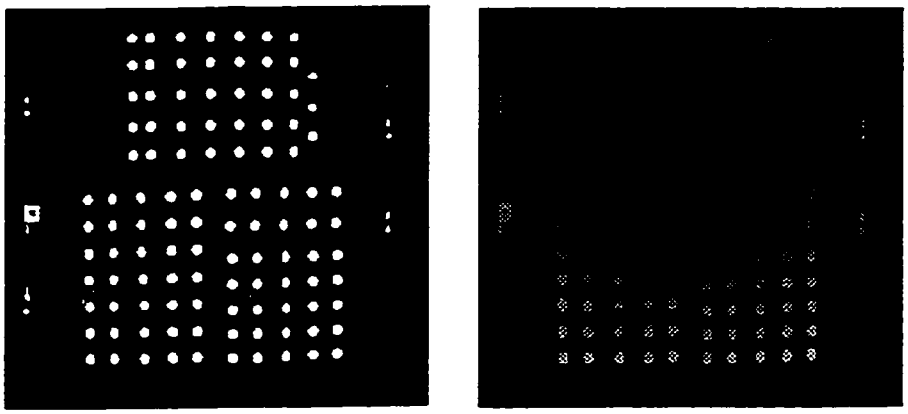

(a) The intensity image and the depth coded image with a low laser power to sense the retro-reflective targets.

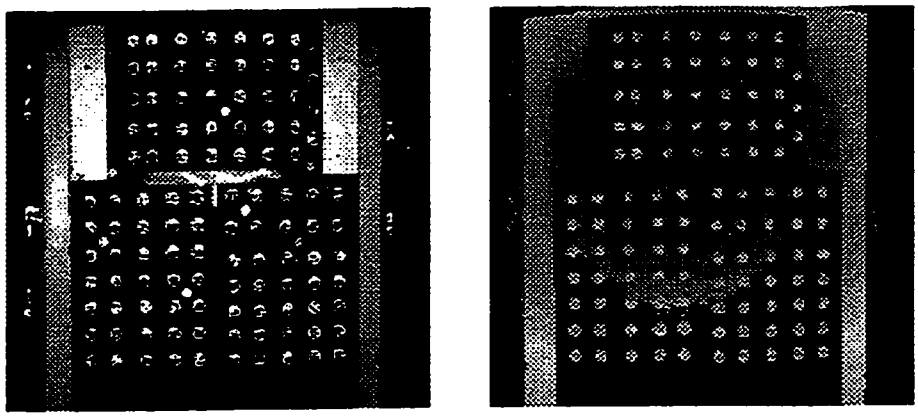

(b) The intensity image and the depth coded image with a higher laser power to sense the surface of the target field.

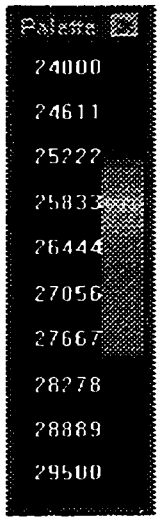

(c) Image palette.

Figure 4.17: The LSS images.

4.4.2 Observation Repeatability

The observations of the LSS are the image point coordinates **i** and **j** and the corresponding depth value **p**. The system has auto-synchronization diodes that compensate for temperature and drift effect to provide good measurement repeatability. To examine the repeatability of the LSS, images of the target field are acquired at

distances of 0.6 m, 1.1 m, 1.6 m, and 2.1 m. For each distance, at least three images are taken over a one to two hour time period. Two tests are used. The first one measures the repeatability of the image-coordinate measurements of the target centres and their corresponding p values. The moment preserving method and the centroid method can be used to extract the target centres. The second test measures the repeatability of the depth value measurements of a group of pixels at various regions in the image. Figure 4.18a shows a depth-coded image scanned with a laser power high enough to only pick up the targets regions. Figure 4.18b shows a depth-coded image scanned with a suitable laser power (i.e. higher than the laser power used to scan the image in Figure 4.18a) to pick up the surface regions of the target field.

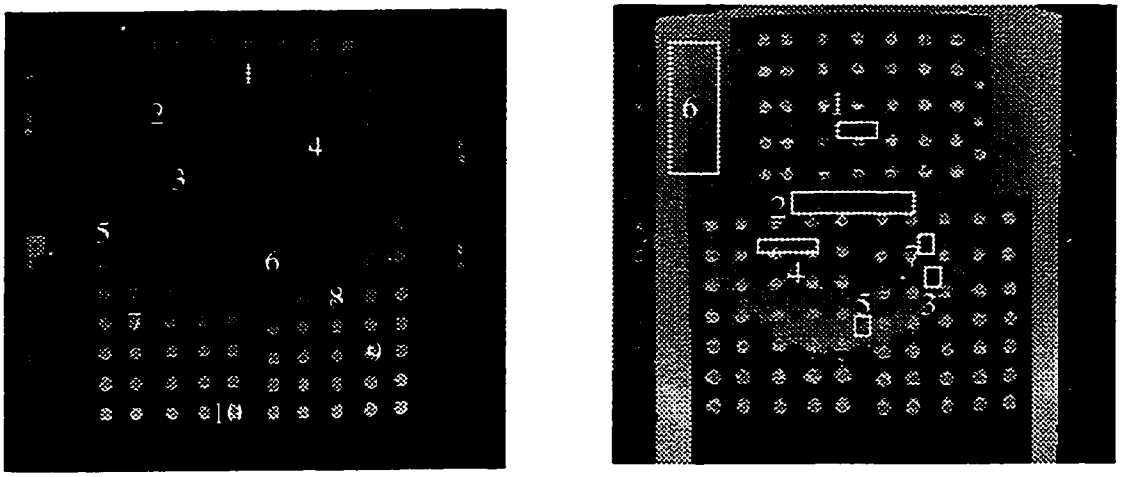

(a) Depth coded image to pick up target surface.

(b) Depth coded image to pick up target field surface.

Figure 4.18: The repeatability regions for images acquired at a depth distance of 2.1 metres from the LSS.

4.4.2.1 Repeatability of Image Coordinates

Units are in pixels	Depth distance of the target field from the LSS							
	At 0.6 metres		At 1.1 metres		At 1.6 metres		At 2.1 metres	
	i-axis	**j-axis**	**i-axis**	**j-axis**	**i-axis**	**j-axis**	**i-axis**	**j-axis**
RMS_{ave}	0.05	0.05	0.077	0.077	0.07	0.07	0.063	0.063
σ_{error}	0.023	0.021	0.002	0.008	0.009	0.012	0.004	0.021
mean error	0.015	0.016	0.002	-0.002	-0.016	0.023	0.001	0.003
max error	0.035	0.018	0.007	0.016	-0.031	0.044	0.008	0.058
min error	0.014	0.014	-0.004	-0.016	-0.06	-0.009	-0.007	-0.040

Table4.1: Repeatability measurements of the difference in target centre coordinates extracted from a set of repeated images.

The moment preserve method is used to detect target edges. The extracted edges are then used to fit an ellipse using the least squares adjustment method. The image coordinate of the adjusted ellipse centre is the centre of the detected target. The calculated root mean square value of the residuals provides a measure of the precision of the extracted target centre. In Table 4.1, $\mathbf{RMS_{ave}}$ is the average of the root mean square values of the selected target centres, extracted from repeated images at a specific depth distance. The selected targets are shown in Figure 4.18. The standard deviation (σ_{error}), mean error, maximum error, and minimum error are the statistics of the difference in target centre coordinates extracted from a set of repeated images. Each image set is a repeated scan (at least two scans) of the target field at a specific depth distance.

As shown in the table, the repeatability measures have maximum mean errors of -0.016 pixels and 0.023 pixels for the **i** and **j** coordinates, respectively. The maximum standard deviations are ±0.023 pixels and ±0.021 pixels for the **i** and **j** coordinates, respectively. The maximum error in pixels is 0.058 and the minimum error is -0.009.The maximum standard deviation of the observed target centre coordinates is 0.077 of a pixel.

4.4.2.2 Repeatability of Depth Values

In Table 4.2, $\mathbf{p_{pixel}}$ is the registered value of the pixel that contains the centre of the target. $\mathbf{p_{interpol}}$ is the interpolated value from the registered values of the four pixels that surround the centre of the target. The standard deviation (σ_{error}), mean error, maximum error, and minimum error are the statistics of the difference in the $\mathbf{p_{pixel}}$ and $\mathbf{p_{interpol}}$ values of the selected targets extracted from a set of repeated images, relative to the first scanned image in the set.

Units: pixel's registered depth value	Depth distance of the target field from the LSS							
	At 0.6 metres		At 1.1 metres		At 1.6 metres		At 2.1 metres	
	$\mathbf{p_{pixel}}$	$\mathbf{p_{interpol}}$	$\mathbf{p_{pixel}}$	$\mathbf{p_{interpol}}$	$\mathbf{p_{pixel}}$	$\mathbf{p_{interpol}}$	$\mathbf{p_{pixel}}$	$\mathbf{p_{interpol}}$
σ_{error}	1.03	1.43	0.47	0.29	0.56	0.45	0.00	0.40
mean error	1	1.3	0.06	0.03	-0.09	-0.10	0.00	0.00
max error	3	3.66	1	1.00	1	1.00	0	0.10
min error	-1	-.21	-1	-0.70	-2	-1.20	0	-0.04

Table4.2: Repeatability measurements of the difference in p values of the selected target extracted from a set of repeated images and relative to the first scanned image.

The repeatability measures have a mean registered value that varies from 1.3 for images at a depth distance of 0.6 metres to 0.003 for images at a depth distance of 2.6 metres. The standard deviation (σ_{error}) also varies from ±1.43 for images at a depth distance of 0.6 metres to ±0.4 for images at a depth distance of 2.6 metres. The maximum error is 3.66 and the minimum error is -2.

In Tables 4.3 and 4.4, the repeatability measures are taken for the selected surface regions and the surface regions of the selected targets shown in Figure 4.18. The standard deviation (σ_{error}), mean error, maximum error, and minimum error are the statistics of the difference in the pixel-registered values of these regions between repeated images in one set. Each images set is a scan of the target field at a specific depth distance with the LSS lens set either to infinity or focusing mode.

From Tables 4.3 and 4.4, the repeatability measures of selected surface regions have mean registered values that vary according to the position of the region in the image. For example, the maximum mean registered value at the centre of the image is 0.043 and the maximum near the edges is ±0.63. Similarly, the maximum standard deviation (σ_{error}) at the centre of the image is ±1.07 and the maximum near the edges of the image is ±2.85. The maximum error and the minimum error at the centre of the image are 4 and −7, respectively, and near the edges of the image are 9 and −12, respectively.

Units: pixel's registered depth value	The depth distance of the target field from the LSS is at 0.6 metres							
	Selected surface regions					Target surface regions		
	Centr	Bottom	Top	Left	Right	Centre	Top	Bottom
σ_{error}	0.30	0.77	0.90	0.59	0.57	0.77	2.68	2.19
mean error	.042	0.56	-0.63	0.25	0.03	0.35	-0.35	-0.10
max error	2	2	1	2	2	2	8	10
min error	-2	-1	-2	-1	-1	-2	-8	-10
Units: pixel's registered depth value	The depth distance of the target field from the LSS is at 1.1 metres							
	Selected surface regions					Target surface regions		
	Centr	Bottom	Top	Left	Right	Centre	Top	Bottom
σ_{error}	0.58	0.75	1.45	1.78	2.32	0.42	0.43	0.41
mean error	-0.03	-0.08	-0.06	0.02	-0.05	-0.13	-0.13	0.13
max error	3	9	8	7	9	1	1	1
min error	-3	-8	-6	-7	-8	-1	-1	-1
Units: pixel's registered depth value	The depth distance of the target field from the LSS is at 1.6 metres							
	Selected surface regions					Target surface regions		
	Centr	Bottom	Top	Left	Right	Centre	Top	Bottom
σ_{error}	0.55	2.53	2.34	2.85	2.52	0.23	0.45	.0.47
mean error	0.04	.12	0.03	0.05	0.02	0.06	0.13	0.21
max error	2	8	6	8	6	1	1	1
min error	-2	-6	-6	-8	-8	-1	-1	-1
Units: pixel's registered depth value	The depth distance of the target field from the LSS is at 2.1 metres							
	Selected surface regions					Target surface regions		
	Centr	Bottom	Top	Left	Right	Centre	Top	Bottom
σ_{error}	0.8	1.94	2.11	2.03	2.43	0.36	0.42	0.37
mean error	0.04	.16	0.05	.16	0.41	-0.15	0.01	0.1
max error	4	9	7	8	6	1	2	1
min error	-4	-8	-6	-7	-9	-1	-2	-1

Table4.3: Repeatability measurements of the difference in the pixel-registered values of selected regions between repeated images. The LSS lens is set to focus mode.

For target surface regions, repeatability measure is similar to surface regions. The mean registered value at the centre of the image is 0.35 and near the edges of the image is 0.35.

The standard deviation of the error at the centre of the image is ±0.77 and near the edges of the image is ±2.68. The maximum error and the minimum error at the centre of the image are 2 and –2, respectively, and near the edges of the image are 8 and –10, respectively. The maximum error is 2 and the minimum error is -2.

Units: pixel's registered depth value	The depth distance of the target field from the LSS is at 2.1 metres							
	Selected surface regions					Target surface regions		
	Centre	Botto	Top	Left	Right	Centre	Top	Bottom
σ_{error}	1.07	2.39	2.66	0.78	0.83	0.25	0.25	0.48
mean error	0.04	-0.27	0.41	-0.33	-0.3	-0.07	-0.09	-0.2
max error	4	9	9	4	3	1	1	1
min error	-7	-12	-10	-3	-4	-1	-1	-1

Table4.4: Repeatability measurements of the difference in the pixel-registered values of selected regions between repeated images. The LSS lens is set to infinity mode.

Note that in Table 4.3, the repeatability measures of surface regions are more accurate than target regions for a target field mounted at 0.6 metre from the LSS, but not for the other target field positions. The explanation for that is the sensitivity of the laser ray to the reflective material of the targets when it is very close to the LSS. This was noticeable during measurements. Especially, adjusting the laser power of the LSS to pickup the target regions at a depth distance of 0.6 metre and at the same time maintaining minimum noise level.

4.4.2.3 Summary of Repeatability measurements

From the above testing results one can conclude that when using retro-reflective targets the following standard deviations values of the observations are reasonable: ±3 for the registered value **p**, and ±0.08 pixels for the image coordinates **i** and **j**.

4.4.2.4 Repeatability and Calibration Results

For calibration purposes, a rigid target field with a grid of regular spaced circular targets was construct at the University of Calgary engineering machine-shop. It was not feasible to use retro-reflective targets. Instead of that, the targets were made of circular targets engraved on a plastic sheet. The targets engraved such that they are equally spaced at 63.5 mm (2.5 inch). The foreground color of the sheet is white and the core color is black, see Figure 4.21.

The precision determined using this type of targets is lower than using retro-reflective targets. The precision for the image coordinates **i** and **j** ranges from ±0.09 to ±0.21 pixels. The precision of the depth value **p** also ranges up to ±6 registered values. This shows that retro-reflective targets provide better precision than using black and white targets made of smooth surface plastic sheet.

The calibration results show that the average values of the standard deviation values of the adjusted observations $(\hat{C}_i)$ are: ±4.6 for the registered value **p**, ±0.17 pixels for the image coordinates **i** and ±0.16 pixels for the image coordinates **j**. However, The

standard deviation values of the observations ($\mathbf{C}_\ell$) used in the least squares adjustment that provided acceptable estimated variance factor are: ±10 for the registered value **p**, ±0.5 pixels for the image coordinates **i** and **j**.

4.4.3 Predicted Precision of LSS Measurements

The collinearity equations of the LSS, Equations 4.26, 4.27 and 4.28, are used to derive the expected LSS spatial precision. The law of propagation of errors is applied to these equations to estimate the precision of spatial coordinates X, Y, and Z as a function of the standard deviation of the observations. The observations are the depth values and the rotational angles **P**, θ, and ϕ respectively, are replaced by the associated registered measurements as a function of the observations according to Equations 4.1 and 4.3. These measurements are the registered depth values and the image coordinates $\mathbf{p}_o$, **i**, and **j**, respectively. Assuming that these observations are uncorrelated, the expected precision using **P**, θ, and ϕ are derived for each coordinate (see Beraldin et. al. 1993) and are given as:

$$\sigma_X(P,\theta,\phi,\sigma_\theta,\sigma_\phi,\sigma_P)=\left[\partial X/\partial\theta(P,\theta,\phi)^2\,\sigma_\theta{}^2+\partial X/\partial\phi(P,\theta,\phi)^2\,\sigma_\phi{}^2+\partial X/\partial P(P,\theta,\phi)^2\,\sigma_P{}^2\right]^{0.5}$$

Equation 4.48

$$\sigma_Y(P,\theta,\phi,\sigma_\theta,\sigma_\phi,\sigma_P)=\left[\partial Y/\partial\theta(P,\theta,\phi)^2\,\sigma_\theta{}^2+\partial Y/\partial\phi(P,\theta,\phi)^2\,\sigma_\phi{}^2+\partial Y/\partial P(P,\theta,\phi)^2\,\sigma_P{}^2\right]^{0.5}$$

Equation 4.49

$$\sigma_Z(P,\theta,\phi,\sigma_\theta,\sigma_\phi,\sigma_P)=\left[\partial Z/\partial\theta(P,\theta,\phi)^2\,\sigma_\theta{}^2+\partial Z/\partial\phi(P,\theta,\phi)^2\,\sigma_\phi{}^2+\partial Z/\partial P(P,\theta,\phi)^2\,\sigma_P{}^2\right]^{0.5}$$

Equation 4.50

The expected precision using $\mathbf{p_o}$, **i**, and **j**, are derived for each coordinate and are given as:

$$\sigma_X(p0,i,j,\sigma_i,\sigma_j,\sigma_{p0})=\left[\begin{array}{l}\partial X/\partial\theta(p0,i,j)^2\,\sigma_\theta(i,\sigma_i)^2+\partial X/\partial\phi(p0,i,j)^2\,\sigma_\phi(i,j,\sigma_j)^2+\\ \partial X/\partial P(p0,i,j)^2\,\sigma_P(p0,i,\sigma_{p0})^2\end{array}\right]^{0.5}$$

Equation 4.51

$$\sigma_Y(p0,i,j,\sigma_i,\sigma_j,\sigma_{p0})=\left[\begin{array}{l}\partial Y/\partial\theta(p0,i,j)^2\,\sigma_\theta(i,\sigma_i)^2+\partial Y/\partial\phi(p0,i,j)^2\,\sigma_\phi(i,j,\sigma_j)^2+\\ \partial Y/\partial P(p0,i,j)^2\,\sigma_P(p0,i,\sigma_{p0})^2\end{array}\right]^{0.5}$$

Equation 4.52

$$\sigma_Z(p0,i,j,\sigma_i,\sigma_j,\sigma_{p0})=\left[\begin{array}{l}\partial Z/\partial\theta(p0,i,j)^2\,\sigma_\theta(i,\sigma_i)^2+\partial Z/\partial\phi(p0,i,j)^2\,\sigma_\phi(i,j,\sigma_j)^2+\\ \partial Z/\partial P(p0,i,j)^2\,\sigma_P(p0,i,\sigma_{p0})^2\end{array}\right]^{0.5}$$

Equation 4.53

where $\partial/\partial P(P,\theta,\phi)$, $\partial/\partial\theta(P,\theta,\phi)$ and $\partial/\partial\phi(P,\theta,\phi)$ or $\partial/\partial P(p0,i,j)$, $\partial/\partial\theta(p0,i,j)$ and $\partial/\partial\phi(p0,i,j)$ are the partial derivatives of the **X**, **Y** and **Z** collinearity equations with respect to θ, ϕ and **P**, or with respect to i, j, and p0, respectively. The standard deviations $\sigma_\theta(i,\sigma_i)^2$, $\sigma_\phi(i,j,\sigma_j)$ and $\sigma_P(p0,i,\sigma_{p0})$ are calculated with respect to the standard deviations of the image coordinates and the registered depth value σ_i, σ_j, and σ_{po}, respectively. Their values are given according to their repeatability measures

(discussed in Section 4.4.2.3) as follows: ±0.08 pixels, ±0.08 pixels, and ±3 registered depth value, respectively.

The standard deviations σ_θ and σ_ϕ correspond to the precision of the two galvanometers of the X and Y axes rotational mirrors and σ_p is the precision of the peak detector of the CCD sensor. The values of σ_θ and σ_ϕ are according to the specifications of the galvanometers and are given as 60 microradians (see Beraldin et. al. 1993).). From Equations 4.3 and 4.43, the equivalent predicted precision of the rotational angles in terms of the image coordinates i and j can be derive to be: σ_i=σ_j=0.044 pixels, which are almost half the value of the repeatability measures for retro-reflective targets.

According to Baribeau and Rioux (1991a), the laser speckle impinging on the position detector limits the measurement of the depth value p. The predicted noise is assumed to behave like a Gaussian process and the estimated fluctuation of p determined by that noise is approximately:

$$\sigma_p = \frac{1}{\sqrt{2\pi}} \frac{\lambda}{D\cos(2\alpha)} f_0 \qquad \text{Equation 4.54}$$

where λ is the wavelength of the laser source (λ = 8.22e-08 mm) and **D** is the lens diameter (**D** = 18 mm). In a well-designed system and when enough light is collected, the predicted precision value is $\sigma_p \approx$ **3.1** micrometres (see Beraldin et. al. 1993). From

Equations 4.1, the equivalent predicted precision of the peak detector in terms of the registered depth value p0 can be derived to be: $\sigma_{p0} \approx$ **4.0** registered depth value.

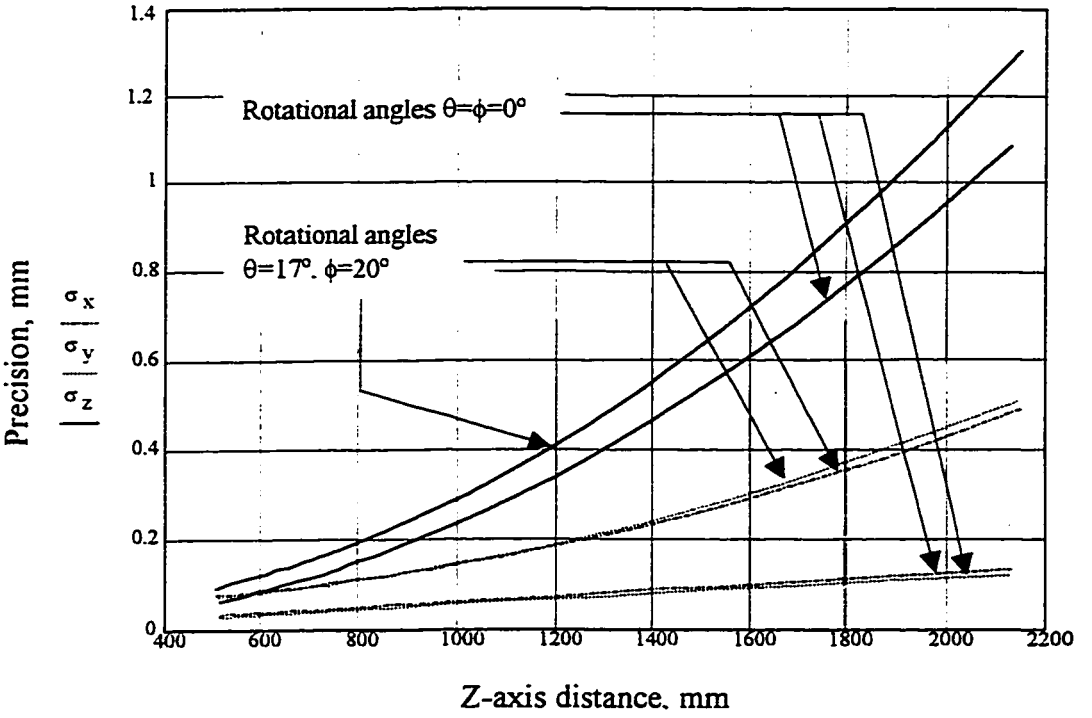

Figure 4.19a: The LSS expected precision based on the galvanometers and the peak detector precision (i.e. $\sigma_\theta = \sigma_\phi = 60$ μrad and $\sigma_p \approx$**3.1** μm) for the static case and the dynamic case with rotational angles set to maximum.

Figures 4.19a, illustrate the expected precision of the LSS for two cases based on the predicted precision of the peak detector and the precision of the galvanometers (i.e. $\sigma_\theta = \sigma_\phi = 60$ microradians and $\sigma_p \approx$ **3.1** micrometres). The fist case is the static geometry case (i.e. zero X-axis and Y-axis rotation angles). The second case is the dynamic case with the rotation angles set maximum (i.e. the X-axis rotation angle is 17 degrees, and the Y-axis rotation angles is 20 degrees).

Similarly, Figure 4.19b, illustrate the expected precision of the LSS for two cases based on the repeatability measures of the registered depth value p_0 and the image coordinates i and j (i.e. $\sigma_i=\sigma_j=0.08$ pixels $\approx$109.1 microradians and $\sigma_{p_0} \approx 3 \approx 2.4$ micrometres).

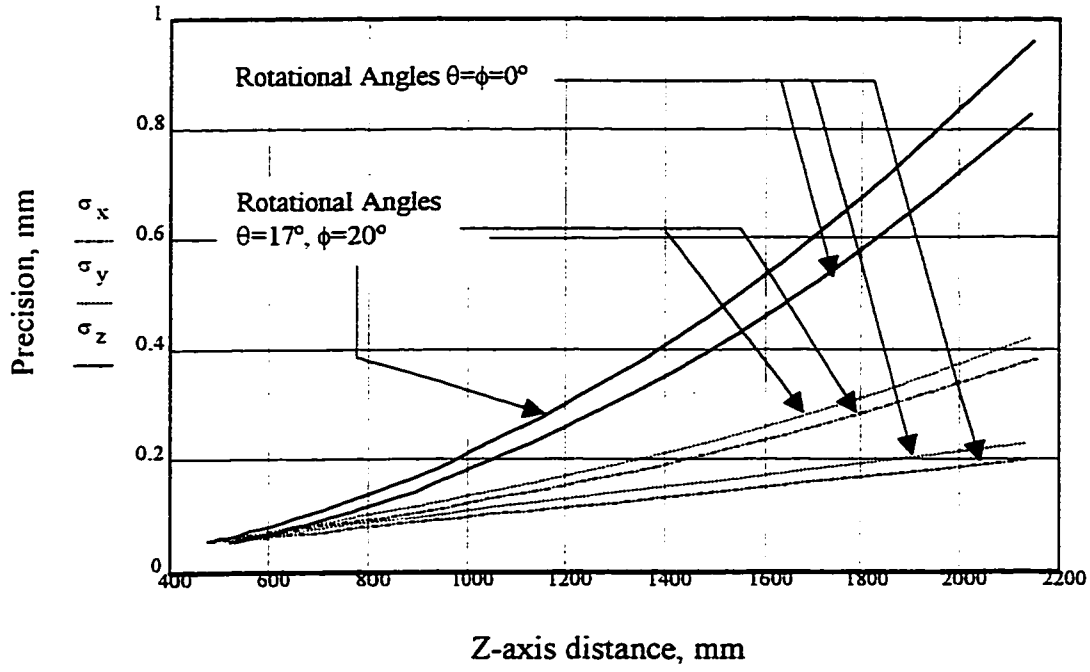

Figure 4.19b: The LSS expected precision based on the repeatability measures of the depth value p_0 and the image coordinates i and j (i.e. $\sigma_i = \sigma_j = 0.08$ pixels and $\sigma_{p0} \approx 3$ registered depth value) for the static case and the dynamic case with rotational angles set to maximum.

The partial derivatives of the **X**, **Y** and **Z** collinearity equations with respect to θ and ϕ ($\partial/\partial\theta(P,\theta,\phi)$ and $\partial/\partial\phi(P,\theta,\phi)$) values increase with the increase of the rotational angles X-axis and Y-axis. Figures 4.19a and 4.19b show the difference in the expected precision between the static case and the dynamic case with the rotational angles set to maximum.

4.4.3.1 Predicted Precision based on the Calibration Results

Figures 4.20a illustrates the expected precision (for both the static case and the dynamic case with rotational angels set to maximum) using the average values of the standard deviation values of the adjusted observations (i.e. $\sigma_i = 0.17$, $\sigma_j = 0.16$ pixels and $\sigma_{po} \approx 4.5$ registered depth value).

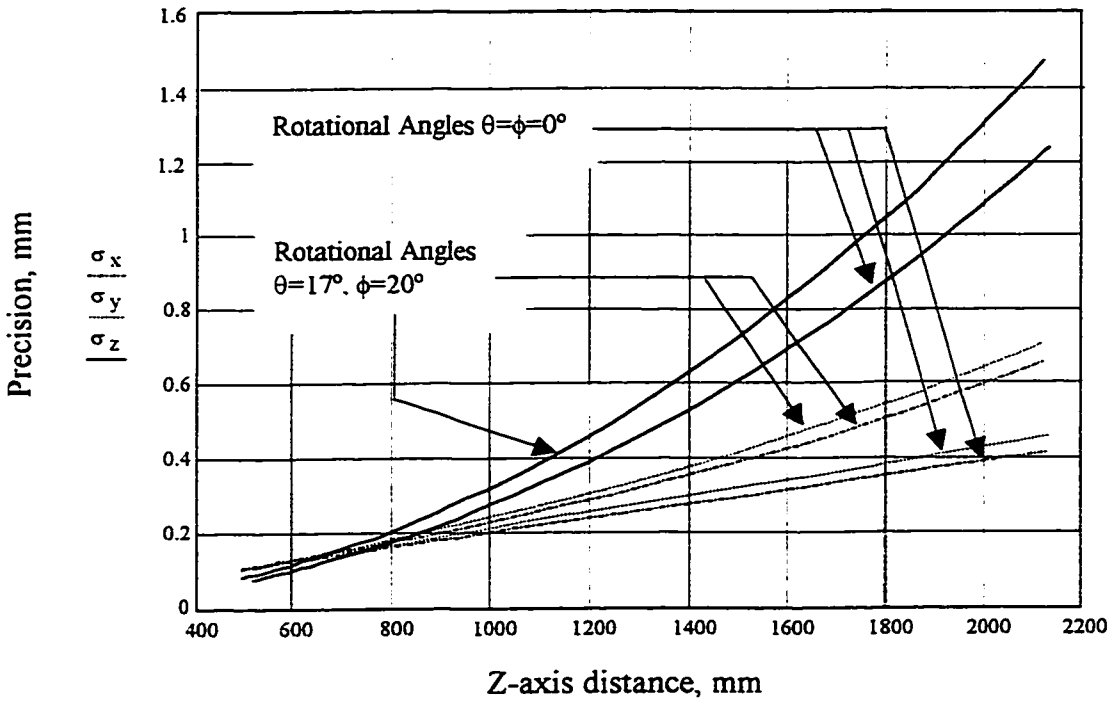

Figure 4.20a: The LSS expected precision based on the standard deviation values of the adjusted observations (i.e. the image coordinates i and j with $\sigma_i = 0.17$, $\sigma_j = 0.16$ pixels and the depth registered value p_o with $\sigma_{po} \approx 4.5$ registered depth value).

Figure 4.20b illustrates the expected precision based on the used standard deviation values of the observations in the least squared adjustment that provided acceptable estimated variance factor (i.e. $\sigma_i = \sigma_j = 0.5$ pixels and $\sigma_{po} \approx 10$ registered depth value).

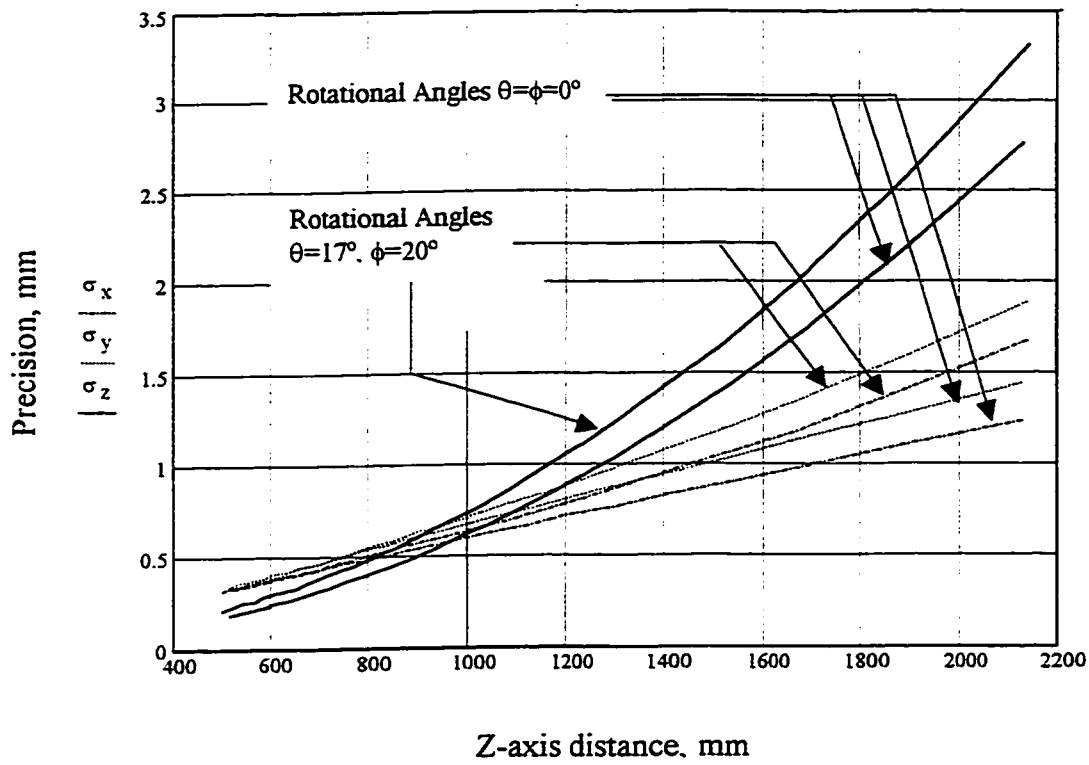

Figure 4.20b: The LSS expected precision based on the used standard deviation values of the observations in the least squares adjustment (i.e. the image coordinates i and j with $\sigma_i = \sigma_j = 0.5$ pixels and the depth registered value p_o with $\sigma_{po} \approx 10$ registered depth value).

4.4.4 Precision and Some Design Aspects

4.4.4.1 The Tilt Angle of the Fixed Mirrors α and the Triangulation Angle γ

According to Equation 4.4 ($\gamma = 4\alpha - \pi$), the angle γ is defined in terms of the angle α. It is important to note from the equation that the angle α cannot be $\pi/4$, which results in a triangulation angle γ equal to zero. This means that there is no return signal as the depth distance $\mathbf{Z_0}$ goes to infinity ($\mathbf{Z_0}$ = denominator/sin (4.α)). Consequently, the smaller the triangulation angle the larger the depth distance $\mathbf{Z_0}$. On the other hand, the larger the angle α and consequently the angle γ, the larger the distortions caused by the Sheimpflug condition, the mirror thickness and the laser-source tilt angle. In fact the best angle to decrease these distortions to a minimum is $\pi/4$. Therefore, according to the design specifications of the LSS, the chosen angle α was 46.05 degrees, which gives a triangulation angle γ of 4.2 degrees.

4.4.4.2 The Tilt Angle of the Position Detector β

Equation 3.3 ($P_\infty = f_0 \sin(\gamma)/\cos(\beta - \gamma) = (f_0 - f)/\sin(\beta)$) defines $\mathbf{P_\infty}$ in terms of the effective focal length $\mathbf{f_0}$, the angle γ, and the angle β. Rearranging Equation 3.3 ($f_0 = f\cos(\beta - \gamma)/(\cos(\beta - \gamma) - \sin(\beta)\sin(\gamma))$) defines the effective focal length $\mathbf{f_0}$ in terms of the focal length **f**, the angle γ, and the angle β.

The above relation is useful when designing the internal geometry of the LSS to optimize precision. When the focal length **f** and the angle γ are kept constant, the angle β is directly proportional to the effective focal length $\mathbf{f_0}$. Thus, increasing the angle β for example, causes $\mathbf{P_\infty}$ to be larger and the depth distance $\mathbf{Z_0}$ to be smaller. Since the sensor has a fixed length, then increasing $\mathbf{P_\infty}$ improves the measurement's precision for depth distances larger than $\mathbf{Z_0}$, and decreases for depth distances smaller than $\mathbf{Z_0}$. Therefore, the design criterion is dependent on the required precision for a required range of depth distances. One design criterion for a precise close range LSS is to set $\mathbf{P_\infty}$ to be approximately half of the sensor length. Therefore, depth distances that range from the standoff distance to $\mathbf{Z_0}$ are measured using half the sensor length, and depth distances that range from $\mathbf{Z_0}$ to ∞ are measured on the other half, see Figure 4.1 and Figure 3.2.

4.5 Instrument Calibration

One method used to calibrate the LSS at the NRC is the Look-up Table Technique with Linear Interpolation where the data is obtained using the Oblique Plane Method, see Beraldin et. al. (1992, 1994). Another method also developed at NRC by El-Hakim (El-Hakim, 1995 and Beraldin et. al. ,1993), uses a model-based approach and least squares adjustment. This section explains the details of a similar method.

4.5.1 Model-based Approach

The purpose of calibration for imaging metrology has been defined as determining the interior geometry of a camera in order to achieve the greatest possible positioning accuracy, Lichti (1996). A model-based approach uses fitting techniques with special criteria to solve for the unknown parameters. This can be achieved by finding the best fit of measured coordinates of object space points and corresponding image coordinates and depth values within the proposed mathematical model. The method used to fit the data is the least squares adjustment method using an implicit (combined or mixed) model linearization.

Two approaches can be used to determine a set of calibrated LSS parameters. The basic photogrammetric calibration philosophy is based on using the comprehensive geometric (and distortion where appropriate) modeling of the image space of the camera system, independent of the target scene. Thus, calibration models are expressed solely in terms of

image space parameters. The other approach is the self-calibration method, which is the recovery of image space calibration parameters simultaneously with the exterior orientation parameters (sensor position and orientation) and object space coordinates (Fraser et. al., 1995). This thesis uses the basic photogrammetric calibration approach to determine the LSS calibration parameters.

In the implicit model, the observations and the parameters are implicitly related. If $\hat{X}$ denotes the vector of **u** adjusted parameters and $\hat{l}$ denotes the vector of **n** adjusted observations, the nonlinear mathematical model of the LSS has the form:

$$F\left(\hat{l}, \hat{X}\right) = 0 \qquad \text{Equation 4.55}$$

where F corresponds to the X, Y and Z coordinate functions for each point, which are the collinearity equations, Equations 4.32, 4.33 and 4.34. The total number of equations is three times the number of object space points included in the solution and is denoted by **m**.

4.5.2 Model Linearization

Expanding the function using a Taylor series expansion and retaining only the linear terms linearizes the nonlinear mathematical model. The known point of expansion is at $\mathbf{X_o}$ and $\mathbf{l_o}$, where $\mathbf{X_o}$ is the vector of the approximate values of the unknown parameters and $\mathbf{l_o}$ is the vector of the observations. The linearized model has the following form:

$$A \cdot \hat{\delta} + B \cdot \hat{r} + W = 0 \qquad \text{Equation 4.56}$$

in which:

$\hat{\delta} = \hat{X} - X_O$ is the estimated vector of corrections to the approximate values of the unknown parameters (i.e. sensor, internal, interior orientations, exterior orientations, and distortion parameters). The better the approximate values of $\mathbf{X_0}$ the smaller is the correction vector. The dimension of the vector is **u**.

$\hat{r} = \hat{l} - l_O$ is the residual vector, which is the set of small differences between the actual observations (i.e. **i, j** images space coordinates and **p** depth values for each object space coordinate) and the observations that would perfectly fit the adjusted coordinates. The dimension of the vector is **n**.

$A = \left.\frac{df}{dx}\right|_{X_o, l_O}$ is the coefficient design matrix (dimensions **m,u**) evaluated for the vector of the unknown parameters.

$B = \left.\frac{df}{dl}\right|_{X_o, l_O}$ is the coefficient design matrix (dimensions **n,m**) evaluated for the vector of the observations.

$W = F(l_O, X_O) - B \cdot \hat{r}$ is the estimated misclosure vector. The first term on the right-hand side of the equation is the evaluated value of the mathematical function, Equation 4.55, at the point of expansion, and the second term results

from the linearization, Equation 4.56, which compensates for using the residual **r** in the equation. The dimension of the vector is **m,1**.

4.5.3 Least Squares Adjustment Criteria

The least-squares adjustment method is used when the number of equations, **m**, is more than the number of unknowns, **u**, since no unique solution can be made for the unknowns. Thus the **n** observations have to be corrected or adjusted to best fit the mathematical model (of **m** equations). The least-squares criteria is used to solve this problem by minimizing the sum of the squares of the weighted residuals (corrections to the observations $\mathbf{l_0}$), as follows:

$$\hat{r}^T \cdot C_l^{-1} \cdot \hat{r} \quad \rightarrow \quad \min \qquad \text{Equation 4.56}$$

where $\mathbf{C_l}$ is the covariance matrix of the observations. A solution is obtained by introducing a vector of Lagrange multipliers **K** and minimizing $\hat{r}^T \cdot C_l^{-1} \cdot \hat{r}$. The correction vector to initial estimates of the unknowns is given by, see CISM (1987), and Leick (1990):

$$\hat{\delta} = -\left[A^T \left(BC_l B^T\right)^{-1} A\right]^{-1} \cdot \left[A^T \left(BC_l B^T\right)^{-1} \cdot W\right] \qquad \text{Equation 4.58}$$

The covariance matrix for the correction vector and for the unknowns is:

$$C_{\hat{x}} = C_{\hat{\delta}} = N^{-1} = \left[A^T \left(BC_l B^T \right)^{-1} A \right]^{-1} \qquad \text{Equation 4.59}$$

The residuals vector (correction vector to the observations) is:

$$\hat{r} = -C_l \cdot B^T \left(BC_l B^T \right)^{-1} \cdot \left[A \cdot \hat{\delta} + W \right] \qquad \text{Equation 4.60}$$

Substituting for $M = \left(BC_l B^T \right)$, the covariance matrix for the residuals is:

$$C_{\hat{r}} = C_l \cdot B^T M^{-1} \cdot B C_l - C_l \cdot B^T M^{-1} \cdot \left[A \cdot C_{\hat{x}} A^T \right] M^{-1} \cdot B C_l \qquad \text{Equation 4.61}$$

The covariance matrix for the adjusted observations is:

$$C_{\hat{l}} = C_l - C\hat{r} \qquad \text{Equation 4.62}$$

The estimated variance factor is given by:

$$\hat{\sigma}_o^2 = \frac{\hat{r}^T \cdot C_l^{-1} \cdot \hat{r}}{m - u} \qquad \text{Equation 4.63}$$

4.5.4 The Unified Approach Solution

The unified approach allows the incorporation of exterior information about the parameters, see Mikhail (1976). This approach allows some parameters to be treated as fixed values, and allows the corrections to the approximate values of some parameters to

be restricted within certain limits. For example, if a parameter is given an infinitely large variance, that is its weight is equal zero, then it is allowed to vary freely in the adjustment. On the other hand, if the parameter is given a zero variance or a weight that approaches infinity, then the parameter is simply not allowed to change in the adjustment with the consequence that its residual value will be zero and it would assume the classical meaning of a constant.

This can be incorporated into the solution by minimizing the sum of squares of the weighted parameters, in addition to the sum of squares of the weighted residuals, where $\mathbf{C_x}$ is the a priori covariance matrix of the parameters. The criteria is given by:

$$\hat{r}^T \cdot C_l^{-1} \cdot \hat{r} + \hat{\delta} C_x^{-1} \hat{\delta} \rightarrow \min \qquad \text{Equation 4.64}$$

The approach also allows one to use parameter constraint equations. This addition, in many cases, solves problems related to poor geometry and/or to high correlation between some parameters, and hence helps the solution to converge. To incorporate this, the sum of the squares of the residual vector associated with the constraint equations is minimized in addition to Equation 4.64, where $\hat{r}_C$ and $\mathbf{C_c}$ are the adjusted residual and the covariance matrix associated with the observations and/or the parameters in the constraint equation respectively. The criteria becomes:

$$\hat{r}^T \cdot C_l^{-1} \cdot \hat{r} + \hat{r}_c^T \cdot C_c^{-1} \cdot \hat{r}_c + \hat{\delta} C_x^{-1} \hat{\delta} \rightarrow \min \qquad \text{Equation 4.65}$$

The unified approach model is given by:

$$F_1\left(\hat{l},\hat{X}\right)=0 \quad \text{and} \quad F_2\left(\hat{X}\right)=0 \qquad \text{Equation 4.66}$$

The linearized form is:

$$A\cdot\hat{\delta}+B\cdot\hat{r}+W=0 \qquad \text{Equation 4.67}$$

$$A_c\cdot\hat{\delta}-r_c+W_c=0 \qquad \text{Equation 4.68}$$

Note that $\mathbf{A_c}$ is the design matrix, and $\mathbf{W_c}$ is the misclosure vector associated with the constraint equation. The solution becomes:

$$\hat{\delta}=-\left[N+N_C+C_x^{-1}\right]^{-1}\cdot\left[U+U_C+C_x^{-1}\cdot W_x\right] \qquad \text{Equation 4.69}$$

$$\text{where: } M=\left(BC_l B^T\right) \qquad \text{Equation 4.70}$$

$$U=\left[A^T M^{-1} W\right] \quad \text{and} \quad U_c=\left[A_c{}^T C_c{}^{-1} W_c\right] \qquad \text{Equation 4.71}$$

The normal equations are:

$$N=\left[A^T M^{-1} A\right] \quad \text{and} \qquad \text{Equation 4.72}$$

$$N_C=\left[A_C{}^T C_C{}^{-1} A_C\right] \qquad \text{Equation 4.73}$$

The misclosure vectors are:

$$W=F_1(l_O,X_O)-B\cdot\hat{r}, \quad W_C=F_2(X_O)-\hat{r}_C \quad \text{and} \quad W_X=\hat{X}-X_O \qquad \text{Equation 4.74}$$

The covariance matrix for the unknowns is:

$$C_{\hat{x}} = \left[N + N_C + C_x^{-1} \right]^{-1} \qquad \text{Equation 4.75}$$

The residuals of the observations and the residuals associated with the constraint equations are given as:

$$\hat{r} = -C_l \cdot B^T M^{-1} \cdot \left[A \cdot \hat{\delta} + W \right] \qquad \text{Equation 4.76}$$

$$\hat{r}_C = A_C \cdot \hat{\delta} + W_C \qquad \text{Equation 4.77}$$

The covariance matrix for the residuals of the observations is:

$$C_{\hat{r}} = C_l \cdot B^T M^{-1} \cdot B C_l - C_l \cdot B^T M^{-1} \cdot \left[A \cdot C_{\hat{x}} A^T \right] M^{-1} \cdot B C_l \qquad \text{Equation 4.78}$$

The covariance matrix for the adjusted observations is:

$$C_{\hat{l}} = C_l - C\hat{r} \qquad \text{Equation 4.79}$$

The estimated variance factor is given by:

$$\hat{\sigma}_o^{\,2} = \frac{\hat{r}^T C_l^{-1} \hat{r} + \hat{r}_c^{\,T} C_c^{-1} \hat{r}_c + \left(\hat{X} - X\right) C_x^{-1} \left(\hat{X} - X\right)}{m + m_c + m_x - u} \qquad \text{Equation 4.80}$$

where $\mathbf{m_c}$ is the number of constraint equations. The estimated variance factor should be close to unity if the input variances were appropriately scaled and there were no gross errors.

4.5.4.1 Constraint Equations

Two constraint equations are used for the LSS calibration. The first equation is based on Equation 4.2, given as:

$$P_x = f_0 \sin(4\cdot\alpha) \,/\, \cos(\beta - 4\cdot\alpha), \qquad \text{Equation 4.81}$$

The second constraint equation is based on Equation 4.3 and given as

$$\phi_0 = J\cdot\delta\phi \qquad \text{Equation 4.82}$$

where J is half the size of the total image size (e.g. for a 512X512 image, J is 256).

4.5.5 Iteration and Convergence Criteria

Since the mathematical model is nonlinear, the solution must be iterated. In the first iteration, the approximate values of the parameters and the observations are used (i.e. X_o and l_o). In the subsequent iterations the approximate values of the parameters and the observations should be updated as follows:

$$\hat{X}_i = \hat{X}_{i-1} + \hat{\delta}_i \quad \text{and} \quad \hat{l}_i = l_O + \hat{r}_i \qquad \text{Equation 4.83}$$

The design matrices $\mathbf{A}^i$, $\mathbf{B}^i$, and $\mathbf{A_c}^i$, and also the misclosure vector $\mathbf{W}^i$ and $\mathbf{W_c}^i$ should be re-evaluated using the updated parameters and observations of the previous iteration (i.e. $\hat{X}_{i-1}$ *and* $\hat{l}_{i-1}$). The convergence criteria could be one of the following:

$$\left| \left(\hat{r}^T \cdot C_l^{-1} \cdot \hat{r} \right)_i - \left(\hat{r}^T \cdot C_l^{-1} \cdot \hat{r} \right)_{i-1} \right| < \varepsilon_1 \qquad \text{Equation 4.84}$$

$$\text{or } \left| \hat{\delta}_i - \hat{\delta}_{i-1} \right| < \varepsilon_2 \quad \text{or} \quad \left| \hat{\delta}_i \right| < \varepsilon_3 \qquad \text{Equation 4.85}$$

where ε_1, ε_2, and ε_3 are small positive numbers.

4.5.6 Control Points and Datum Definition

Excluding all external sources of information, Photogrammetric observations are made exclusively in sensor space. These quantities, plus the interior geometry parameters, contain all the necessary information to define the shape of a three-dimensional object space scene or points (Fraser, 1984). Similarly, the observations of the LSS are used to define a three-dimensional object space scene or points based on the LSS interior orientation parameters and internal parameters. However, these coordinates are only defined with respect to the camera space coordinate system. To link the camera space coordinate system with the object space coordinate system, the exterior orientation parameters of LSS have to be determined and, hence, the object space datum is required.

In the context of camera calibration, the control points are considered to be fixed, and are measured in the object space coordinates, via other instruments such as an electronic theodolite system. The observations of the LSS (i.e. image coordinates **i**, and **j** and the depth value **p**) are in the image space coordinate system. There are twenty-seven unknown parameters to be solved, which are: two sensor, nine interior, four interior

orientation, six exterior orientation, a scale factor and five distortion parameters. Each control point is fixed in the adjustment and provides three equations, and hence, at least nine control points in different planes are required. Note that to handle the rank defect in the normal equation matrix, explicit definition of twenty seven datum parameters is required, with seven of them eliminating the rank defect of the external orientation parameters and the LSS scale parameters (one for scale, three for position and three for orientation).

However, to improve the LSS precision results, more control points should be used to calibrate a particular volume. The word fixing implies that these points are not included in the normal equations.

4.5.7 Stability of the Calibration Solution

In order to get a stable solution and to minimize numerical problems, the normal matrix is re-arranged according to its numerical diagonal values (i.e. the first row in the normal matrix has the smallest diagonal value and the last row has the largest diagonal value). The PixelSize value is given by the manufacturer and, hence, is deleted from the solution. Also, Pscale is replaced by PixelScale as follows (PixelScale is equal to one):

$$p=p_0\, PixelScale\, \frac{PixelSize}{64} - SensorLength + P_\infty \qquad \text{Equation 4.86}$$

Adding the geometric relationship between the parameters P_∞, f_0, β, and $\alpha 1$, Equation 4.81, as a constraint equation to the least square solution with proper weighting, also, helped to stabilize the solution and achieve better precision.

Parameter	Calibration set #1			
	Approximate value(±)	Adjusted value(±)	A priori standard deviation value(±)	A posteriori standard deviation value(±)
X_0	0 mm	3.47 mm	100 mm	0.195 mm
Y_0	0 mm	4.66 mm	100 mm	1.010 mm
Z_0	0 mm	18.96 mm	100 mm	1.000 mm
θ_0	-16.16 deg	-16.8834 deg	60 arc-min	4.430 arc-min
$\delta\theta$	3.79 arc-min	3.8362 arc-min	10 arc-min	0.0051 arc-min
ϕ_0	19.58 deg	-20.0057 deg	60 arc-min	2.309 arc-min
$\delta\phi$	4.59 arc-min	4.6889 arc-min	10 arc-min	0.0089 arc-min
β	49.8358 deg	49.8358 deg	0.5 arc-sec	0.0 arc-sec
$2\alpha 1$	95.15 deg	92.0689 deg	30 arc-min	0.0872 arc-min
S	26.67 mm	26.67 mm	0.001 mm	1e-08 mm
d	48 mm	48 mm	0.001 mm	1e-07 mm
dx	11 mm	11 mm	0.01 mm	1e-06 mm
hz	-1 mm	-1.34 mm	2 mm	0.301 mm
hy	46 mm	47.46mm	2 mm	0.948 mm
f_0	108.8 mm	109.14 mm	1 mm	0.086 mm
P_∞	11.267 mm	11.2673 mm	0.01 mm	5e-05 mm
Pixel Scale	1	1	0.001	1e-08
Pixel Size	0.05 mm	0.05 mm	deleted	------
λ	1	1	Fixed	------
d_1	0.0	-0.00015743449	0.0	2.38e-5
d_2	0.0	7.54e-010	0.0	7.13e-11
d_3	0.0	-6.24e-012	0.0	5.07e-12
d_4	0.0	-7.53e-005	0.0	2.19e-05
d_5	0.0	7.16e-012	0.0	4.74e-12
ω	0.0 arc-min	-35.40 arc-min	0.0 arc-min	1.171 arc-min
Φ	0.0 arc-min	11.60 arc-min	0.0 arc-min	4.406 arc-min
K	0.0 arc-min	0.137 arc-min	0.0 arc-min	0.911 arc-min

Table 4.5a: The calibration set #1 results.

Parameter	Calibration set #2			
	Approximate value(±)	Adjusted value(±)	A priori standard deviation value(±)	A posteriori standard deviation value(±)
X_0	0 mm	3.77 mm	100 mm	0.169mm
Y_0	0 mm	4.04 mm	100 mm	1.284mm
Z_0	0 mm	21.53 mm	100 mm	1.237mm
θ_0	-17.0 deg	-17.09 deg	60 arc-min	4.113 arc-min
$\delta\theta$	3.8 arc-min	3.8516 arc-min	10 arc-min	0.0052 arc-min
ϕ_0	20.0 deg	-20.04 deg	60 arc-min	3.019 arc-min
$\delta\phi$	4.60 arc-min	4.6960 arc-min	10 arc-min	0.0117 arc-min
β	49.8358 deg	49.8358 deg	0.5 arc-sec	0.0 arc-sec
$2\alpha 1$	95.15 deg	92.085 deg	30 arc-min	0.1634 arc-min
S	26.67 mm	26.67 mm	0.001 mm	1e-08 mm
d	48 mm	48 mm	0.001 mm	1e-07 mm
dx	11 mm	11 mm	0.01 mm	1e-06 mm
hz	-1 mm	-2.36 mm	2 mm	0.350 mm
hy	46 mm	45.97mm	2 mm	1.208 mm
f_0	108.8 mm	109.09 mm	1 mm	0.114 mm
P_∞	11.33 mm	11.339 mm	0.01 mm	5e-05 mm
Pixel Scale	1.	1.00026	0.01	0.00048
Pixel Size	0.05 mm	0.05 mm	deleted	------
λ	1	1.00271	0.001	0.0008
d_1	0.0	-0.000144	0.0	2.06e-5
d_2	0.0	-1.03e-09	0.0	5.53-11
d_3	0.0	1.91e-013	0.0	6.14e-12
d_4	0.0	-3.28e-005	0.0	9.66e-06
d_5	0.0	4.56e-012	0.0	797e-12
ω	0.0 arc-min	-35.91 arc-min	0.0 arc-min	0.892 arc-min
Φ	0.0 arc-min	18.07arc-min	0.0 arc-min	4.168 arc-min
K	0.0 arc-min	-2.01 arc-min	0.0 arc-min	0.962 arc-min

Table 4.5b: The calibration set #2 results.

Additionally, to stabilize the solution each parameter is weighted according to its influence on the adjustment, and also its actual physical value. Table 4.5 provides the a priori standard deviation values (note that the weight constraint value is 1/ the a priori standard deviation value) for each parameter.

Another encountered problem that affected the stability and convergence of the solution is the high correlation between some parameters. One problem is the correlation between the initial angle ϕ_0 and the external orientation angle ω, the rotation about the vertical-axis (the X-axis). Because of this correlation, convergence was not possible. Once Equation 4.82 was added as a constraint equation to the least square solution with proper weighting, convergence was achieved. This shows that by reinforcing the relationship between the initial angle ϕ_0 and the corresponding step angle $\delta\phi$, the correlation value between the external orientation angle ω and the initial angle ϕ_0 was decreased and convergence was possible.

Another correlation problem is the correlation between the scale factor λ and the initial angles (θ_0 and ϕ_0), the effective focal length $\mathbf{f}_0$, and the PixelScale parameters. To solve this problem, two approaches are used.

In the first approach, the control points used are distributed over depth distances ranging from 0.65 m to 1.15 m. The scale factor is fixed. The weight constraints values used in the adjustment (1/ a priori standard deviation values) and the resulted a posteriori standard deviation values are shown in Table 4.5, calibration set #1.

The RMS (root mean square) values of the errors between the control points coordinates and their calculated values using the calibrated parameters for the X, Y and Z axes are: ±0.615 mm, ±0.713 mm and ±0.553 mm, respectively. Note that the registered depth values, $\mathbf{p}_0$, of the control points used in this approach (i.e. over depth distances ranging

from 0.65 m to 1.15 m) are positioned to the left of the principal point on the CCD sensor. This could be the reason of this correlation.

In the second approach, the control points used are distributed over depth distances ranging from 0.6 m to 1.6 m. The weight constraints values (1/ a priori standard deviation values) used in the adjustment and the resulted a posteriori standard deviation values are shown in Table 4.5, calibration set #2. Note that the registered depth values, $\mathbf{p_0}$, for the control points are positioned over the total length of the CCD sensor (i.e. on both sides of the principal point).

The RMS (root mean square) values of the errors between the control points coordinates and their calculated values using the calibrated parameters for the X, Y and Z axes are: ±0.666 mm, ±0.618 mm and ±0.713 mm, respectively. The distribution of the control points in the second approach solved the correlation problem, however, the RMS values show that the first approach provided better precision for depth values. Hence, the calibrated values resulted from the first calibration set is used in this thesis.

4.5.8 Calibration Procedure

Three steps are taken for the LSS calibration. The goal of the first step is to test the calibration program and check the correlation effects of the LSS parameters. Perfect simulated data is used for this step. When the exterior orientation angles are removed from the adjustment, the solution converges immediately after the first iteration. Once

these orientation angles are introduced, the solution does not converge due to the high correlation between the exterior orientation angle ω, and the interior orientation angle ϕ_0. Hence, Equation 4.82 is used as a constraint equation to control the angle ϕ_0, which helped to solve this problem.

In the second step, random errors are introduced in the simulated data. The solution converges, with the aid of the two constraint Equations 4.81 and 4.82, as long as the introduced random errors are less than the following standard deviations of the observations : σ_i=**0.2**, σ_j=**0.2**, and σ_p=**5**). Also, the least squares solution in this step converges without the need of weight constraints or the need to remove or fix any of the LSS parameters.

In the third step, the acquired data is used. Because of the high non-linearity of the geometric and the distortion modeling and also the high correlation found among the LSS parameters, a special adjustment procedure is used to achieve convergence. The following are the steps used to determine a good set of calibrated parameters:

1. A rigid target field (TF) with a grid of regular spaced circular targets was construct at the University of Calgary engineering machine-shop. The TF was made of circular targets engraved on a plastic sheet. The targets engraved such that they are equally spaced at 63.5 mm (2.5 inch). The foreground color of the sheet is white and the core color is black, see Figure 4.21.

2. The TF is positioned at depth distances of approximately 0.60 m, 0.85 m, 1.15 m, 1.35 m, 1.60 m and 1.95 m from the LSS. For each depth distance, the TF is approximately positioned such that its coordinate system is parallel to the LSS coordinate system. This is done by adjusting the TF position, so that, the calculated Z-axis coordinates of edge targets on the TF have the same depth value. The calculation is based on the LSS observations (i.e. the i and j coordinates of the target centres and their registered depth values p) and the approximate values of the unknown parameters.

3. For each TF position, the centres of the circular targets were surveyed using an electronic theodolite system and their coordinates were estimated using to the network adjustment method. Also, for each TF position, the LSS scanned the target field with an image size of 512X512 and field of view of 40°X34° (40 degrees along the horizontal axis and 34 degrees along the vertical axis), see Figure 4.21.

4. The surveyed coordinates of the TF, for the various depth distances, are transformed (i.e. seven parameters transformation using the Cayley-Rodregoez rotation matrix approach) to the LSS coordinate system.

5. The weight constraints values used are shown in Table 4.5.

6. The J value of the constraint equation, Equation 4.82, is 256 (512/2).

7. The PixelSize parameter and the scale factor are removed from the adjustment.

8. Six to eight iterations are normally needed for the solution to converge.

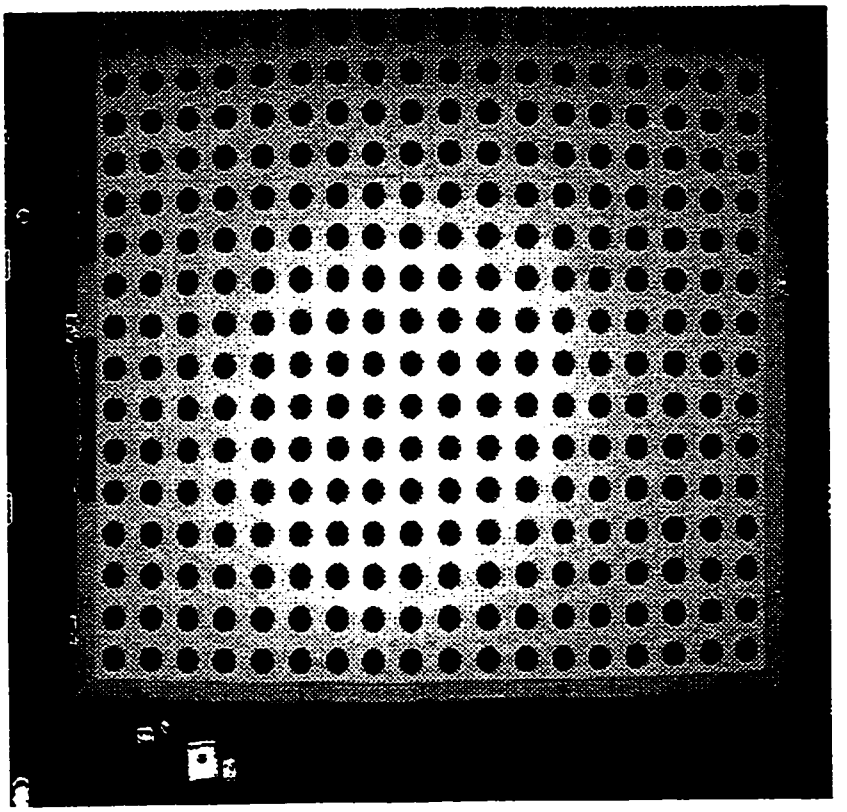

Figure 4.21: The target field used for the LSS calibration.

4.5.9 Calibration Results

The RMS values of the errors between the control points coordinates and their calculated values using the calibrated parameters for the X, Y and Z axes are: ±0.615 mm, ±0.713 mm and ±0.553 mm, respectively.

The standard deviation values of the observations (C_l) used in the least squares adjustment that provided acceptable estimated variance factor are: ±10 for the registered value **p**, ±0.5 pixels for the image coordinates **i** and **j**. The resultant estimated variance factor from the least squares solution is 1.18.

The average values of the standard deviation values of the adjusted observations $\left(\hat{C}_l\right)$ are: ±4.6 for the registered value **p**, ±0.17 pixels for the image coordinates **i** and ±0.16 pixels for the image coordinates **j**.

If movements are introduced, the calibrated parameters solution should provide a much better precision for these movements than the nominal (approximate) parameters solution. To explore this, a small target field with circular targets mounted on a 2-D translation stage is used to introduce movements. Figure 4.22b illustrates the first mounting configuration of the 2-D translation stage to introduce vertical movements (the LSS X-axis). Figure 4.22a illustrates the second mounting configuration of the 2-D translation stage to introduced movements along the horizontal axis and the depth axis, which are the LSS Y- and Z-axes.

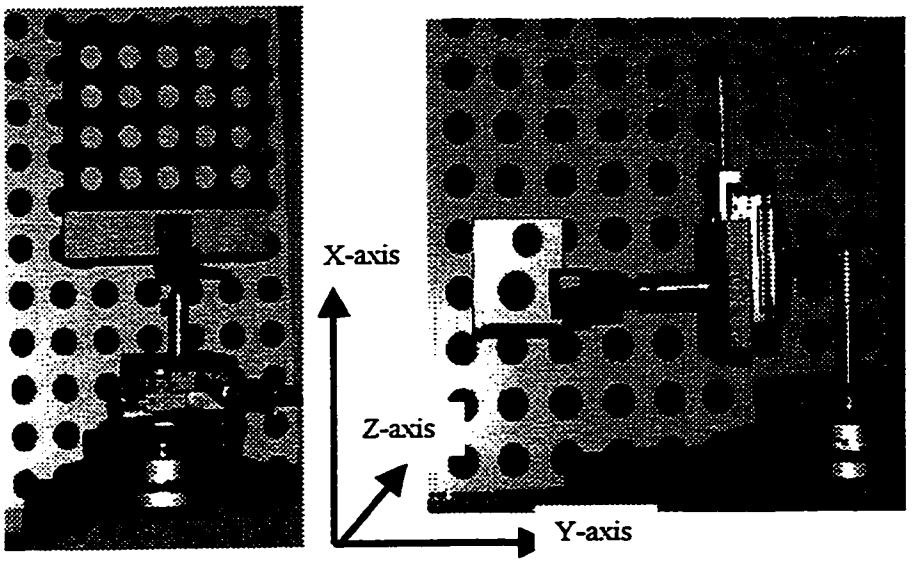

Figure 4.22: The mounting configurations of the 2-D translation stage. (a) The configuration to introduce horizontal and depth movements. (b) The configuration to introduce vertical movements.

4.5.9.1 Deformation Measurements at Depth Distance of 1.2 Metres

In the first configuration, Figure 4.22b, movements are introduced using the 2-D translation stage along the X-axis (Vertical axis). The introduced movements in targets coordinates are shown in Table 4.6. Figure 4.23 shows the deformation errors of the introduced movements along the X-axis. These errors are calculated using the calibrated parameters.

Introduced movements along the X-axis (mm)	Epoch									
	1	2	3	4	5	6	7	8	9	10
	0.25	0.5	0.75	1.0	1.5	2.0	5.0	10.0	15.0	25.0

Table 4.6: Introduced movements along the X-axis in millimetres

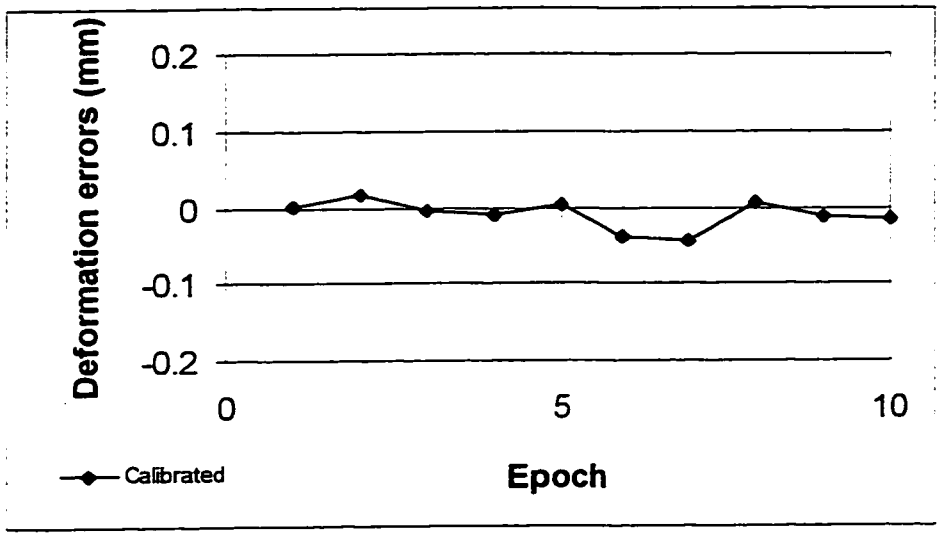

Figure 4.23: The deformation errors calculated based on the calibrated parameters (the introduced movements are along the X-axis at a depth distance of 1.2 m).

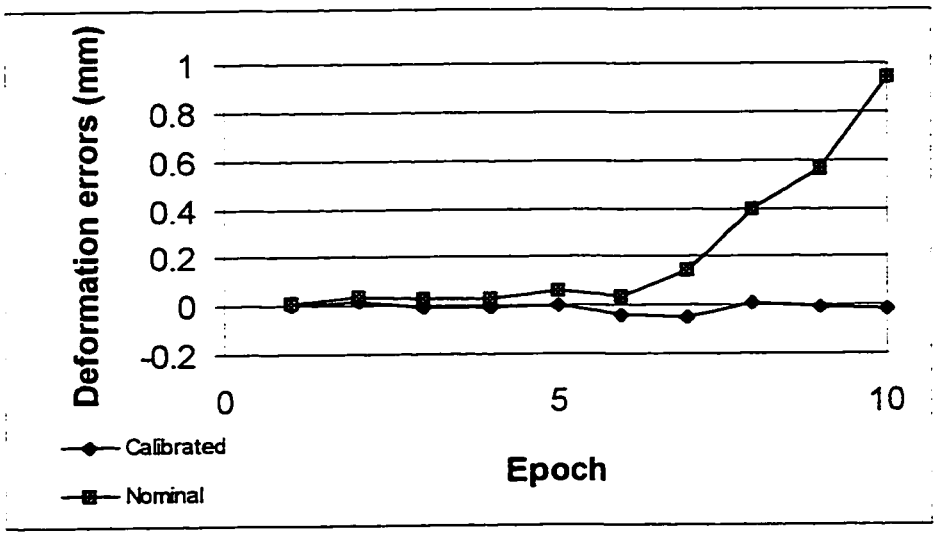

Figure 4.24: The deformation errors calculated based on the calibrated parameters and the nominal parameters (the introduced movements are along the X-axis).

Figure 4.24 illustrates the degraded precision if the nominal parameters are used instead of the calibrated parameters. The root mean square values of the errors are: ±0.02 mm

when using calibrated parameters, and ±0.305 mm when using the nominal parameters. In the second configuration, Figure 4.22a, movements are introduced using the translation stage along the Y- and Z- axes (Horizontal and Depth axes, respectively) according to Table 4.7. The rows in the table correspond to the Y-axis and the Z-axis introduced movements, respectively. Figure 4.25 shows the deformation error vectors between the measured and the introduced movement vectors. The introduced movement vector is calculated from the introduced movements (using the translation stage) along the Y- and Z-axes. The measured vector is calculated from the LSS measurements based on the calibrated parameters.

Introduced movements	Epoch									
	1	2	3	4	5	6	7	8	9	10
Y-axis (mm)	0.0	-5.0	5.0	25.0	45.0	45.0	45.0	45.0	45.0	45.0
Z-axis (mm)	5.0	5.0	5.0	5.0	5.0	-5.0	-15.0	-25.0	-35.0	-45.0

Table 4.7: Introduced movements along the Y and Z-axes in millimetres

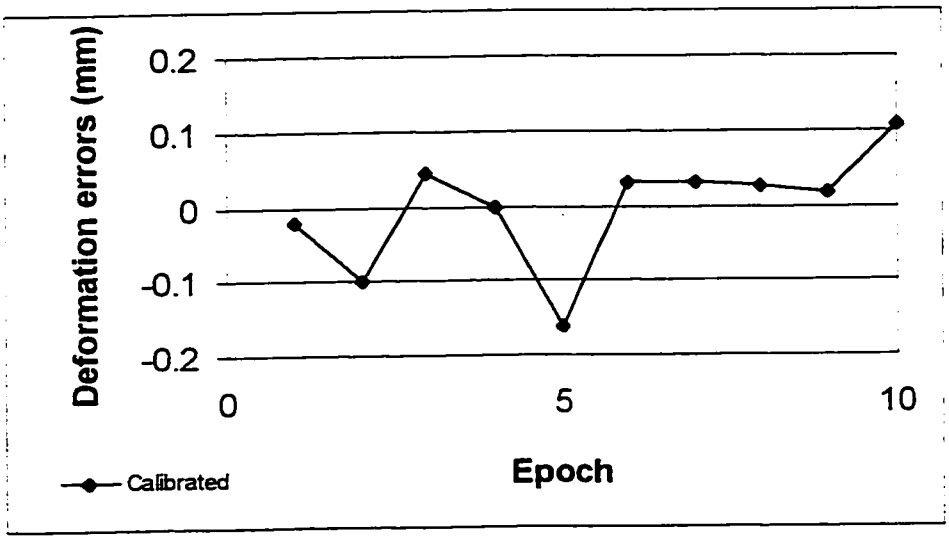

Figure 4.25: The deformation error vectors calculated based on the calibrated parameters due to the introduced movements along the Y and Z-axes at a depth distance of 1.2 m.

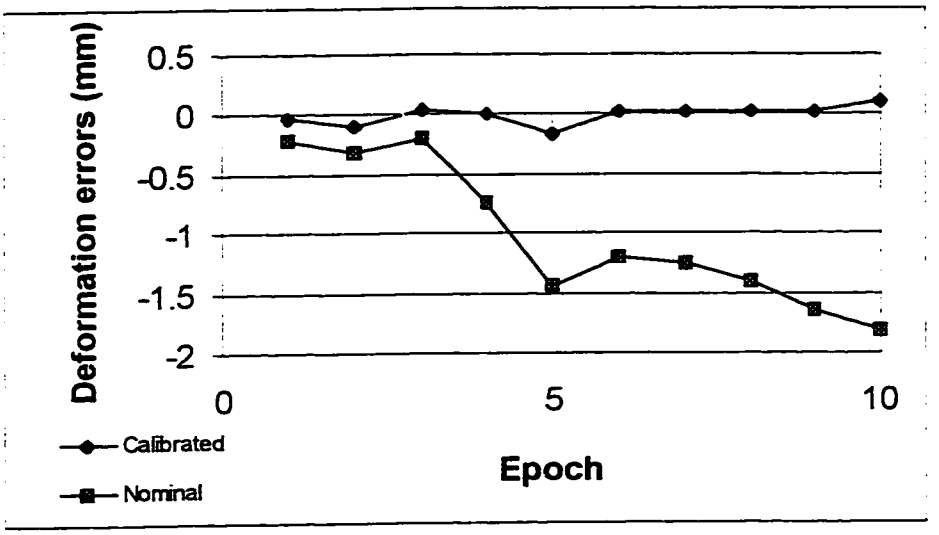

Figure 4.26: The deformation error vectors calculated based on the calibrated parameters and the nominal parameters due to the introduced movements along the Y and Z-axes at a depth distance of 1.2 m. The measured errors are the difference between the measured and the introduced movement vectors.

Figure 4.26 illustrates the degraded precision if the nominal parameters are used instead of the calibrated parameters. The root mean square values of the errors are: ±0.072 mm when using the calibrated parameters, and ±0.654 mm when using the nominal parameters.

Figures 4.27 shows the deformation errors along X, Y and Z axes. The errors are the difference between the introduced movements using the translation stage along the Y and Z axes (according to Table 4.9) and the LSS measured movements. The LSS measured movements are calculated based on the calibrated parameters. The root mean square values of the errors are: ±0.023 mm, ±0.074 mm, and ±0.041 mm along the X-, Y- and Z-axes, respectively.

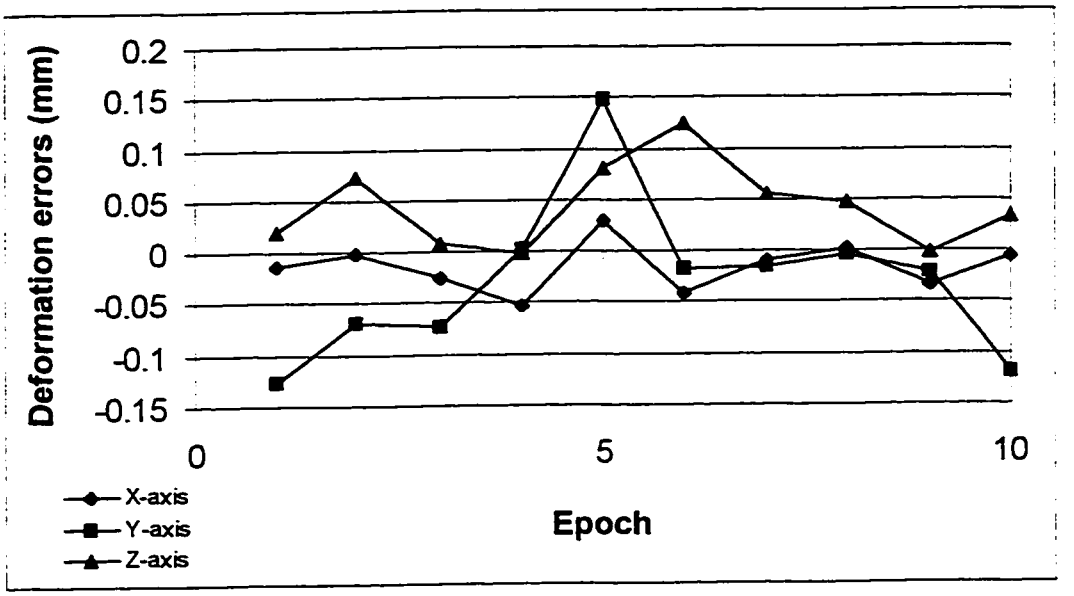

Figure 4.27: The X, Y and Z axes deformation errors calculated based on the calibrated parameters due to the introduced movements along the Y and Z axes at a depth distance of 1.2 m.

4.5.9.2 Deformation Measurements at Depth Distance of 1.5 Metres

Similar to the depth distance case of 1.2 metres, movements are introduced along the X-axis of the translation stage (see the first configuration, Figure 4.22b) as shown in Table 4.8. Next, movements are introduced along the Y- and Z-axes of the translation stage (see the second configuration, Figure 4.22a) according to Table 4.9. Figures 4.28, 4.29, 4.30, 4.31a and 4.31b are similar to Figures 4.23, 4.24, 4.25, 4.26 and 4.27, respectively.

Introduced movements along the X-axis(mm)	Epoch									
	1	2	3	4	5	6	7	8	9	10
	0.0	0.25	0.5	0.75	1.0	1.5	2.0	5.0	25.0	50.0

Table 4.8: Introduced movements along the X-axis in millimetres

Epoch	Introduced movements (mm)	
	Y-axis	Z-axis
1	0.0	0.0
2	0.25	0.0
3	0.5	0.0
4	0.75	0.0
5	1.0	0.0
6	1.5	0.0
7	5.0	0.0
8	10.0	0.0
9	25.0	0.0
10	50.0	0.0
11	50.0	0.25
12	50.0	0.5
13	50.0	0.75
14	50.0	1.0
15	50.0	1.5
16	50.0	2.0
17	50.0	5.0
18	50.0	10.0
19	50.0	25.0
20	50.0	50.0

Table 4.9: Introduced movements along the Y- and Z- axes in millimetres.

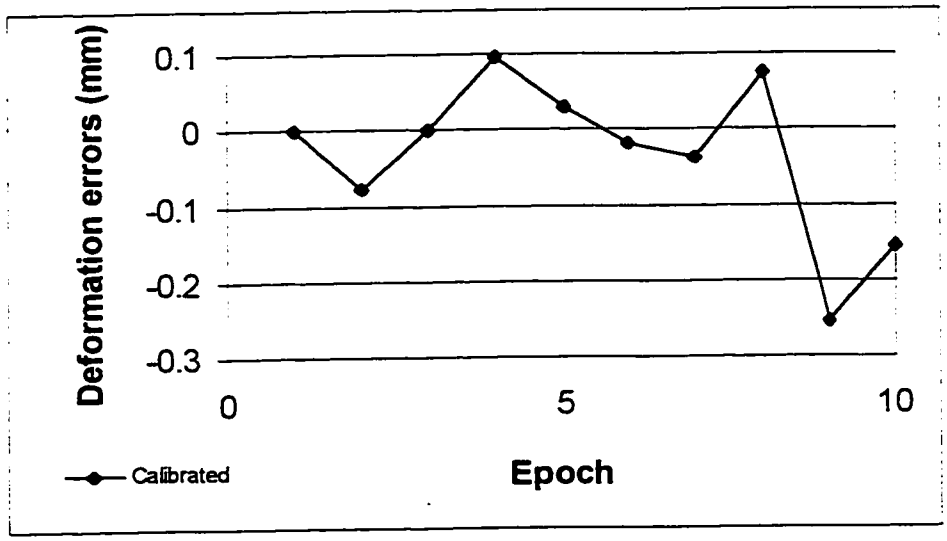

Figure 4.28: The deformation errors calculated based on the calibrated parameters (the introduced movements are along the X-axis at a depth distance of 1.5 m).

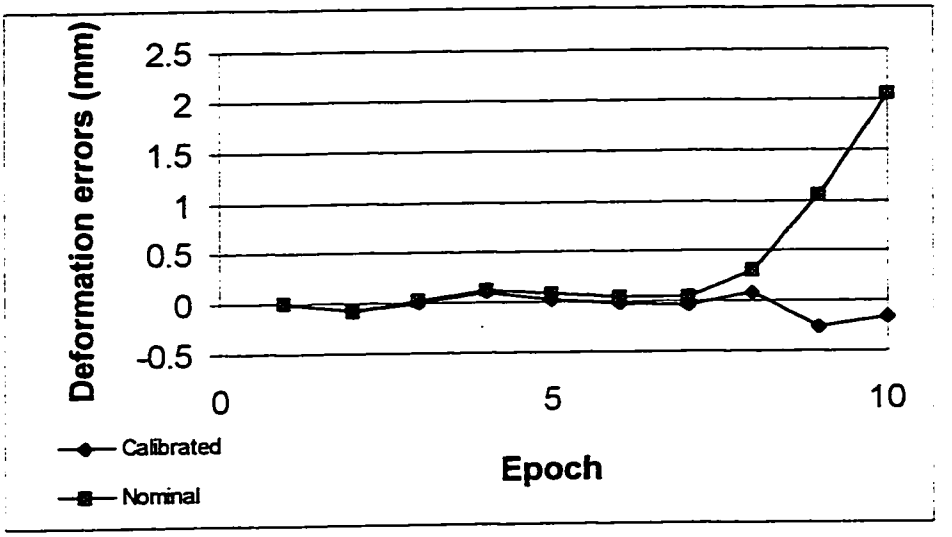

Figure 4.29: The deformation errors calculated based on the calibrated parameters and the nominal parameters (the introduced movements are along the X-axis).

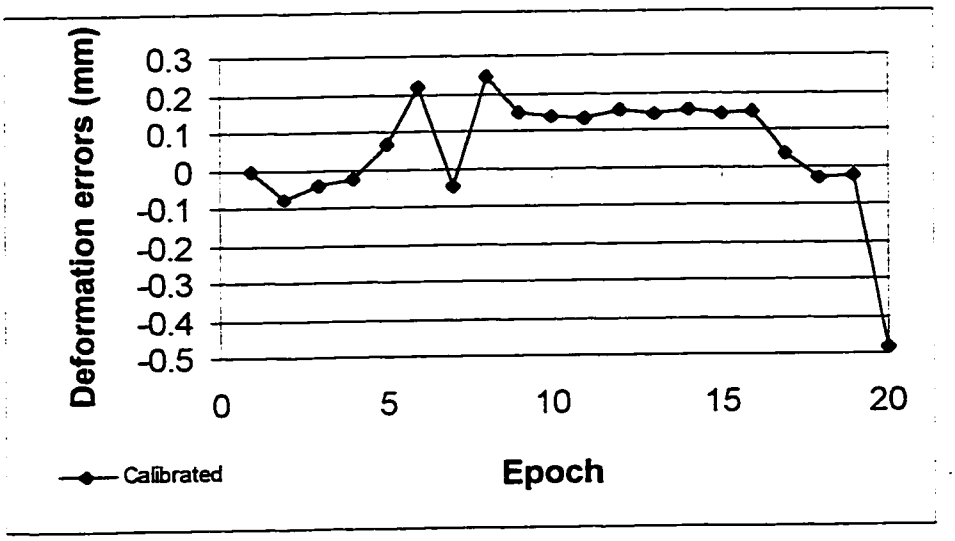

Figure 4.30: The deformation error vectors calculated based on the calibrated parameters due to the introduced movements along the Y and Z-axes at a depth distance of 1.5 m.

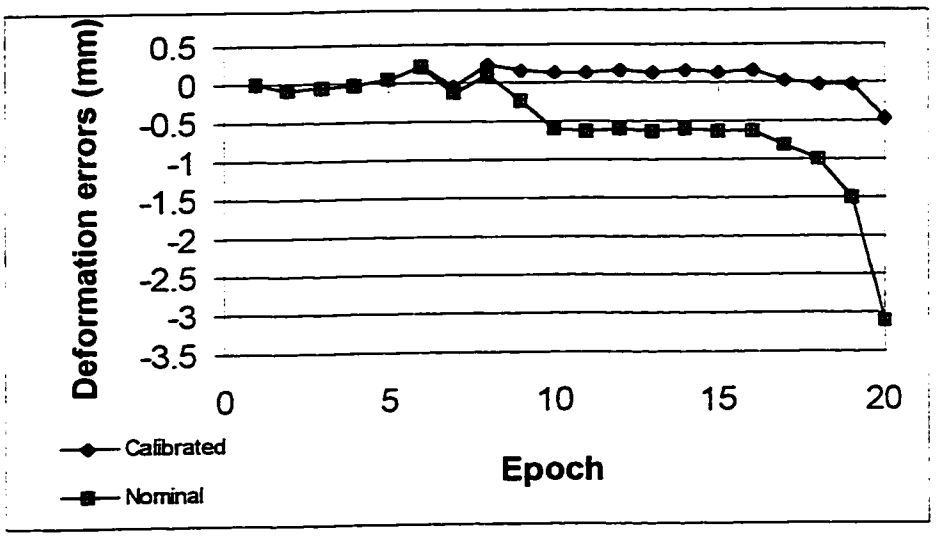

Figure 4.31a: The deformation error vectors calculated based on the calibrated parameters and the nominal parameters due to the introduced movements along the Y and Z-axes at a depth distance of 1.2 m. The measured errors are the difference between the measured and the introduced movement vectors.

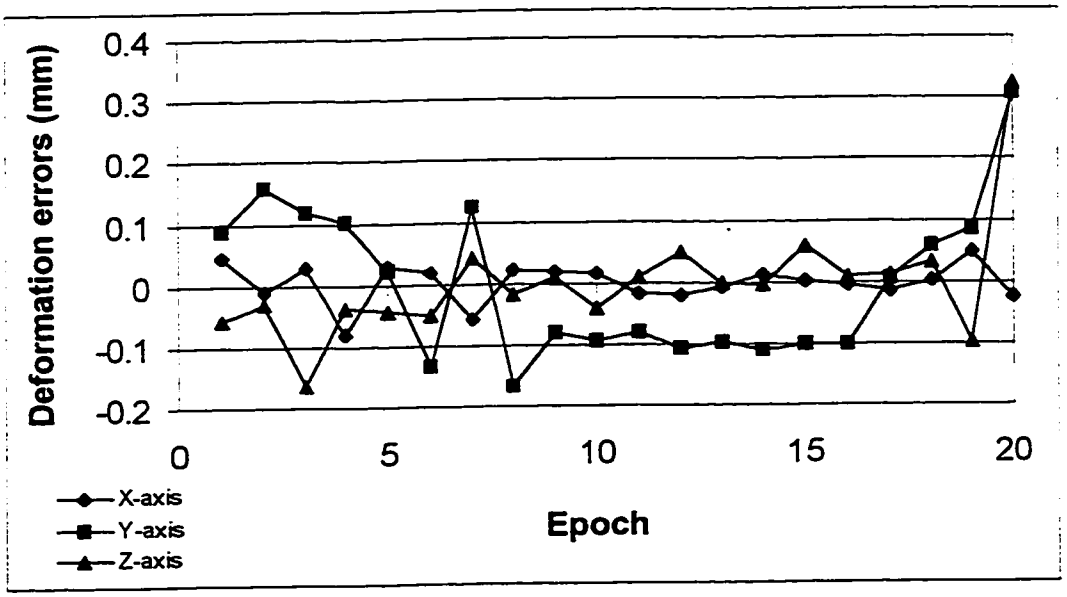

Figure 4.31b: The X, Y and Z axes deformation errors calculated based on the calibrated parameters due to the introduced movements along the Y and Z axes at a depth distance of 1.2 m.

The root mean square values of the deformation errors due to introduced movements along the X-axis, the first configuration, are: ±0.106 mm when using the calibrated parameters, and ±0.674 mm when using the nominal parameters.

The root mean square values of the deformation error vectors due to the introduced movements along the Y- and Z-axes, the second configuration, are: ±0.158 mm when using the calibrated parameters, and ±0.742 mm when using the nominal parameters. The root mean square values of the errors are ±0.032 mm, ±0.125 mm, and ±0.092 mm along the X-, Y- and Z-axes, respectively.

The results show that the deformation measurements for a depth distance of 1.2 metres are more accurate than at a depth distance of 1.5 metres. This confirms that the instrument provides better precision for closer depth distances. However for both depth distances the results prove that the LSS should provide acceptable precision for deformation measurement applications within this range of depth distances.

4.5.9.3 Absolute and Relative Measurements

The calibration is carried out over the total field of view of the LSS and of approximately a depth of 0.6 metres with a standoff distance of 0.6 metres. The control points used for the calibration are positioned approximately at depth distances of 0.65 metres and 1.15 metres (see the target field figure, Figure 4.21).

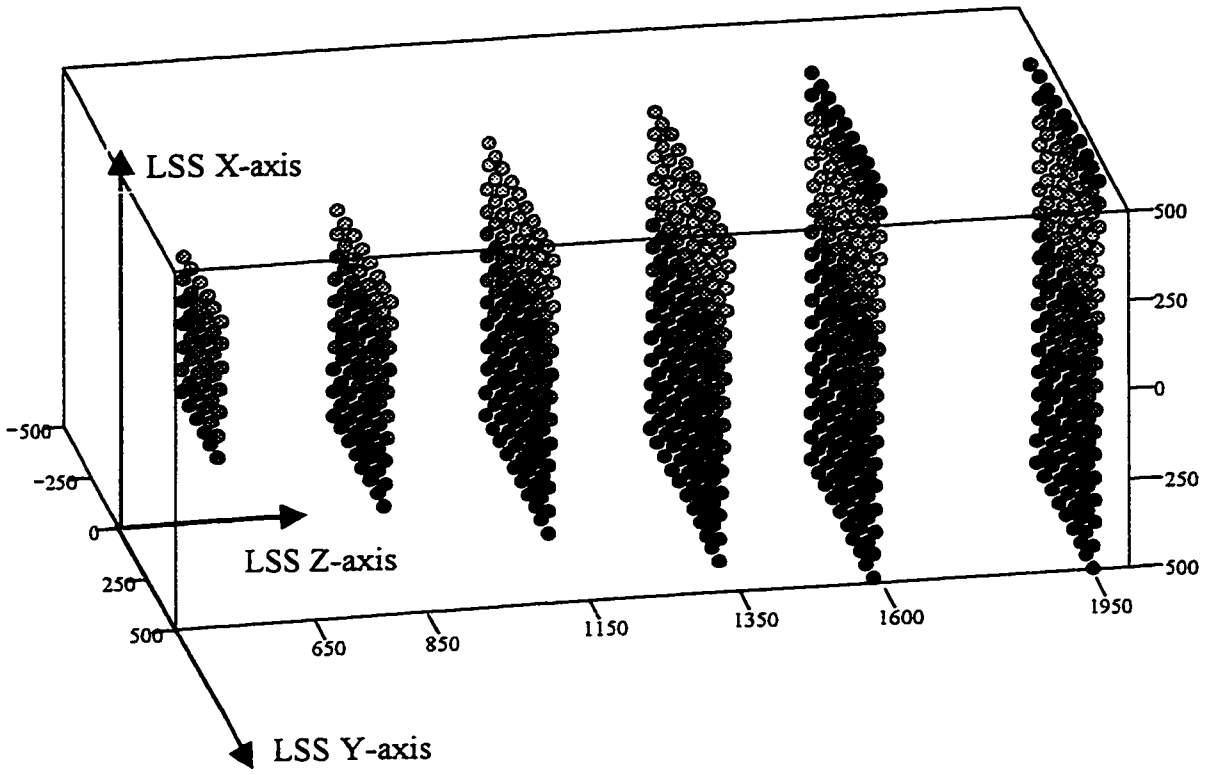

Figure 4.32: The circular target coordinates of the target field at the following depth distances: 0.65 m, 0.85 m, 1.15 m, 1.35 m, 1.60 m and 1.95 m.

Figure 4.32 shows the circular target coordinates of the target field, obtained with calibrated parameters, at the following depth distances: 0.65 m, 0.85 m, 1.15 m, 1.35 m, 1.60 m and 1.95 m. The coordinates of the target centres at these depth distances are

measured using an electronic theodolite system and the network adjustment method. The precision of the measured coordinates is between 0.05 to 0.1 mm and ,hence, these measurement are used as reference coordinates to evaluate the accuracy of the LSS coordinate measurements of the target centres.

Depth Distance (m)	Errors (mm)								
	X-axis (Vertical axis)			Y-axis (Horizontal axis)			Z-axis (Depth axis)		
	Mean	Median	RMS	Mean	Median	RMS	Mean	Median	RMS
0.65	-0.05	-0.13	0.46	-0.03	-0.05	0.6	0.10	0.06	0.43
0.85	0.14	0.12	0.60	0.03	0.04	0.78	0.44	0.40	0.60
1.15	0.06	0.08	0.95	0.10	0.06	0.98	-0.22	-0.44	1.11
1.35	0.04	0.03	1.50	0.14	0.26	1.74	-0.38	-0.54	3.83
1.60	0.11	0.19	1.93	0.28	0.28	1.30	0.80	0.60	2.57
1.95	0.60	0.65	2.36	0.87	0.84	1.22	3.95	3.58	2.78

Table 4.10: Statistics of the absolute coordinate measurements.

Depth Distance (m)	Errors (mm)								
	X-axis (Vertical axis)			Y-axis (Horizontal axis)			Z-axis (Depth axis)		
	Mean	Median	RMS	Mean	Median	RMS	Mean	Median	RMS
0.65	—	—	—	—	—	—	—	—	—
0.85	-0.025	-0.02	0.38	-0.06	-0.06	0.06	-0.24	-0.27	0.31
1.15	0.018	-0.01	0.49	-0.10	-0.10	0.14	0.76	0.78	0.49
1.35	0.08	0.05	0.63	-0.17	-0.13	0.20	1.43	1.40	0.68
1.60	0.16	0.07	0.76	-0.31	-0.29	0.17	1.20	1.19	0.84
1.95	-0.33	-0.31	0.98	-0.82	-0.81	0.17	-1.80	-1.73	0.92

Table 4.11: Statistics of the relative coordinate measurements.

Table 4.10 shows the mean, median and RMS of the absolute measurement errors (calibrated parameters are used). Similarly, Table 4.11 shows the mean, median and RMS of the relative measurement errors (calibrated parameters are used). Relative measurements are calculated with respect to the depth distance 0.65 metres.

Note that the RMS values of the relative coordinate measurements, see Table 4.11 and Figure 4.40, are similar to the expected precision values shown in Figure 4.20b. The expected precision shown in the figure is calculated based on the standard deviation values of the observations used in the least squares adjustment that resulted in an acceptable estimated variance factor.

Figures 4.33, 4.35 and 4.37 illustrate the error behavior in the X-, Y- and Z-axes of the absolute measurements. Similarly, Figures 4.34, 4.36 and 4.38 illustrate the error behavior in the X-, Y- and Z-axes of the relative measurements with respect to the depth distance 0.65 metres. Figures 4.39 and 4.40 show the RMS in the X-, Y- and Z-axes of the absolute measurements and of the relative measurements, respectively.

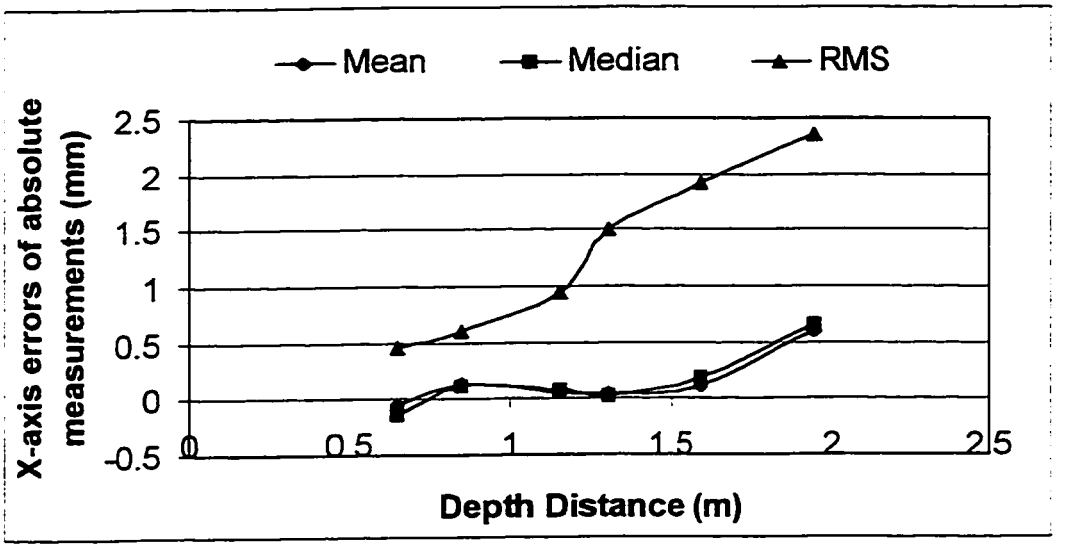

Figure 4.33: The mean, median and RMS of the X-axis absolute measurements.

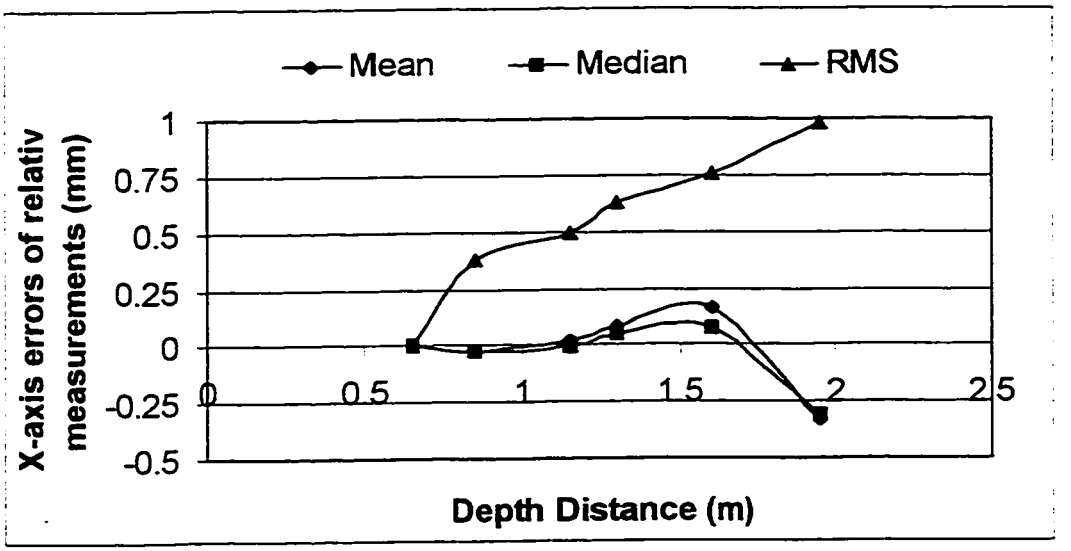

Figure 4.34: The mean, median and RMS of the X-axis relative measurements.

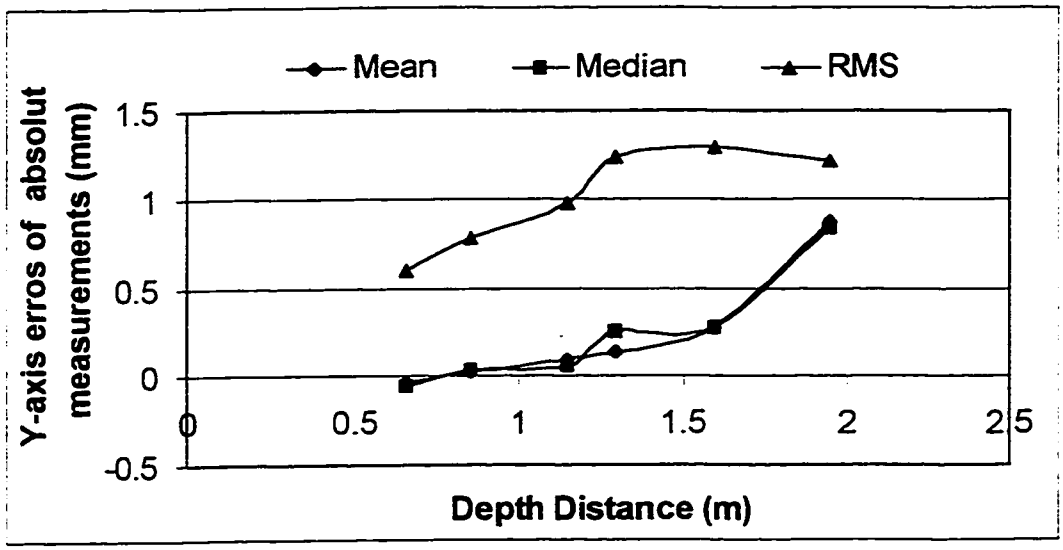

Figure 4.35: The mean, median and RMS of the Y-axis absolute measurements.

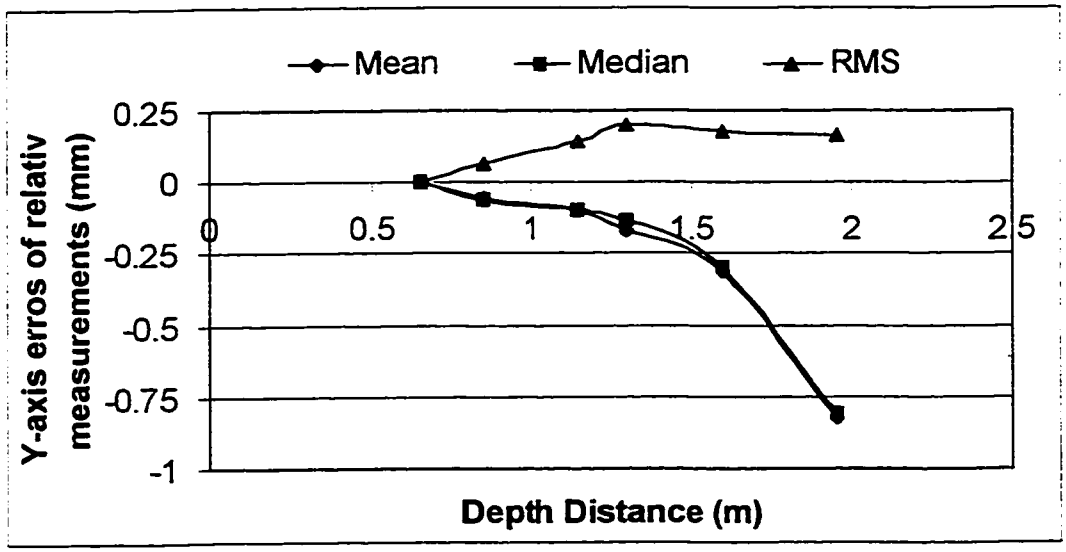

Figure 4.36: The mean, median and RMS of the Y-axis relative measurements.

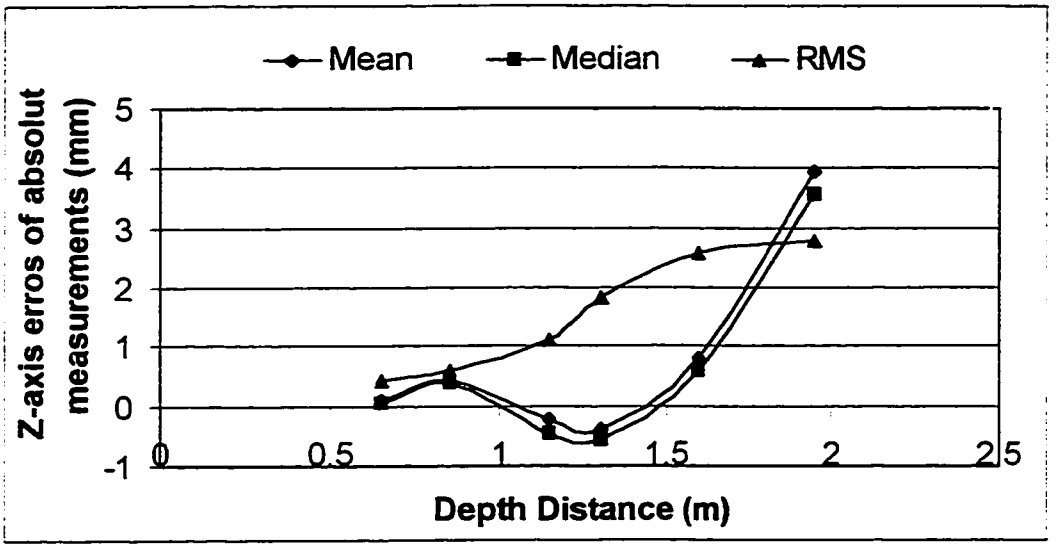

Figure 4.37: The mean, median and RMS of the Z-axis absolute measurements.

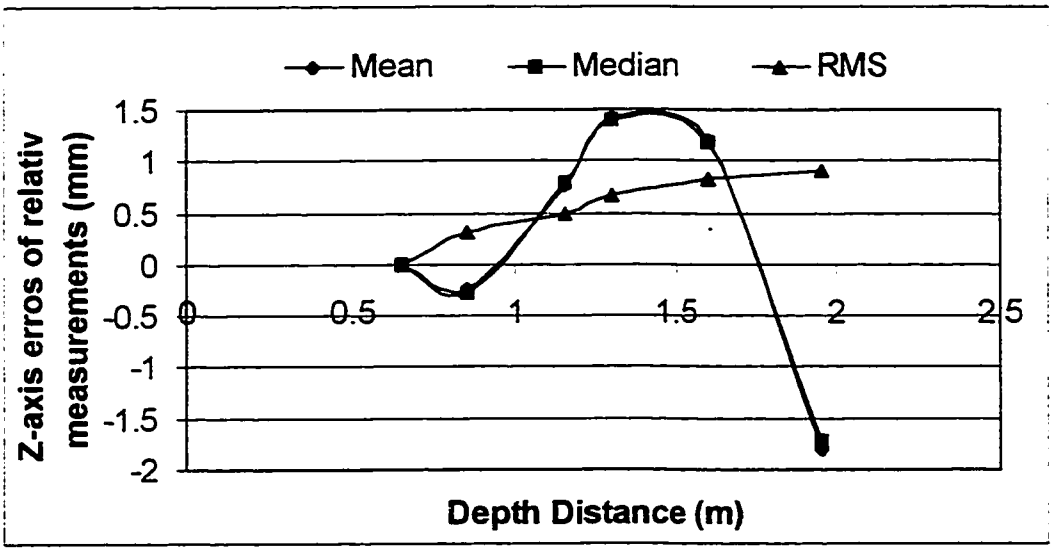

Figure 4.38: The mean, median and RMS of the Z-axis relative measurements.

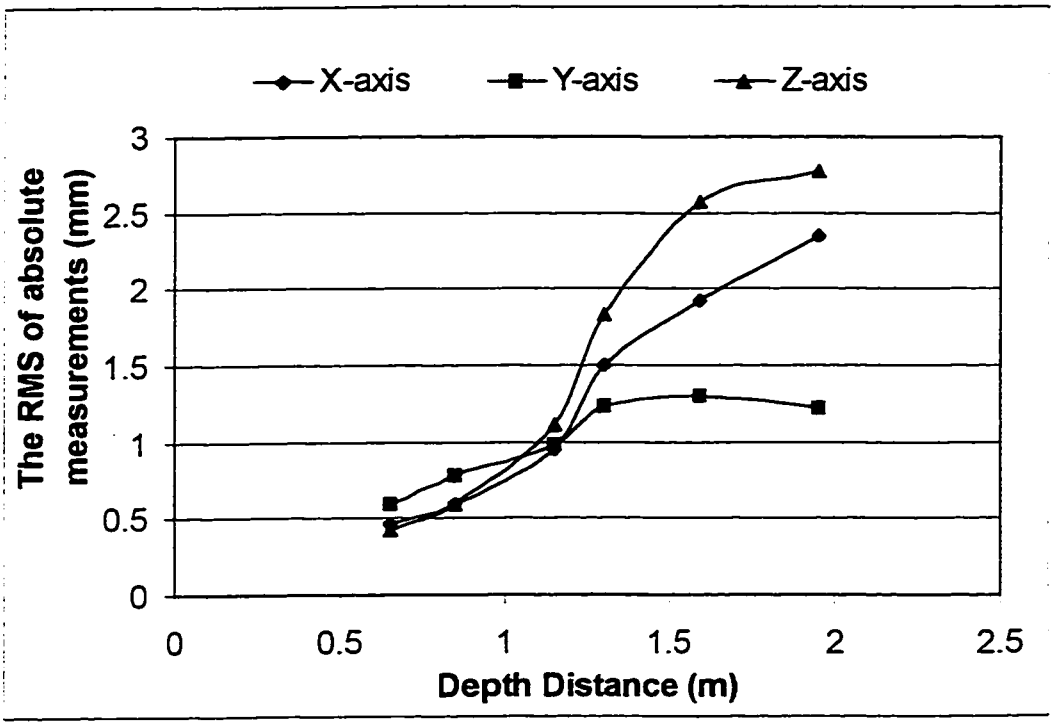

Figure 4.39: The RMS of the X-, Y- and Z-axes absolute measurements.

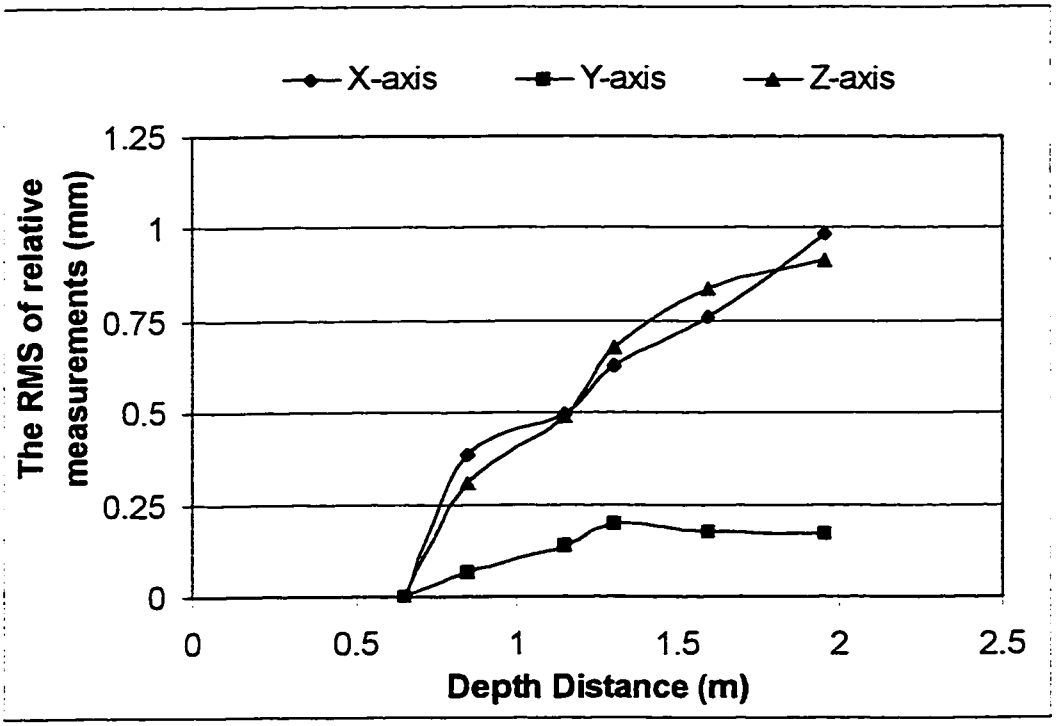

Figure 4.40: The RMS of the X-, Y- and Z-axes relative measurements.

From the figures, the following is concluded:

1. The RMS values of the relative coordinate measurements, see Table 4.11, are similar to the expected precision values calculated based on the variance values of the observations used in the least squares adjustment.

2. The mean and median errors are nearly the same. The mean errors for measurements at depth distances that are less than 1.25 metres are almost zero. This shows the reliability of the calibration. (Note that the calibration volume is carried out for depth distances between 0.65 m and 1.15 m from the LSS.)

3. The mean errors and the RMS values of the X-axis and the Y-axis (the vertical and horizontal axes) measurements are smaller than those for the Z-axes (the depth axis) measurements. Also, the mean errors values are closer to zero than the RMS values along the X- and the Y-axes. This is not the case along the Z-axis. This shows the poor quality of the LSS depth measurements.

4. The RMS values along the X-, Y- and Z-axes are nearly equal and similar in behavior for absolute measurements at depth distances less than 1.25 metres. However, in the case of relative measurements, only the X-axis and the Z-axis are nearly similar and equal. The Y-axis has better RMS values for depth distances that are less than 1.25 metres. This may indicate that most of the systematic errors of the Y-axis are eliminated.

5. Finally, the accuracy of the relative measurements shows a drastic improvement in comparison to the accuracy of the absolute measurements.

4.5.9.4 Discussion of the Results

The absolute and relative measurement results, using calibrated parameters, show that the LSS has better RMS values and mean errors for the calibrated depth distances (between 0.6 metres and 1.25 metres). Also, the relative measurements are more accurate than the absolute measurements. This is important since relative measurements are normally used.

The deformation measurement results show that the calibrated parameters can be used to provide results suitable for industrial applications in which required precision for movements are in the order of 0.1 mm.

CHAPTER FIVE

DEFORMATION MEASUREMENT APPLICATIONS USING A LOCAL SCALING APPROACH

5.1 Introduction

The first objective of this chapter is to focus on using the LSS for industrial deformation monitoring applications and to demonstrate its capabilities. Secondly, the software developed to use the LSS for industrial deformation measurements is explained. Finally, this chapter discusses whether the system is suitable to fulfill the need of industrial applications to recover precise surface deformations (e.g. in operating machinery). An example of such applications is illustrated in Figure 5.1.

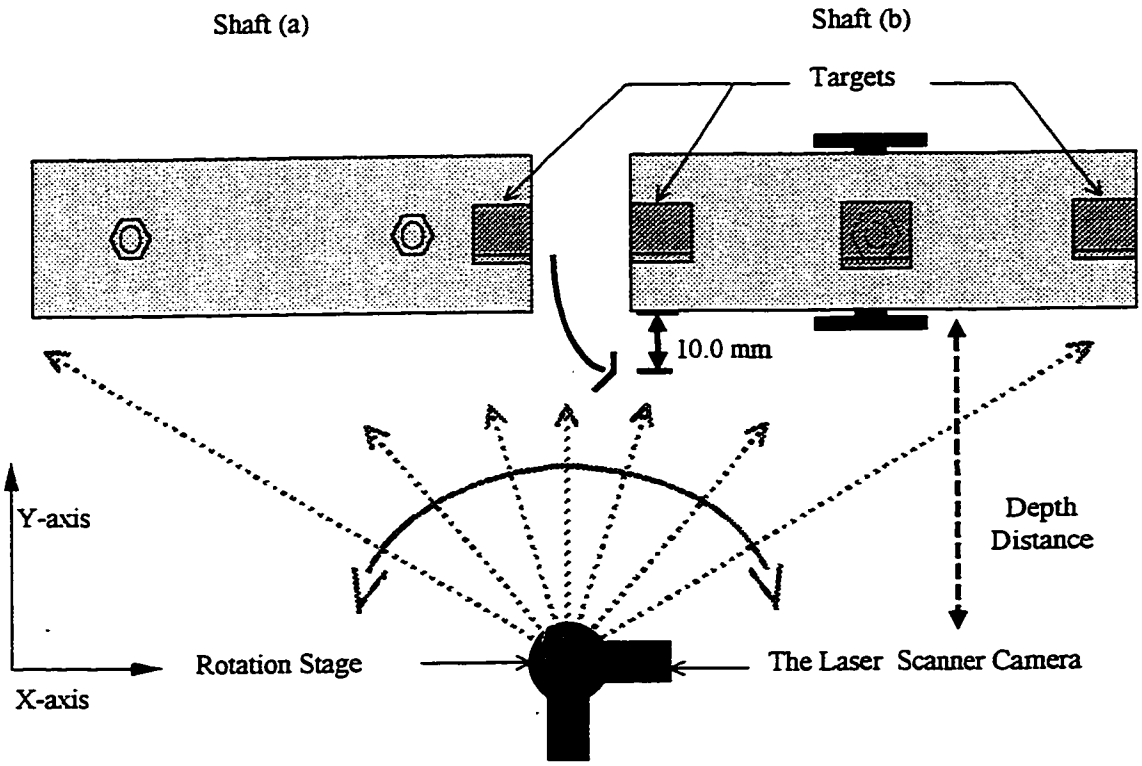

Figure 5.1: The LSS and a mechanical test rig: Shaft (b) is rotated counter-clockwise to move the end by 10.0 mm (Top view).

Figure 5.1 shows the top view of a typical industrial setup. The laser scanner used is a dual-axis scanner with a rotation stage. The depth distance between the laser scanner and the mechanical test rig is about 1.00 m. Targets are mounted on top of the shafts. Movements were introduced by rotating shaft (b) (counter-clockwise) about its Z-axis to move the end 10.00 mm. The mechanical test rig is scanned before and after introducing movement, producing for each case a depth coded image and an intensity image.

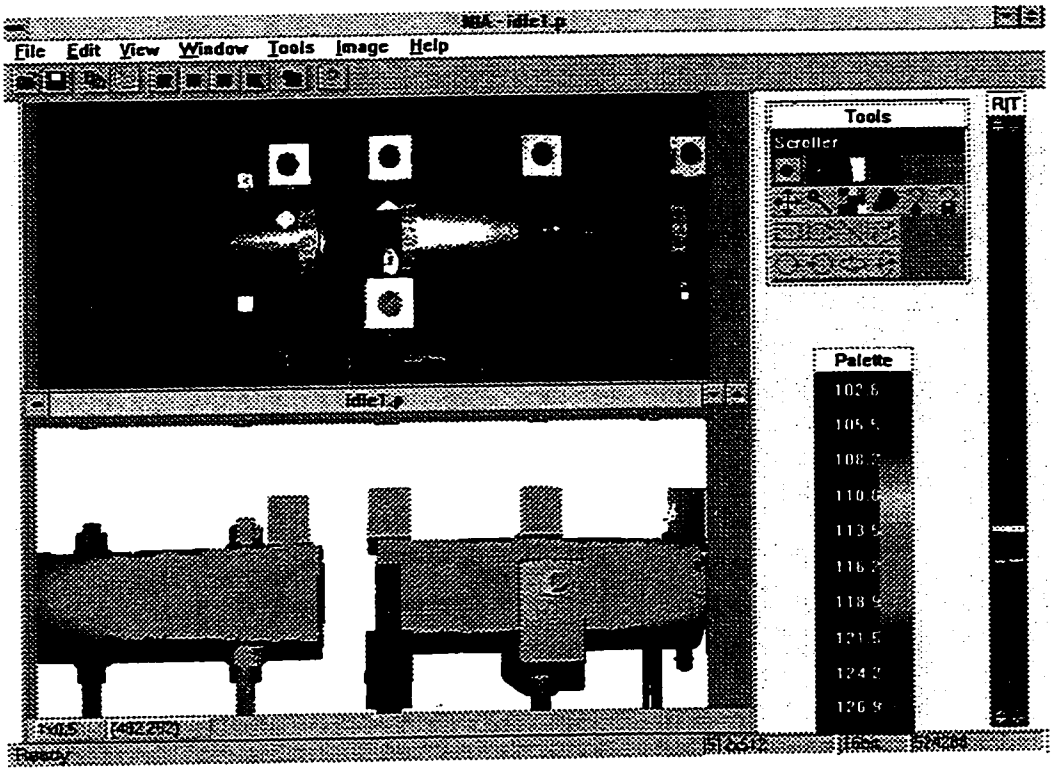

Figure 5.2: Platform of the image tools software: The intensity image and the depth coded image of the scanned mechanical test rig.

Figure 5.2 shows the platform of the Image Tools software. The upper image is the intensity image displayed in gray values and the lower image is the depth-coded image displayed in colors. As shown in the color palette box, the colors represent scaled ranges

(i.e. distances from the camera position to surface points in the scene). The upper right dialog box shows the different tools used to process laser images.

Figure 5.3 shows the result of scaling the direct difference between two depth-coded images (the image scale is obtained from the previous analysis). The upper left image in the Image Tools platform figure shows the surface movements displayed in colors. The movement values for each color are displayed in the color palette. A profile of these movements along a cross-section is shown at the lower left side.

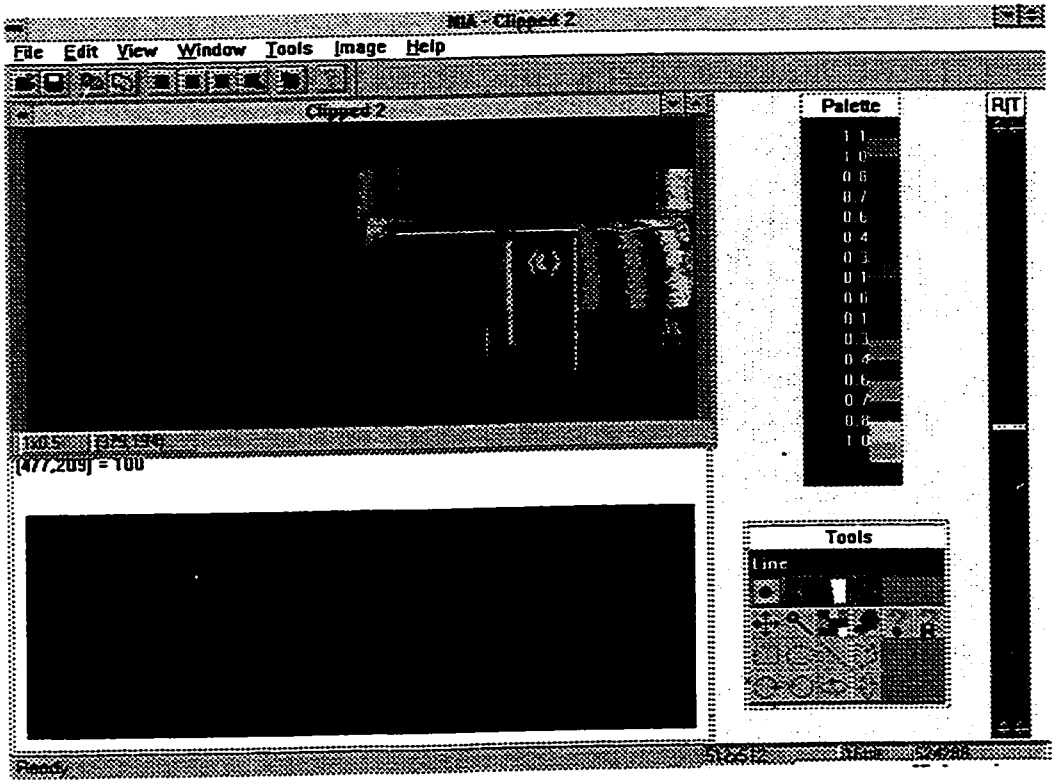

Figure 5.3: Platform of the image tools software: Introduced surface movement of the mechanical test rig.

5.2 Software Development Applications

Software development is an important and useful step in research work since it provides the required tools to utilize the measuring system to produce good, reliable and precise results. The software discussed and explained briefly in this section is developed for PCs and runs under both Windows NT and Windows 95 operating systems. The software developed handles the LSS operation, controlling and image acquisition, image displaying, processing and digitization, edge detection and target finding, and surface deformation representation.

5.2.1 Image Acquisition: The Laser Scanner Interface Software

The interface software acts as a link between the user's commands from a PC-based machine and the LSS operating system, and is used for scanning and acquiring the required images. The software handles various tasks. It sets and controls the various acquisition modes such as Raster or Lissajous mode, image dimension and resolution, field of view and the various camera parameters, laser power, acquisition direction, focusing mode, and also controls the rotation stage speed and acceleration. The software also sets up and initializes the LSS, synchronizes and acquires images, and transfers, retrieves and saves images between the LSS and the PC-based machine.

Figure 5.4 shows the interface platform and some of its dialog boxes. In the figure, the upper left dialog box sets the position and the scan field of view. The upper right dialog

box specifies the required image resolution in pixels. The lower left dialog box controls the rotation angle and the speed of the rotation stage, and the lower right dialog box starts the acquisition of an image.

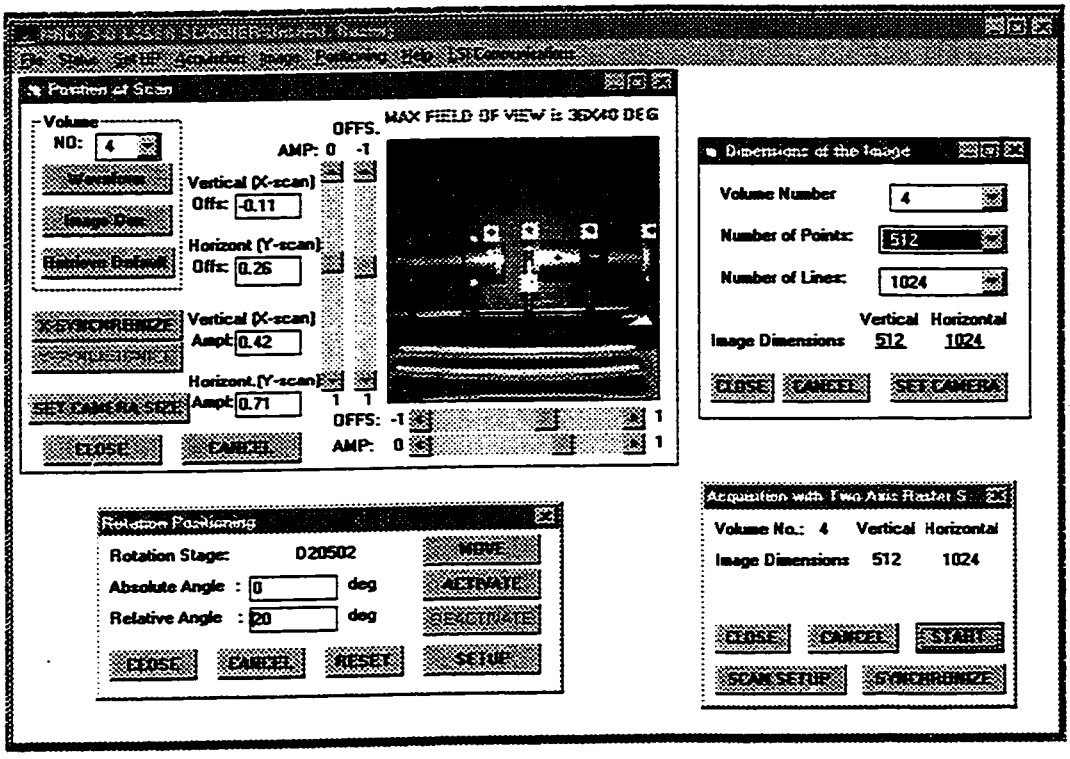

Figure 5.4: The interface software platform.

5.2.2 Image Displaying Processing and Digitization

Image processing techniques are well developed for conventional and CCD cameras. The laser scanning system is a recently developed technology that uses different concepts for image acquisition than the other cameras. Also, due to the research environment the author developed this software re-addressing image processing techniques and making use of the wide dynamic range of the LSS images (i.e. the digital pixel value of the LSS

images is a two byte value). The software is also designed to be suitable for processing CCD images (see Obidowsky et. al., 1995), see Appendix A1.

5.2.3 Precise Edge Detection and Target Location

Two methods are used to locate the edges of circular targets from intensity images. These are the moment preserving method and the centroid method. The moment preserving method (Tabatabai et. al. 1984) also can be used to locate the edges of vertical or horizontal planes or lines. A least square adjustment is then used to precisely determine the centre of a circular targets or the parameter a line, see Appendix A2. Cosandier and Chapman (1992) explained the procedure of applying the moment preserving algorithm in detail to extract the centre of a circular target.

5.2.4 Surface Deformation Representation

In Figure 5.3, the upper image shows the surface deformations or movements that occurred due to the introduced movements. The palette bar in the figure illustrates the size of movements for each color displayed in the image. The following has been developed in the software to display surface deformation:

- Pixel shifting and image subtractions.
- Local scaling for re-mapping surface deformation.
- Color coding for surface deformation.

5.3 Deformation Measurements

5.3.1 Deformation Measurements Methodology

The suggested methodology to use the LSS for surface deformation measurements is as follows:

1. Determine the number of tie/control or reference points required, depending on the field of view, datum transformation and scaling areas. These points should be distributed and installed over the required scanned volume.

2. Select the suitable image dimensions and field of view in the "Position of Scan" dialog box, using the Interface software discussed in Section 5.2.1,.

3. Adjust the LSS laser power to return enough energy to the LSS sensor, according to the type of scanned surfaces and/or targets. Two images may be scanned with different laser powers, one image with a laser power that suits the target surface and the other image with a laser power that suits the object surface.

4. Scan the images for the required epochs, using the interface software.

5. Examine the depth coded and the intensity images, using the image display software,.

6. Determine the image coordinates of the targets for each epoch, using target fitting in the image display software.

7. Determine the target Cartesian coordinates, using the adjusted LSS parameters resulting from the calibration program. This helps to determine target movements, and also to derive shaft direction and misalignment.

8. Use the relative scaling method to determine surface deformations, using the image display software.

5.3.2 The LSS Calibration

The process of scaling the measured variables (depth coded image output) to a standard unit system (e.g. metric units) with a high level of confidence and transforming these values to a general coordinate system (e.g. rectangular coordinate system), and determining the re-mapping function is called camera calibration.

A calibration program has been developed for the purpose of the PEDS research work. The calibration solves for twenty-nine LSS parameters. The parameters consist of: two sensor parameters (PixelSize and Pscale), nine internal parameters (**d**, **S**, $\mathbf{h_y}$, $\mathbf{h_z}$, $\mathbf{f_0}$, $\mathbf{P_\infty}$, β, α, and **dx**), four interior orientation parameters (θ, $\delta\theta$, ϕ, and $\delta\phi$), one scale factor, six exterior orientation parameters ($\mathbf{X_0}$, $\mathbf{Y_0}$, $\mathbf{Z_0}$, ω, Φ, and K), and five distortion parameters. The solution requires a minimum of nine control points covering the volume of interest. The more control points are used the more precise the calibration. To achieve best precision for target extraction, the control points should be retro-reflective circular targets. The intensity image is used to extract the target center (**i** and **j**) of these targets to sub-pixel accuracy by fitting an ellipse to the edges of these targets using a moment

preserving algorithm. The image coordinates for each target are defined as **p, i and j**, where **p** is the pixel-registered value extracted from the depth-coded image for the extracted target centre **i** and **j**. An iterative-nonlinear simultaneous least squares adjustment method is used to determine the values of the internal, external, and distortion parameters of the LSS.

The derived expected precision of the LSS, discussed in Section 4.4, provides an ideological measure of the capabilities of the system. The average standard deviations for objects at 1.5 metres are ±0.6 mm in the Z-axis direction, and ±0.2 mm in both X and Y axes. As soon as the object distance from the camera increases to more than 2.00 metres, the precision starts to decrease rapidly. For example, the standard deviation in the Z-axis direction for a distance of 2.00 metres is 1.00 mm, for 3.00 metres is 2.20 mm, and for 4.00 metres is 3.7 mm.

In industrial applications, small movements (0.1 mm to 5 mm) are common in operating machinery. Section 4.9 proves that the precision of measured deformations is better than the LSS expected precision, and could meet the industry's requirements for depth distances within 1.5 metres.

5.3.3 Local Scaling Approach

Local scaling is a simple approach used to illustrate surface deformation and does not require the development of sophisticated software (Rioux, 1993). The approach deals directly with raw data and requires less processing time for visual representations. The surface and point movements are defined as the difference between two depth-coded images for different scans in pixel dimensions. In industrial applications, usually, relative movements (deformations) are required rather than the absolute values. Hence, local scaling could be used to determine deformations and carry out surface re-mapping. However, it is important that this approach should provide an adequate precision.

The local scaling procedure is as follows:

1. The LSS should be approximately mounted such that it is perpendicular to the scene of interest and is at the same height. Also, the depth distance should be within 1.0 metre.

2. The depth value of the target center can be either the average of the four registered pixel values surrounding the center, or the registered pixel value of the pixel containing the centre.

3. These control points could be retro-reflective circular targets. The centre of each target is determined (using the intensity image) by fitting a rotated ellipse to the edge of the circular target. If required for future work, centre determination can be

improved by constraining the target area inside the ellipse edge by fitting a plane to the depth coded pixel values of that area.

4. The scale is introduced locally in the specific area of the scene. The differences between the depth registered values of points of interest (e.g. control points) are scaled according to the differences in their depth distances from the LSS or according to their Z-axis coordinates. The image coordinates **i** and **j** are scaled according to the differences between their horizontal and vertical distances or to their X- and Y-axes coordinates.

5. For precise scale determination, the X, Y, and Z coordinates of the points of interest can be measured, with respect to a reference system, using an electronic theodolite system or the LSS. The LSS provides updated coordinates values for different epochs, which can be used to determine the shaft's exterior orientation parameters with respect to the LSS coordinates system.

6. The control points also can be used to locally determine the pixel shifting for both axes, pixel-wise ($\mathbf{P'_X=P_{X1}-P_{X2}}$, $\mathbf{P'_Y=P_{Y1}-P_{Y2}}$), between two images. This will result in better estimation for surface movements when the images are subtracted.

7. These points will enable one to locally determine the orientation parameters to transform the image axes to the axes of interest (e.g. shaft axes) for monitoring point movements.

8. Another alternative to retro-reflective targets is the use of spherical targets for local scale determination. Using a proper threshold in the intensity image, and using centroid method, one can determine the centre of the sphere approximately. Fitting a sphere surface, using the depth coded image, results in determining the centre as well as the radius of the sphere to sub-pixel accuracy. The actual sphere dimensions can then be used to introduce the local scaling at that specific point in the scene. This might be more accurate in providing true localization at a specific area and/or point in the scene.

5.3.4 Lab Tests

Two tests were carried out at NRC labs. In both tests the scaling was introduced only by measuring a distance along the Z-axis direction between two points in the scene. The first one was carried out on a mechanical test rig and the second one on a motorized test rig, Al-Hanbali and Teskey (1994). The LSS used was the NRC system, not the one owned by the University of Calgary. MR. L. Cournoyer, NRC, helped us to acquire the required data for both tests.

A third test was carried out on a mechanical test rig at The University of Calgary lab using the University-owned LSS. The test was carried for workshop demonstration purposes and the precision results obtained are similar to the first test results, see Figure 5.1, 5.2 and 5.3 (Al-Hanbali and Laurent, 1995).

5.3.4.1 Mechanical Test Rig and Local Scaling Results

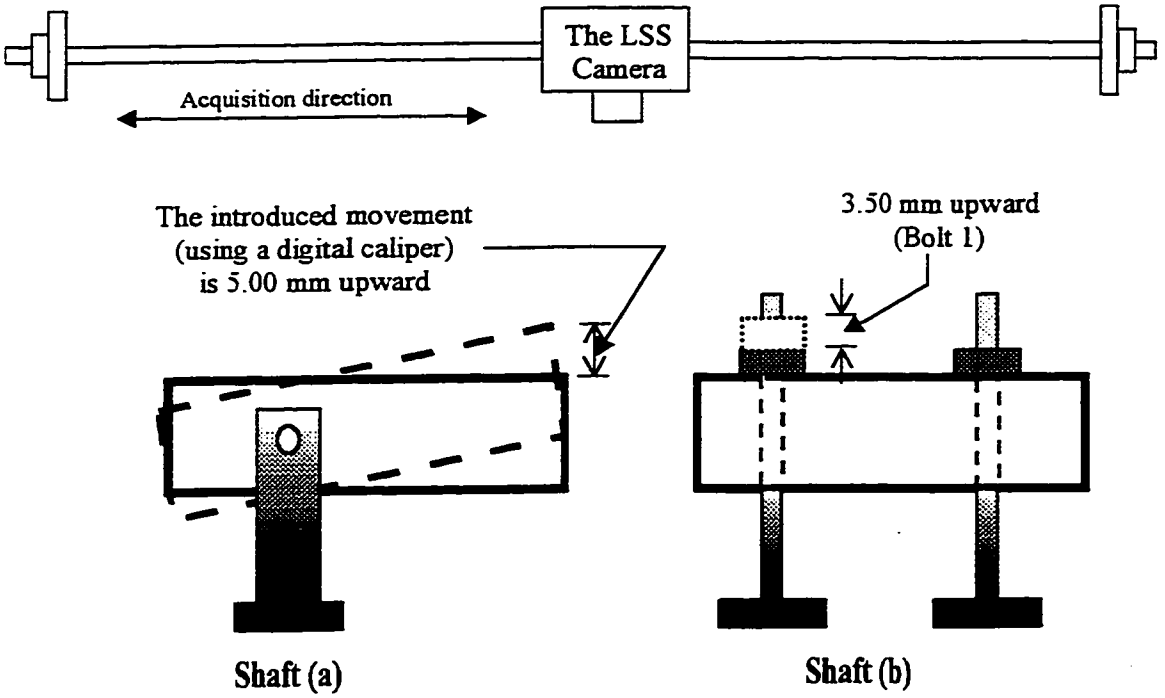

Figure 5.5: Mechanical test rig with introduced shaft movements (front view).

The test was carried out on a static alignment test rig. The test rig was set up so that small changes in coaxial alignment could be introduced between two, 4-inch diameter aluminum pipes. A single-axis laser scanner with a translation stage was used for this test. The test rig was 0.75 metres from the LSS. Figure 5.5 shows the introduced movements in the test rig along the Z-axis direction of the laser scanner. Shaft 'a' is rotated upward around its pivot, so that its end is shifted 5 mm upward. Bolt '1' is screwed upward, so that its movement is 3.50 mm.

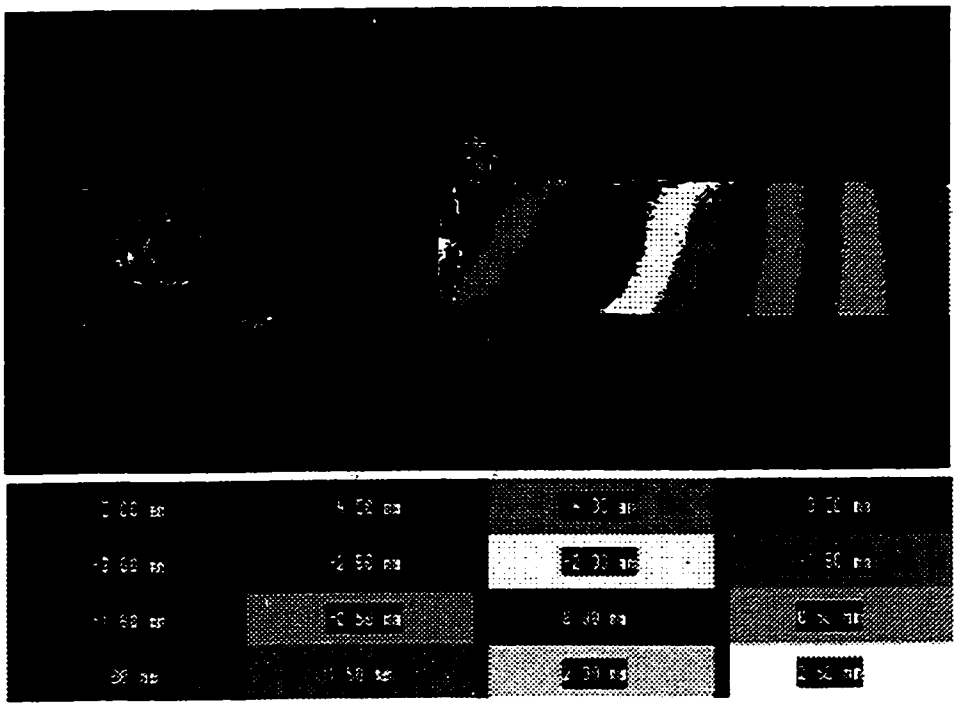

Figure 5.6a: Surface deformation of the mechanical test rig.

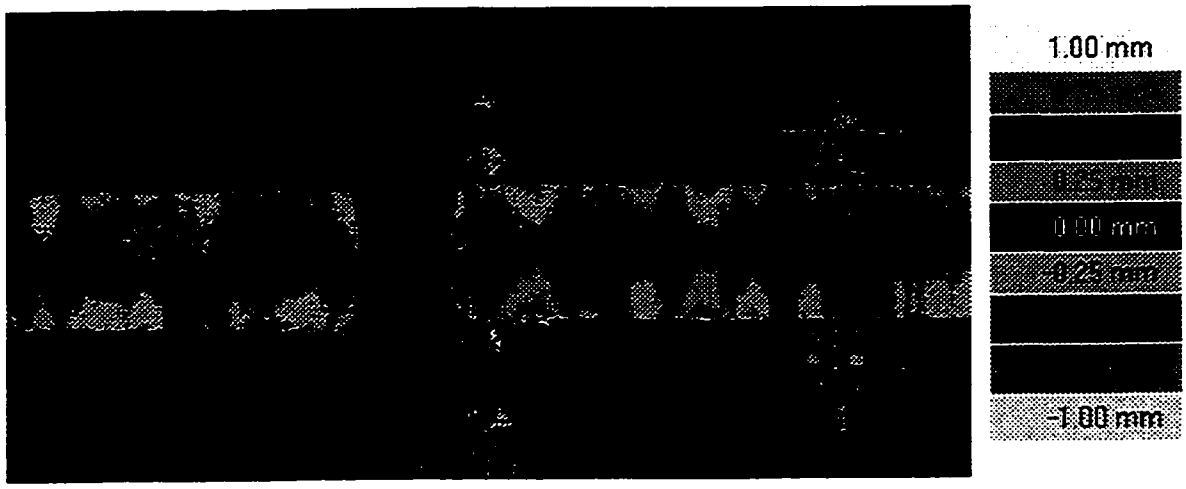

Figure 5.6b: Noise level on the surface of the mechanical test rig.

The surface movements are displayed in the form of a color-coded image, see Figure 5.6a, where each color represents a specific range of movements. Figure 5.6b shows the noise level of the LSS in the Z-axis direction which is about ±0.2 mm precision (see the edges of the shaft in the image).

5.3.4.2 Motorized Test Rig and Local Scaling Results

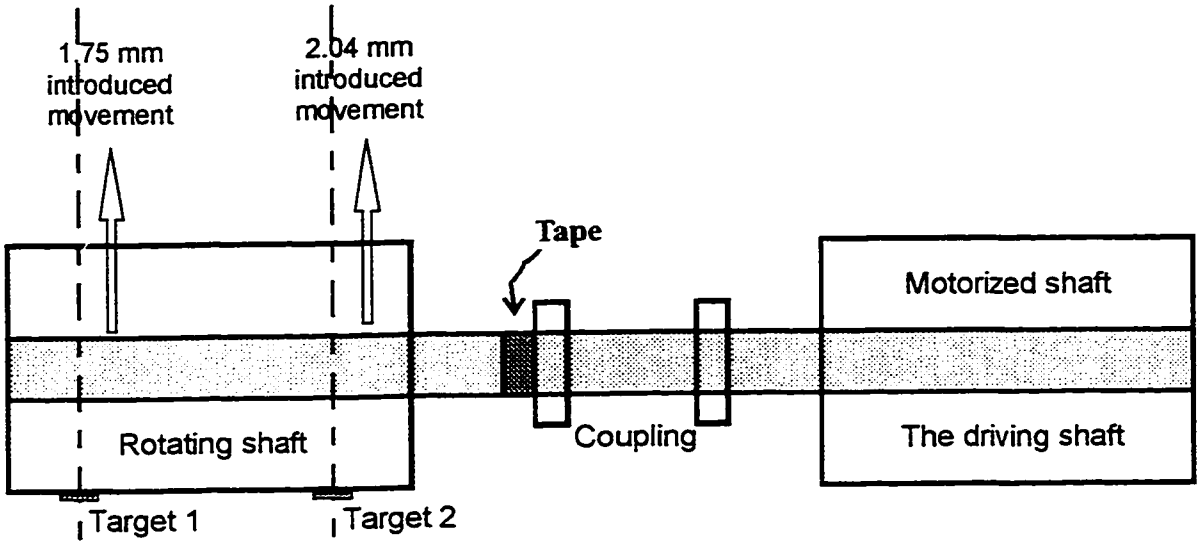

Figure 5.7: Motorized test-rig with introduced shaft movements (top view).

The test was carried out on a motorized alignment test rig. A single-axis laser scanner with a rotation stage was used for this test. The motorized rig was 1.75 metres from the LSS. Figure 5.7 shows the introduced movements in the Z-axis direction of the scanner. The rotating shaft, along with its box, is displaced 1.75 mm along target '1' axis and 2.04 mm along target '2' axis. These movements were introduced using a digital caliper with 0.01 mm resolution. Figure 6.8 shows the surface deformations caused due to the box movement. Notice the high noise level, which is directly related to the depth distance of

the motorized test rig from the LSS camera (i.e.1.75 metres). The precision for surface movement (i.e. the rotating shaft surface area) was about ±1 mm and for target movements (i.e. the target area on the rotating shaft) was about ±0.5 mm.

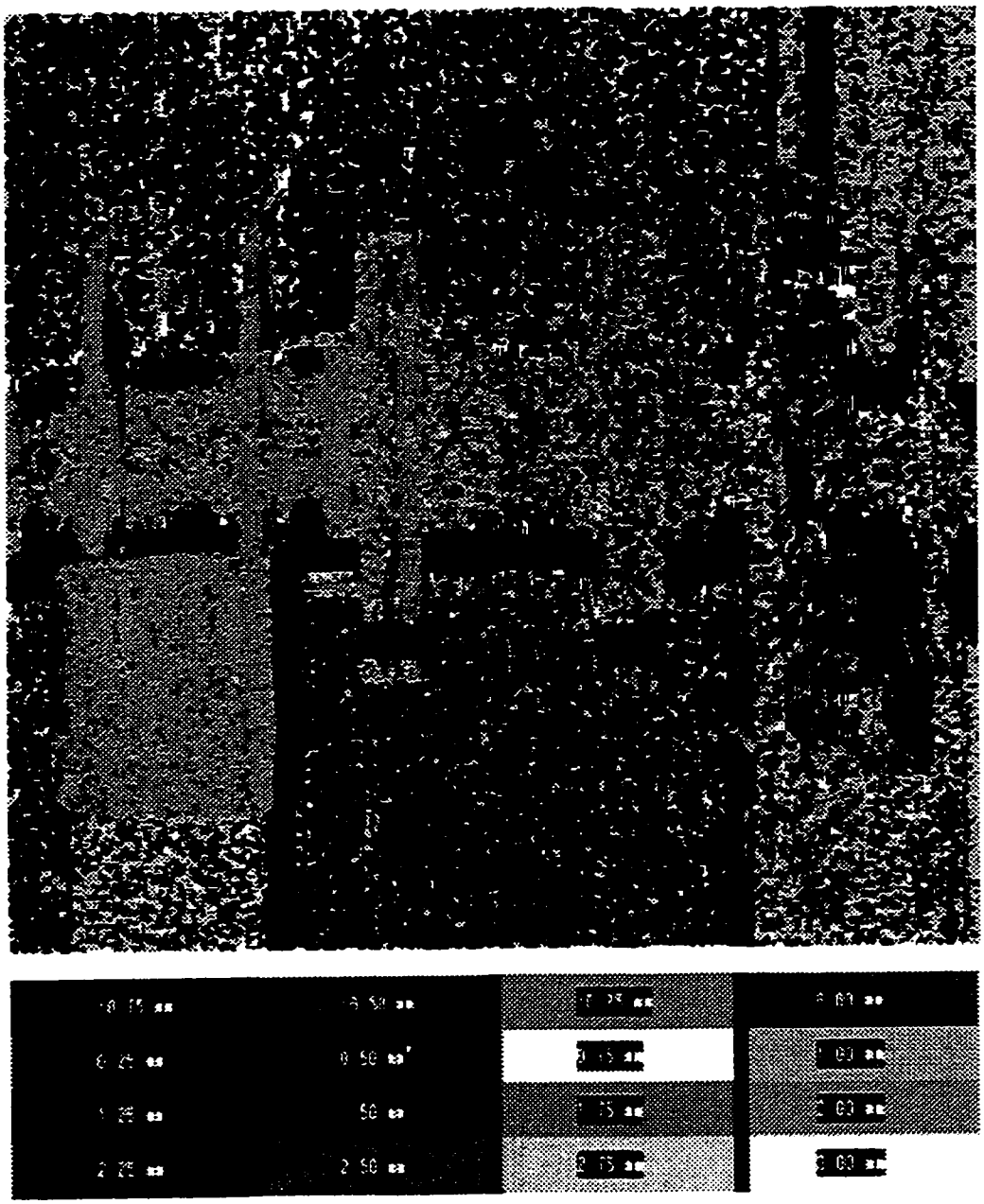

Figure 5.8: Surface deformation on the surface of the motorized test-rig.

5.3.4.3 Discussion of the Local Scaling Results

The color-coded images that illustrate surface deformations based on depth distances provide important and useful information to diagnose and pinpoint machinery surface movement trends. Table 5.1 summarizes the lab test results and the corresponding expected precision. The results show that the achieved instrument precision, using the local scaling approach, is approximately equal to the expected precision of the LSS derived from the mathematical model for calibration purposes. Thus, surface deformations can be reliably and precisely extracted by using the local scaling approach, although it is a simple procedure.

Test	Depth Distance (m)	Local Scaling Precision (mm)	LSS Expected Precision (mm)
Static test rig	0.75	0.2	0.15
Motorized test rig	1.75	1.0	0.85

Table 5.1: The precision results of the local scaling approach compared to the LSS expected precision.

5.3.5 On-Site Test: Sheerness Generating Station

5.3.5.1 Test Objective and Control Field

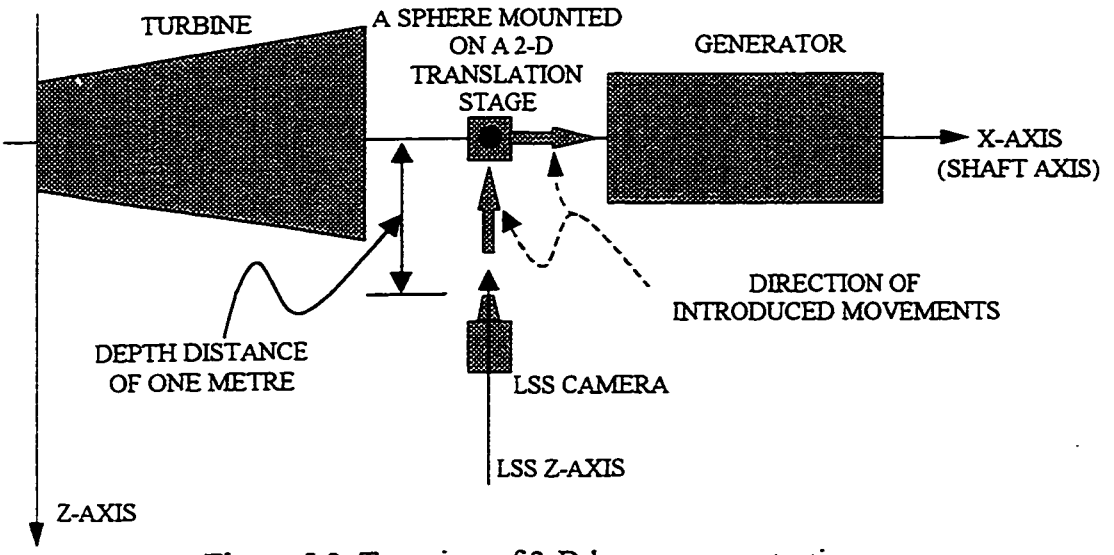

Figure 5.9: Top view of 3-D laser scanner testing.

Testing was carried out to determine the effect of on-site conditions (i.e. vibrations, high temperature, and refraction effects) on the precision of the LSS measurements using the local scaling approach. The testing was done at the Sheerness Generating Station. MR. L. Cournoyer, NRC, helped us to acquire the required data for the test. Figure 5.9 shows the LSS camera, the turbine-generator combination, and the 2-D translation stage where movements were introduced. The 2-D translation stage was mounted on the machinery coupling cover as shown in Figure 5.10a. . The LSS used was a dual-axis scanner with a rotation stage. The machines were running smoothly under steady-state operating conditions at a temperature of about 40° C.

The control field was composed of a sphere mounted on the 2-D translation stage as shown in Figure 5.10b. A stick-on target was affixed to the lower fixed base of the stage to provide a fixed reference point. The LSS camera was positioned such that its Z-axis was approximately perpendicular to the shaft axis and its height was at about the same height of the sphere. The depth distance from the LSS camera to the sphere is 1.00 metre.

(a) (b)

Figure 5.10: (a) The machinery coupling and the 2-D translation stage. (b) Three-D re-mapping of the sphere and the translation stage.

Figure 5.11a shows a depth-coded image of the machinery coupling cover. Figure 5.11b shows the profile of the flange of the cover with the approximate dimensions in millimetres, of the cross-section A-A shown in Figure 5.11a. To scale the flange dimensions, local scaling was applied to the specific area (in the scene) in the depth-coded image that is based on the tape-measured depth distance of the flange from the LSS camera. The measured width of the flange scales horizontally pixel's size.

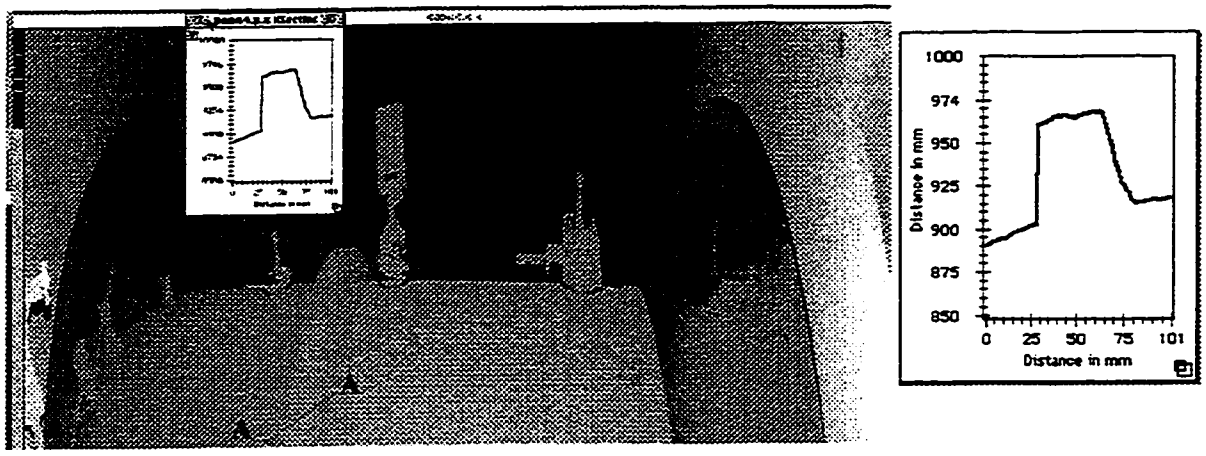

(a) (b)

Figure 5.11: (a) Depth coded image of the machinery coupling and the 2-D translation stage. (b) The flange's approximate dimensions in millimetres.

5.3.5.2 Introduced Movements and Local Scaling

To simulate shaft deformations on the sphere surface, the translation stage is used to displace the sphere along the Z-axis and the X-axis (shaft axis), as shown in Figure 5.9. First, the following movements are introduced along the Z axis: 0.5 mm, 0.75 mm, 1.0 mm, 1.5 mm, 2.0 mm, 2.5 mm, 3.0 mm, 4.0 mm, and 5.0 mm. Then, movements are similarly introduced along the X-axis (i.e. 0.5 mm, 0.75 mm, 1.0 mm, 1.5 mm, 2.0 mm, 2.5 mm, 3.0 mm, 4.0 mm, and 5.0 mm), maintaining the shifted position of the sphere along the Z-axis (the shift is 5.0 mm from initial position). Finally, the sphere is positioned at its initial position (i.e. no movement along the Z-axis and the X-axis). The sphere and the translation stage are scanned twice at their initial position, and then scanned after each introduced gradual movement.

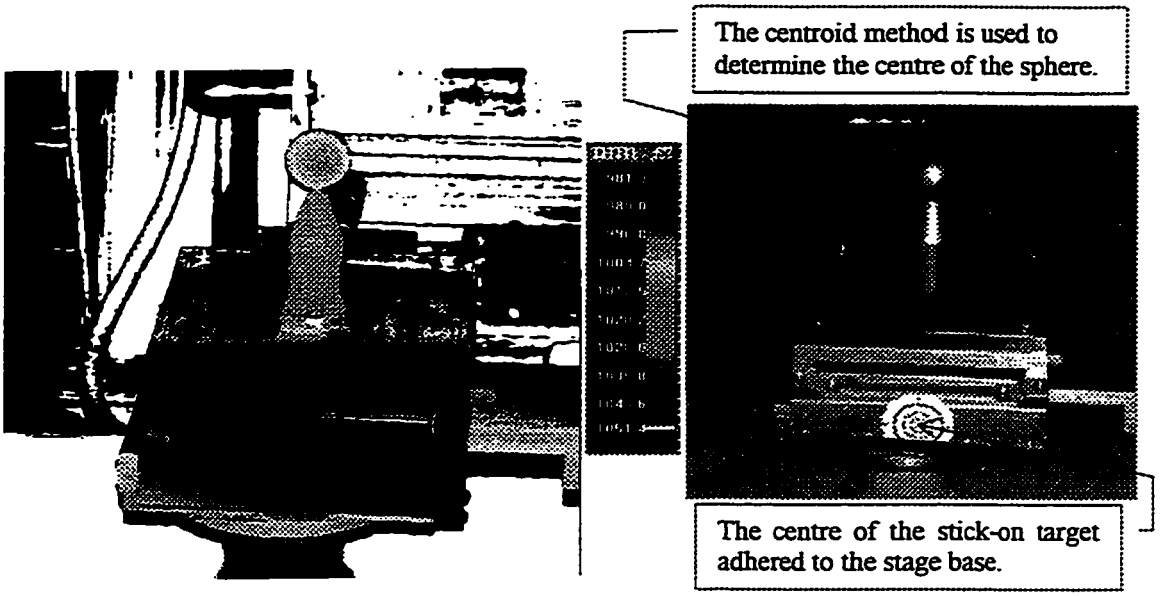

Figure 5.12: (a) Depth coded image of the sphere and the 2-D translation stage. (b) Intensity image of the sphere and the 2-D translation stage.

Figure 5.12a shows a depth-coded image of the sphere and the translation stage, and the color palette used to display the image. The color palette bar illustrates the depth values, scaled in millimetres, for the shown color ranges. Figure 5.12b shows the intensity image. Note that the scale is locally introduced into the area of interest (i.e. the sphere and the translation stage) based on the measured depth distance between the sphere and the LSS camera using a tape. (e.g. The closest registered depth value between sphere surface and the LSS camera is 18709 scaled over the 1000.0 mm depth distance, which results in an introduced local scale of **1 to 18.7**). The depth-coded image is used to provide information related to the depth distance, which corresponds to the Z-axis.

The intensity image is used to define the centre of the sphere using the centroid method, and is also used to define the centre of the circular stick-on target affixed to the lower

base of the 2-D translation stage. The lower base of the stage moves the sphere horizontally along the X-axis, see Figure 5.12b. The intensity image is also used to scale the pixel dimension along the horizontal and vertical axes, which correspond to the X-axis and the Y-axis, respectively. The horizontal and the vertical scales are determined by scaling the diameter of the sphere (25.4 mm) over the number of pixels that constitute the diameter of the sphere in the image along the horizontal and vertical axes. (e.g. The horizontal pixel dimension is 25.4 mm/59 pixels = 0.4305 mm, the vertical pixel dimension is 25.4 mm/64 pixels = 0.3969 mm.)

The centre of the sphere and the centre of the stick-on target are used to determine the pixel shifts along the X and Y axes between images of two epochs. Surface deformation is determined by subtracting the registered values of the two images, taking into consideration the pixel shifts. The resultant image represents the surface deformation between the two epochs. The deformation at an area is measured by taking the mean and the standard deviation of all of the pixel's registered values in the selected area of interest, see for example areas I and II in Figure 5.13. These values are then scaled to provide the local surface deformation of the area.

Figure 5.13 illustrates the noise level, color-coded, between two images of the same epoch. The color palette also shows the color-coded scaled deformations in millimetres. The mean and the standard deviation values of area I are –0.92 and ±3.7, and the scaled values are -0.05 mm and ±0.2 mm, respectively. The mean and the standard deviation

values of area II are -0.82 and ±3.5, and the scaled values are –0.044 mm and ±0.19 mm, respectively.

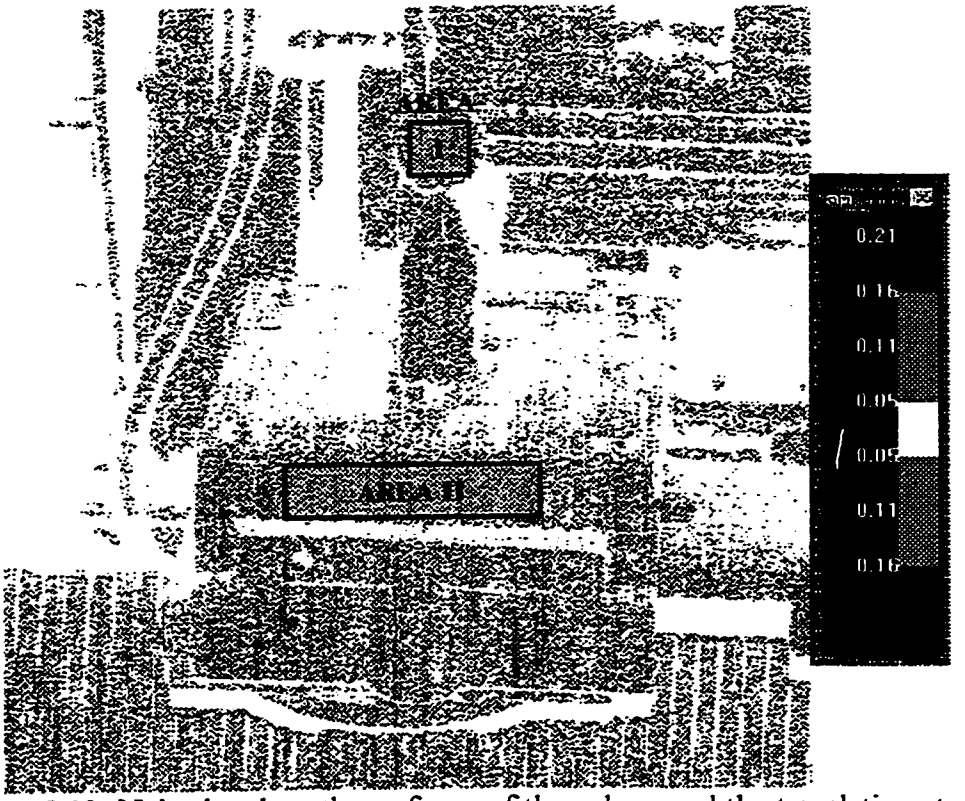

Figure 5.13: Noise level on the surfaces of the sphere and the translation stage.

The determined precision of the noise level of the LSS for on-site conditions is ±0.2 mm for a depth distance of 1.00 metre. Thus, the determined precision is approximately equivalent to the expected LSS precision (i.e. ±0.2), which is derived from the mathematical model and based on lab testing environment. This indicates that the LSS can deliver reliable measurements for on-site conditions (e.g. vibration effects and high temperature effects of about 40° C).

5.3.5.3 Local Scaling Results

Table 5.2 shows the introduced movement and the difference in image coordinates of the centre of the sphere for each epoch. The centre is extracted using the centroid method. The image coordinate differences are determined by subtracting the centre coordinates of the sphere of each epoch from the sphere's initial position. These values correspond to the actual pixel shift along the horizontal and the vertical axes of the image. The integer values shown in the table are the pixel shifts used for image subtraction to determine the surface deformations in each epoch.

Epoch	Introduced Movement		Image coordinate difference of the centre of the sphere relative to the initial position					
			Horizontal axis			Vertical axis		
	Z mm	X mm	Pixel shift		mm	Pixel shift		mm
			Actual	Integer		Actual	Integer	
E1	0.0	0.0	0.1	0	0.043	0.1	0	0.040
E2	0.5	0.0	-0.01	0	-0.004	-0.39	0	-0.155
E3	0.75	0.0	-0.61	0	-0.263	-0.81	1	-0.321
E4	1.0	0.0	-0.79	-1	-0.340	-0.33	1	-0.131
E5	1.5	0.0	-1.2	-1	-0.517	-1.17	-1	-0.464
E6	2.0	0.0	-0.8	-1	-0.344	-1.8	-2	-0.714
E7	2.5	0.0	-1.11	-1	-0.478	-1.77	-2	-0.703
E8	3.0	0.0	-1.27	-1	-0.547	-2.23	-2	-0.885
E9	4.0	0.0	-1.19	-1	-0.512	-3.15	-3	-1.250
E10	5.0	0.0	-0.93	-1	-0.400	-3.96	-4	-1.572
E11	5.0	0.5	-0.12	0	-0.052	-4.27	-4	-1.695
E12	5.0	0.75	0.15	0	0.065	-3.51	-4	-1.393
E13	5.0	1.0	1.19	1	0.512	-3.58	-4	-1.421
E14	5.0	1.5	2.48	2	1.068	-3.77	-4	-1.496
E15	5.0	2.0	3.59	4	1.545	-3.97	-4	-1.576
E16	5.0	2.5	4.12	4	1.774	-4.25	-4	-1.687
E17	5.0	3.0	5.97	6	2.570	-4.53	-4	-1.798
E18	5.0	4.0	8.48	8	3.651	-3.83	-4	-1.520
E19	5.0	5.0	10.38	10	4.469	-3.84	-4	-1.524
E20	0.0	0.0	0.55	0	0.237	-0.45	0	-0.179

Table 5.2: The introduced movement and the image coordinates difference of the sphere centre for each epoch, relative to the sphere's initial position.

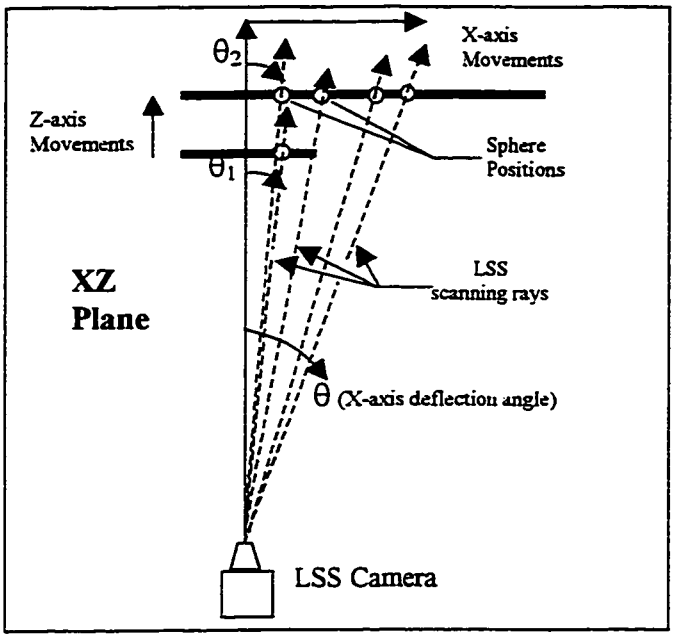

Figure 5.14a: Introduced movements and the scanning mechanism along the XZ plane.

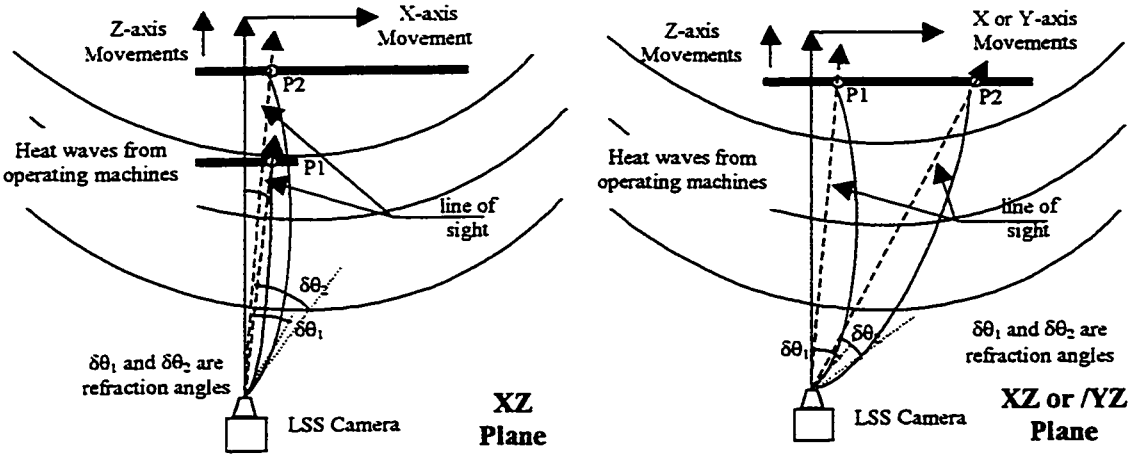

Figure 5.14: (b) Refraction effects due to introduced movements along the depth axis (c) Refraction effects due to introduced movements along the horizontal or the vertical axes.

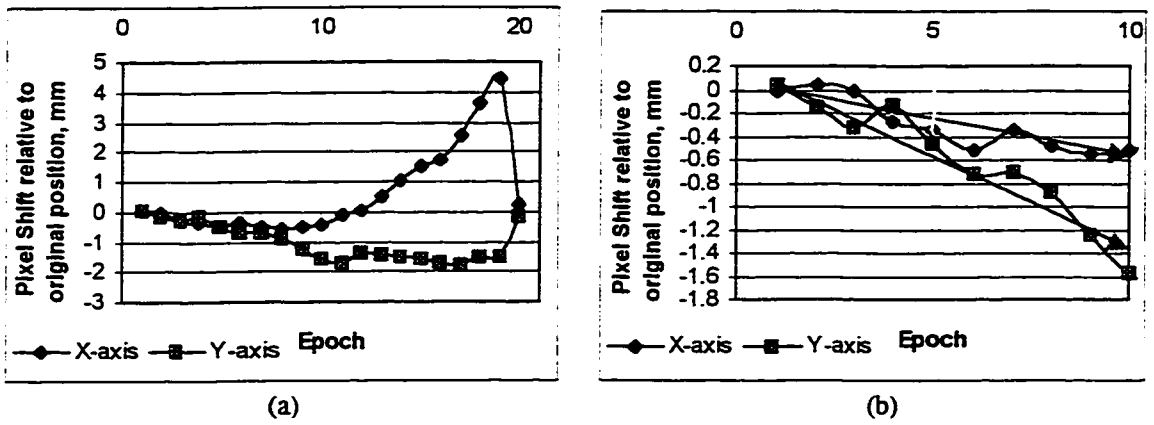

Figure 5.15: (a) Scaled pixel shifts for all epochs. (b) Scaled pixel shifts for the epochs that correspond to the introduced depth movements.

The pixel shifts scaled in millimetres shown in Figure 5.15 are caused by the introduced movements of the sphere along the horizontal and the vertical axes of the image. Note that because the centre of the sphere is not at the centre of the LSS image, the introduced depth movements cause small pixel shifts in the position of the sphere centre between epochs along the horizontal and the vertical axes. These shifts correspond to different scanning angles along the X- and Y-axes for each introduced depth movement, see for example the X-axis scanning angles θ_1 and θ_2 in Figure 5.14. The value of the pixel shift increases as the introduced depth distance increases, and also increases when the point of interest is further away from the centre of the image. Thus, the shift along the vertical axis of the centre of the sphere is larger than the shift along the horizontal axis, since the sphere is further away vertically than horizontally from the centre of the image. For example, the vertical and the horizontal pixel shifts for a 5.0 mm introduced depth distance are 0.32 mm and 0.05 mm, respectively).

However, the measurement values shown in Table 5.2 and Figure 5.15b are much larger than the expected shifts which means the presence of error sources. The source that is believed to cause these errors is the refraction effect due to the horizontal and the vertical temperature gradients between the LSS and the sphere.

Figure 5.14b shows the refraction effect due to an introduced depth distance between points P1 and P2. Similarly, Figure 5.14c shows the refraction effect due to an introduced horizontal or vertical distance between points P1 and P2. Figure 5.14b illustrates that the refraction angle (i.e. angles $\delta\theta_1$ and $\delta\theta_2$) increases the with increase of measured depth distances. These angles should introduce errors in the horizontal and the vertical measurements. However, if the introduced movement is along the horizontal or the vertical, see Figure 5.14c, the refraction angles (i.e. angles $\delta\theta_1$ and $\delta\theta_2$) should almost be the same when this introduced movement is very small. Hence, the relative movement between these two points should eliminate the refraction effect.

Figure 5.15b shows that the pixel shift relative measurements along the vertical axis increases with the increase of the introduced depth measurements (i.e. epoch E1 to epoch E10). However, these measurements become almost constant when there are no introduced depth movements (see the Y-axis pixel-shift relative measurements in Figure 5.15a for epochs E10 to E19). This is more obvious when epoch E10 is used instead of Epoch E1 as a reference epoch for relative measurements, see Figure 5.16.

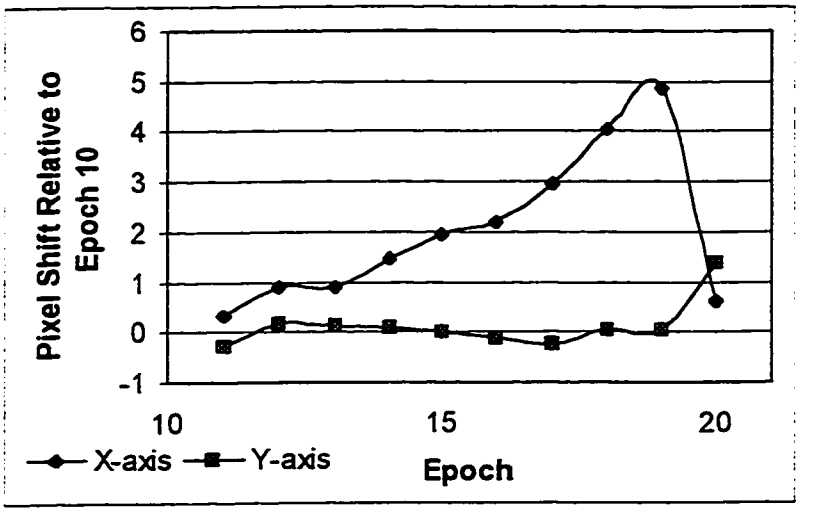

Figure 5.16: Scaled pixel shifts for the epochs that correspond to the introduced movements along the X-axis relative to the epoch E10.

Epoch	Introduced Movement		Coordinate difference of the centre of the sphere relative to epoch E10 position					
			X-axis coordinates			Y-axis coordinates		
	Z mm	X mm	Pixel shift		mm	Pixel shift		mm
			Actual	Integer		Actual	Integer	
E11	5.0	0.5	0.81	1	0.349	-0.68	0	-0.270
E12	5.0	0.75	2.08	2	0.895	0.45	0	0.179
E13	5.0	1.0	2.12	2	0.913	0.38	0	0.151
E14	5.0	1.5	3.41	3	1.468	0.19	0	0.075
E15	5.0	2.0	4.52	5	1.946	0.0	0	0.000
E16	5.0	2.5	5.11	5	2.200	-0.29	0	-0.115
E17	5.0	3.0	6.90	7	2.970	-0.57	0	-0.226
E18	5.0	4.0	9.41	9	4.051	0.13	0	0.052
E19	5.0	5.0	11.31	11	4.869	0.12	0	0.048
E20	0.0	0.0	1.48	1	0.637	3.51	4	1.393

Table 5.3: The introduced movement and the image coordinates difference of the sphere centre for each epoch relative to epoch E12.

Table 5.3 shows that the measured pixel shifts along the vertical axis (Y-axis) relative to epoch E10 (i.e. epochs E11 to E19) are almost negligible. Also, the precision is within the expected precision of the LSS, which is ±0.2 mm. Similarly, the horizontal measured

pixel shifts (X-axis) are also comparable to the actual introduced movements along the X-axis and that the precision is within the expected precision of the LSS. This shows that the errors do not increase with time but are associate with the type of introduced movement which is affiliated with refraction effects.

Note that in epoch E20, the sphere is moved back to its original position and therefore, refraction effects are not negligible relative to epoch E10 (Table 5.3), however, are considered negligible relative to the original position (Table 5.2).

Epoch	Introduced Movement		Measured Z-axis surface deformation							
			Area I				Area II			
	Z mm	X mm	Average		σ		Average		σ	
			Reg.	mm	Reg.	mm	Reg.	mm	Reg.	mm
E1	0.0	0.0	-0.96	-0.05	3.5	0.19	-0.82	-0.04	3.5	0.19
E2	0.5	0.0	8.3	0.44	3.6	0.19	8.8	0.47	3.6	0.19
E3	0.75	0.0	14.92	0.80	3.3	0.18	15.62	0.84	3.5	0.19
E4	1.0	0.0	19.43	1.04	3.5	0.19	19.19	1.03	3.5	0.19
E5	1.5	0.0	29.65	1.59	4.5	0.24	28.37	1.52	4.5	0.24
E6	2.0	0.0	36.87	1.97	4.2	0.22	37.23	1.99	4.0	0.21
E7	2.5	0.0	45.21	2.42	4.4	0.24	44.42	2.38	4.5	0.24
E8	3.0	0.0	52.31	2.80	4.6	0.25	52.7	2.82	4.6	0.25
E9	4.0	0.0	69.0	3.69	6.0	0.32	68.5	3.66	4.2	0.22
E10	5.0	0.0	82.92	4.43	7.0	0.37	85.05	4.55	6.5	0.35
E11	5.0	0.5	82.44	4.41	7.1	0.38	85.26	4.56	5.5	0.29
E12	5.0	0.75	80.87	4.32	8.0	0.43	85.9	4.59	6.9	0.37
E13	5.0	1.0	81.62	4.34	6.8	0.36	85.21	4.56	6.1	0.33
E14	5.0	1.5	81.16	4.34	8.5	0.45	85.0	4.55	5.5	0.29
E15	5.0	2.0	81.13	4.29	8.7	0.47	84.58	4.52	5.8	0.31
E16	5.0	2.5	80.19	4.28	8.5	0.45	84.26	4.51	6.5	0.35
E17	5.0	3.0	80.02	4.15	8.5	0.45	83.6	4.47	6.0	0.32
E18	5.0	4.0	77.55	4.15	8.0	0.43	82.27	4.40	6.1	0.33
E19	5.0	5.0	77.6	4.15	8.5	0.45	81.7	4.37	6.5	0.35
E20	0.0	0.0	10.0	0.53	3.5	0.19	9.89	0.53	3.5	0.19

Table 5.4: Precision and depth distance measurement results using the local scaling approach.

Table 5.4 shows the measured depth distances and precision, for each epoch, for area I and area II shown in Figure 5.13. Figure 5.17 illustrates that measured depth distances are comparable to the actual introduced Z-axis movements within the precision range of the LSS. However, once the X-axis movements are introduced, the errors in the measured depth distances increase and the measured precision decrease with the increase of these introduced X-axis movements. In Figure 5.18, the difference in the color distribution between case (x) and case (xi) also illustrates this observation.

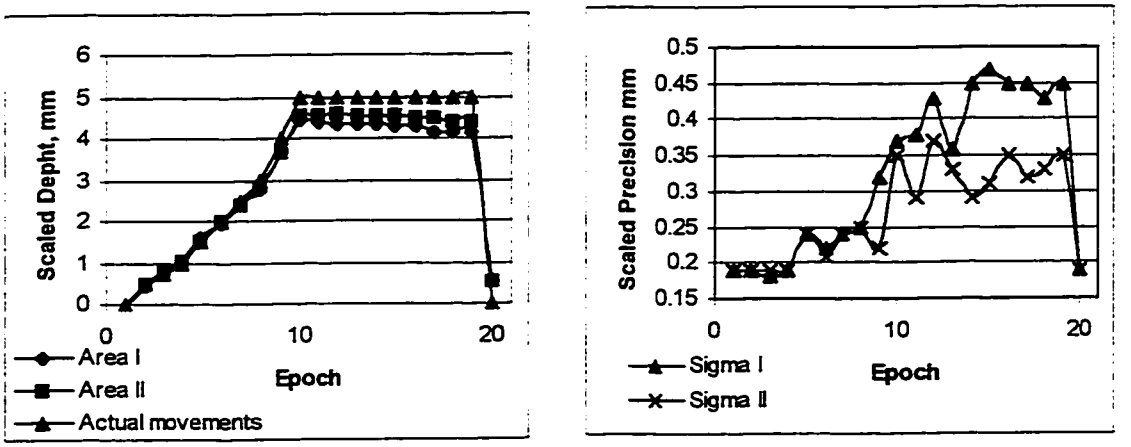

(a) Scaled depth distances (b) Scaled precision

Figure 5.17: Scaled measured depth distances and their corresponding precision compared to the actual introduced movements.

Figure 5.18 illustrates the measured surface deformation color-coded for various epochs relative either to the initial position (E1) or to epoch E10. The color palette shows the

measured depth movements scaled in millimetres. Case (xiii) illustrates the refraction effects. Case (vii) shows that refraction effects can be minimized or removed if the suitable reference image is used to measure relative movements. The figure also illustrates that the use of a plane surface as a reference object or control point provides better precision, and thus more uniform color representations, than using a spherical surface.

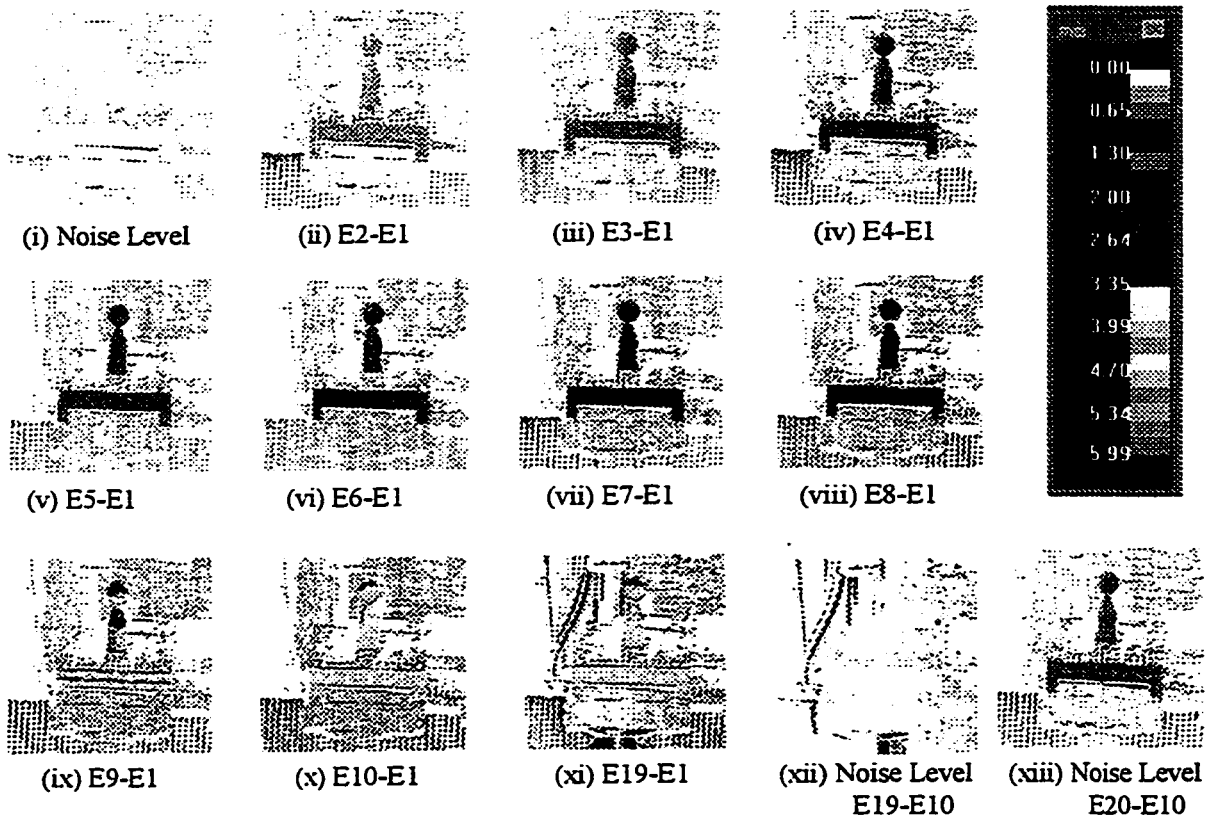

Figure 5.18: Surface deformation for various epochs relative either to the initial position (E1) or to epoch E10. The color palette shows the measured depth movements, color-coded, scaled in millimetres.

5.3.5.4 Discussion of the Local Scaling Results

The results show that by using the local scaling approach the achieved instrument precision ranges from 0.20 for small depth movements (up to 2.0 mm) to 0.35 mm for large depth movements, see Table 5.4 and Figure 5.17b. The results also show that the precision decreases when movements are introduced along the other axes. The expected precision of the LSS derived from the mathematical model for calibration purposes is about 0.18 mm. Thus, the use of the local scaling approach to extract surface deformations provides reliable precision if the measured movements are small.

The test shows that refraction effects can be a real problem if refraction is not diagnosed and removed. The on-site test proves that the LSS can operate and provide reliable measurements under high temperatures (about 40°C) and vibration effects. Also, the LSS precision determined using local scaling approach is not enough for industrial deformation application (i.e. 0.1 mm). However, local scaling provides non-contact surface deformation measurements, and is a simple and a quick approach. The approach can be used to show deformation trends on a surface of a machine or an object.

CHAPTER SIX

SUMMARY, CONCLUSIONS AND RECOMMENDATIONS

6.1 Summary and Conclusions

The following characteristics summarize the usefulness of the LSS for dynamic deformation measurements:

It is fast in comparison to other survey methods and can therefore be used to measure short-term deformations. For example, the LSS can measure short-term deformations such as movements caused by changes in temperature or operating forces in machinery.

It is flexible in defining the size of the image and volume required to be scanned.

It only requires a single station setup.

It is a non-contact measurement instrument.

It is relatively insensitive to site conditions (e.g. light, incidence angle, shadow effects).

It can monitor deformation of the surface of an object as well as point or target movements.

The following software programs for the LSS deformation measurements were developed at The University of Calgary:

1. Image acquisition software.
2. Image display, processing, filtering and digitization software.
3. Precise edge detection and target location software.
4. Local scaling and surface deformation software.

5. Calibration software using the least squares adjustment method.

The following summarizes the assumptions applied to the LSS:

6. The Sheimpflug condition is satisfied for all deflection angles to maintain the optimal focusing criteria.

7. The auto-synchronization mechanism is achieved by neglecting the effects of the rotating mirror's thickness, the laser source tilt angle, and any mirror mounting imperfections.

8. The lens model is replaced by a pin-hole model to simplify the derivation of the mathematical model.

9. The various effects of the galvanometers are ignored.

The modified NRC distortion model (NRC sheets, 1995) used in this thesis is a third order polynomial function. The model absorbs the distortion effects in the depth values p, the X-axis rotational angle θ and the Y-axis rotational angle ϕ. The model is based on the following effects: Sheimpflug condition, auto-synchronization and the laser-source tilt angle effect, auto-synchronization and the rotating mirror thickness effect, the lens model and radial lens distortion, and the compensation of the step angle along the Y-axis rotation mirror.

The collinearity equations, the modified distortion model and the theoretical and analysis aspects of the LSS calibration have been described in detail. The methodology and analysis for deformation measurement evaluation have also been presented. The in-lab as well as on-site test findings are summarized as follows:

1. Repeatability tests, for a circular retro-reflective target, indicate that the following standard deviation values of the observations are reasonable: ±3 for the registered value p, and ±0.08 pixel for the image coordinates i and j.

2. The local scaling approach: deformation measurement precision ranges from 0.20 mm for small depth movements (up to 2.0 mm) to 0.35 mm for large depth movements. See Table 5.4 and Figure 5.17b. The results also show that the precision decreases when movements are introduced along the other axes. Thus, the use of the local scaling approach to extract surface deformations provides reliable precision if the measured movements are small.

3. The on-site testing shows that refraction effects can be a real problem if refraction is not diagnosed and removed. The testing also proves that the LSS can operate and provide reliable measurements under high temperature (about 40°C) and vibration effects.

4. The results show that the achieved instrument precision, using the local scaling approach, is approximately equal to the expected precision of the LSS derived from the mathematical model for calibration purposes. Thus, surface deformations can be reliably and precisely extracted using the local scaling approach, which is a simple and a quick procedure.

5. The LSS calibration: the absolute and relative measurements have mean and median error values that are nearly the same. The mean errors for measurements at depth distances that are less than 1.25 metres are almost zero. See Tables 4.8 and 4.9. Also, the X-axis and the Y-axis measurements have better mean errors and RMS values than the Z-axes.

6. The absolute and relative measurement results show that the LSS has better RMS values and mean errors for the calibrated depth distances (between 0.6 metres and 1.25 metres). This shows the reliability of the calibration. Also, the relative

measurements are more accurate than the absolute measurements. This is important since relative measurements are normally used.

7. The LSS calibration: the mean and the RMS of deformation measurement errors for a depth distance of 1.2 metres are: 0.05 mm and ±0.069 mm, -0.027 mm and ±0.071 mm, and 0.04 mm and ±0.039 mm along the X-axis, Y-axis and Z-axis respectively. Also, the mean and the RMS of deformation measurement errors for depth distance of 1.5 metres are 0.043 mm and ±0.114 mm, 0.033 mm and ±0.163 mm, and 0.174 mm and ±0.186 mm, along the X-axis, Y-axis and Z-axis respectively.

8. The achieved accuracy using the calibrated parameters is better than the LSS expected precision for these depth distances.

9. The large difference in accuracy between the calibrated parameters and the nominal parameters solutions validates that the calibration procedure followed in this thesis can provide successful results.

10. The deformation measurement results prove that the calibrated parameters provide reliable and precise measurements. Furthermore, this demonstrates that the LSS deformation measurement precision can be satisfactorily implemented in industrial applications (i.e. 0.1 mm precision), thereby achieving the major objective of the DAP research.

6.2 Recommendations

As is the case with most research work, there is generally a wide latitude for further development and investigation. This holds true in the case of the LSS study to improve the precision of the LSS measurements and the estimation of the LSS calibrated parameters.

One research direction is to improve, via mathematical functions, the mapping or the fitting of the LSS distortions. For example, the implementation of higher degree polynomials would be an interesting investigation into improving the distortion model.

Another interesting investigation is to find suitable geometrical relations between the LSS calibrated parameters and the controlled data field that can resolve correlation's problems and minimize the use of weight constraints (e.g. see Section 4.5.7).

The derivation of the mathematical model could be modified to take into consideration any non-orthogonality problems that might occur due to mounting imperfections of the X-axis rotating mirror with respect to the Y-axis rotating mirror, and also with respect to the two fixed mirrors. This can be done by assuming small tilt angles between the mirror's axes of interest and introduce their effects in the derived collinearity equations. This has been under the investigation of the NRC.

The LSS software development could be extended. For example, some acquisition strategies are not yet implemented in the LSS interface software such as a Lissajous acquisition mode or a raster acquisition mode using the X-axis galvanometer of the LSS and a translation stage or a rotation stage. Also, the calibration program would be much faster if developed using the C++ language instead of the MathCAD software. (The MathCAD software is used because of its capabilities in visual mathematical derivations which makes it easier to handle the complexity of the LSS mathematical model and its derived design matrices. The software, also, has the capability to perform programming tasks.) Furthermore, there is an opportunity available to modify and add more functionality to the image display, processing and digitization software that can be used for both LSS images and CCD stereo system images.

REFERENCES

Al-Hanbali, N. N. (1993) "Three-Dimensional Rotation Measurements for Industrial Alignment," M. Sc. Thesis, 93 pp., Department of Geomatics Engineering, The University of Calgary, Calgary, 1993.

Al-Hanbali, N. N., and Teskey, W. F. (1993). "Low-Cost Three-Dimensional Rotation Measurements for Industrial Alignment," Proceedings of the Seventh International FIG Symposium on Deformation Measurements, Canadian Institute of Geomatics, Ottawa, pp. 193-204.

Al-Hanbali, N. N. (1993a). "Demonstration: Laser Scanning System," The First Workshop of the Dynamic Alignment Project, Dept. of Geomatics Eng., The University of Calgary, Calgary, Alberta, November 5, 3pp.

Al-Hanbali, N. N., and Teskey, W. F. (1994). "Three-Dimensional Dynamic Deformation Monitoring using a Laser Scanning System," SPIE Conference, Videometrics III, Boston, Massachusetts, November 2-4, Vol. 2350, pp. 83-92.

Al-Hanbali, N. N. (1994). "Demonstration: Laser Scanning System," The Second Workshop of the Dynamic Alignment Project, Dept. of Geomatics Eng., The University of Calgary, Calgary, Alberta, November 18, 3pp.

Al-Hanbali, N. N. and N. St. Laurent (1995). "Demonstration: Laser Scanning System," The Third Workshop of the Dynamic Alignment Project, Dept. of Geomatics Eng., The University of Calgary, Calgary, Alberta, November 18, 3pp.

Baribeau, R., Rioux. (1991a). " Influence of Speckle on Laser Range Finders," Applied Optics Vol. 30, No. 20, July, pp. 2873-2878.

Baribeau, R., Rioux. (1991b). " Centroid Fluctuency of Speckled Targets," Applied Optics Vol. 30, No. 26, Sept., pp. 3752-3755.

Bayly, D. A., (1993) "Precise Measurement of short Distances with a Theodolite Mounted Substance Bar," Proceedings of the Seventh International FIG Symposium on Deformation Measurements, Canadian Institute of Geomatics, Ottawa, pp. 217-225.

Beraldin, J.-A., Baribeau, R., Rioux, M., Blais, F. and Godin, G. (1992). "Model-Based Calibration of a Range Camera," Proceedings of the Eleventh IAPR International Conference on Pattern Recognition, The Hague, The Netherlands, August 30-September 3, pp. 167-193.

Beraldin, J.-A., El-Hakim, S. F. and Cournoyor, L. (1993). "Practical Range Camera Calibration," SPIE Conference, Videometrics II, Boston, Massachusetts, September 9-10, Vol. 2067, pp. 21-31.

Beraldin, J.-A., Rioux, M., Blais, F., Godin, G. and Baribeau, R. (1994). "Calibration of an Auto-synchronized Range Camera with Oblique Planes and Collinearity Equation Fitting," NRC Report, ERB-1041, National Research Council of Canada, Institute for Information Technology, Ottawa, Ontario, November, 25pp.

Besl, Paul J. (1988). "Active, Optical Range Imaging Sensors," Machine Vision Applications, Vol. 1, No. 2, pp. 127-152.

Blais, F. and Rioux, M.. (1986). "Real-Time Numerical Peak Detector," Signal Processing, September, Vol. 11, No. 2, pp. 145-155.

Blais, F., Rioux, M. and Beraldin, J.-A. (1988). "Practical Consideration for a Design of a High Precision 3-D Laser Scanner System," SPIE Proceedings, Dearborn, Michigan, June 28-29, Vol. 959, pp. 225-246.

Blais, B., Rioux, M. and Maclean, S. G. (1991). "Intelligent, Variable Resolution Laser Scanner for the Space Vision System," Proceedings of the International Society for Optical Engineering (SPIE), Orlando, Florida, April 3-5, Vol. 1482, pp. 473-479.

Blais, F., Beraldin, J.-A., Cournoyor, L., Domey, J. and M. Rioux, (1992). "Three-Dimensional Pavement Inspection Using a Laser Range Sensor," TAC Annual Conference, Quebec City, Quebec, 10pp.

Blais, F., Beraldin, J.-A., Rioux, M., Couvillon, R. A. and Maclean, S. G. (1993). "Development of a Real-Time Tracking Laser Range Scanner for Space Applications," Workshop on Computer Vision for Space Applications, Antibes, France, September 22-24, pp. 161-171.

Boulanger, P., Godin, G. and Rioux, M. (1992). "Application of 3-D Active Vision to Rapid Prototyping and Reverse Engineering", Proceedings of the Third International Conference on Rapid Prototyping, Datyon, OH, June7-10, pp.213-223, NRC 33229.

Boulanger, P. (1993). "Reverse Engineering of Complex Surfaces Based on a new Hierarchical Segmentation Method," SPIE Conference, Videometrics II, Boston, Massachusetts, September 9-10, Vol. 2067, pp. 186-197.

CISM. (1987). Papers for the CISM Adjustment and Analysis Seminars, 2nd Edition, January, edited by E. J. Krakiwsky.

Cosandier D., Chapman M. A. (1992). "High Precision Target Location for Industrial Metrology," Proceedings of SPIE Conference, Videometrics, Boston, Massachusetts, November 15-16, Vol. 1820, pp. 111-122.

El-Hakim, S. F. and Beraldin, J.-A., (1994). "On the Integration of Range and Intensity Data to improve Vision-Based Three-Dimensional Measurements," Proceedings of SPIE Conference, Videometrics III, Boston, Massachusetts, November 2-5, Vol. 2350, pp. 306-321.

El-Hakim, S. F. and Beraldin, J.-A., (1995). "Configuration Design for Sensor Integration," Proceedings of SPIE Conference, Videometrics IV, Philadelphia, Pennsylvania, October 23-26, Vol. 2598, pp. 274-285.

El-Hakim, S. F. (1995). "3-D Range-Camera Calibration," User manual draft, National Research Council of Canada, Institute for Information Technology, Ottawa, Ontario, January, 20pp.

Fraser, C. S. (1984) "Network Design Considerations for Non-Topographic Photogrammetry," Photogrammetric Engineering and Remote Sensing, 50 (8), pp. 1115-1126.

Fraser, C. S., Shortis, M. R., Ganci, G. (1995) "Multi-Sensor System Self-Calibration," Proceedings of SPIE Conference, Videometrics IV, Philadelphia, Pennsylvania, October 23-26, Vol. 2598, pp. 2-19.

Fuss, B. C. and Teskey, W. F. (1993) "New and Existing Techniques for the Alignment of Rotating Machinery," Proceedings of the Seventh International FIG Symposium on Deformation Measurements, Canadian Institute of Geomatics, Ottawa, pp. 173-186.

Lichti, D. D. (1996) "Constrained Finite Element Method Self-Calibration," M. Sc. Thesis, 97 pp., Department of Geomatics Engineering, The University of Calgary, Calgary, 1996.

Leick, Alfred. (1990). GPS Satellite Surveying, with a contribution by Steven Lambert, John Wiley & Sons, New York,

Manual of Photogrammetry, (1980), American Society of Photogrammetry, 4th edition Falls Chuch, Va, USA, pp.733,734.

Mikhail, E. M., Ackerman, F., (1976), Observations and Least Squares, Harper and Row Publishers, New York, NY.

Moffitt, F. H., Mikhail, E. M., (1980), Photogrammetry, Harper and Row Publishers, New York, NY, third edition.

NRC sheets, January 1995, the sheets show the AutoCAD drawing of the internal geometry of the LSS, and provide the derived collinearity equations and the distortion model of the LSS.

NRC, Institute for Information Technology, Annual Report 1993/1994, National Research Council of Canada, Ottawa, Canada, ISSN 1183-9082.

Obidowski, R. M., Teskey, W. F., and Gaidadjiev R. (1995). "Integration of Sensors with Videometry for industrial Machinery Monitoring SPIE Conference, Videometrics IV, Philadelphia, Pennsylvania, October 23-26, Vol. 2598, pp. 295-304.

Rioux, M. (1984). "Laser Range Finder Based on Synchronized Scanners," Applied Optics, November, Vol. 23, No. 21, pp. 3837-3844.

Rioux, M., Bechthold, G., Taylor, D. and Duggan, M. (1987). "Design of a Large Depth of View Three-Dimensional Camera for Robot Vision," Optical Engineering, December, Vol. 26, No. 12, pp. 1245-1250.

Rioux, M.(1994). Personal communications.

Rioux, M., Godin, G., Blais, F. and Baribeau, R. (1993). "Differential Inspection of Shapes Using Optical 3-D Measurements," Optical 3-D Measurement Techniques II Conference, Zurich, Switzerland, October 4-7, 8pp.

Rioux, M. (1994)."Digital 3-D Imaging; Theory and Applications," SPIE Conference, Videometrics III, Boston, Massachusetts, November 2-5, Vol. 2350, pp. 2-15.

Sequeira, V., GonCalres, J. G. M. and Ribeiro, M. I. (1995). "3D Scene Modeling from Multiple Range Views," Proceedings of SPIE Conference, Videometrics IV, Philadelphia, Pennsylvania, October 23-26, Vol. 2598, pp. 114-127.

Tabatabai Ali J., Mitchell O. Robert, O. (1984). "Edge Location to Sub-pixel Values in Digital Imagery," IEEE Transactions on Pattern Analysis and Machine Intelligence, March, Vol. PAMI-6, No. 2, pp.188-201.

Teskey, W. F. and Lovse, J. W. (1994). "The Potential of Laser Scanning for Dynamic Deformation Monitoring," Proceedings of the International Federation of Surveyors (FIG) 20th Congress, Melbourne, Australia, March 5-12, Vol. 6, pp. 603.1/1-603.1/10.

Teskey, W. F., Obidowski, R. M. and Al-Hanbali. N. N. (1994). "Measurements of Machinery Deformations by High-Precision Survey methods," Journal of Surveying and Land Information Systems, Vo.54, No.1, pp. 1-10.

Teskey, W.F., Lovse, J.W., and Al-Hanbali, N.N. (1995a), Deformation, Alignment and Vibration in a Large Turbine-Generator Set, Journal of Surveying Engineering, Vol. 122, No. 2, pp. 65-79.

Teskey, W. F., Obidowski, R. M. and Mugford. S. J. (1995b). "Recent Improvements in Optical Alignment Methods," Reliability, Vol.2, No.3, pp.14-18

APPENDIX A

A1 Image Displaying Processing and Digitization

The software is designed to be suitable for processing LSS and CCD images. The program created is a Multiple-Document Interface (MDI) program. An MDI program is a program that contains several documents, each with its own window, called a child window, which is always contained within a single parent form. The child window can be an image display window, a text window, or a histogram window etc. In the following sections, the various abilities of the software (e.g. displaying raw data images and related data information, drawing histograms, zooming, thresholding, drawing regions of interest, transforming the image according to a specific color palette index, and changing color) are discussed briefly.

Multiple Document Interface Parent Form: Executing the program will display the parent window. From the File Menu, the user can open as many child windows as needed, close the active ones, close all opened child windows, save an active displayed image in a child window, or exit the program. Clicking the mouse on the Window option in the Menu will display a list of all child window names. The user can switch to any child window in this list.

Tools Template: The Tools template is a child window of the MDI program, see Figures 5.2 and 5.3. This window provides the user with all the needed tools for image display, analysis, digitizing, and edge detection. The user can open an image for display, close the

image, open another image, or zoom the displayed image. The user can examine the raw pixel values of the image, and change the color palette. One can also draw overlay tools to form a region of interest and draw a histogram or a cross-section and display the overlay data information for this region. Another important feature is the control of editing and displaying an image within certain threshold values and color index values. Tools available on the tool bar are selecting, copying, subtracting, clipping, and showing information options of a selected region or an entire image. Once the information dialog box is displayed, the user can choose to display the histogram or to draw a contour image, or a cross-section image if the region of interest is a line.

Raw Data Images: Once the user clicks the "Open Image" button, and chooses the extension of the LSS images (i.e. *.p for depth coded images or *.i for intensity images) a new dialog box is prompted to specify the size of the chosen image before displaying the image. The program is also capable of opening other types of raw images. Once the user specifies a filename with an extension *.raw, another dialog box is prompted to specify the size of the image header, the image size (i.e. number of columns and number of rows in pixels), and the type of the image raw data. The registered value of each pixel in raw image data can be either 8 bits (one byte) or 16 bits (two bytes). The two bytes pixel can be specified as unsigned type and can be swapped. These options are important when dealing with digital cameras. For example, a typical CCD camera produces 8 bit raw data images. The LSS produces unsigned 16 bit raw data images. Also, if these images are from the OS9 system (the laser scanner internal processor system), then the bytes must to

be swapped, see the LSS image types displayed in Figures 5.2 and 5.3. Finally an image can be saved and converted into various formats.

Zooming: The user can control the horizontal and vertical magnification factors, zoom the image in and out, or set the image to its original size. The magnification factor for both axes is displayed in the box at the right bottom corner under the image display box. Each time the zoom factor is changed, the magnification box is automatically updated.

Overlay Tools and Region of Interest: The overlay tools developed for this program are the pin tool, hand tool and four regions of interest tools (rectangular, ellipse, line, and free hand). For any region of interest, the user can display a histogram, a cross-section or a contour, and the data information. A brief description of these tools is as follows:

1. **Pin Tool:** Redisplays the image with a magnification factor of one. The pixel's registered value and the pixel coordinates at the mouse position are displayed in the box under the image display box when the mouse moves over the image.

2. **Hand Tool:** Allows the user to move the image inside the image display box. The region of interest tools or the magnification factor does not affect it.

3. **Region of Interest Tools:** Draws, using a mouse, a shape surrounding the region of interest using one of the following tools:

- **Rectangular Tool:** draws a rectangle.
- **Ellipse Tool:** draws an ellipse.
- **Line Tool:** draws a line.
- **Free Hand Tool:** draws any closed shape.

4. **Data set Information and Histogram:** These options are only operational if the region of interest is selected. The information displayed is the number of pixels inside the selected region or image, the maximum, the minimum and the mean pixels values. This information is based on all pixels included inside the region of interest including the pixels underneath the drawn tool.

5. **Contour or Cross-section Image:** If the region of interest selected is a line, then cross-section image of the pixels underneath the drawn line is displayed, see the bottom image displayed in Figure 5.3. For the other regions of interest, a contour cross-section is drawn.

6. **Transformation:** The region can be flipped or mirrored vertically and horizontally. The image can also be rotated ninety degrees clock-wise or counter-clock wise.

Threshold: Changing the maximum and/or the minimum threshold values will cause the program to re-allocate the color index size of the color palette to the values between the maximum and minimum threshold. It will thus cause the transformation to be re-applied and the image to be re-displayed. In this transformation, any value more than the

maximum threshold will be re-assigned the color of the maximum color index palette and vise versa.

Filtering Masks: Several filtering masks are provided for image analysis, digitization, noise removal and edge preservation. These masks are smooth, sharpen, low pass, high pass, mean, median, laplace, gradient and custom filters.

Transformed Color Index, Color Palette Editor and Color Palette: Color index transformation controls the number of colors used to display the raw data image within the specified number. This is useful for displaying surface deformations, where each range of movements can be assigned a specific color. Pressing the palette button in the tool template displays the color palette editor, which is useful for displaying an image in certain colors and color gradients. The user can create a new color palette, load a color palette, edit a color palette, or save a color palette. The index size of any color palette can be within the range 0 to 255. An index value of zero means there is only one color in the palette, and 255 means there are 256 colors (from 0 to 255). The color palette shown in Figure 5.2 or 5.3 shows the assigned range of pixels registered values for each color. The palette allows the scaling of these registered values as illustrated in the figures.

A2 Precise Edge Detection and Target Location

The procedure to measure the centre of a target using the software is:

- Draw a rectangular window around the target of interest using the "Rectangle Tool". Make sure that the target is completely inside the window.
- Select the method to extract the target center from the Tools template (i.e. either the moment preserving method or the centroid method). A dialog box is prompted asking the following information: the color of the circular target (either black or white), the least squares adjustment method (i.e. parametric or combined), and the mask value. If the value of the mask is not known, the user can first draw a histogram of that window to help identify the value.
- Click OK to extract the adjusted parameters of the target centre.
- The data can be saved to a chosen text file.

A similar procedure is used to measure the straight-line parameters. First, draw a rectangular window around the fitted-line of interest using the Rectangle Tool. Note that the window has to be rectangular and proportional to the length of the fitted line. Comparing the height and the width of the window will determine whether the line of interest is horizontal or vertical. It is important that the fitted-line be longer than the width of the window if the line is horizontal and longer than the height of the window if the line is vertical. Clicking the "Line Fitting" button extracts the adjusted parameters of the straight line.

IMAGE EVALUATION
TEST TARGET (QA-3)

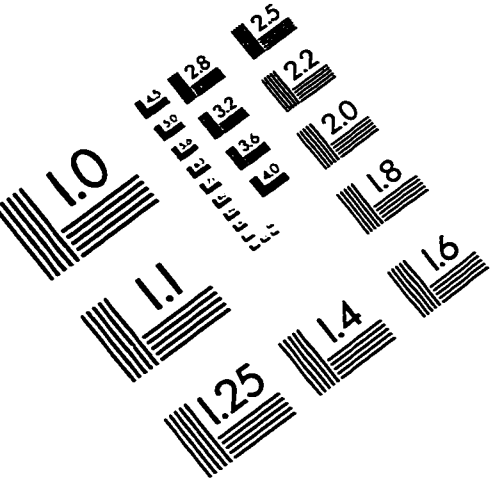

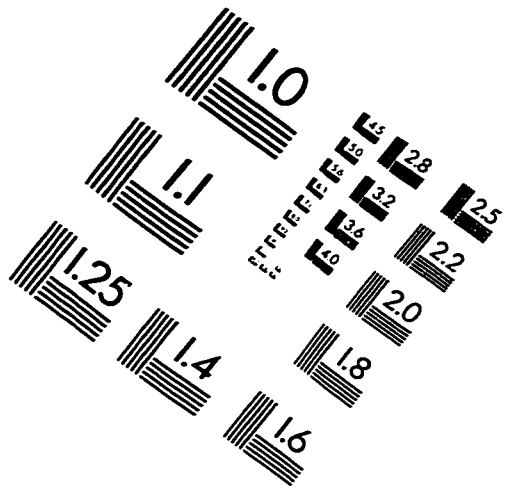

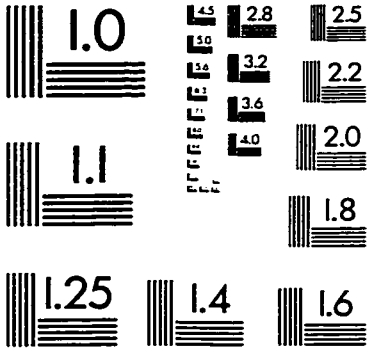

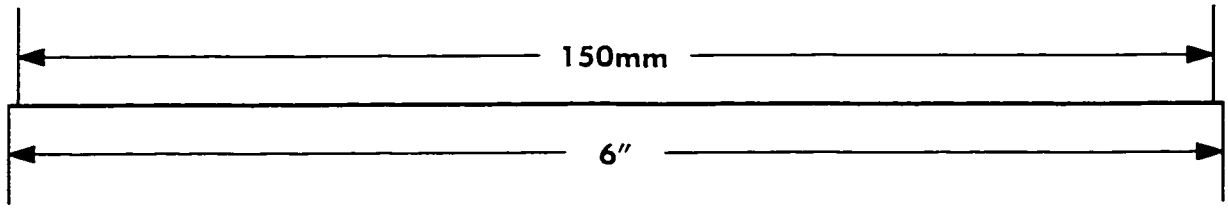

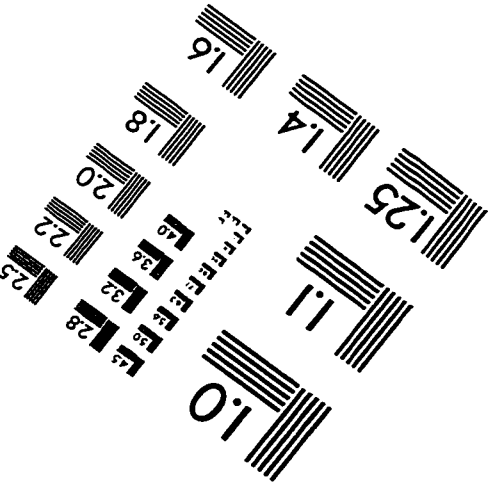

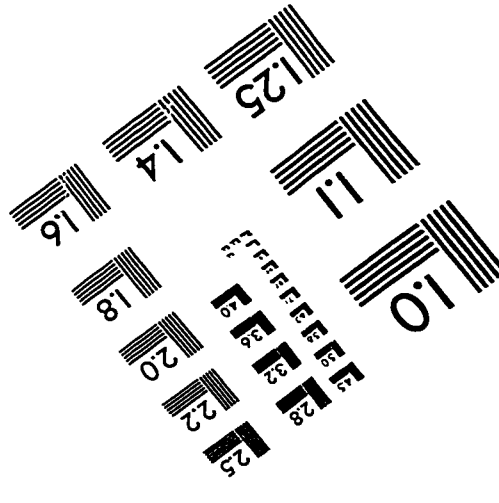

APPLIED IMAGE, Inc
1653 East Main Street
Rochester, NY 14609 USA
Phone: 716/482-0300
Fax: 716/288-5989